T-rHEX: Modeling and Optimization of a Novel Turbo Recuperator Heat Exchanger Concept for Waste Heat Recovery Systems

Fluid and thermal modeling of diffusers operating with non-ideal compressible swirling flows

Enrique Manuel Barrera Alvarez

Delft University of Technology

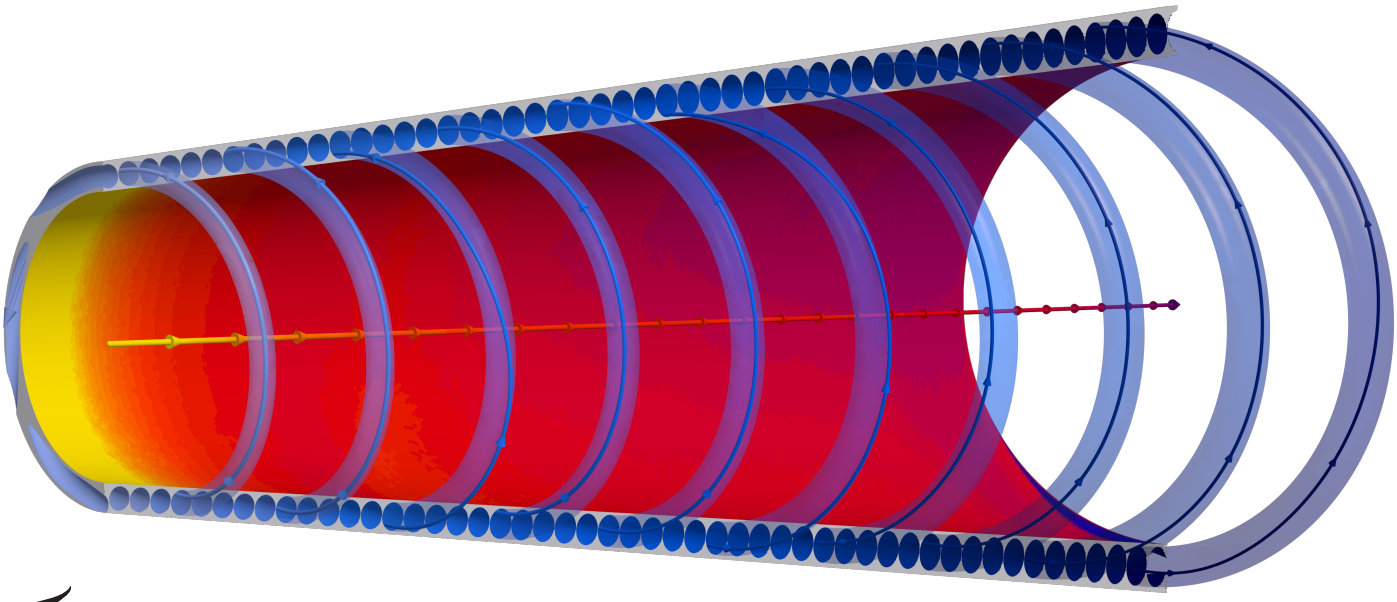

TU Delft

T-rHEX: Modeling and Optimization of a Novel Turbo Recuperator Heat Exchanger Concept for Waste Heat Recovery Systems

Fluid and thermal modeling of diffusers operating with non-ideal compressible swirling flows

by

Enrique Manuel Barrera Alvarez

to obtain the degree of Master of Science

at the Delft University of Technology,

to be defended publicly on Friday December 12, 2025 at 10:30 AM.

Student number:	5243629
Project duration:	March, 2025 – November, 2025

Thesis committee:

Chair:	Prof.dr.ir P. Colonna di Paliano	TU Delft
Supervisor:	Dr.ir. M. Pini	TU Delft
External examiner:	Dr. S.J. Hulshoff	TU Delft

An electronic version of this thesis is available at http://repository.tudelft.nl/.

TU Delft

Acknowledgements

I would like to express my gratitude to the individuals who have played a significant role throughout my studies at TU Delft. This period has been instrumental in shaping me both as an engineer and as a person.

I sincerely thank Professor Pini. You have given me the motivation to keep improving my knowledge on this complicated field of engineering. I thank you for not only placing your trust in me with this project, but also for your guidance on topics that, prior to this work, I would have considered beyond my reach.

I extend my gratitude to several close friends whose support has been invaluable. First, I thank Matei for reliably showing up for me, from high school all the way to this day. I also thank Vishwa for consistently bringing his positivity and humor, even during challenging periods. Lastly, I thank Serban for not only being the greatest assignment partner to work with but also someone who has always made time for me when needed. I wish each of you the very best, and I am confident that you will go on to achieve remarkable things.

Lastly, I wish to thank my girlfriend Daria for her unconditional support through these stressful moments. You have been my anchor and I can never thank you enough for it. I would also like to thank my family, especially my father, my mother and my sister for always being there for me. They have given me the opportunity to be where I am today, and without their support, this would not have been possible.

"Una persona con pasión en lo que hace está comprometida de corazón."- Papá

Enrique Manuel Barrera Alvarez
Delft, December 2025

Abstract

This final Master Thesis study is part of a project within the Propulsion & Power Group at the Delft University of Technology. The study investigates the feasibility of a Turbo-recuperator Heat Exchanger (T-rHEX) as a novel compact regeneration concept for the Organic Rankine Cycle waste heat recovery system that resembles the ORCHID facility. The motivation rises from the need to increase cycle efficiency and power density of the system by recuperating thermal energy discharged through the turbine diffuser, thereby reducing the required size of the primary heat exchangers. The T-rHEX concept is such that the coolant channels are wrapped around the exterior of the diffuser wetted surface so that the diffuser operates simultaneously converting kinetic energy to pressure and as a heat exchanger.

To analyze the fluid dynamic and thermal performance characteristics of the T-rHEX, an in-house low fidelity quasi-1D model (`T-rHEX`) is developed. This tool discretizes the diffuser into cells where geometry, flow and thermal properties are stored based on solver results. Given the known local properties, global properties are obtained in order to quantify both heat exchanger performance and fluid dynamic performance of both streams. Using the existing ORCHID turbine diffuser as a recuperator increases the thermal efficiency of a baseline high-temperature ORC system in simple configuration from **12.11%** to **12.53%**, corresponding to a **0.42** percentage point gain and a **3.5%** relative improvement.

In order to further improve ORC efficiency, the geometry of the diffuser is parametrized and optimized in order to maximize the aero-thermal performance of regenerative diffuser using the low fidelity model. The resulting optimized T-rHEX provides a **1.05** percentage point gain in ORC thermal efficiency with respect to the baseline configuration without regeneration, improving heat exchanger effectiveness and compactness while maintaining an acceptable level of diffuser pressure recovery.

To verify the results, a high fidelity (3D) conjugate heat transfer model is constructed to capture 3D effects such as flow separation and solid–fluid interaction. The comparison between low and high fidelity model results shows that the low fidelity model is comparatively accurate, capturing trends well in terms of fluid dynamics and global heat transfer behavior when the flow remains attached. In the case of strong non-axisymmetric flow effects are present (such as separation), the accuracy of the low fidelity model breaks down.

Overall, numerical results demonstrate that the T-rHEX concept improves cycle efficiency compared to the original cycle without recuperation. The addition of a compact recuperator such as the T-rHEX not only reduces thermal duty of the primary heat exchanger components of the cycle but also increases diffuser pressure recovery due to cooling effect.

Contents

List of Figures

List of Tables

Nomenclature

List of abbreviations

Abbreviation	Definition
BZT	Bethe-Zel'dovich-Thompson
CFD	Computational Fluid Dynamics
ECS	Environmental Control System
EoS	Equation of State
HMC	High Molecular Complexity
LMC	Low Molecular Complexity
LMTD	Logarithmic Mean Temperature Difference
N1D-Flow	Non-ideal quasi 1 Dimensional Flow
NICFD	Non-Ideal Compessible Fluid Dynamics
Ntu	Number of heat transfer units
ORC	Organic Rankine Cycle
ORCHID	Organic Rankine Cycle Hybrid Integrated Device
SLSQP	Sequential Least Squares Programming
T-rHEX	Turbo-recuperator Heat EXchanger
WHR	Waste Heat Recovery
XDSM	eXtended Design Structure Matrix

List of symbols

Symbol	Definition	Unit
A_c	Cross-sectional area	[m^2]
A_s	Surface (wetted) area	[m^2]
$\dot{C}$	Thermal capacitance (heat capacity rate)	[W/K]
C_p	Diffuser pressure coefficient	[-]
F	Heat exchanger correction factor	[-]
N	Normalised temperature difference	[-]
Ntu	Number of heat transfer units	[-]
P_V	Compactness parameter	[m]
$\dot{Q}$	Heat transfer rate	[W]
R	Specific gas constant	[J/(kg K)]
R_{TC}	Thermal capacitance ratio	[-]
$\mathrm{R_{total}}$	Thermal resistance	[K/W]
$\mathcal{R}_{universal}$	Universal gas constant	[J/(mol K)]
Re	Reynolds number	[-]
Re_D	Reynolds number based on diameter	[-]
T	Temperature	[K]
U	Overall heat transfer coefficient	[W/(m^2 K)]
V	Volume	[m^3]
W	Work	[J]
$\dot{W}_{pump}$	Pump power	[W]
Z	Compressibility factor	[-]
a	Intermolecular attraction parameter (EoS)	[Pa m^6/mol^2]
b	Co-volume parameter (EoS)	[m^3/mol]
c_f	Friction coefficient	[-]
c_p	Specific heat capacity at constant pressure	[J/(kg K)]

Symbol	Definition	Unit
c_v	Specific heat capacity at constant specific volume	[J/(kg K)]
d_H	Hydraulic diameter	[m]
e	Specific internal energy	[J/kg]
h	Specific enthalpy	[J/kg]
h_c	Convective heat transfer coefficient	[W/(m^2 K)]
k	Thermal conductivity	[W/(m K)]
p	Pressure	[Pa]
$\dot{q}$	Heat flux	[W/m^2]
r_{eq}	Equivalent radius	[m]
s	Specific entropy	[J/(kg K)]
u	Velocity (magnitude or axial)	[m/s]
$\vec{u}$	Velocity vector	[m/s]
α	Swirl angle	[rad]
α_t	Twist angle	[rad]
$\delta_{curvature}$	Curvature ratio	[-]
ϵ	Heat exchanger effectiveness	[-]
η_{rankine}	Rankine cycle thermal efficiency	[-]
μ	Dynamic viscosity	[kg/(m s)]
ρ	Density	[kg/m^3]
τ	Shear stress	[Pa]
v	Specific volume	[m^3/kg]
$\vec{\omega}$	Vorticity vector	[s^{-1}]

1 Introduction

Fossil fuels have been powering the aviation sector since their early days. The Wright brothers used a gasoline fed 4 cylinder four-stroke engine to power the first sustained flight back in 1903[1]. Ever since, our dependence on fossil fuels for commercial aircraft has led to environmental concerns.

Current aviation fuels such as unleaded kerosene (Jet A-1), or naphta-kerosene blends (Jet B) provide a highly dense source of energy, as well as higher performance characteristics, such as higher self-combustion pressure and temperature. These properties make it ideal for aircraft to use as energy source. Despite efforts to switch to less pollutant alternative fuels, current aero engine technology implementations with such carbon emitting fuels cannot be matched in terms of power-to-weight ratio and cost-effectiveness. This makes transition to greener alternatives a challenging topic in the future.

A significant portion of the energy released during the combustion process in engines is lost as heat, which contributes to inefficiencies in energy conversion. Although modern aero engine technology is able to convert this energy into thrust in a highly efficient manner, the nature of the process will always result in excess unused thermal energy being released into the atmosphere. Based on conservative estimates, 150 TWh of electricity could be generated on a yearly basis if this exhaust thermal energy was recovered [16]. Therefore, research is underway to develop methodologies for capturing this 'lost' energy, thereby improving efficiency, reducing fuel consumption, and significantly lowering emissions.

1.1. Organic Rankine Cycle

The Rankine cycle is a thermodynamic process that converts thermal energy into mechanical work through the expansion of a phase-change working fluid. Heat from a high-temperature source vaporizes the fluid, which then expands through a turbine before being condensed and pumped back to the evaporator. In its conventional form, the cycle uses water as the working fluid, which confines effective heat recovery to comparatively high-temperature sources because of water's saturation properties.

Replacing water with an organic compound yields an Organic Rankine Cycle (ORC), whose lower boiling point and fluid specific thermophysical characteristics allow the recovery of low to medium temperature heat streams, including gas turbine exhaust flows in aerospace and industrial settings [8]. In the high temperature ORC configurations, with heat source temperatures around $670\,\mathrm{K}$, the selection of suitable organic fluids enables more favorable saturation properties and expansion behavior than water, which translates into improved cycle efficiency and thus mass specific power for given design constraints. These advantages make high temperature ORCs particularly well suited for integration into propulsion systems where heat sources are available but space, mass, and cooling capacity are limited.

Implementation of waste heat recovery (WHR) in aero engines has been explored across several architectures [8]. In turboshaft configurations, exhaust gases feed an evaporator, while condensation is achieved by rejecting heat to ambient air, either via a ram-air duct or by placing the condenser in the bypass duct, thus forming an air-cooled ORC bottoming unit (i.e., an ORC whose condenser uses external airflow rather than a liquid coolant loop). Integrating evaporator, air-cooled condenser, pump, and expander yields a closed-loop Rankine cycle that, with an organic working fluid, recovers shaft-compatible power without imposing a liquid cooling system on the airframe. The schematic in Figure 1.1 illustrates such an integration on a turboshaft engine, where air cooled heat rejection is the key enabler for compact, WHR system [8].

[1] https://www.wright-brothers.org/Information_Desk/Just_the_Facts/Engines_&_Props/1903_Engine.htm

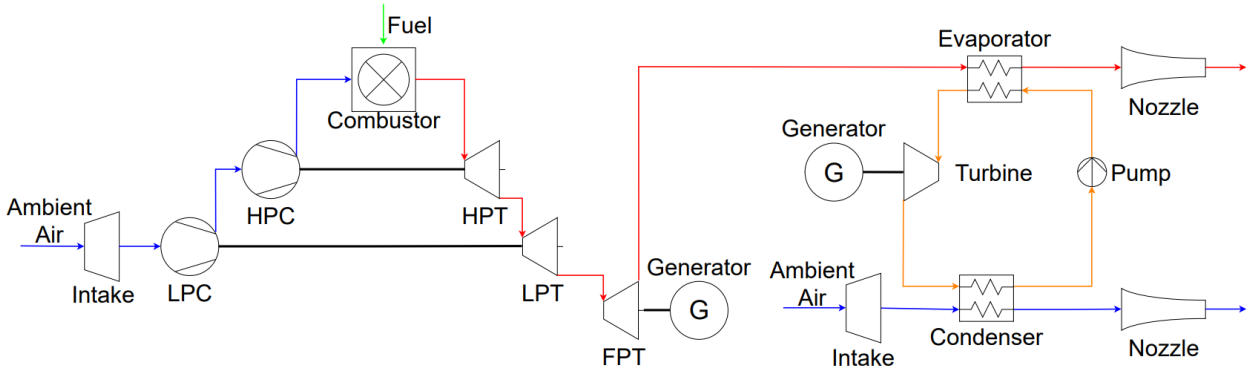

Figure 1.1: Process flow diagram of a turboshaft engine with an air-cooled ORC bottoming unit [8].

Building on that concept, Krempus demonstrates mission-level benefits that depend strongly on how the air-cooled condenser is integrated. When the ORC replaces a conventional APU for ground power (CC-APU), the aircraft sees 0.6% mission fuel reduction. For combined-cycle turboshaft (CC-TS) propulsion, savings are approximately 1.5%. Lastly, for a combined-cycle turbofan (CC-TF) with condensers placed in the bypass duct, savings reach approximately 4% [8]. The contrast between CC-TS and CC-TF arises largely from condenser placement: ram-air ducts versus fan-bypass integration change pressure losses, heat-sink temperature, and installation drag, which in turn set ORC duty, mass-specific power, and net aircraft benefit [8]. These findings indicate that carefully integrated ORC systems can deliver meaningful efficiency gains, pointing to substantial research opportunities for further improving WHR performance in both aerospace propulsion and industrial sectors.

1.2. The ORCHID turbine

At Delft University of Technology, a novel concept for waste heat recovery is being investigated through the Organic Rankine Cycle Hybrid Integrated Device (ORCHID), a small scale Organic Rankine Cycle (ORC) turbine designed to extract additional electrical power from the residual thermal energy of propulsion and power generation systems. This experimental facility has been developed to study and validate the performance of non-conventional small scale turbomachinery operating with organic fluids. The ORCHID program provides an essential platform for investigating non-ideal compressible fluid dynamics (NICFD) phenomena under laboratory conditions. Experimental data obtained from the facility are used to validate computational fluid dynamics (CFD) simulations and to improve the fluid dynamic design of the turbine and associated components.

Beyond its role as a research testbed for fundamental NICFD studies, the Propulsion & Power Group of the Faculty of Aerospace Engineering at TU Delft is examining the potential of the ORCHID turbine as a waste heat recovery (WHR) device. In this configuration, the turbine is integrated into a closed loop ORC in which an organic working fluid undergoes phase transition between liquid and dense vapor states. The turbine expands the heated dense vapor, converting recovered exhaust heat into useful mechanical work. To maximize the work extracted by the turbine and enhance the overall cycle efficiency, a diffuser is coupled downstream of the turbine to recover static pressure from exhaust kinetic energy. Because diffusers are voluminous and influence both system performance and integration feasibility, ongoing research aims to refine their design to achieve higher compactness and effectiveness.

One of the emerging research directions associated with the ORCHID turbine concerns the recovery of residual thermal energy from the turbine exit flow. Colonna proposed employing the diffuser as an active recuperative element, transferring heat from the turbine exhaust to a surrounding coolant channel to improve the closed cycle thermal efficiency[2]. This concept, referred to as the Turbo-recuperator Heat Exchanger (T-rHEX), repurposes the diffuser as a combined fluid dynamic and heat exchange component in which the coolant fully envelops the diffuser walls. While preliminary estimates have demonstrated the potential of the T-rHEX concept, higher fidelity numerical models are still required for comprehensive verification and optimization of the T-rHEX. The present study advances this baseline design by developing an improved low fidelity model suitable for preliminary performance assessment and by extending it with a high fidelity model that increases accuracy on performance results and captures additional physical phenomena not represented in the low fidelity approach.

1.3. Research questions

As discussed previously, a gap remains in the current literature regarding the application of Organic Rankine Cycle (ORC) systems for waste heat recovery, particularly in the use of recuperative components to extract additional thermal energy from turbine exhaust flows when employing organic working fluids. Existing studies rarely address the integration of recuperators capable of operating under the thermodynamic and geometric constraints typical of compact ORC systems. This highlights the need to evaluate the feasibility and potential performance benefits of implementing regenerative diffusers that operate simultaneously as diffusers and thermal recuperators downstream of the ORC turbine.

The present work introduces the Turbo-recuperator Heat Exchanger (T-rHEX) concept and evaluates its performance for a representative high-temperature ORC system in simple cycle configuration. The aim of this project is to quantify the fluid dynamic and thermal performance of the ORC recuperator and to assess its impact on overall cycle efficiency. This leads to the following primary research question:

Research Question RQ

What are the fluid dynamic and thermal performance characteristics of the T-rHEX when integrated into a high-temperature Organic Rankine Cycle waste heat recovery system?

To answer the primary research question, different aspects of the recuperator contributing to the system's performance are considered individually. These are evaluated separately in order to answer the primary research question.

Research Sub-Question RSQ1

To what extent does integrating and optimizing the T-rHEX geometry improve the thermal efficiency of a high-temperature organic Rankine cycle waste-heat recovery system?

Research Sub-Question RSQ2

To what extent does adopting a cross-flow heat exchanger arrangement within the T-rHEX influence its thermal performance?

Research Sub-Question RSQ3

How accurately does the low fidelity (1D) model predict the heat transfer performance of the T-rHEX recuperator compared to the high fidelity (3D) model?

2
Theoretical background

The concept of the T-rHEX covers many aspects of fluid dynamics and thermodynamics. To ensure adequate modeling, these concepts are to be well accounted for. The use of an organic fluid introduces discrepancies when applying models that assume ideal gases, such as air. To account for such discrepancies, the non-ideal gas effects are to be accounted for. Additionally, the implications of integrating the diffuser as a heat exchanger component within the ORC requires understanding of heat transfer effects on heat exchanger performance and fluid behavior. Lastly, to adequately model the diffuser flow, 3-dimensional flow effects on diffusers must be well understood.

2.1. Non-ideal compressible flows

This section is aimed at understanding the effects of non-ideal, compressible flows and their underlying assumptions. Firstly, non-ideal gasses are compared to ideal gasses, in order to understand the critical differences in order to accurately model organic fluids. Secondly, the effects of molecular complexity are given, in order to understand their effects on 1 dimensional (1D) flows. Lastly, the effects of compressibility on gasses are also described, to understand the effects of thermal compressibility and flow (aerodynamical) compressibility.

2.1.1. Comparison of ideal gas to non-ideal gas

For complex fluids, it is important to understand the differences between an ideal or perfect gas and a non-ideal gas. Ideal gases are modeled under the assumption that molecular interactions and the volume occupied by molecules are negligible. These assumptions lead to the well-known ideal gas laws, which are extensively used in thermodynamic and aerodynamic derivations.

$$p\upsilon = \frac{\mathcal{R}_{universal}}{M_{molar}}T = RT \tag{2.1}$$

Implementing the ideal gas assumption can significantly affect fluid properties. Consider thermodynamical properties of a fluid such as internal energy (e) and enthalpy (h).

$$\mathrm{d}e = c_\upsilon \mathrm{d}T + \left[T\left(\frac{\partial p}{\partial T}\right)_\upsilon - p\right]\mathrm{d}\upsilon \tag{2.2}$$

$$\mathrm{d}h = c_p dT + \left[\upsilon - T\left(\frac{\partial \upsilon}{\partial T}\right)_p\right]\mathrm{d}p \tag{2.3}$$

Equation 2.2 and Equation 2.3 can be derived from first and second law of thermodynamics equations combined with the Maxwell relations. These describe the changes in internal energy and enthalpy for any gaseous fluid. Considering now the ideal gas law (Equation 2.1) and substituting into both Equation 2.2 and Equation 2.3 leads to the cancellation of terms non-dependable on temperature changes.

$$\mathrm{d}e = \left(\frac{\partial e}{\partial T}\right)_\upsilon \mathrm{d}T + \tfrac{\left(\frac{\partial e}{\partial \upsilon}\right)}{T}\mathrm{d}\upsilon \approx c_\upsilon \mathrm{d}T \tag{2.4}$$

$$\mathrm{d}h = \left(\frac{\partial h}{\partial T}\right)_p \mathrm{d}T + \tfrac{\left(\frac{\partial h}{\partial p}\right)}{T}\mathrm{d}p \approx c_p \mathrm{d}T \tag{2.5}$$

As a result, assuming ideal gas leads to temperature being the only main contributor dictating the energy of a fluid, effectively decoupling energy from pressure and specific volume/density. In reality, all fluids exhibit real-gas effects and cannot be assumed to behave ideally for all thermodynamic states. These non-ideal gases have pressure and volume contributions to internal energy and enthalpy changes which cannot be ignored.

Most organic vapors deviate significantly from ideal gas behavior. Organic fluids are usually made of complex molecules, often containing polar groups and hydrocarbon chains that experience Van der Waals forces, dipole-dipole interactions, and in some cases, hydrogen bonding. These effects have an impact on their thermodynamic properties, causing them deviate from those predicted by the ideal gas model.

To account for the non-ideal discrepancies, Equation of State (EoS) models are implemented, allowing the calculation of fluid thermodynamic properties. These EoS models are usually built using experimental data, numerical results, or a combination of both. EoS models like the Van der Waals, Soave-Redlich-Kwong or Peng-Robinson equations are commonly used to better account for non-ideal gas behavior. A simple, but effective and widely used volumetric EoS model is the Van der Waals equation:

$$p = \frac{RT}{\upsilon - b} - \frac{a}{\upsilon^2} \tag{2.6}$$

Equation 2.6 accounts for the finite volume of gas molecules, represented by the co-volume parameter (b), as well as the effects of attractive intermolecular forces, represented by the parameter (a). Both terms may be treated as constants or expressed as functions of thermodynamic properties, depending on the model used. To group together all non-ideal effects, the compressibility factor (Z) is utilized:

$$Z = \frac{p\upsilon}{RT} \tag{2.7}$$

The compressibility factor determines how close the non-ideal gas behaves when compared to an ideal conditions. The computation of the compressibility factor as well as other thermodynamic properties will be elaborated upon in subsection 2.1.3.

To fully consider thermodynamic aspects of a non-ideal gas, a set of secondary thermodynamic variables are considered. These set of thermodynamic variables are key to the understanding how temperature, pressure and specific volume are linked with respect to the effects of non-ideal.

Table 2.1: Secondary thermodynamic properties relevant for the study of non-ideal quasi-1D flows[16].

Property	Definition	Ideal gas
Isobaric compressibility	$\beta_p = \frac{1}{\upsilon}\left(\frac{\partial \upsilon}{\partial T}\right)_p = \frac{1}{T} + \frac{1}{Z}\left(\frac{\partial Z}{\partial T}\right)_p$	$\frac{1}{T}$
Isothermal compressibility	$\beta_T = -\frac{1}{\upsilon}\left(\frac{\partial \upsilon}{\partial p}\right)_T = \frac{1}{p} - \frac{1}{Z}\left(\frac{\partial Z}{\partial p}\right)_T$	$\frac{1}{p}$
Isentropic pressure-specific volume exponent	$\gamma_{p\upsilon} = -\frac{\upsilon}{p}\left(\frac{\partial p}{\partial \upsilon}\right)_s = \frac{\gamma}{\beta_T p}$	γ
Isentropic pressure-temperature exponent	$\gamma_{pT} = -\frac{p}{T}\left(\frac{\partial T}{\partial p}\right)_s = \frac{\gamma-1}{\gamma}\frac{\beta_T\, p}{\beta_p\, T}$	$\frac{\gamma-1}{\gamma}$
Fundamental derivative of gas dynamics	$\Gamma = 1 + \frac{\rho}{c}\left(\frac{\partial c}{\partial \rho}\right)_s$	$\frac{\gamma+1}{2}$
Grüneisen parameter for fluids	$G = \frac{\upsilon}{c_\upsilon}\left(\frac{\partial p}{\partial T}\right)_\upsilon = \gamma_{p\upsilon}\gamma_{Tp}$	$\gamma - 1$

The effects of compressibility of a fluid are particularly relevant for non-ideal gases, where deviations from ideal gas behavior arise due to strong intermolecular interactions and high fluid densities. To account for these effects, both the isothermal and isobaric compressibility terms are introduced in the derivation of the thermodynamic relations. The isobaric compressibility (β_p) expresses how the specific volume varies with temperature at constant pressure and captures the fluid's thermal expansion. Conversely, the isothermal compressibility (β_T) quantifies how the specific volume changes with pressure at constant temperature. Non-ideal gasses have an additional contribution to changes in specific volume due to changes in the compressibility factor.

For isentropic processes, the temperature, pressure and specific volume can be linked using the isentropic exponents. For non-ideal gasses, these exponents differ from just simply the specific heat capacity ratio (γ). The pressure–specific volume exponent ($\gamma_{p\upsilon}$) relates pressure and specific volume through $p\upsilon^{\gamma_{p\upsilon}} =$ constant and simplifies to γ for ideal gases. Similarly, the pressure–temperature exponent (γ_{pT}) governs the relationship

$Tp^{-\gamma_{pT}} =$ constant and equals $(\gamma - 1)/\gamma$ for ideal gases. Effects of isobaric and isothermal compressibility play a direct role in the isentropic exponents, representing the deviation from the ideal gas model.

Finally, the fundamental derivative (Γ) effects the curvature of isentropic and the variation of sound speed with density, while Grüneisen parameter links thermodynamic variables to molecular vibrational modes, providing a quantitative measure of molecular complexity. Since both parameters are central to understanding the effects of molecular complexity, their roles are discussed in detail in subsection 2.1.2.

2.1.2. Effect of molecular complexity

For single-phase non-ideal fluids, the molecular complexity of a fluid is generally characterized by the size, shape, and chemical composition of its molecules. Organic fluids such as siloxanes are composed of large elongated molecules, categorizing them as molecular complex fluids, thus understanding the effects of molecular complexity is of importance when working with organic fluids such as siloxanes.

The fundamental derivative of gas dynamics (Γ) characterizes the behavior of the fluid by considering the isentropic variation of speed of sound with changes of density. The value of Γ depends strongly on molecular complexity and thermodynamic state of the fluid.

Low molecular complexity (LMC) fluids experience weak intermolecular forces. The effect of molecular complexity on the fundamental derivative of gas dynamics is therefore weak. For LMC fluids where $\Gamma_{min} > 1$, the speed of sound increases during isentropic compression and decreases during isentropic expansion, similar to polytropic ideal gas flows[4].

High molecular complexity (HMC) fluids experience strong intermolecular forces that cause non-monotonic speed of sound variations with density. The effect of HMC fluids becomes significant, the fundamental derivative of gas dynamics is found to be between 0 and 1 ($1 > \Gamma_{min} > 0$). Within this regime, the variation of speed of sound opposes to expected ideal gas variations, where speed of sound decreases upon compression and increases upon expansion. However, the non-monotonic effects are not sufficiently strong for other thermodynamic properties of the fluid to vary qualitatively from the ideal gas behavior. Due to this reason, the gas dynamics of LMC and HMC fluids is referred to as classical[4].

For very high molecular complexity fluids, known as Bethe-Zel'dovich-Thompson (BZT) fluids, where states can be characterized by $\Gamma_{min} < 0$, the non-ideal effects are sufficiently strong to cause significant qualitative differences from the ideal gas behavior. These effects are categorized as non-classical gas dynamics. So far BZT fluids have only been tested within laboratories for scientific purposes, thus under rare circumstances, an organic working fluid can be categorized as a BZT fluid[4].

For the ORCHID diffuser configuration, Colonna computed the variation of Γ along the flow path, concluding the fundamental derivative remains between 0 and 1. This indicates that the working fluid (hexamethyldisiloxane: MM) behaves according to classical gas-dynamics principle under the operating conditions of the ORCHID diffuser. Consequently, non-ideal effects due to molecular complexity are expected to be present, showing only quantitatively different from their corresponding ideal gas flow results.

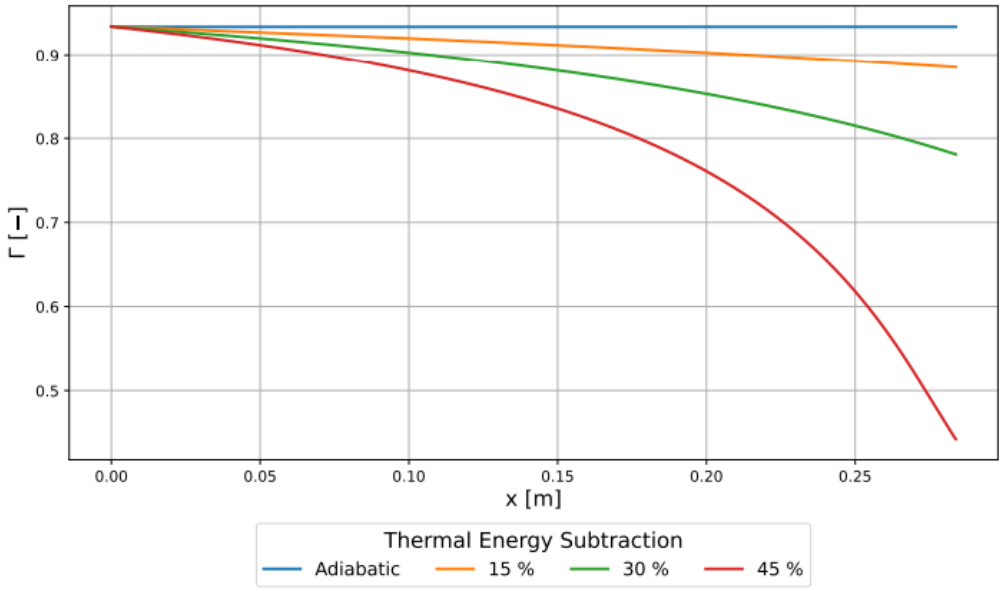

Figure 2.1: Fundamental derivative trend for MM (siloxane) as the working fluid for different levels of wall cooling. Geometry of the diffuser was taken with reference to the ORCHID diffuser[2].

Additionally, Figure 2.1 shows that increasing wall cooling decreases Γ but does not drive it below 0, remaining consistent with that of a high molecular complexity (HMC) fluid. Although cooling lowers the fundamental derivative, the effect is insufficient to qualitatively depart from classical gas-dynamics. Consequently, while quantitative deviations from the ideal-gas model are observed, the qualitative flow behavior remains consistent with classical gas-dynamics predictions.

To consider molecular complexity in heat transfer effects, Tosto shows how the Grüneisen parameter is inversely proportional to molecular complexity, with additional terms accounting for compressibility effects[16]. As the size of the molecules increases, the number of degrees of freedom also increases, introducing additional molecular motion. High molecular complexity fluids can distribute their internal energy into more degrees of freedom, thus translational motion receives a smaller part of energy, leading to smaller temperature changes. This is reflected in the high specific heat capacity values of the HMC fluids. As seen in Table 2.1, the Grüneisen parameter is also inversely proportional to the specific heat capacity of the fluid. Therefore, for HMC fluids, the Grüneisen parameter is lower compared to LMC fluids[16]. Colonna investigated the effect of molecular complexity on temperature, showing static temperature plots in which LMC fluids exhibit much greater temperature differences than HMC fluids [2]. This property enables HMC fluids to transfer energy efficiently with smaller temperature variations, helping the working fluid remain within the same phase during operation.

To conclude on the effects of HMC fluids, Colonna built a low fidelity model code for quasi-1D flows to predict the change of thermodynamic variables along a diffuser for both adiabatic and cooled conditions.

Table 2.2: Comparison of LMC and HMC fluids in compressible swirling flows for adiabatic and cooled cases, indicating qualitatively which fluid shows a greater change between inlet and exit conditions[2].

	Adiabatic	Cooling (45% heat extraction)
Mach number	LMC ≈ HMC	LMC > HMC
Absolute velocity	LMC ≈ HMC	LMC > HMC
Static temperature	LMC > HMC	LMC > HMC
Static pressure	LMC > HMC	LMC > HMC
Total pressure	LMC > HMC	LMC < HMC
Swirl angle	LMC > HMC	LMC > HMC

Table 2.2 presents the normalized difference between Hydrogen (treated as a Low Molecular Complexity (LMC) fluid) and MM (treated as a High Molecular Complexity (HMC) fluid) thermodynamic properties, without

considering the overall results of the thermodynamic variables along the channel. In general, it can be concluded that the use of an HMC fluid results in a reduced variation of thermodynamic properties in response to changes in area, heat transfer, and wall friction effects. However, this effect is not always uniform, as some influences may interfere with each other. This phenomenon is particularly evident in thermodynamic variables such as total pressure, where the opposing effects of friction and cooling interact, with the local dominance of one effect determining the overall outcome. Overall, LMC fluids exhibit much steeper gradients along the flow, indicating that even under identical flow expansion and cooling conditions, their thermodynamic properties fluctuate far more than those of HMC fluids.

In conclusion,the implementation of an organic working fluid has many benefits over implementing a LMC fluid. HMC fluids, such as organic fluids, allow for higher amounts of energy transfer without requiring large temperature changes. This makes them ideal for ORC systems since exhaust temperatures are relatively small. Using an HMC fluid allows for extracting larger amounts of thermal energy at lower temperature differences between streams, making them ideal for the use in ORC systems.

2.1.3. Effect of Compressibility

Flow compressibility can be interpreted from both thermodynamic and aerodynamic perspectives. From a thermodynamic standpoint, compressibility effects describe the deviation from ideal gas behavior. This deviation is characterized by the compressibility factor (Z), defined as the ratio between the specific volume of the non-ideal gas and that of an ideal gas at the same temperature and pressure:

$$Z = \frac{\upsilon}{\upsilon_{\text{ideal}}} \tag{2.8}$$

A value of $Z = 1$ corresponds to ideal gas behavior, whereas deviations from unity reflect the influence of intermolecular forces and the finite co-volume occupied by non-ideal gas molecules.

From an aerodynamic perspective, flow compressibility is identified through variations in the flow field, most notably by the divergence of the velocity field. In a compressible flow, a non-zero divergence represents local density variations within the flow. Although molecular interactions do not appear explicitly in this kinematic description, they indirectly influence the flow through their effect on thermodynamic properties such as density and pressure. The deviation between compressible and incompressible flow behavior decreases with increasing molecular complexity[4]. In HMC fluids, the larger number of internal degrees of freedom increases specific heat capacities, allowing thermal energy to be absorbed internally rather than converted into temperature and density variations. As a result, the flow becomes less sensitive to compressibility effects.

When compressibility effects are small, the flow may be approximated as incompressible, meaning that the velocity field is divergence-free ($\nabla !\cdot ! \vec{u} = 0$). In such cases, density and other thermodynamic properties are decoupled from the kinematics of the flow. Considering an incompressible flow implies that the kinematic flow field does not change thermodynamic field quantities but it does not assume constant thermodynamic properties. For example, for constant temperature, an incompressible flow would lead to constant density. However, if temperature varies, density gradients may still exist due to thermal effects rather than compressibility.

Overall, it is important to distinguish between aerodynamic compressibility, associated with variations in velocity and density fields, and thermodynamic compressibility, which arise due to deviations from ideal gas behavior. While factors such as molecular complexity influence both, each contributes distinctly to the overall flow behavior. Consequently, aerodynamic and thermodynamic compressibility should be assessed individually.

2.2. Integrated Turbine-Heat Exchanger

Traditional Rankine cycles have long been employed to recover energy from heat sources and convert it into mechanical power. Historically, steam power plants demonstrated the effectiveness of this process by generating high pressure steam in boilers and expanding it through steam turbines to produce mechanical work. The Rankine cycle consists of a heat intake stage, a work extraction stage, and a condenser stage. Additionally, a pump is required to overcome pressure losses across the condenser to achieve the required mass flow rate. The thermal efficiency of a Rankine cycle is defined as the ratio of the net work output to the total heat input supplied to the cycle.

$$\eta_{\text{rankine}} = \frac{\dot{W}_{\text{net}}}{\dot{Q}_{\text{input}}} = \frac{\dot{W}_{\text{turbine}} - \dot{W}_{\text{pump}}}{\dot{Q}_{\text{input}}} \tag{2.9}$$

Rankine cycles operating with steam generally exhibit modest thermal efficiencies, limited by the temperature difference between the heat source and the sink. However, when integrated into combined cycle configurations, for instance, by coupling a gas turbine with a Rankine bottoming cycle such as in Figure 1.1, the overall system efficiency can be significantly increased. This makes Rankine cycles particularly suitable for waste heat recovery applications, where they can effectively utilize residual thermal energy from other processes.

For the implementation of waste heat recovery (WHR) systems, the limited temperature difference between the heat source and sink constrains the thermal efficiency of Rankine cycles operating with low-grade heat sources and low thermal capacitance. The use of an organic working fluid enables greater thermal power exchange at smaller temperature differences, improving heat recovery effectiveness. Depending on the application, ORC systems operate with temperature differences between the source and sink ranging from approximately $30\,\mathrm{K}$ to $500\,\mathrm{K}$, delivering electrical outputs from a few kilowatts up to several hundred megawatts [16].

Although the adoption of an organic fluid improves heat absorption and rejection characteristics, the overall cycle efficiency remains comparatively low. Tosto shows that the integration of a regenerator can further enhance thermodynamic efficiency by up to 1.2%, by transferring residual thermal energy from the turbine exhaust to the liquid stream at the pump inlet[16]. This reduces external heat input requirements and thereby increases the overall efficiency of the system. However, such regenerative configurations typically require complex heat exchangers, which increase system mass, cost, and design complexity.

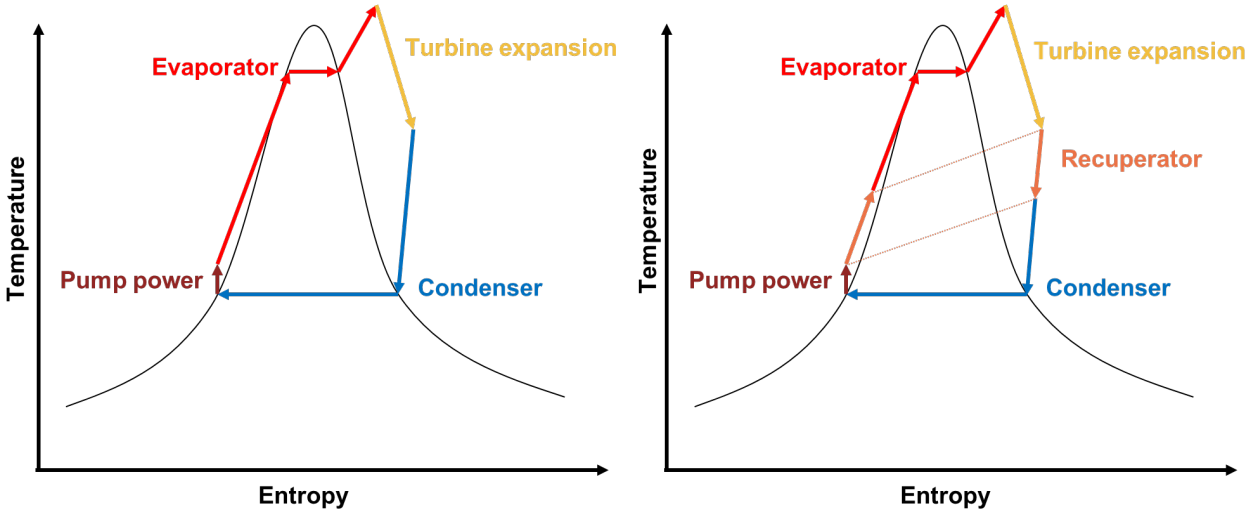

Figure 2.2: Temperature-Entropy diagrams with superheating comparing basic cycle to cycle with a recuperator.

The aim of this project is to integrate a recuperative element into the ORC system to improve cycle efficiency without increasing overall mass or design complexity. The proposed concept repurposes the turbine diffuser as a combined aerodynamic and thermal component, capable of recovering both pressure and thermal energy from the turbine exhaust flow. In this configuration, the diffuser not only converts exit kinetic energy into static pressure to match the condenser pressure, but also transfers residual thermal energy through its walls to a coolant channel upstream of the condenser. This dual functionality enables effective heat recuperation without excessive additional weight.

Conventional diffusers are designed solely for pressure recovery, using a geometrically divergent passage that converts dynamic pressure into static pressure. Their performance depends on flow uniformity, boundary layer development, and separation avoidance, all of which influence pressure recovery and total pressure losses. In the recuperative diffuser concept, these aerodynamic considerations must be coupled with thermal transport effects, as wall heat exchange alters the temperature, density, and viscosity distributions across the flow. The following section describes the specific design principles and performance characteristics of this integrated turbine–heat exchanger configuration.

2.2.1. Concept reasoning

Airborne ORC waste heat recovery systems have shown to be a possible method of saving fuel and increasing efficiency for propulsion and power systems. The model considered by Krempus[8] proved that, without

regeneration, fuel savings up to 4% have been achieved. Considerations to further improve heat recovery are limited both by size and weight, constraining the design scope to incorporate a recuperator within the waste heat recovery system of an aircraft.

To further improve efficiency at a fixed turbine power output, the thermal duty of the cycle must be reduced. In an ORC, the evaporator supplies heat to the working fluid to reach the turbine inlet conditions. By incorporating a recuperator, part of this energy is recovered from the turbine exhaust, reducing the external heat input required in the evaporator. Consequently, the total thermal duty decreases, leading to a higher overall cycle efficiency.

The recuperator itself is a heat exchanger, as it provides a thermal path from the hot exit gas of the turbine to the cold condensed liquid from the condenser. An important drawback of heat exchangers is their bulkiness, an unwanted feature for further improvements since previous designs were limited by size and weight. A solution proposed by Colonna considers the turbine diffuser itself as the heat exchanger, allowing for a countercurrent configuration between the cold liquid around the outside of the diffuser walls and the hot exit gases of the turbine[2]. Since the surface of the diffuser must be present, the increase of structural weight is minimal, only accounted for by additional coolant channeling. On the contrary, by implementing the diffuser as a heat exchanger, the thermal duty of the cycle can be decreased, allowing for reduction in sizes of the condenser and evaporator which would lead to an overall increase in power density of the system and a potential reduction in fuel consumption.

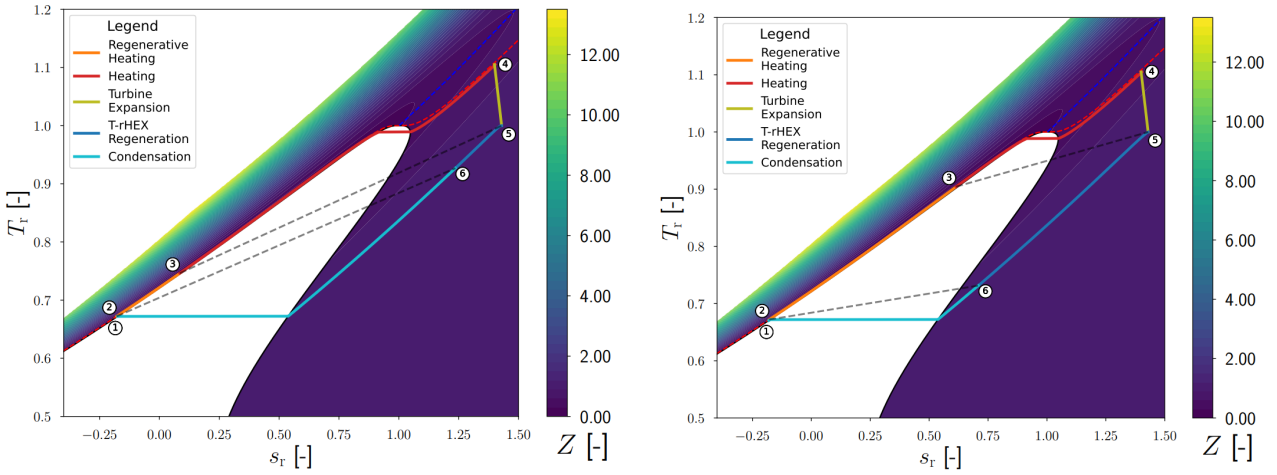

(a) Regeneration considering 15% of total thermal duty.

(b) Regeneration considering 48% of total thermal duty.

Figure 2.3: Temperature–entropy diagrams of the ORC for different degrees of ideal regeneration, expressed as a percentage of total heat input [2].

Figure 2.3 shows the Temperature-Entropy (T-s) diagram with compressibility factor (Z) contours for the same ORC with different levels of regeneration. The cycle stages are numbered according to nomenclature used by Colonna[2]. Figure 2.3 shows the significant effect of difference in regeneration and the thermal duty performed by the evaporator. At the exit of the turbine (point 5), the gasses remain far from their condensation point. Without a recuperator, this thermal rejection would be performed fully by the condenser. By means of a recuperator (from point 5 to 6), part of this thermal rejection can be used for heating of the coolant (from point 2 to 3) once the fluid is at liquid phase after leaving the condenser. The increased heat transfer capacity of the recuperator not only improves the efficiency of the ORC, but also increasing total cycle efficiency. Colonna estimates that 15% regeneration would give a total efficiency increase of **2.08** percentage points, while 48% regeneration would give a total efficiency increase of **11.33** percentage points[2]. While the benefits of implementing a turbine diffuser as a recuperator are evident, its practical feasibility remains uncertain. The large amount of recovered energy may induce undesired phase transitions or prove infeasible under certain flow conditions. To better understand these limitations, subsection 2.2.2 examines the influence of heat transfer on the thermodynamic behavior of the working fluid.

2.2.2. Effect of heat transfer on fluid flows

Heating or cooling a fluid alters its thermodynamic state. The thermal energy carried by the flow is expressed through its thermal inertia, defined by the product of enthalpy and mass flow rate. In non-ideal gases, heat

transfer processes are inherently nonlinear. Thus it is important to understand how thermodynamic variables interact. This subsection explains the effects of heat transfer on heat exchanger performance and on diffuser pressure recovery.

Fundamental of heat exchangers

There are three primary heat transfer mechanisms, these being conduction, convection and radiation. To adequately model heat transfer within the recuperator, it is important to understand which heat transfer mechanism is dominant. Since the system under consideration only deals with relatively low temperatures, the thermal power transferred due to radiation is negligible compared to convection and conduction. Additionally, while conduction has an important role in heat transfer between diffuser flow and coolant channel flow, convection is more restrictive since it dominates the capabilities of exchanging thermal power between the fluid channels and the walls. This makes conduction relevant for unsteady problems, while steady conduction may be treated as a thermal resistor in series with convection thermal resistors (more on this in subsection 3.1.4).

To account for the thermal convection capabilities of both channels, the thermal capacitance is considered (Equation 2.10).

$$\dot{C} = \dot{m} c_p \tag{2.10}$$

$$\dot{Q} = \dot{m} c_p \Delta T = \dot{C} \Delta T \tag{2.11}$$

Fluids with higher thermal capacitance can store and transport greater amounts of thermal energy for the same temperature difference than fluids with lower thermal capacitance. To maximize thermal capacitance, both the mass flow rate and the specific heat capacity must be considered. The mass flow rate is primarily dictated by the power capacity of the plant, as given by ($\dot{W} = \dot{m}\, \Delta h_{\text{turbine}}$). Increasing mass flow rate would either raise the flow velocity, potentially inducing transonic losses, or require a larger flow cross-section, which would increase the system weight. Due to these weight constraints, variations in mass flow rate are not addressed in this study. The specific heat capacity of the working fluid depends on intrinsic thermophysical properties such as phase state, molecular complexity, and thermodynamic condition. Since the objective of a waste heat recovery (WHR) system is to maximize heat transfer from low to medium temperature sources, fluids with higher thermal capacitance such as organic working fluids, are preferred over simple molecular fluids such as steam or air. These maximize thermal capacitance of the channels, allowing to extract more thermal energy at a limited temperature difference between heat source and sinks.

Heat exchanger arrangement also plays a crucial role in heat transfer capabilities. There are three main flow arrangements for heat exchangers:

- **Counterflow:** The fluids enter at opposite ends, having opposite flow directions.
- **Co-current/Parallel:** Both fluids enter the heat exchanger at the same end, having the same flow direction.
- **Cross-flow:** The fluids move perpendicular to each other, having flow directions coinciding at a 90 degree angle.

In practice, heat exchangers often employ combinations of flow arrangements to maximize their thermal effectiveness. These configurations guide the working fluids along specific flow paths. However, at the heat transfer surface, the three fundamental flow arrangements govern the manner in which heat is exchanged between the fluids.

Consider a hot fluid channel exchanging heat with a cold fluid channel. Both fluids are not mixed at any point and there are no phase changes within the channels. As the hot channel is cooled and the cold channel is heated, the temperature difference between them decreases, which in turn reduces the heat transfer. If the channels are arranged in countercurrent flow arrangement, the temperature difference is approximately constant for channels given similar thermal capacitance. In contrary, if there is a difference in thermal capacitance between channels, the channel with highest thermal capacitance undergoes a smaller temperature change, thus the temperature difference between channels changes.

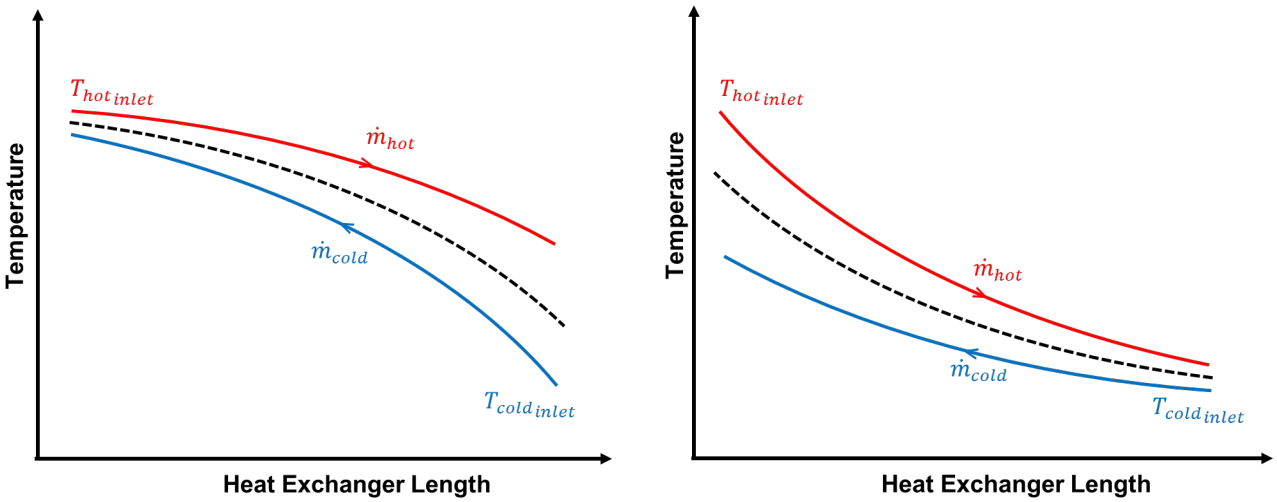

(a) Hot channel thermal capacitance larger than cold channel thermal capacitance.

(b) Cold channel thermal capacitance larger than hot channel thermal capacitance.

Figure 2.4: Temperature distributions along heat exchangers for countercurrent flow arrangement.

Figure 2.4 shows how thermal capacitance limits the heat exchanger capacity depending on the configuration and difference in thermal capacity between channels. If the thermal capacity of the hot channel is higher than the cold channel, the cold channel will see a larger temperature change. For the idealized case, the cold channel will eventually reach the hot channel inlet temperature. This is known as the hot end pinch [5]. Likewise, if the cold channel has higher thermal capacity than the hot channel, the temperature decrement within the hot channel is higher, leading to an idealized cold end pinch [5]. In practice, a pinch is never achieved due to a finite heat transfer surface area.

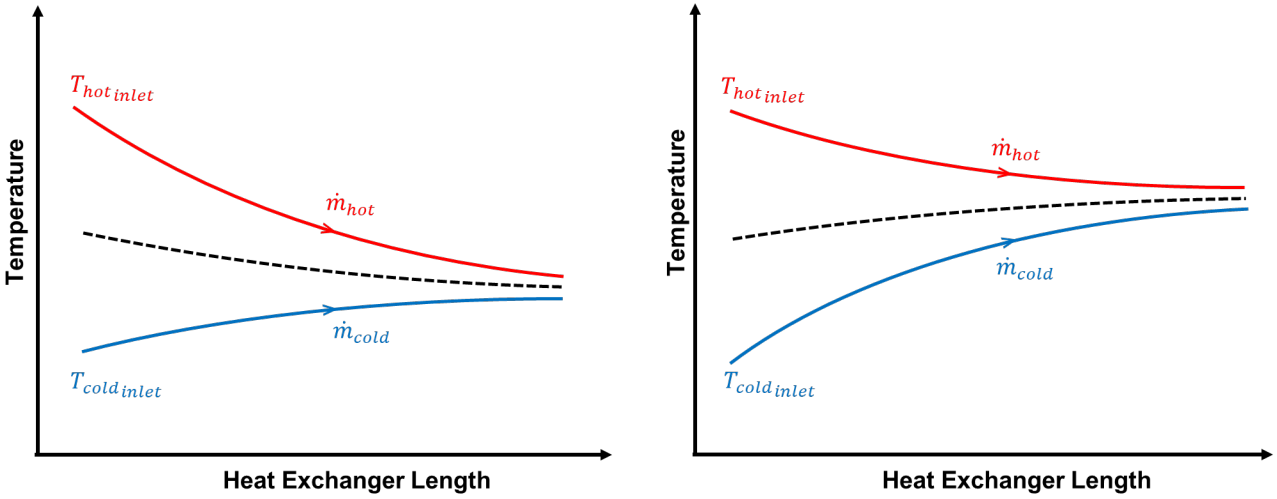

(a) Cold channel thermal capacitance larger than hot channel thermal capacitance.

(b) Hot channel thermal capacitance larger than cold channel thermal capacitance.

Figure 2.5: Temperature distributions along heat exchangers for co-current flow arrangement.

For heat exchangers arranged in co-current flow, the temperature difference is always highest at the inlet independently of thermal capacitance of the fluids. Additionally, for co-current flow arrangements, the exit temperature of the hot channel is always higher than the exit temperature of the cold channel. This is not strictly the case for countercurrent flow arrangement, which allows for higher temperature changes within the channel (as shown in Figure 2.4).

The thermal capacitance of the channels for a co-current flow heat exchangers have a direct effect on the exit temperatures . Figure 2.5 shows that the channel with highest thermal capacitance undergoes a smaller

temperature change. For idealized co-current flow arrangement, a stable state is reached at the outlet, where the limiting temperature is imposed by the highest thermal capacity channel. In practice, a pinch is never achieved due to finite heat exchanger surface area.

Cross-flow heat exchangers can no longer be considered in 1D. As temperature gradients are now introduced perpendicular to the flow, the temperature profiles can no longer be assumed uniform (Figure 2.7a). Cross-flow temperature exchange limits can be concluded based on their overall flow direction. Although locally flows are perpendicular, the net overall flow is countercurrent or co-current. As an example, consider a traditional shell-and-tube heat exchanger. Locally, the tubes are perpendicular to the shell flow. However, the shell flow is curved at ends, returning the flow across the tubes in a counterdirected or codirected manner. This process is repeated until reaching the shell outlet. Depending on the arrangement of the shell inlet and outlet, the shell flow may overall be countercurrent or co-current, which will dictate the temperature limits of the heat exchanger.

To model the 2D effects of cross-flow heat exchange a correction factor (F) is used. This factor scales the effects due to cross-flow perpendicular temperature gradients by comparing a cross-flow arrangement to a perfect countercurrent flow arrangement.

$$F = \frac{\Delta T_{LMTD_{\text{counterflow}}}}{\Delta T_{LMTD_{\text{cross-flow}}}} \tag{2.12}$$

By definition, cross-flow does not need to be perfectly perpendicular. The cross-flow factor represents the influence of a transverse flow component. This factor is typically obtained from semi-empirical correlations derived from experimental data for common heat exchanger geometries [5]. For complex geometries for which experimental data is unavailable, the correction factor must be determined either through dedicated experiments or by applying simplified geometric models to enable numerical estimation.

Up to this point, no phase change has been considered. However, some heat exchangers are specifically designed to account for processes with phase change. Phase change involves the transfer of thermal energy to supply the latent heat required by the working fluid, during which the temperature remains constant.

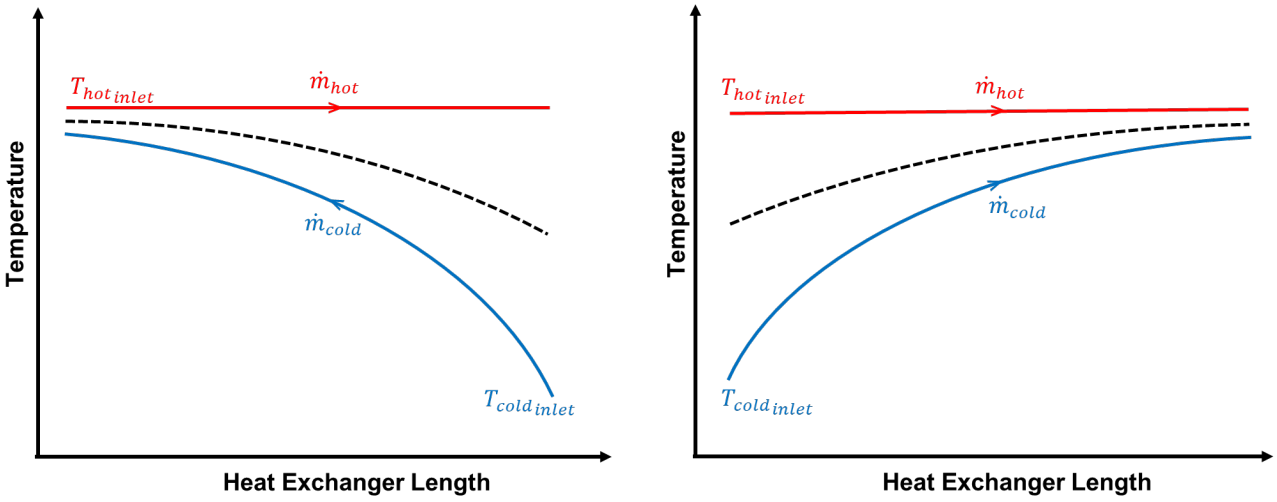

(a) Heat exchanger in countercurrent flow arrangement.

(b) Heat exchanger in co-current flow arrangement.

Figure 2.6: Temperature distributions along heat exchangers with condensation within hot channel and no phase change within the cold channel.

Fluids undergoing phase change have infinite thermal capacity, since phase changes are isothermal processes. Figure 2.6 shows how condensation in the hot channel leads to no temperature drop for both countercurrent and co-current flow arrangements. For a heat exchanger with equal geometrical and inlet properties, if one of the channels undergoes a phase change fully across the heat exchanger, then both countercurrent and co-current flow arrangement would result in the same result.

For cross-flow heat exchangers, due to hot channel having a constant temperature, no 2D temperature gradients develop across the heat exchanger. This results in uniform temperature distributions within both channels

(Figure 2.7b). For cross-flow heat exchangers with channels of equal wetted surface area to countercurrent flow heat exchangers, the correction factor equals to one as the logarithmic mean temperature difference (LMTD) is equal. However, if geometric differences between channels exist, the cold-side outlet temperature may deviate from the countercurrent case, and the correction factor may therefore differ from unity.

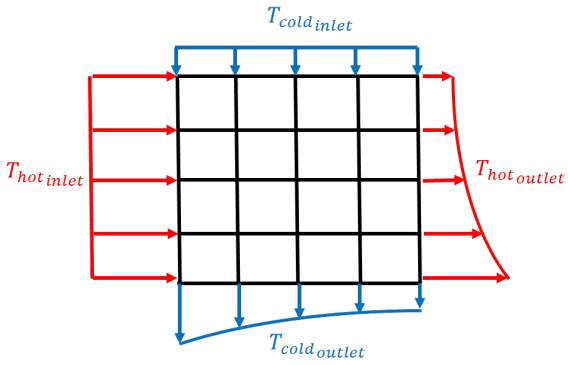

(a) Temperature distribution given constant phase flows.

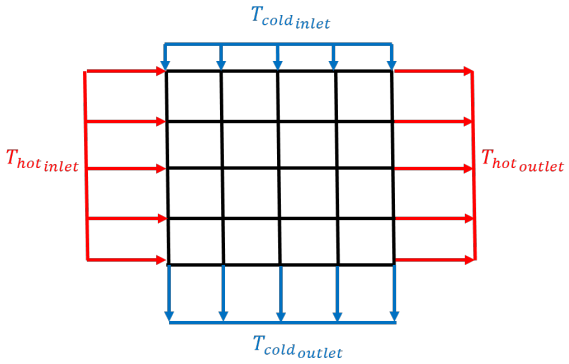

(b) Temperature distribution given a phase change on the hot channel.

Figure 2.7: Temperature distribution for cross-flow arrangement heat exchangers.

A direct comparison between Figure 2.6a and Figure 2.4 shows that a heat exchanger with a channel undergoing phase change achieves a larger temperature difference between channels and, consequently, a higher thermal effectiveness. However, phase change within the diffuser flow can degrade diffuser performance. Therefore, the design of the T-rHEX recuperator aims to avoid condensation within the diffuser to ensure proper turbine–diffuser coupling. Future studies may explore the feasibility of multiphase diffuser flows.

Effects of heat transfer on total pressure

A non-intuitive aspect of heat transfer in fluid flows is the effect of heating or cooling on total pressure. It is often assumed that pressure and temperature vary similarly. For instance, in turbomachinery systems such as compressors, pressure increases are achieved through mechanical work input, which raises the total enthalpy of the flow. This added energy manifests as simultaneous increases in both temperature and pressure. However, as this section will show, such a relationship does not hold for all thermodynamic processes.

Consider the definition of specific heat and specific enthalpy given in Equation 2.13 and Equation 2.14 in differential form.

$$\text{đ}q = \mathrm{d}e + \text{đ}w = \mathrm{d}e + p\,\mathrm{d}v \tag{2.13}$$
$$\mathrm{d}h = \mathrm{d}e + p\,\mathrm{d}v + v\,\mathrm{d}p \tag{2.14}$$
$$\text{đ}q \leq T\,\mathrm{d}s \tag{2.15}$$
$$\mathrm{d}h = T\,\mathrm{d}s + v\,\mathrm{d}p \tag{2.16}$$

Specific heat (q) is and amount of heat per unit mass added into the system. Specific heat is present in the first law of thermodynamics with $\text{đ}q$ being the quantity of specific heat supplied to the fluid, $\mathrm{d}e$ is the internal energy of the fluid, and $p\mathrm{d}v$ is the work done by the fluid. It is important to note that heat is a path-dependent transfer process, not a state function; therefore, gradients of specific heat are only a mathematical concept. In contrast, specific enthalpy is a state function (path independent), accounting for both internal energy and flow work. From this point onward, all quantities are considered specific to eliminate the effect of mass. The heat supplied equals the enthalpy change only for an isobaric process ($q = \mathrm{d}h$), such as in the combustion process of a Brayton cycle. Conversely, the combustion process in an Otto cycle is isochoric, meaning some heat supplied increases the internal energy. Therefore, the heat added to a system cannot generally be equated to a change in enthalpy, as it may also involve a change in pressure.

The second of law of thermodynamics can be used to determine if a process is reversible or irreversible (Equation 2.15). The entropy within the system may be changed if the system undergoes reversible processes ($\text{đ}q = T\mathrm{d}s$) such as heat transfer, or irreversible processes ($\text{đ}q < T\mathrm{d}s$) such as viscous dissipation. Following Greitzer's analogy, Equation 2.15 can be modified in order to split off the processes[3].

$$\mathrm{d}s = \frac{\text{đ}w_{\text{loss}}}{T} + \frac{\text{đ}q}{T} = \mathrm{d}s_{\text{irrev}} + \mathrm{d}s_{\text{rev}} \tag{2.17}$$

Let us now consider an adiabatic flow, thus no heat transfer, and no irreversibilities such as friction losses. Both components of Equation 2.17 are null, thus the process is isentropic. This processes can be related to work scenarios such as ideal compression and expansion processes. Looking at Equation 2.16, it can be seen that the enthalpy change provided isentropically will lead to a proportional pressure change. Consider a compression process, the isentropic total enthalpy rise will lead to an increase in total pressure. On the other hand, an isentropic expansion process, the reduction in total enthalpy would lead to a reduction in total pressure.

Let us now consider a non-isentropic process with heat transfer. Equation 2.16 can be considered in terms of the total variables. Substituting Equation 2.17 gives the relation for total enthalpy, total temperature and total pressure.

$$\mathrm{d}h_t = T_t \left(\mathrm{d}s_{\text{irrev}} + \mathrm{d}s_{\text{rev}}\right) + \upsilon_t \mathrm{d}p_t \tag{2.18}$$

$$\mathrm{d}h_t = \cancel{\mathrm{d}}q + \cancel{\mathrm{d}}w = T\mathrm{d}s_{\text{rev}} + \cancel{\mathrm{d}}w \tag{2.19}$$

The total enthalpy change must be equal to the difference between the heat added/removed from the system and the mechanical work done.

Joining Equation 2.18 and Equation 2.19 gives the stagnation pressure-energy equation, given in Equation 2.20.

$$T_t \mathrm{d}s_{\text{rev}} + T_t \mathrm{d}s_{\text{irrev}} + \upsilon_t \mathrm{d}p_t = T\mathrm{d}s_{\text{rev}} + \cancel{\mathrm{d}}w \tag{2.20}$$

Further manipulations can be done by expanding components and shifting all terms to the right hands side in order to have a full energy balance equation.

$$\mathrm{d}s_{\text{rev}} \left(T_t - T\right) + T_t \mathrm{d}s_{\text{irrev}} + \upsilon \mathrm{d}p_t - \cancel{\mathrm{d}}w = 0 \tag{2.21}$$

As seen in Equation 2.21, the reversible term will always be positive, since the total temperature will always be greater than static. Considering heat transfer only without irreversibilities, nor any mechanical work done, Equation 2.21 can be further simplified to Equation 2.22.

$$\upsilon \mathrm{d}p_t = -\mathrm{d}s_{\text{rev}} \left(T_t - T\right) \tag{2.22}$$

As it can be seen in Equation 2.22, a heat transfer process which corresponds to the reversible entropy generating process leads to an inverse effect on total pressure[3].

For flow heating without irreversible losses or work done, the total pressure decreases while the total temperature increases, which is the opposite in comparison to the previously discussed case for isentropic flows undergoing work. In the case of work done to the flow, given no heat transfer or irreversible losses, total pressure increase along with total temperature as shown in Equation 2.21. On the other hand, for cooling flows, the reversible entropy decrease leads to an increase in total pressure. This phenomena can be exploited for diffuser flows, allowing to achieve higher pressure recovery by the implementation of cooling.

2.2.3. Effect of Turbine-Diffuser coupling with heat transfer

Turbomachinery components often operate with high meridional Mach number flows, resulting in large exhaust velocities. These velocities carry not only thermal energy but also significant kinetic energy. To recover part of this kinetic energy, a diffuser is installed downstream of the turbine to convert exit kinetic energy into static pressure. Increasing the turbine back pressure allows the fluid to discharge at the desired design condenser pressure, as well as maximize turbine work extraction.

To analyze the effect of turbine–diffuser coupling, enthalpy–entropy (h–s) diagrams are used to evaluate the work extracted by both the turbine and the diffuser. The turbine inlet conditions are taken from the ORCHID turbine to reproduce realistic operating conditions. To ensure comparable turbine performance, the model assumes constant turbine efficiency. Furthermore, the inlet kinetic energy to the diffuser is assumed to be proportional to the turbine exit kinetic energy, following the repeating-stage hypothesis. These assumptions reduce the accuracy of the results but remain useful for a preliminary analysis of the effects of heat transfer on turbine–diffuser coupling.

To account for variations within the diffuser, Greitzer's influence matrices are implemented [3]. This set of differential equations captures the effects of friction, heat transfer, and area variation along the diffuser. The equations are discretized for numerical solution using a first-order forward difference (Euler) scheme applied

to the one-dimensional system. This system, coupled with the turbine's thermodynamic equations, is solved iteratively, since the turbine inlet conditions and the static back pressure (p_{exit}) are prescribed.

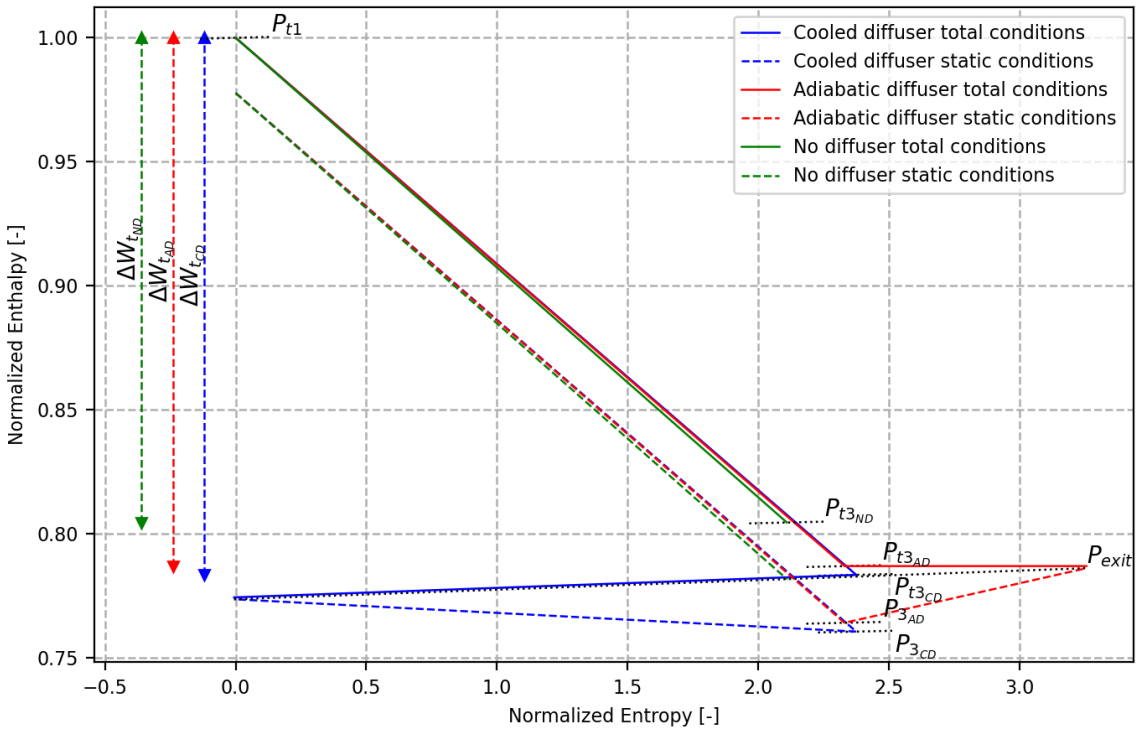

Figure 2.8: Enthalpy-entropy diagram comparison.

As seen in Figure 2.8, the model simulates 3 turbine-diffuser configurations. Firstly, the turbine with no diffuser is presented as "No Diffuser = ND". This model allows for the turbine to discharge the fluid at back pressure conditions. Next, an adiabatic diffuser is coupled to the turbine. This configuration is represented as "Adiabatic Diffuser = AD". Lastly, a cooled diffuser coupled to the turbine is also considered. This configuration is represented as "Cooled Diffuser = CD". Figure 2.8 shows that both enthalpy and pressure decrease across the turbine, consistent with the thermodynamic behavior described in subsection 2.2.2. The diffuser configurations, however, exhibit different trends. Since the diffuser performs no mechanical work on the flow, variations arise from heat transfer and frictional effects. In the adiabatic diffuser, entropy increases due to irreversible losses caused by friction within the passage. In contrast, in the cooled diffuser, entropy decreases because the reversible entropy reduction from heat removal exceeds the irreversible entropy generation produced by friction.

An important observation can be made regarding the work extracted by the turbine. As discussed in subsection 2.2.2, coupling a diffuser to the turbine increases the total work output. Matabuena reports that incorporating a diffuser into a radial turbine can enhance energy extraction by up to 10%[9]. This improvement is more pronounced at low pressure ratios and high turbine exit Mach numbers. Conversely, pressure losses due to viscous dissipation slightly reduce the net work extracted. In the case of cooled diffusers, the combined effects of heat transfer and friction come into play. According to Colonna [2], cooled diffusers mitigate the impact of losses within the diffuser, enabling additional flow expansion within the diffuser. Consequently, when comparing the cooled diffuser with the adiabatic configuration, further work can be extracted by the turbine, as illustrated in Figure 2.9.

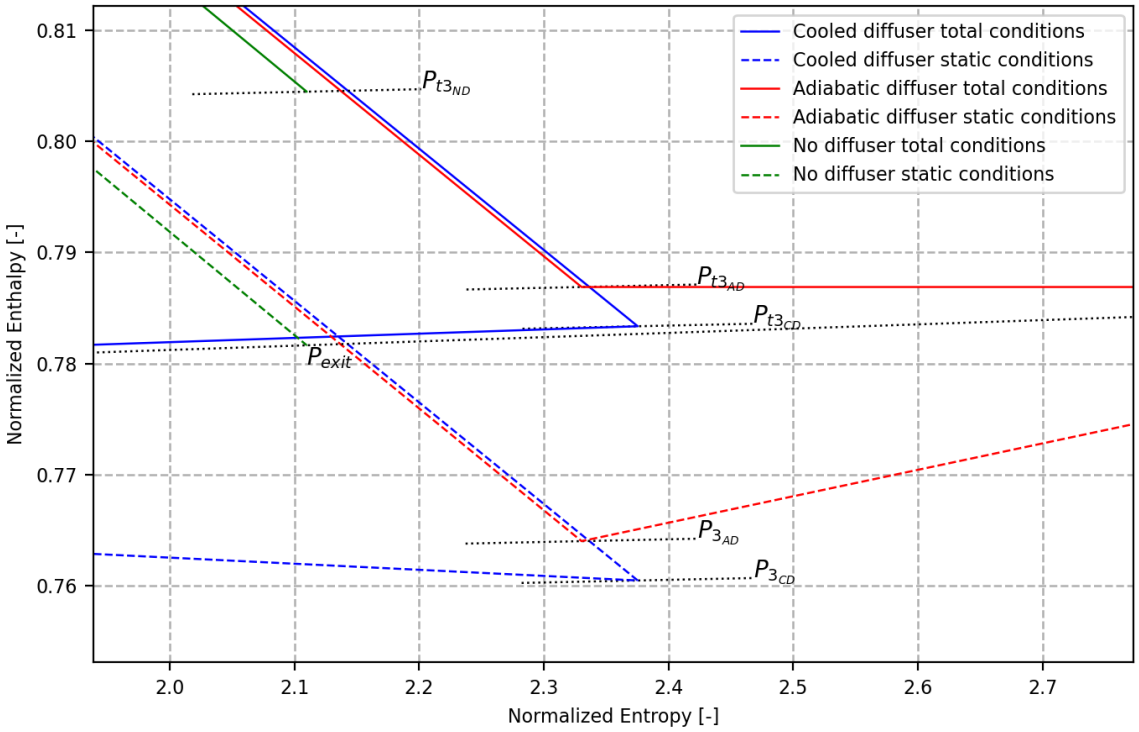

Figure 2.9: Detailed view of the enthalpy-entropy diagram comparison.

To conclude the discussion on turbine–diffuser coupling, pressure effects must be considered. Within a diffuser, the static pressure increases. Therefore, coupling a turbine to a diffuser allows the turbine exit static pressure to be lower than the required back pressure, enabling recovery of kinetic energy and its conversion into a static pressure rise. The total pressure in an adiabatic diffuser decreases due to irreversible viscous losses, while in a cooled diffuser, the total pressure variation depends on the balance between viscous dissipation and cooling effects. Implementing a cooled diffuser enables the turbine design to be optimized for a specific work output in combination with a known diffuser heat transfer performance. The model presented here employs fixed cooling values chosen to demonstrate qualitatively the benefits of cooled diffusers.

2.2.4. Effect of heat transfer on Boundary Layer Stability within Diffuser Flows

Boundary layer stability is a critical aspect in order to ensure adequate performance of the diffuser when expanding the flow. Fluid behavior such as separation and transition dictates how effective the diffuser is able to increase pressure as well as promote heat transfer. In terms of transition, turbulent boundary layers have the upper hand over laminar boundary layers due to their additional kinetic energy component. This additional kinetic energy component present within the turbulent mixing of the flow promotes both fluid attachment as well as convective heat transfer. Transition from laminar to turbulent flow occurs when small disturbances within the boundary layer grow and become unstable, leading to chaotic and irregular motion. In 3D flows, this process develops through the amplification of primary instabilities such as Tollmien–Schlichting (T–S) waves typically triggered by wall imperfections, vibrations, or pressure fluctuations. Although the transition process involves complex, nonlinear instability growth, experimental data show that its onset can be effectively correlated to the flow's Reynolds number [5, 13]. Consequently, in 1D models, transition is commonly approximated as a function of the local Reynolds number, providing a simplified yet practical representation of the laminar-to-turbulent boundary layer shift.

Another important aspect of boundary layer behavior is flow separation. Separation occurs when the boundary layer, having decelerated under the influence of an adverse pressure gradient, loses sufficient momentum to overcome the increasing pressure in the flow direction. As a result, the near-wall flow velocity decreases to zero and eventually reverses, causing the boundary layer to detach from the surface. To analyze separation and the influence of heat transfer on its onset, a boundary layer stability criterion can be established, relating the local pressure gradient and thermal effects to the momentum balance within the flow.

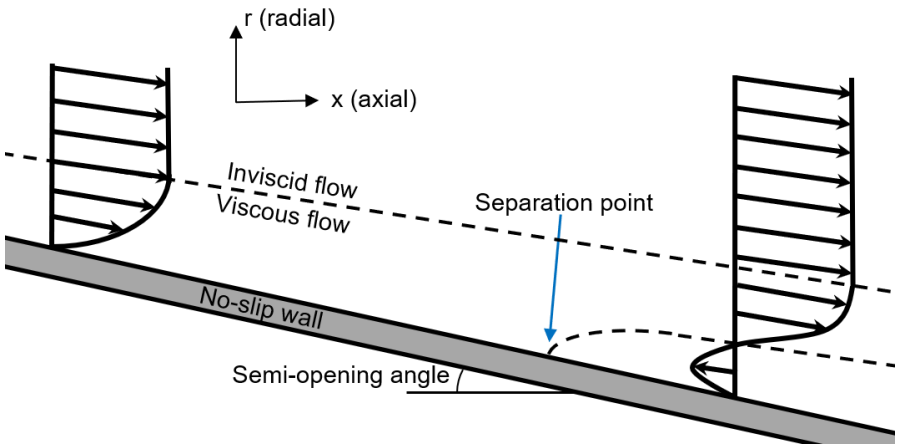

Figure 2.10: Development of a stable boundary layer to a separated boundary layer.

A separated flow can be identified by the profile of velocity within the boundary layer (Figure 2.10). Consider a flat plate (x = axial direction and y (= r) = perpendicular direction), an attached flow displays a convex velocity profile, where the velocity increases as you go further away from the wall. On the other hand, a separated flow implies there is reverse flow is present, displays a concave velocity profile. To understand mathematically separation, velocity gradients need to be considered. A convex velocity profile indicates that the velocity gradient is decreasing as you go further away from the wall ($\frac{\partial^2 u}{\partial y^2} < 0$), whereas a concave profile indicates that the velocity gradient increases as you go further from the wall($\frac{\partial^2 u}{\partial y^2} > 0$). In order to ensure stability, the velocity profile at the wall must be convex. This can also be shown numerically, as given in Figure 2.11.

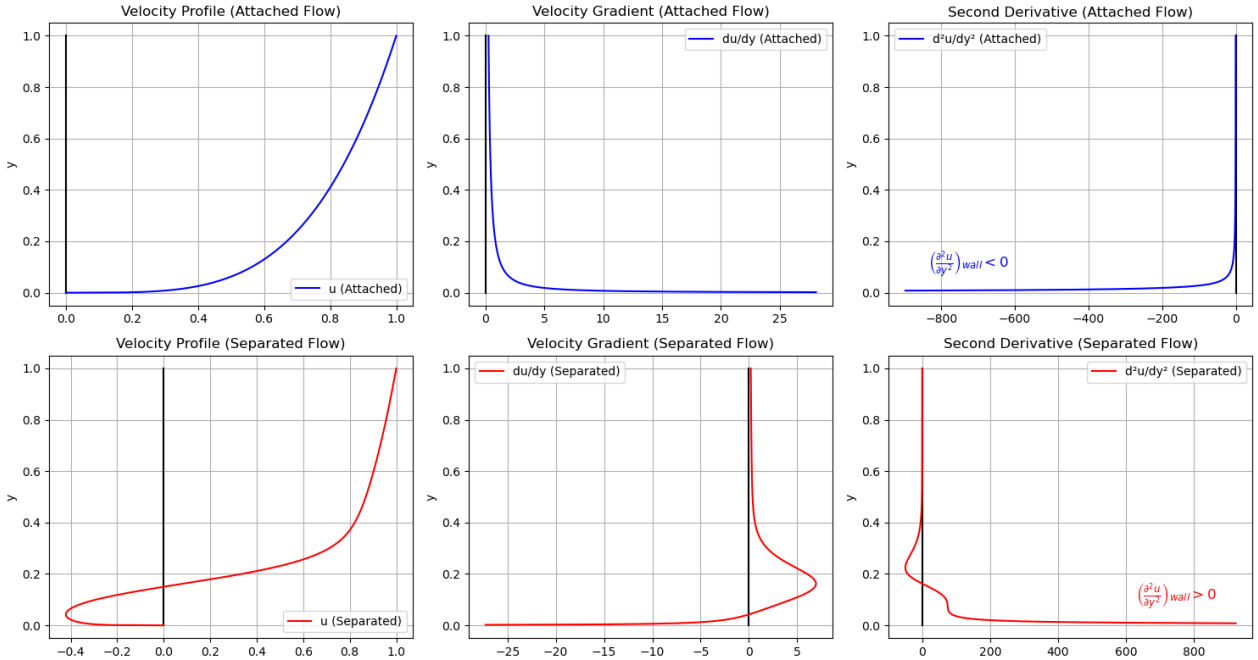

Figure 2.11: Visualization of boundary layer velocity profiles for an attached flow and a separated flow.

Considering the axial momentum equation for 1D flows, at the wall, Colonna derives the condition given in Equation 2.23. Viscosity of a gas-like fluid follows temperature. For a cooled channel, the gradient of temperature along the perpendicular direction is positive. Therefore the gradient of viscosity along the perpendicular direction is also positive. Colonna uses this finding to conclude that cooling promotes boundary layer stability

for a 1D flow[2].

$$\left(\frac{\partial^2 u}{\partial y^2}\right)_{\text{wall}} = \frac{1}{\mu}\frac{\partial p}{\partial x} - \frac{1}{\mu}\frac{\partial \mu}{\partial y}\left(\frac{\partial u}{\partial y}\right)_{\text{wall}} \tag{2.23}$$

$$\frac{\partial \mu}{\partial y} \geq 0 \tag{2.24}$$

This conclusion is valid for 1D flows assuming laminar, steady and incompressible flow. Although steady and incompressible flow assumptions are considered be valid within the boundary layer for the scope of this study (subsection 2.1.3), laminar flows and 1D (no radial gradients) are not valid. In order to obtain a valid stability criterion, equations are re-derived from mass and momentum conservation equations using Einstein notation.

$$\frac{\partial \rho}{\partial t} + \frac{\partial \left(\rho u_i\right)}{\partial x_i} = 0 \tag{2.25}$$

$$\frac{\partial \left(\rho u_i\right)}{\partial t} + \frac{\partial \left(\rho u_i u_j\right)}{\partial x_j} + \frac{\partial p}{\partial x_i} - \frac{\partial \tau_{ij}}{\partial x_j} - X_{\text{body}} = 0 \tag{2.26}$$

A Reynolds decomposition ($u =< u > +u'$) is implemented, which splits up the velocity into the average flow component and the turbulent fluctuations. Additionally, the surface shear of the Newtonian fluid component is dependent on the velocity gradient and fluid viscosity ($\tau_{ij} = \mu\frac{\partial u_i}{\partial x_j}$). With the given steady flow ($\frac{\partial}{\partial t} = 0$), incompressible flow ($\frac{\partial (u_i)}{\partial x_i} = 0$) and no external body forces ($X_{\text{body}} = 0$) assumption within boundary layers and new implementations, Equations 2.25 & 2.26 can be rewritten in the form of time averaged Reynold's Averaged Navier Stokes equations as given in Equation 2.27.

$$\langle u_j \rangle \frac{\partial \left(\langle u_i \rangle\right)}{\partial x_j} + \frac{\partial \left(\langle u_i' u_j' \rangle\right)}{\partial x_j} + \frac{1}{\rho}\frac{\partial \langle p \rangle}{\partial x_i} - \frac{1}{\rho}\left(\mu \frac{\partial^2 \langle u_i \rangle}{\partial x_j^2} + \frac{\partial \mu}{\partial x_j}\frac{\partial \langle u_i \rangle}{\partial x_j}\right) = 0 \tag{2.27}$$

To get to Equation 2.27, one must use commutation properties of first and second derivatives, allowing for all linear terms to cancel out average of fluctuations ($\langle \frac{\partial}{\partial x}\left(u'\right)\rangle = \frac{\partial}{\partial x}\left(\langle u' \rangle\right) = 0$). This leaves the only non-linear (convection) term of Equation 2.27 to remain with fluctuation contribution, which is known as the Reynolds stress tensor. Additionally, the viscous term must also account for variations in viscosity, since the flow will undergo heat transfer near the walls. Lastly, using the product rule and incompressibility, the convection term for the average flow can be simplified by removing the contribution of the divergence of the flow ($\frac{\partial}{\partial x_j}\left(< u_i u_j >\right) = < u_i > \cancel{\frac{\partial (< u_j >)}{\partial x_j}} + < u_j > \frac{\partial (< u_i >)}{\partial x_j}$).

To adapt to no dependencies on perpendicular direction, equation is transformed from Cartesian to cylindrical coordinates using $y = r\sin\theta$ and $z = r\cos\theta$. Additionally, two assumptions will be made. The first one is scale similarity principle (as described by Greitzer[3]), where perpendicular components of viscousity are much greater than axial components of viscousity ($\frac{\partial \tau_{xx}}{\partial x} << \frac{\partial \tau_{xr}}{\partial x}$), thus the axial viscousity component is neglected. Secondly, the diffuser is radial symmetric, where variations along the tangential direction are null ($\frac{\partial}{\partial \theta} = 0$). Applying transformation and assumptions give Equation 2.28 as the conservation of momentum in the axial direction. The full derivation can be found in Appendix A.

$$\frac{1}{\mu}\frac{\partial \langle p \rangle}{\partial x} - \frac{1}{\mu}\frac{\partial \mu}{\partial x}\frac{\partial \langle u_x \rangle}{\partial x} - \frac{1}{\mu}\frac{\partial \mu}{\partial r}\frac{\partial \langle u_x \rangle}{\partial r} - \frac{1}{r}\frac{\partial \langle u_x \rangle}{\partial r} = \frac{\partial^2 \langle u_x \rangle}{\partial r^2} < 0 \tag{2.28}$$

To better understand Equation 2.28, the known terms of the equation for diffuser flows are given a color. Positive terms along the diffuser are given in blue, while negative terms along the diffuser are given in orange. For stability of a boundary layer due to heat transfer, the gradient of viscosity with radius ($\frac{\partial \mu}{\partial r}$) must be positive, while the gradient of viscosity with axial direction ($\frac{\partial \mu}{\partial x}$) must be negative.

For a cooling channel, at the wall the temperature gradient will be positive, thus when using a gas-like fluid, the radial viscosity gradient will be positive. However, diffuser flows increase static properties of the fluid, including static temperature, thus the temperature gradient is positive leading to an unwanted positive axial viscosity gradient. However, considering the effects of cooling, the axial temperature gradient is significantly reduced, which overall decreases the axial viscosity gradient, decreasing the negative contribution of the term ($\frac{1}{\mu}\frac{\partial \mu}{\partial x}\frac{\partial \langle u_x \rangle}{\partial x}$) towards boundary layer stability. Combining both effects leads to concluding that **cooling enhances boundary layer stability**.

2.3. 3-dimensional effects on diffusers

This chapter introduces relevant three-dimensional effects of diffuser flow and convective heat transfer properties. So far, 1D models developed within this study work have assumed quasi-1D flow, thus variation in both the radial and tangential components of the flow have been neglected. To improve modeling accuracy, inclusion of a radial and tangential variation are required to achieve realistic results.

Convection is a heat exchanger process that is dominated by the boundary layer of a flow that is at a different temperature than the surface. As the boundary layer dictates the velocity profile close to a wall, a thermal boundary layer also develops, leading to a strong temperature variation close to the wall. The thermal diffusivity between the diabatic wall and the fluid dictates the energy transport behavior in the thermal boundary layer. The analogy of kinematic and thermal boundary layers allow for understanding how turbulence plays a role in convective heat transfer.

As discussed previously in subsection 2.2.4, the influence of heat transfer on boundary-layer stability was analyzed for three-dimensional flows. The thermal boundary layer directly affects the behavior of the kinematic boundary layer, with cooling shown to enhance diffuser stability by increasing wall viscosity and delaying separation. To capture these effects accurately, it is essential to account for both local heat transfer effects and the turbulence modeling approach.

2.3.1. Local effects on convective heat transfer rate

Convective heat transfer is strongly influenced by local near wall phenomena. Depending on these local effects, significant deviations may arise between 1D model predictions and the actual flow behavior. As previously discussed, boundary layer profiles determine the shear stress between the fluid and the wall. Any modification to these profiles can therefore lead to substantial changes in the convective heat transfer rate. While many factors influence boundary layer development, their treatment is addressed through turbulence modeling in the following subsection. The present discussion focuses on thermal effects such as separation bubbles, buoyancy induced thermal mixing, and (baroclinic) thermal instabilities.

Separation bubbles form localized recirculating regions with limited interaction with the main flow. These zones act as thermal barriers between the bulk fluid and the heated or cooled surface, reducing the local heat transfer coefficient. In addition to affecting heat transfer, separation also decreases the pressure recovery of the diffuser. For this reason, avoiding flow separation is essential when designing a turbine-diffuser recuperator.

Buoyancy arises from temperature dependent density variations and modifies convective transport depending on surface orientation. For a cooling surface located above the fluid (top cooled), the cooled fluid adjacent to the surface looses temperature, thus becomes denser, and sinks due to buoyancy. This effect is followed by warmer fluid from the central flow being drawn towards the surface of the diffuser due to buoyancy, naturally enhancing thermal mixing, and therefore improving heat exchange at the top surface.

On the other hand, for a cooling surface beneath the fluid (bottom cooled), the cooled dense fluid remains adjacent to the surface and produces flow stratification that suppresses thermal mixing and reduces heat transfer. This buoyancy effect leads to a difference between the heat transfer rate between the top and bottom surfaces of the diffuser. Additionally, along sidewalls, descending dense fluid forces warmer fluid to circulate into the vacated region. This effect leads to generation of circulation at the sidewalls, which increases thermal mixing and therefore increases convective heat transfer rate.

Heat transfer also influences vorticity. Density gradients produced by heating or cooling interact with pressure gradients, generating additional vorticity through the baroclinic torque effect. This mechanism directly contributes to the vorticity transport equation, which governs the generation and dissipation of vorticity in the flow[3].

$$\frac{D\vec{\omega}}{Dt} = -\nabla \times \left(\frac{1}{\rho}\nabla p\right) \approx -\frac{1}{\rho^2}\nabla\rho \times \nabla p \tag{2.29}$$

Baroclinic torque is caused by misalignment of density and pressure gradients. These can be caused by temperature gradients, but also other flow phenomena such as shock waves. Baroclinic torque contributes to the vorticity transport equation, having a direct impact on vorticity advection. In a diffuser, axial pressure gradients are expected. Additionally, due to heat transfer, radial temperature gradients are expected. As density is expected to change following temperature gradients, baroclinic instabilities are expected in regions where both temperature and pressure gradients are high.

2.3.2. Turbulence modeling

Turbulence has a major influence on convective heat transfer, making accurate turbulence modeling essential. Turbulent motion spans a wide range of spatial and temporal scales that depend on the Reynolds number. The largest scales, characterized by the integral length scale, are associated with the characteristic dimension of the flow or the external forcing mechanism. The smallest scales correspond to the Kolmogorov microscales, which depend on the turbulence dissipation rate and the kinematic viscosity (Equation 2.30). Together, these scales form the energy cascade that represents the complete turbulence spectrum.

To fully capture all turbulence scales, a direct numerical simulation (DNS) must be performed. DNS requires a computational mesh fine enough to resolve every turbulent eddy across the entire spectrum. Near solid walls, turbulence scales become progressively smaller, demanding finer grid resolution and resulting in a significant increase in computational cost.

$$\eta_{\text{kolmogorov}} = \left(\frac{\nu^3}{\epsilon}\right)^{1/4} \tag{2.30}$$

$$N_{\text{points}} \geq \frac{L_{\text{integral}}}{\eta_{\text{kolmogorov}}} \tag{2.31}$$

$$Re = \frac{u^{'} L}{\nu} \tag{2.32}$$

$$N^3_{\text{points}} \geq \frac{L^3_{\text{integral}} \epsilon^{3/4}}{\nu^{9/4}} = Re^{9/4} \tag{2.33}$$

The resulting DNS mesh requires N_{points} per dimension, thus N^3_{points} in 3D simulations. By using the turbulent Reynolds number definition (Equation 2.32) and assuming turbulence dissipation rate equals the inertial energy flux, the cost can be approximated to the Reynolds number. From Equation 2.33, it can be seen that for medium Reynolds number flows, a DNS simulation becomes too expensive to perform. Therefore an alternate solution must be performed.

To reduce computational cost, turbulence must be modeled rather than fully resolved. The two main approaches are Reynolds Averaged Navier Stokes (RANS) and Large Eddy Simulation (LES). RANS models solve only for the mean flow field, representing all turbulent effects through averaged quantities. LES, on the other hand, resolves the largest and most energetic turbulent structures in space and time, while modeling only the smaller, dissipative scales.

RANS modeling decomposes the velocity solution into a mean value and a fluctuation component. Replacing this solution into the Navier Stokes equations and averaging the solution, all the linear terms result with the averaged solution component remaining. On the other hand, the non-linear component (convection) term results in an additional terms (recall Equation 2.27). By placing all averaged terms on the left and the fluctuation terms on the right, we obtained the RANS equation, where the left hand side solves for the mean value term and the right hand side (known as the Reynolds stress tensor) represents all effects of fluctuations on the mean flow.

$$RHS = -\nabla \cdot \langle u' u' \rangle \tag{2.34}$$

The Reynolds Stress Transport equation is composed of advection, turbulent diffusion, viscous diffusion, pressure diffusion, pressure strain correlation, production and dissipation. These terms are highly non-linear and require further decomposition and modeling. Reynolds Stress Models (RSM) aim to directly solve model transport equations for all components of the unknown Reynolds stress tensor. Although RSM provides superior results flows with strong streamline curvature (such as the coolant channel flows) and anisotropic turbulence induced secondary flows, RSM requires solving at least 6 additional transport equations which becomes both computationally expensive and prone to slow or even unstable convergence.

Alternatively, a simpler modeling approach is obtained when considering eddy viscosity models (EVM). EVMs assume the Reynolds stress tensor to be proportional to the mean strain rate, with proportionality factor (eddy viscosity) ν_t.

$$-\langle u_i' u_j' \rangle \approx 2\nu_t S_{ij} - \frac{2}{3}\delta_{ij} k \tag{2.35}$$

The mean strain rate (S_{ij}) represents the local flow strain caused by local cross-flow gradients, while the turbulent kinetic energy k is the local kinetic energy of all fluctuation components. By introducing Equation 2.35,

the modeling problem is reduced from 6 independent components of the Reynolds stress tensor to one scalar field of eddy viscosity (ν_t). Therefore, the model includes the turbulence stresses by augmenting the molecular viscosity with an eddy viscosity.

To model the eddy viscosity, Prandtl mixing-length models are used [13]. The mixing length (l_m) represents the characteristic distance a turbulent eddy travels before losing its identity and mixing with the surrounding fluid. The mixing length is specified as a function of position within a boundary layer. As turbulent length scales become smaller close to the wall, the mixing length scales needs its own modeling depending on the region within the boundary layer [13]. Applying an adequate boundary layer law of the wall model to find an adequate mixing length scale results in the zero-equation model (Equation 2.36). The simplicity of the model allows for least computational cost, however, accuracy of the model is highly dependent on accuracy of mixing-length model.

$$\nu_t = l_m^2 \left\| \frac{\partial < u_i >}{\partial x_j} \right\| \tag{2.36}$$

$$\nu_t = l_m \sqrt{k} \tag{2.37}$$

In order to improve accuracy, turbulence kinetic energy is included (Equation 2.37). Turbulence kinetic energy is the symmetric part of the Reynolds stress tensor. To solve for it, a transport equation is obtained for turbulent kinetic energy ($\frac{Dk}{Dt}$). Most of the terms in the kinetic energy transport equation are simpler, allowing for modeling of each transport term individually. The inclusion of turbulence production, diffuser, advection and dissipation results in improved predictions over algebraic zero-equation models. Nevertheless, the length scale (l_m) still requires to be specified, making one-equation and zero-equation models unreliable for internal flows or flow separation[13].

In order to lose the dependency on mixing-length modeling, a two-equation model can be implemented. Two equation models assume isotropic turbulence and equilibrium of turbulence production and dissipation, thus the mixing-length model can be written as a function of kinetic energy (k) and dissipation rate (ϵ).

$$l_m = C_D \frac{k^{3/2}}{\epsilon} \implies \nu_t = C_D \frac{k^2}{\epsilon} \tag{2.38}$$

As a consequence, two transport equations are to be solved for k and ϵ. Similarly to the one-equation model, the unknown terms of the transport equation of k are modeled. On the other hand, the exact transport equation for ϵ contains unclosed terms that are difficult to model. Therefore, an approximate form of the equation is formulated following the structure of the transport equation for k. Solving both equations allows you to obtain acceptable results for flows without strong pressure gradients or curvature. These anisotropic influences are not predicted well due to the assumption of the Reynolds stress proportional to mean strain rate[13].

$$\omega = \frac{\epsilon}{k} \tag{2.39}$$

Alternatively, other two-equation models have been formulated in the past. A well known model is the $k-\omega$ model. This model is expressed similarly to the $k-\epsilon$ model, but using an approximate form of the ω transport equation instead of ϵ. Wilcox, the author of the model, describes how for boundary layer flows, the $k-\omega$ model is superior in its treatment of the viscous near wall region, and in its accounting for the effects of streamwise pressure gradients[13]. However, the treatment of non-turbulent free stream boundaries is problematic. A nonzero (non-physical) boundary condition on ω is required, and the calculated flow is sensitive to the value specified. This makes the $k-\omega$ model more suitable to internal flows with pressure gradients and separation, but very sensitive to inflow conditions and free stream conditions[13].

Menter proposed a two-equation model designed to yield the best results for the $k-\epsilon$ and $k-\omega$ models[13]. The use of a blending function within the transport equations allows to switch between models, in order to improve overall results. Close to the wall, the blending function goes to zero, thus using the $k-\omega$ model. While far from the wall, the blending function goes to unity, thus using the $k-\epsilon$ model. The model known as the SST $k-\omega$ model is widely used in commercial CFD codes for complex problems such as heat transfer, combustion and multi-phase flows due to its favorable results over previously presented models.

Other EVMs such as the Spalart-Allmaras model implement different transport equations, allowing to reduce the computational cost and robustness compared to SST $k-\omega$. The Spalart-Allmaras model implements an approximate form of the transport equation for a functional of the Eddy viscosity. Although the model does not represent any underlying physical theory, the results provides good results for transonic flows and boundary

layer separation[13]. Nevertheless, the model is insensitive to irrotational straining (such as shear layers or reattachment points), and overpredicts mixing in flows dominated by free shear (such as jet or injection flows).

Large Eddy Simulation (LES) operates by separating the turbulent flow field into resolved and unresolved scales through spatial filtering. Scales larger than a chosen filter width are resolved, while smaller subgrid scales are modeled. This separation is achieved using a filtering operation, either explicitly through a kernel filter or implicitly through the computational mesh. Kernel filters only partially removes small scales due to the Fourier transform relationship between physical and spectral space. In practice, the filter width is typically proportional to the local grid spacing. The mesh resolution itself effectively limits small scales representation, acting as an implicit filter. The unresolved subgrid turbulence scales are accounted for through the filtered Navier–Stokes equations, which introduce the SGS stress tensor representing the effect of the eliminated scales on the resolved field. Since this tensor cannot be computed exactly from the resolved variables, it must be modeled using an appropriate subgrid-scale closure.

Smagorinsky's EVM remains the most widely used SGS approach due to its simplicity and numerical robustness, offering reasonable near-wall behavior but showing poor correlation with the exact SGS stresses and limited accuracy in shear flows [13]. Scale-similarity models improve this correlation by reconstructing the structure of the unresolved stresses from the resolved field, yet they provide insufficient dissipation, which can lead to energy buildup at small scales and numerical instability. Approximate deconvolution models offer higher fidelity by partially recovering the filtered velocity field but are computationally demanding and require additional stabilization. Hybrid RANS–LES or zonal models can reduce cost by applying different turbulence treatments in distinct flow regions, although they often suffer from transition inaccuracies such as log-layer mismatch.

In conclusion, the ability of LES to resolve large turbulent structures enables more accurate prediction of complex flow behavior compared with RANS models. Wall-bounded heat transfer predictions depend on both the resolved and subgrid-scale representations of turbulence. Implementing LES would enhance the modeling of vortex stretching and baroclinic effects near cooled walls, leading to improved predictions of convective heat transfer. However, due to the nature of the CHT simulation complexity, and due to RAM and runtime limitations, LES is considered too computationally expensive, not feasible for the present study. Instead, RANS with an appropriate turbulence model is used to provide preliminary qualitative insight into three-dimensional effects relative to the one-dimensional model. As RANS relies on modeled transport equations, some loss of accuracy is expected. Future work work may consider the implementation of LES, or Detached Eddy Simulation (DES) in future investigation of turbulence effect on heat transfer near cooled walls.

3
Low fidelity modeling of T-rHEX

3.1. Model methodology

In order to develop an improved design based on the T-rHEX baseline prediction by Colonna [2], an improved low fidelity (1D) model must be built. This modeling tool can be found on the Bitbucket repository of the Power & Propulsion group. The modeling tool, given the name of `T-rHEX.py`, consist of geometrical parameters that fully define the geometry of the diffuser and the coolant channel, as well as the inlet conditions of each fluid stream. This section will elaborate upon how the tool was built, its usage and limitations.

3.1.1. N1D-Flow

In order to compute the behavior of NICFD, a simple but efficient solver should be used. For these reasons, a one-dimensional (1D) approach derived by Tosto has been used. Tosto extended the quasi-1D compressible flow framework originally formulated by Greitzer, who derived the influence coefficients for ideal gas flows, to account for non-ideal compressible behavior[16, 3]. In his formulation, Tosto replaced the ideal gas assumptions with thermodynamic derivatives using seconday thermodynamic variables as listed in Table 2.1, to describe the coupling between area change, heat transfer, friction, and flow properties under non-ideal fluid conditions. Colonna used the influence matrices to develop `N1D-Flow`, an in-house Non-Ideal Compressible Fluid Dynamics quasi-1D solver[2]. This tool allows to calculate channel properties with a fixed mass flow rate accounting for free swirl, wall heat transfer and friction effects.

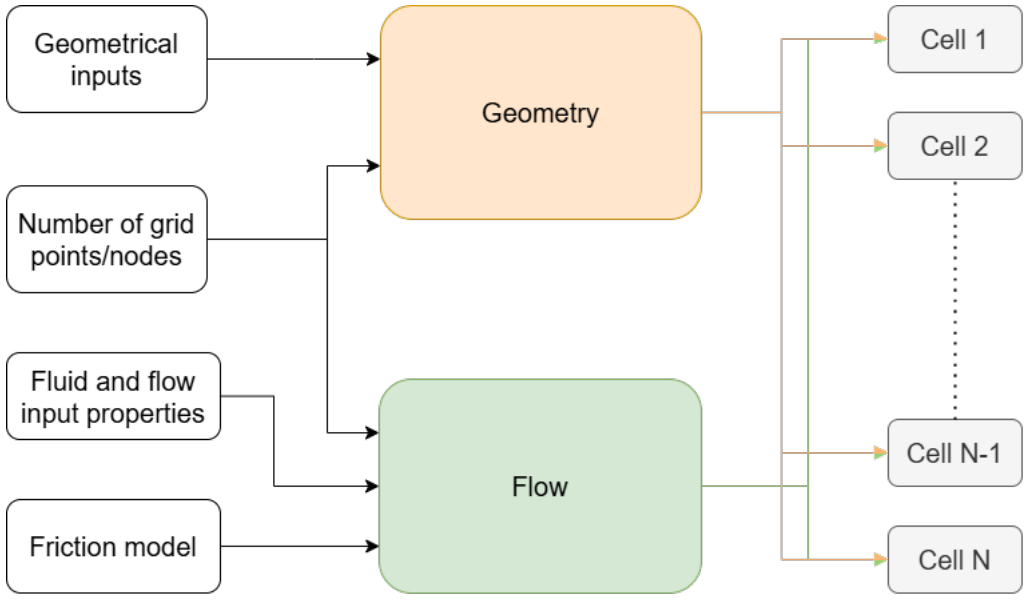

Figure 3.1: N1D-Flow hierarchy structure.

`N1D_Flow` is a one-dimensional simulation tool that discretizes the flow domain into an array of computational cells. Each cell contains its own flow and thermodynamic properties, while a global geometry class defines the spatial distribution and geometric characteristics along the domain. The solver, implemented in the global `Flow.py` module, integrates the governing equations using a backward Euler scheme, where spatial gradients are evaluated through the influence coefficients derived by Tosto [16]. The grid resolution, specified by the

user as the number of cells or grid points, is examined in section 3.2 to assess its effect on numerical accuracy. Because of the sequential solution structure, inlet boundary conditions,including mass flow rate, total temperature, total pressure, and flow angle, must be prescribed. Thermodynamic properties are evaluated using REFPROP, accessed through the Python interface CoolProp [1], to ensure accurate treatment of non-ideal fluid behavior. The code outputs 1D flow distributions of all relevant properties along the diffuser at each grid point.

3.1.2. Modifications to N1D-Flow

In order to maximize usability and improve accuracy of `N1D-Flow`, a few modifications have been implemented. This new version of `N1D-Flow` allows for variable semi-opening angle, heat flux and friction along the diffuser.

Geometry class

The first major modification was the geometrical properties along the grid. Previously, a constant semi-opening angle was the only way to specify the geometry. The new version of `N1D-Flow` is capable of having a variable semi-opening angles along the diffuser. This can be done either by specifying semi-opening angles or exterior radius for each grid point along the diffuser. By having variable semi-opening angle geometry, the shape of the diffuser does not have to be perfectly conical, allowing for optimization to maximize performance.

Friction

The second major modification was the friction coefficient implementation within `N1D-Flow`. The friction coefficient (fanning friction factor) is constant based on different flow conditions, and is defined as given in Equation 3.1.

$$c_f = \frac{\tau}{\frac{1}{2}\rho u^2} \tag{3.1}$$

Previously, `N1D-Flow` implemented a diffuser friction coefficient model by Carlo Osnaghi, accounting for both wall friction and diffuser adverse pressure gradients effects on friction[12]. Details about this model can be found in section B.1. However, Osnaghi's model breaks down if a variable semi-opening angle approach is implemented. In order to correct for this, the diffuser is reconstructed based on the local semi-opening angle.

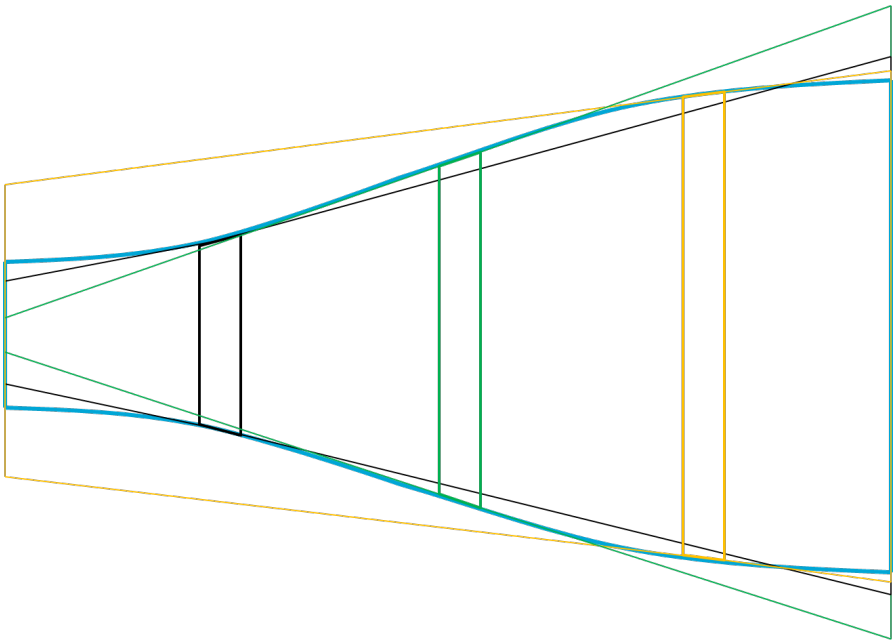

Figure 3.2: Three examples of diffuser reconstructions based on local semi-opening angle to obtain the friction coefficient based on Osnaghi's model.

Figure 3.2 shows the physical diffuser outline in blue. Due to the variable semi-opening angles along the diffuser, Osnaghi's model would fail in predicting friction adequately. As each note within the 1D grid has a fixed radius and semi-opening angle, a constant semi-opening angle diffuser can be reconstructed with the same length as the original diffuser. Figure 3.2 shows three different reconstructions, for each grid point, the

exterior diffuser walls are projected at constant angle until reaching the inlet and outlet of the diffuser. Based on this reconstructed diffuser, the friction coefficient can be computed using Osnaghi's model, which is then saved as a local property of the grid point. This is performed for all grid points in the 1D cell. The method produces better results compared to considering an averaged geometry. On the other hand, for high semi-opening angles, the reconstruction is prone to errors, due to the projection of the exterior walls. To correct for this, the form factor of the diffuser (ϕ_1), is bounded between 2 and 50. This limits the model usage to moderate semi-opening angles.

Alternatively to Osnaghi's model, by discretizing the diffuser using higher number of grid points, each section approaches a constant radius due to the small radial difference, which can then be treated locally as a pipe with an averaged radius. Pipe friction models have been extensively covered both for laminar and turbulent pipe flows. Locally, the friction factor for a pipe is based on turbulence state of the flow, given by the pipe Reynolds number.

$$Re_D = \frac{\rho u d_H}{\mu} \tag{3.2}$$

The characteristics of the pipe Reynolds number is given with respect to the channel's hydraulic diameter, instead of the pipe length since the velocity profile is significantly affected by the cross-sectional area within the pipe, thus the boundary layer development. The newly implemented pipe friction model is build by a combination of empirical models, accounting for laminar, transition and turbulent flows. Additionally, for helicoidal channels where radial variations are present due to centrifugal forces, an extension to the pipe model is implemented, where secondary flows are accounted by multiplying the Reynolds number by the curvature ratio ($\delta_{\text{curvature}}$). More on the adaptation of this pipe frictional models can be found in section B.2.

$$\delta_{\text{curvature}} = \frac{d_{\text{channel}}}{d_{\text{curvature}}} \approx \frac{d_{\text{channel}}}{d_{\text{diffuser}}} \tag{3.3}$$

Usage of the pipe friction models for both diffusers and helicoidal channels only account for wall friction. Other effects contributing to friction, such as separation, are not accounted for. This makes Osnaghi's friction model preferable over pipe friction models in the case of large semi-opening angle changes along the length of the diffuser.

Heat transfer

The third major implementation is the heat transfer implementation within `N1D-Flow`. Originally, a constant value of thermal power was prescribed. Each cell along the diffuser received an equal value of heat flux as a boundary condition on the cell volume. The newer version has implements a variable approach to thermal power by means of importing a thermal power vector. This allows for a thermal power distribution to be prescribed along the diffuser, accounting for heat transfer variations.

Computational efficiency

In efforts to reduce computational efficiency of `N1D-Flow`, an analysis was conduced considering `N1D-Flow` as a stand alone function using a Python library `cProfile`. To conduct a fair test, different grid resolutions were used, while the inlet conditions were kept constant. This analysis only looked into the number of internal function calls and runtime for each function call.

The analysis concluded that the internal function calls that required significantly more computational time than the rest are the `Geometry.py` class copy function to the Flow class, and the extensive and repeated calls to REFPROP made by the `Cell.py` class. To reduce simulation time, `N1D-Flow` now has an option to either perform a deepcopy (`copy.deepcopy`: originally intended to allow multiple usages of the `Geometry.py` class generated for different `Flow.py` conditions), or assigning a memory pointer directly from the `Flow.py` class to the `Geometry.py` class. If a memory pointer is used, the Geometry class generated can only be used once. This is acceptable for certain processes, such as for the purpose of this study.

In terms of REFPROP calls, the solution is limited due to its requirement to compute non-ideal thermodynamic fluid properties within each cell of the grid. However, a small solution was found. For the same fluid, the critical thermodynamic properties are constant, thus only needed to computed once. All reduced properties (properties which consider the fraction of the thermodynamic state divided by the critical state of the fluid) can be calculated directly by calling the constant properties without the need of REFPROP. Combining both efforts, computational time per `N1D-Flow` call has been reduced by 26%, which becomes beneficial during the setup of the optimization process in subsection 3.4.1.

An important consideration arises when evaluating total thermodynamic properties. REFPROP is limited to the validity range of its underlying equation-of-state maps. Since the current implementation of total properties of the fluid are calculated based on the total enthalpy of the flow, for high thermal inertial flows, some properties may be out of range of REFPROP thermodynamic maps. When this occurs, the code's internal handler assigns `NaN` (Not a Number) values to the affected properties. Future work should implement a robust extrapolation or fallback method to handle out-of-range conditions while preserving non-ideal fluid accuracy. For the current implementation, it is recommended to restrict simulations to realistic mass flow rates and inlet temperatures within REFPROP's operational limits.

3.1.3. Geometrical modeling

Colonna concluded his work by finding the optimum length and constant semi-opening angle to maximize heat transfer[2]. This result is given the name of *Baseline T-rHEX*. The baseline T-rHEX implements a countercurrent heat exchanger arrangement, where the coolant passes through an annulus channel around the diffuser surfaces.

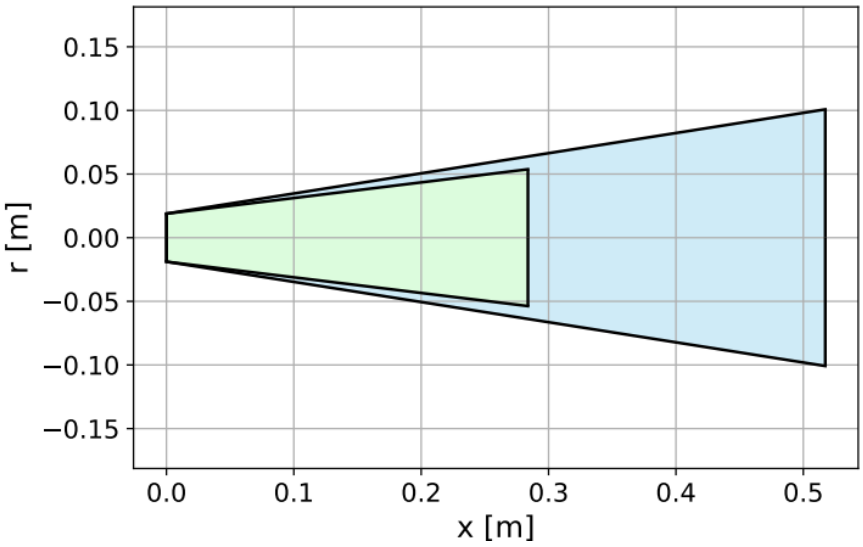

Figure 3.3: Comparison between the baseline T-rHEX geometry (blue) and the original ORCHID diffuser geometry (green)[2].

The baseline T-rHEX configuration shown in Figure 3.3 is expected to deliver a significant improvement in heat exchanger effectiveness due to its larger wetted surface area. However, one of the main design constraints for airborne WHR systems is weight. The T-rHEX exhibits a considerable increase in volume, leading to a proportional rise in component mass. In this study, it is hypothesized that optimizing the diffuser geometry could enhance heat exchanger effectiveness without incurring a substantial volume or weight penalty. This is investigated in subsection 3.4.1.

With respect to the geometric modeling, the diffuser is no longer constrained to a constant semi-opening angle. Instead, it is discretized into a series of cells defined by the number of grid nodes, enabling cells with variable local semi-opening angles. This approach allows for tailoring the diffuser geometry to enhance both heat transfer and pressure recovery performance.

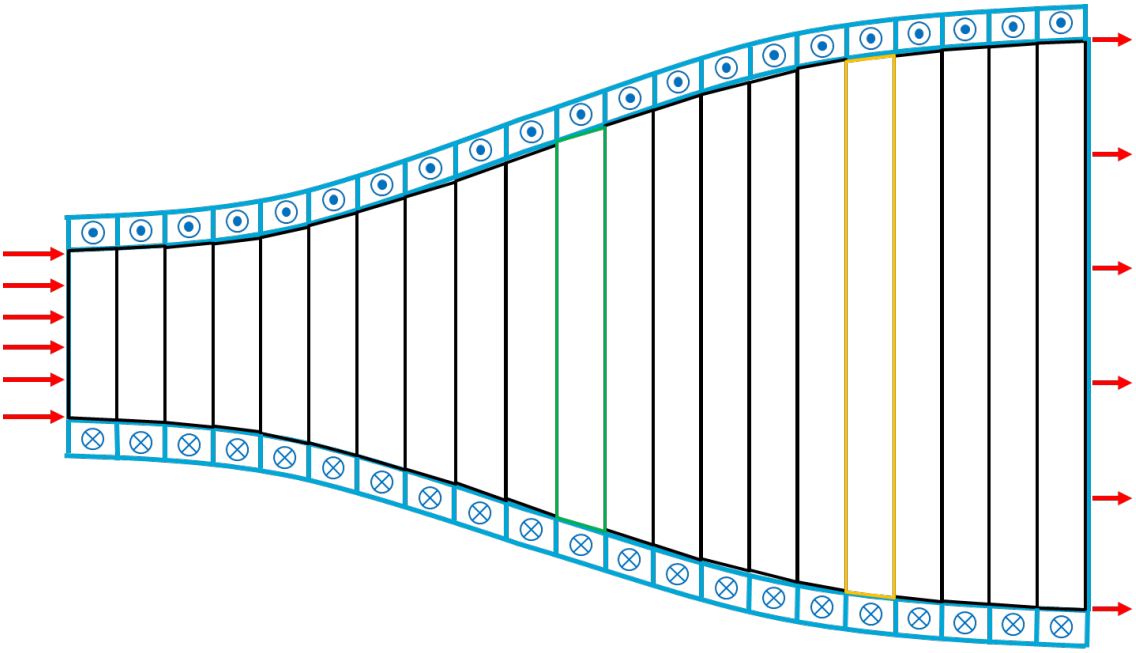

Figure 3.4: Discretization of diffuser with variable semi-opening angle and helicoidal coolant channel path.

Figure 3.4 shows an axial-radial cutout of the diffuser. The coolant channel is placed in a helicoidal path around the diffuser walls. To do so, the following assumptions are taken:

- The coolant channel is assumed to be "tightly packed", meaning there are no gaps between channels. Therefore the diffuser wall is fully covered by the coolant channel(s).
- The channel path is determined by the twist angle (see Figure 3.5b).
- The coolant channels are cylindrical, with diameter depending on twist angle, radius of the diffuser walls, and number of coolant channels (see Equation 3.5).
- Instead, the flow is fully axial within the channel, having no swirl/tangential velocity components due to the small channel diameter.

To discretize the geometry, the recuperator is divided into a series of cells. Each cell consists of two regions separated by the heat-exchanging surface. The outer region represents the coolant channels, defined by known inlet and outlet boundary conditions. Similarly, the inner region corresponds to the diffuser flow passage, also defined by its inlet and outlet conditions. The interface between the two regions coincides with the external surface area of the diffuser. A visual representation of this cell concept is shown in Figure 3.5.

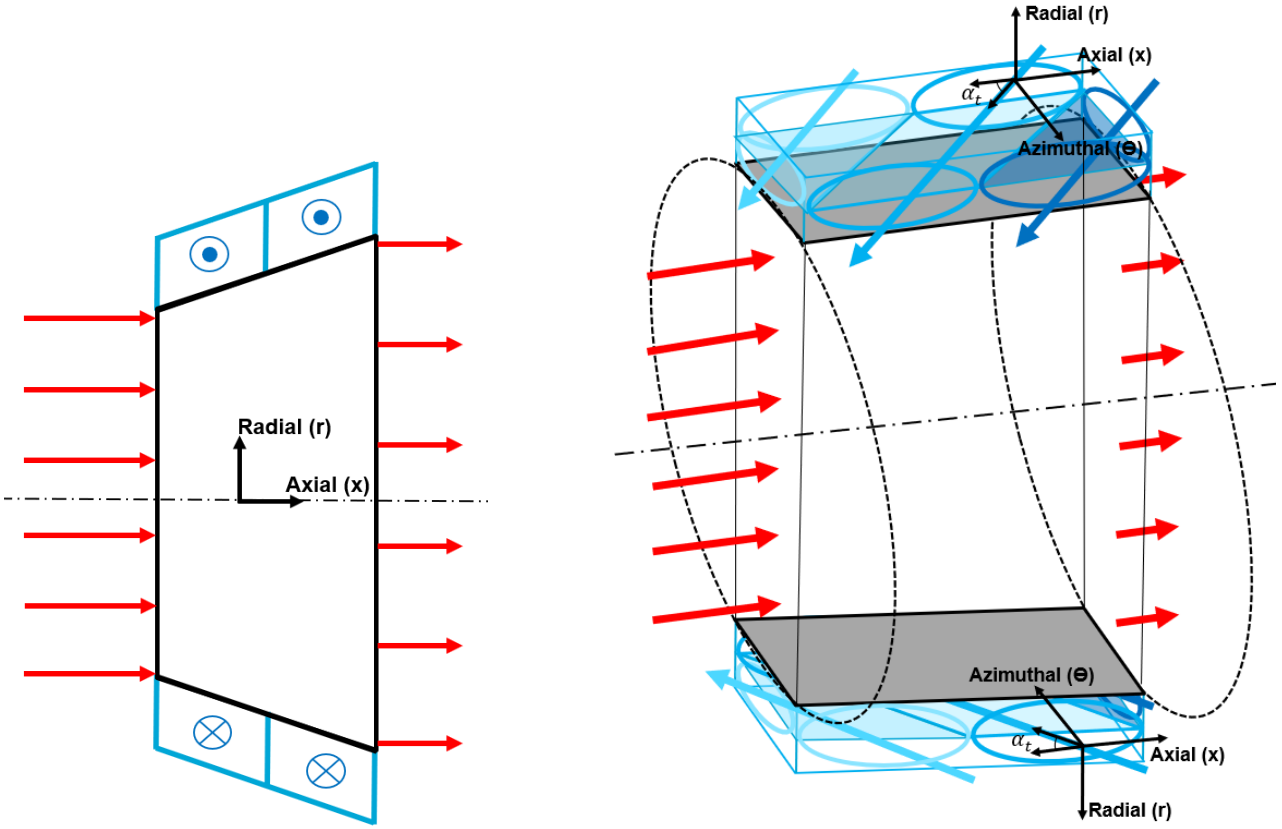

(a) 2D axial-radial cut-out of the cell.

(b) 3D segment of the cell with coolant channel paths.

Figure 3.5: Visualizations in 2D and 3D of a discrete T-rHEX cell.

For a given diffuser geometry, each cell has a prescribed inlet and outlet exterior radii. As the diffuser is axisymmetric, the shape of the cell volume is conical (see Figure 3.5b), therefore the exterior surface area of the cell can be calculated using geometrical properties of a frustum. To calculate the coolant path around the conical cell, the exterior surface area must be simplified from a 3D area to a 2D area. To do so, the exact 3D exterior area is cut axially and laid flat, taking the shape of an arc due to the geometrical properties of a frustum.

Due to the curvature of the 2D diffuser arc, projecting the coolant channel onto the outer surface is nontrivial. To simplify the model, the external surface area of each cell is approximated by an equivalent rectangular area of the same cell width, with the length defined by the circumference corresponding to an equivalent radius (r_{eq}) (see Figure 3.6). This approximation introduces a discretization error, as the frustum-shaped cell is replaced by a cylindrical disk of radius r_{eq}. This simplification facilitates the projection of the coolant channel onto the outer surface while preserving the total external area, thereby conserving heat flux properties. Minor discretization errors may arise from differences in coolant channel path lengths, but these remain negligible for small semi-opening angles or sufficiently refined grids.

The coolant channel is traced along the surface based on the twist angle, and the width of the cell. The twist angle (α_t) is defined in cylindrical coordinates, this being the angle between the axial direction and the coolant flow direction in the axial-azimuthal (tangential) plane. For each cell, a twist angle is defined, which dictates the projection of the coolant path on the surface (see Figure 3.6).

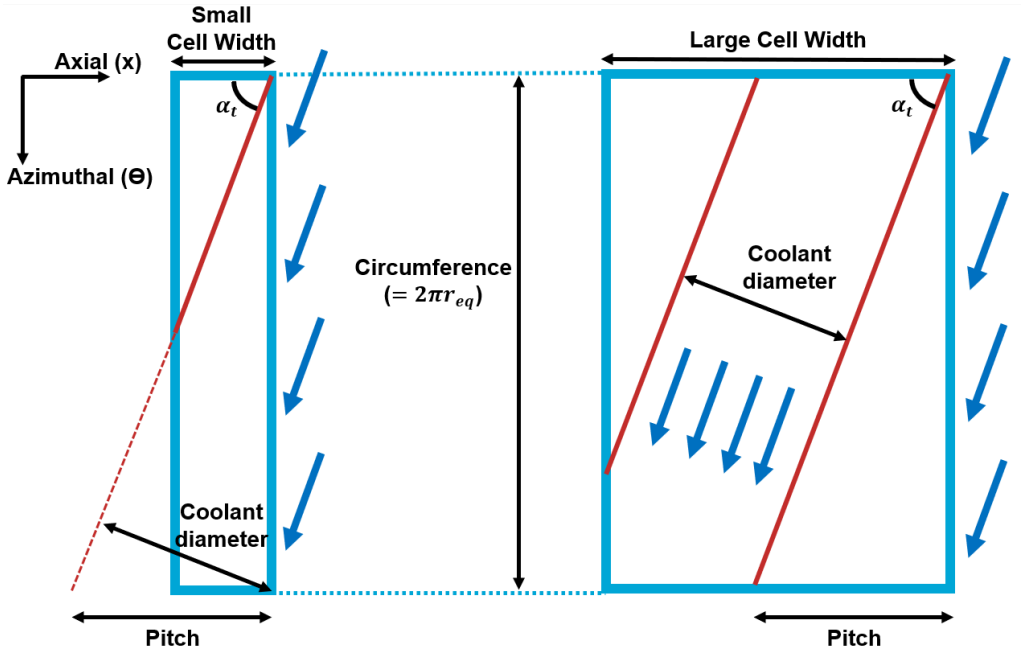

Figure 3.6: Display of coolant channel on top of the rectangular outer surface of the equivalent cylindrical disk for:
Left: A cell with small cell width, representing a finer grid cell.
Right: A cell with large cell width, representing a courser grid cell.

The coolant channel length within each cell is approximated by the flow trajectory along the diffuser exterior surface. For a given cell, this trajectory depends on the twist angle and the cell width. It is important to note that the equivalent radius does not influence the coolant channel length. The equivalent radius, proportional to the diffuser diameter, only affects the coolant channel diameter, whereas the twist angle determines the helical pitch. Consequently, for a fixed twist angle, the coolant channel length depends solely on the diffuser length. In practice, variations in inlet and outlet radii within the cell may slightly alter the channel length. Therefore, a sufficiently refined grid is required to ensure the validity of the cylindrical cell approximation.

$$\Delta L_{\text{coolant}} = f(\alpha_t, \Delta x) \tag{3.4}$$

The coolant channel diameter depends on both the twist angle and the equivalent radius. The twist angle determines the helical pitch, while the equivalent radius defines the local circumference. For a given twist angle, the coolant channel diameter therefore scales proportionally with the diffuser radius. Consequently, the coolant channel diameter and length are independent parameters, each governed by the prescribed diffuser geometry and the imposed twist angle.

$$d_{\text{coolant}} = f(\alpha_t, r_{eq}) \tag{3.5}$$

Figure 3.6 illustrates two cases. The left case corresponds to a coolant channel completing less than one full revolution, while the right case shows a channel exceeding one revolution. `N1D-Flow` treats each cell assuming linear gradients between inlet and outlet conditions. Consequently, increasing the cell width not only amplifies geometric discretization errors but also introduces numerical inaccuracies in the computed coolant channel flow properties. A detailed analysis of discretization effects is presented in section 3.2.

To control the coolant channel diameter and prevent excessively large passages at low twist angles, a subdivision algorithm is implemented. The main helical channel is divided into multiple parallel subchannels according to a prescribed curvature ratio (Equation 3.3). The number of subchannels is determined such that the diameter of each remains below the maximum allowable value imposed by the curvature ratio. Each subchannel is then solved independently using `N1D-Flow`. Mass conservation is ensured by equally distributing the total mass flow among all subchannels. Because the subchannels are arranged helically and run in parallel along the diffuser surface (axi-symmetric along the axial (x) axis), the heat flux distribution is also equally divided between all of the subchannels. The total thermal power exchanged is thus preserved, ensuring both mass and energy conservation in the overall coolant channels.

Once both the diffuser model and the coolant channel are discretized down to the cell size, a T-rHEX mesh can be generated. Each cell within the T-rHEX mesh represents four grid points in`N1D-Flow`, the inlet and outlet

grid points for both the diffuser results and coolant channel results. This way, the T-rHEX cell (`HEX_cell.py`) accounts for the interaction between the coolant channel and the diffuser flow. In subsection 3.1.4, the thermal model is explained taking into account for the cell discretization.

3.1.4. Thermal model

To accurately evaluate the heat transfer performance of the heat exchanger, an appropriate heat transfer model must be implemented. As discussed in subsection 2.2.2, heat transfer between channels under steady-state conditions is governed by convection and conduction. Due to the temperature difference between the hot diffuser flow and the cold coolant flow, a heat transfer sequence is established. Heat is first transferred from the diffuser flow to the wall by convection, then conducted through the wall material from the diffuser walls to the coolant channel walls, and finally transferred from the wall to the coolant flow by convection. A visual representation of this heat transfer sequence is shown in Figure 3.7.

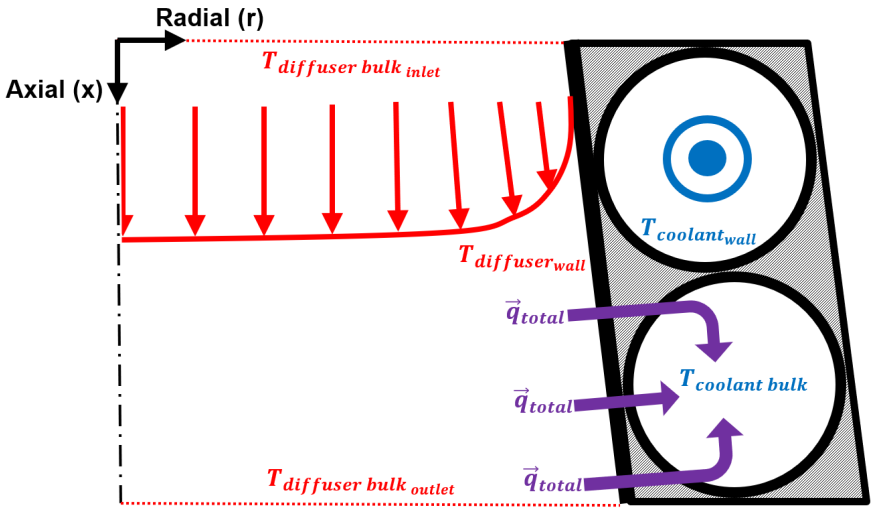

Figure 3.7: Heat transfer visualization between the diffuser and coolant channel.

Although the heat transfer process is inherently three-dimensional, it can be represented as a series of mechanisms and thus simplified to a thermal resistance network.

$$\dot{Q} = \frac{\Delta T}{\mathrm{R_{total}}} \tag{3.6}$$

As heat is conducted through the solid wall, the length and geometry of the conduction path determine its contribution to the overall thermal resistance. For instance, heat flowing into the coolant channel through the sidewalls encounters a longer conduction path and therefore a higher resistance compared with heat transferred through the wall closest to the diffuser surface. To incorporate these three-dimensional effects into a one-dimensional model, an averaging approach is applied. Since previously it was assumed that the coolant channels are "tightly packed", heat enters the coolant channels through the semi-cylindrical wall section adjacent to the diffuser. Assuming that the heat flux variation along the wall is small, a uniform heat flux is applied over the averaged area. The same approximation is used for convective heat transfer between the solid wall and coolant flow, where the heat transfer rate per cell is computed using the wetted area of the diffuser and a constant wall heat flux. The difference in heat flux between the diffuser-solid wall and the solid wall-coolant is therefore dependent on the thermal conductivity and characteristic length of the heat path.

$$\mathrm{R}_{\text{total}} = \mathrm{R}_{\text{convection diffuser}} + \mathrm{R}_{\text{conduction}} + \mathrm{R}_{\text{convection coolant}} \tag{3.7}$$

$$\mathrm{R}_{\text{total}} = \frac{1}{UA_{\text{total}}} \approx \frac{1}{UA_{s_{\text{diffuser}}}} \tag{3.8}$$

$$\mathrm{R}_{\text{convection diffuser}} = \frac{1}{h_{c_{\text{diffuser}}} A_{s_{\text{diffuser}}}} \approx \frac{1}{h_{c_{\text{diffuser}}} A_{\text{total}}} \tag{3.9}$$

$$\mathrm{R}_{\text{conduction}} = \frac{L}{kA} \approx \frac{L_{\text{char}}}{kA_{\text{total}}} \tag{3.10}$$

$$\mathrm{R}_{\text{convection coolant}} = \frac{1}{h_{c_{\text{coolant}}} A_{s_{\text{coolant}}}} \approx \frac{1}{h_{c_{\text{coolant}}} A_{\text{total}}} \tag{3.11}$$

Before developing the thermal model, key assumptions are taken to simplify three-dimensional effects which cannot be captured by one-dimensional models.

- Conduction thermal resistance is very small compared to convection resistance. Therefore, conduction effects are neglected for 1D modeling.
- Coolant channel thermal convection is taken with respect to the diffuser exterior area.
- Coolant channels do not exchange heat between themselves.
- Heat transfer effects due to helicoidal motion induced pressure gradients are negligible at low speeds.

The first assumption is derived from the simplification of the three-dimensional conduction effects and their significance on the overall heat transfer resistance. The coolant channel is discretized with reference to the exterior radius of the diffuser. As the coolant channel is projected onto the diffuser exterior area, the gap between the diffuser walls and the coolant channel walls at its closest point is zero. From a one-dimensional model point of view, since each channel is solved independently, this has no effects on results. However, for the three-dimensional model, this issue becomes significant (see chapter 4). As you move away from the closest point towards the side walls, the conduction heat path length increases, leading to higher local thermal resistance. However, since the distance between the diffuser and coolant sidewalls remains small and the solid wall material has high thermal conductivity, the effect of solid conduction on total thermal resistance can be considered negligible. Neglecting this contribution introduces a minor overestimation of the overall heat transfer rate, which is deemed acceptable for the scope of this low fidelity model.

Based on the first assumption, since conduction effects are neglected, the heat flux out of the diffuser must be equal to the heat flux into the coolant channel, giving rise to the second assumption. Using a uniform heat flux introduces discrepencies between 1D modeling and 3D modeling. For the purpose of the low fidelity model, this assumption is also deemed acceptable.

The third assumption concerns temperature gradients. At the inlet of all coolant channels within a cell, the temperature is assumed uniform (right boundary in Figure 3.6). As the flow progresses along each channel, it is heated uniformly, since all channels share identical geometry and a constant heat flux per cell. Consequently, the temperature rise is equal in all channels, without accounting for possible interactions from neighboring channels. In reality, small temperature differences can occur between adjacent channels in the direction perpendicular to the coolant flow path. The interchannel heat transfer effect becomes more relevant at high twist angles. Nevertheless, the interchannel effect is significantly smaller than the heat transfer due to the diffuser, thus neglected for this low fidelity model.

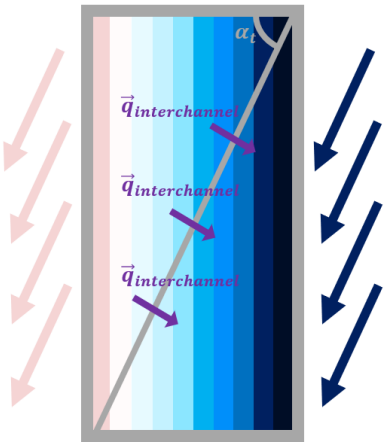

Figure 3.8: Interchannel heat transfer effect due to difference in temperature at the sidewalls.

The fourth assumption is based on velocity profiles due to helicoidal motion induced pressure gradients. Any flow experiencing some curvature will have a radial pressure gradient, inducing a velocity gradient. As the coolant channel is wrapped around the diffuser, the velocity within the coolant channel is greatest at the far wall from the diffuser, while at the near wall, the velocity is smallest. Convection is dependent on Reynolds number. As the velocity decreases at the near wall, the Reynolds number decreases,

which leads to a decrease in convective heat transfer coefficient. The effect is proportional to the centrifugal forces present. High coolant channel bulk velocities or lower curvature radius lead to higher velocity gradients within the coolant channel, leading to overestimated heat transfer rates by the low fidelity model.

The heat transfer solver developed within this study is inspired by "chapter 4 - Surface Comparisons, Size, Shape and Weight Relationships", & "chapter 7 - Thermal Design", of Hesselgreaves' Compact Heat Exchangers book[5]. The thermal solver employs an iterative procedure to determine the thermal power distribution along the recuperator. Each cell in the T-rHEX is initially assumed adiabatic, with zero heat flux. The heat flux is then updated at each iteration following the process shown in Figure 3.9, until convergence is reached. The final solution provides the recuperator's thermal performance and the flow properties of both the diffuser and the coolant channels.

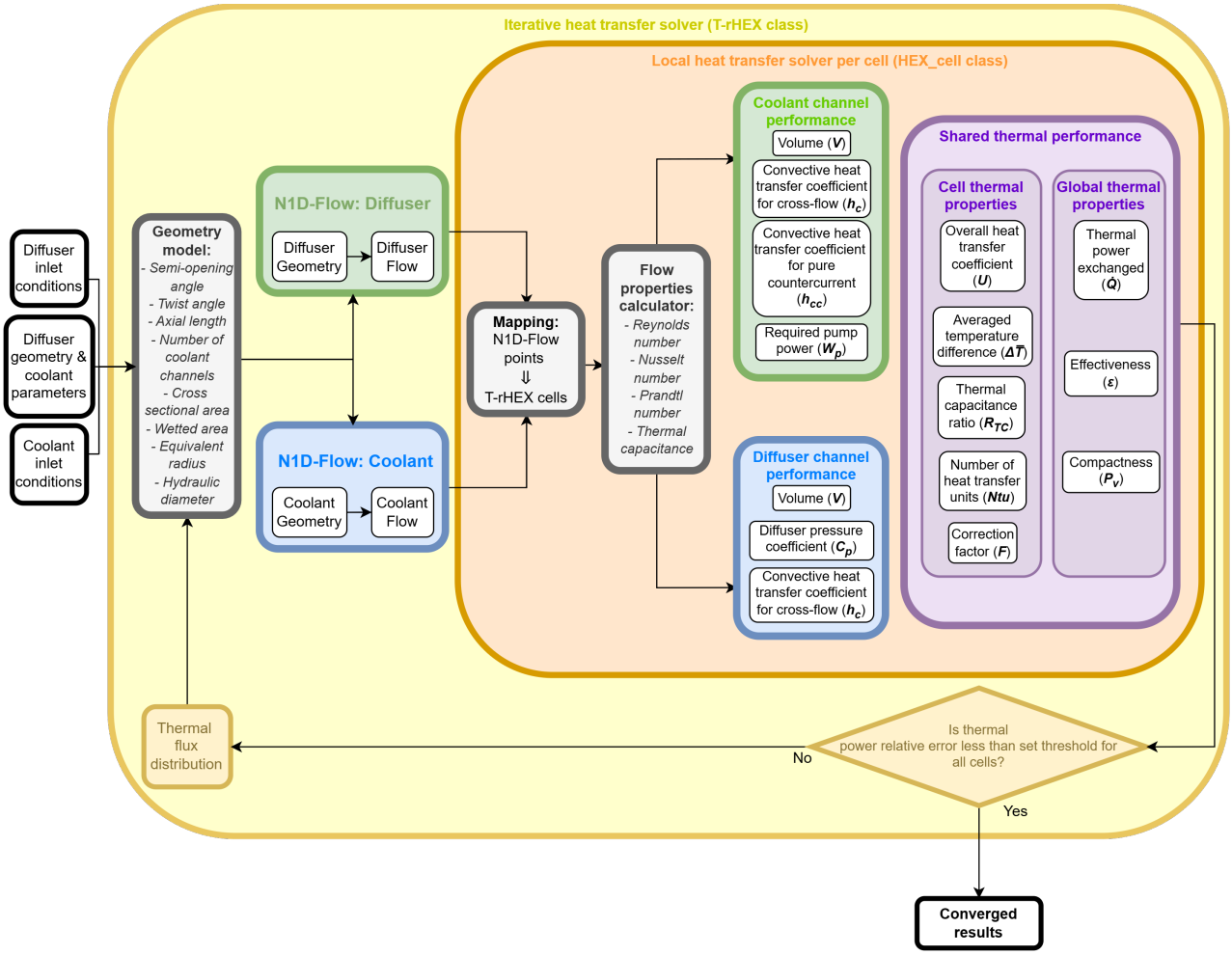

Figure 3.9: Block diagram of the T-rHEX heat transfer solver.

The thermal solver consist of a Geometry model, `N1D-Flow`, and `HEX_cell`. As seen in Figure 3.9, the inlet conditions and diffuser geometry is specified. Based on the diffuser geometry and prescribed coolant parameters, the geometrical model discretizes the recuperator domain, subdividing it into `N_points` number of cells, each with their respective geometrical properties stored.

Once the diffuser geometry and coolant geometries are known, `N1D-Flow` is executed using the same grid resolution as T-rHEX for the cells. Due to the modifications implemented in subsection 3.1.2, variable geometry is imported into the diffuser and coolant channel simulations. `N1D-Flow` returns flow properties of the diffuser and coolant channel along the recuperator.

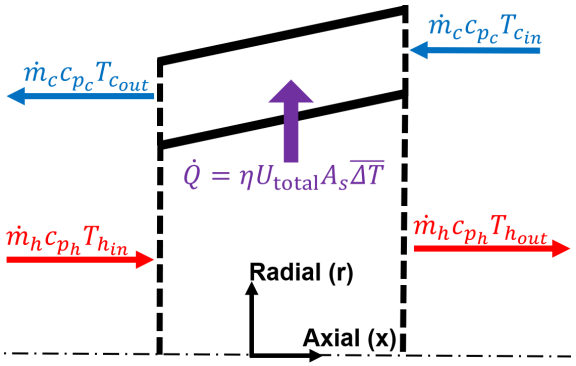

Figure 3.10: T-rHEX cell control volume for energy balance.

Each `T-rHEX.py` cell corresponds to four `N1D-Flow` grid points. Because the coolant is arranged in a countercurrent configuration, the coolant flow direction opposes that of the diffuser flow. As shown in Figure 3.10, energy conservation requires that the difference in thermal inertia between the diffuser inlet and outlet equals the sum of the thermal inertia increments across all coolant channels. This quantity must also be equal to the heat transferred between the diffuser flow and the coolant channels. The conservation of energy within each fluid stream is handled by `N1D-Flow`, but the achievable heat transfer must be computed separately. For this reason, each T-rHEX cell evaluates the heat-transfer capability of the diffuser side, the coolant channels, and their combined performance.

$$\dot{Q} = \eta_{\text{heat transfer}}\, U_{tot}\, A_s\, \overline{\Delta T} = \dot{m}_{hot}\, c_{p_{hot}}\, (T_{hot_{in}} - T_{hot_{out}}) = \dot{m}_{cold}\, c_{p_{cold}}\, (T_{cold_{out}} - T_{cold_{in}}) \tag{3.12}$$

Equation 3.12 states conservation of energy across a cell, where the thermal power rejected by the diffuser flow is equal to the thermal power input by the coolant channel flow. This heat transfer rate is determined by an averaged temperature difference ($\overline{\Delta T}$), heat transfer efficiency ($\eta_{\text{heat transfer}}$), heat transfer coefficient (U_{tot}), and heat transferring area (A_s).

From the known `N1D-Flow` fluid properties, the local averaged temperature difference between channels is calculated ($\overline{\Delta T}$). Given the counterflow arrangement, the logarithmic mean temperature difference (LMTD) model is used to calculate the temperature difference between models ($\overline{\Delta T} \approx \Delta T_{LMTD}$). The LMTD between channels is derived by considering a pure countercurrent arrangement.

$$\dot{m}_h c_{p_h} \frac{\mathrm{d}T_h}{\mathrm{d}x} = \dot{C}_h \frac{\mathrm{d}T_h}{\mathrm{d}x} = -\dot{q}\,\mathrm{d}A \tag{3.13}$$

$$\dot{m}_c c_{p_c} \frac{\mathrm{d}T_c}{\mathrm{d}x} = \dot{C}_c \frac{\mathrm{d}T_c}{\mathrm{d}x} = -\dot{q}\,\mathrm{d}A \tag{3.14}$$

Consider once again Figure 3.10. The decrement thermal inertial within the diffuser stream across an infinitesimally small cell must be equal to the increments in thermal inertial within all coolant channels.For a convective heat transfer process, the heat flux can be expressed as a function of the total heat transfer coefficient (U_{total}) and temperature difference between the two streams. Now taking Equation 3.13 minus Equation 3.14 gives Equation 3.15.

$$\dot{C}_h \left(\frac{\mathrm{d}T_h}{\mathrm{d}x} - \frac{\mathrm{d}T_c}{\mathrm{d}x} \right) = \dot{q} \left(1 - \frac{\dot{C}_h}{\dot{C}_c} \right) dA = U_{\text{total}}\, (T_h - T_c) \left(1 - \frac{\dot{C}_h}{\dot{C}_c} \right) \mathrm{d}A \tag{3.15}$$

For a finite area, Equation 3.15 is integrated between two boundaries enclosing an area. This area represents the discrete cell wetted surface area of the diffuser.

$$\int_{\text{inlet}}^{\text{outlet}} \frac{1}{(T_h - T_c)} \frac{\mathrm{d}\,(T_h - T_c)}{\mathrm{d}x} \mathrm{d}x = \int_{A_s} U_{\text{total}} \left(\frac{1}{\dot{C}_h} - \frac{1}{\dot{C}_c} \right) \mathrm{d}A \tag{3.16}$$

$$\ln \frac{\Delta T_{\text{outlet}}}{\Delta T_{\text{inlet}}} = -U_{\text{total}} A_s \left(\frac{\Delta T_h}{\dot{Q}} - \frac{\Delta T_c}{\dot{Q}} \right) \tag{3.17}$$

Using linearity of differentiation properties and equation rearrangements, the heat transfer rate equation for a pure counterflow is found to be Equation 3.18.

$$\dot{Q} = U_{\text{total}} A_s \frac{\Delta T_{\text{outlet}} - \Delta T_{\text{inlet}}}{\ln\left(\frac{\Delta T_{\text{outlet}}}{\Delta T_{\text{inlet}}}\right)} = U_{\text{total}} A_s \Delta T_{LMTD} \tag{3.18}$$

The LMTD model has been derived based on a pure counterflow arrangement. As discussed in subsection 2.2.2, cross-flow requires additional modeling as temperature gradients are no longer just along the flow direction but also perpendicular to the flow direction. To account for such effect the heat transfer efficiency ($\eta_{\text{heat transfer}}$)is adapted. The model does not directly count for thermal losses. Instead, the effect of cross-flow is accounted for by the use of the correction factor (Equation 2.12).

The correction factor may be modeled using semi-empirical relations for common heat exchangers. As the T-rHEX is a novel concept, no similar experimental or empirical data has been found. For this reason an analytical approach has been implemented.

$$F = \frac{U_{\text{counter}} A_{s_{\text{counter}}}}{U_{\text{cross}} A_{s_{\text{cross}}}} = \frac{Ntu_{\text{counter}}}{Ntu_{\text{cross}}} \tag{3.19}$$

$$\dot{Q} = F U_{\text{total}} A_s \Delta T_{LMTD} \tag{3.20}$$

Equation 3.19 is derived by comparing the heat transfer rate equation of cross-flow arrangement (Equation 3.20) to pure countercurrent arrangement (Equation 3.18). The correction factor can also be defined by the difference in number of heat transfer units.

$$Ntu = \frac{U_{\text{total}} A_s}{C_{min}} \tag{3.21}$$

The number of heat transfer units (Ntu) is defined as the ratio of the overall conductance of a heat exchanger to the minimum heat capacity rate of the two fluid streams. It serves as a non-dimensional index of the ability of the heat exchanger to transfer heat relative to the thermal inertia of the weaker fluid stream. Ntu can be interpreted as a measure of local heat transfer effectiveness, however, for this study it is used to compare the thermal performance of the coolant channel in a cross-flow configuration with that of an equivalent countercurrent configuration. A pure countercurrent coolant channel is constructed based on the axial coolant channel cross-sectional area and on the axial coolant channel length, while the flow and thermodynamic properties are kept constant. This allows to directly obtain the cross-flow effect on convection rate locally. The ratio between the heat transfer rate in cross-flow and the corresponding pure countercurrent value defines the correction factor F.

To find the total heat transfer coefficient, Equation 3.7 needs to be considered. Conduction effects have been neglected, thus the thermal resistance due to conduction is null. Additionally, the only reference area transferring heat is the diffuser exterior walls. As the area is constant, the total heat transfer coefficient depends solely on the convective heat transfer coefficients of the diffuser flow and the coolant flow.

For the purpose of modeling convection, each discretized cell is once again treated as a cylindrical segment with an equivalent radius (r_{eq}). This representation allows the use of pipe flow heat transfer correlations, which are appropriate for internal flows and consistent with convective models from VDI Heat Atlas [10]. Accordingly, both the diffuser flow and the coolant channels are modeled using pipe flow convection correlations for laminar, transitional, or turbulent regimes.

$$h_c = f(Re_D, Pr, d_H, L, k_{fluid}, \delta_{\text{curvature}}) \tag{3.22}$$

Naturally, the use of pipe flow correlations introduces limitations. In the diffuser, adverse pressure gradients influence the development of the thermal boundary layer, which may cause deviations between the true wall heat transfer and the values predicted by pipe correlations. For the coolant channel, an additional correction is applied to account for curvature induced effects, although a simplified formulation is used because more detailed models require knowledge of the wall temperatures, which are not present in the given model. For diffusers with large semi opening angles or coolant channels operating at high velocities, the discrepancy between pipe flow correlations and the actual convective heat transfer may become significant. These effects are further examined in chapter 4.

To conclude on the local heat transfer solver, once the convective heat transfer coefficients are found, their contributions to the thermal resistance network can be summed in series (as shown in Equation 3.7). As all components are known in Equation 3.20, the actual heat transfer rate of each cell is known. The results are then used for the following iteration, as shown in Figure 3.9, where this iterative process is repeated until the difference in heat transfer rate between the actual and previous iteration is smaller than the specified stopping threshold for all cells. Converged results not only provide the achievable distribution of heat flux along the heat exchanger, but also the updated flow properties of both channels.

Global performance of the recuperator can be measured by different additional parameters, which are calculated simultaneously within the thermal solver.

$$\epsilon = \frac{\dot{Q}}{\dot{Q}_{max}} = \frac{\dot{C}_b \left(T_{b_{in}} - T_{b_{out}}\right)}{\dot{C}_{min} \left(T_{b_{in}} - T_{c_{in}}\right)} = \frac{\dot{C}_c \left(T_{c_{out}} - T_{c_{in}}\right)}{\dot{C}_{min} \left(T_{b_{in}} - T_{c_{in}}\right)} \tag{3.23}$$

The effectiveness (ϵ) of a heat exchanger is defined as the ratio of the actual heat transfer rate to the maximum possible heat transfer rate for the given inlet conditions. Effectiveness provides a direct measure of how closely the heat exchanger approaches the theoretical thermal limit (pinch). For a recuperator, maximizing effectiveness is essential to maximize heat recovery and improve the overall cycle efficiency.

$$\dot{W}_{\text{pump}} = \frac{\dot{m}_c \Delta p_c}{\rho_c} \tag{3.24}$$

Another critical performance criterion of the recuperator is the pressure losses of the coolant, and the pump work required to overcome these pressure losses[5]. Similarly to effectiveness, pump power required ($\dot{W}_{\text{pump}}$) can be integrated over all cells to find the total pump power required due to pressure losses across all coolant channels. To maximize the overall cycle efficiency, the pumping power must be minimized, which in turn constrains the coolant channel design to minimize pressure losses.

$$P_V = \frac{4V\sqrt{2\rho\Delta p}}{\left(\dot{m}\, Pr\, N\right)^{\frac{3}{2}}} \tag{3.25}$$

Compactness is a parameter used extensively in heat exchanger design when heat exchanger volume is critical[5]. Compactness takes into account not only volume (V), but also pressure losses (Δp) and normalized temperature differences within the channel ($N = \Delta T / \Delta T_{LMTD}$). As this parameter aggregates several aspects of thermal and fluid dynamic performance, using compactness alone for comparative assessment may lead to misleading conclusions. Instead, compactness remains a useful dimensional parameter that indicates the volume required by a heat transfer surface for a specified thermal duty, as determined by its heat exchanger surface performance[5].

$$C_p = \frac{p_{\text{exit}} - p_\infty}{\frac{1}{2}\rho_\infty u_\infty^2} \tag{3.26}$$

Lastly, pressure coefficient is a critical parameter for the performance of the diffuser. The pressure coefficient gives an indication on how high the exit pressure of the diffuser is compared to the stagnation inlet pressure of the diffuser. Normally, adiabatic and incompressible diffusers give pressure coefficient values between 0 and 1. A value of 0 indicates that the exit pressure is equal to the inlet static pressure, while a value of 1 indicates the exit pressure is equal to the inlet stagnation pressure. Values higher than 1 indicate that exit stagnation conditions are greater than inlet stagnation conditions, likely due to changes in density from compressibility and/or heat transfer effects. As the goal of the recuperator is to integrate the heat exchanger with the diffuser, the diffuser performance on pressure recovery is a critical aspect of this design. Good diffuser pressure recovery aims to obtain the highest possible pressure coefficient.

3.2. Model verification and validation

To ensure `T-rHEX.py` provides accurate results, the code is verified for mass and energy conservation. As the `T-rHEX.py` has both a flow and thermal solver, numerical verification is done separately. Moreover, both friction and coolant model results are compared to experimental data to ensure low fidelity model results are valid.

`N1D-Flow` is used by `T-rHEX.py` as a flow solver to obtain quasi-1D results for non-ideal fluids. As given in section 3.1, `N1D-Flow` operates using a backwards Euler scheme, where discretization plays a large role. The equations derived by Tosto obey conservation of mass and energy[16]. However, the discretized equations do not explicitly conserve mass and energy. These discretization errors therefore lead to mass and energy losses.

Table 3.1: Verification results for mass and energy conservation.

Number of grid points	Diffuser mass flow error [%]	Coolant mass flow error [%]	Diffuser enthalpy error [%]	Coolant enthalpy error [%]	Thermal power error wrt 10^5 grid points [%]	Pressure coefficient error wrt 10^5 grid points [%]	Runtime [sec]
10^1	55.24	40.85	95.27	53.30	34.7	31.5	0.11
10^2	5.35	7.73	56.35	10.59	4.31	1.85	0.81
10^3	0.53	0.84	10.99	1.18	0.520	0.178	15.81
10^4	0.053	0.085	1.21	0.12	0.0479	0.0198	57.91
10^5	0.0053	0.0085	0.12	0.01	-	-	570.89

As seen in Table 3.1, discretization plays an important role in the accuracy of results. Linearized gradients between grid points may dampen underlying effects, leading to loss of mass and energy. Other factors such as mass flow rate and channel length play a smaller role in accuracy given a number of grid points. As shown in Table 3.1, the coolant channel exhibits slightly larger error than the diffuser. This is believed to be due to the larger length of the coolant channels. Since the number of grid points is fixed, the coolant channel length per cell is much larger than the diffuser length per cell. Thus the effect of linearization of gradients within the cells is stronger for the coolant than diffuser. In general, the trend obtained from Table 3.1 shows that increasing resolution of the 1D grid leads to decreasing of mass flow error, at the cost of higher computational time.

Similarly, energy in the form of enthalpy is lost for poorly discretized 1D grids. Enthalpy dissipation is caused when the difference in exit and inlet enthalpy is smaller than heat added/subtracted. As seen in Table 3.1, the diffuser flow experiences more numerical dissipation. There are two primary reasons for numerical dissipation in energy. Firstly, mass dissipation carried over since mass dissipation leads to thermal inertia dissipation. Secondly, the heat flux transferred out of the diffuser exceeds the heat flux received by any single coolant channel, because the total heat transfer is divided equally among all coolant channels. Since the diffuser enthalpy is found to be higher than the coolant enthalpy, it can be concluded that the effect of mass flow rate is smaller than the effect of heat flux in enthalpy error, leading to higher discretization error for the diffuser flow.

In terms of overall results, the total thermal power error and diffuser pressure coefficient errors are proportional to the mass and energy errors. This shows how conservation in mass and energy are critical in order to obtain valid results. For thermal power, choosing a coarse grid leads to under prediction of thermal power, and thus heat exchanger effectiveness. On the other hand, a course grid results in an overestimation of pressure coefficient. The friction and heat transfer effects are affected by coarse grids. As previously discussed, heat transfer is reduced by coarse grids, which also reduces pressure recovery. Since grid coarsening causes pressure recovery coefficients to increase, but also causes a drop in recuperated thermal power, the effect of pressure losses due to friction are decreased. This effect is also present in the coolant channel, as coarse 1D grids lead to an underestimation of coolant pressure loses and thus under prediction of required pump power to overcome such pressure losses.

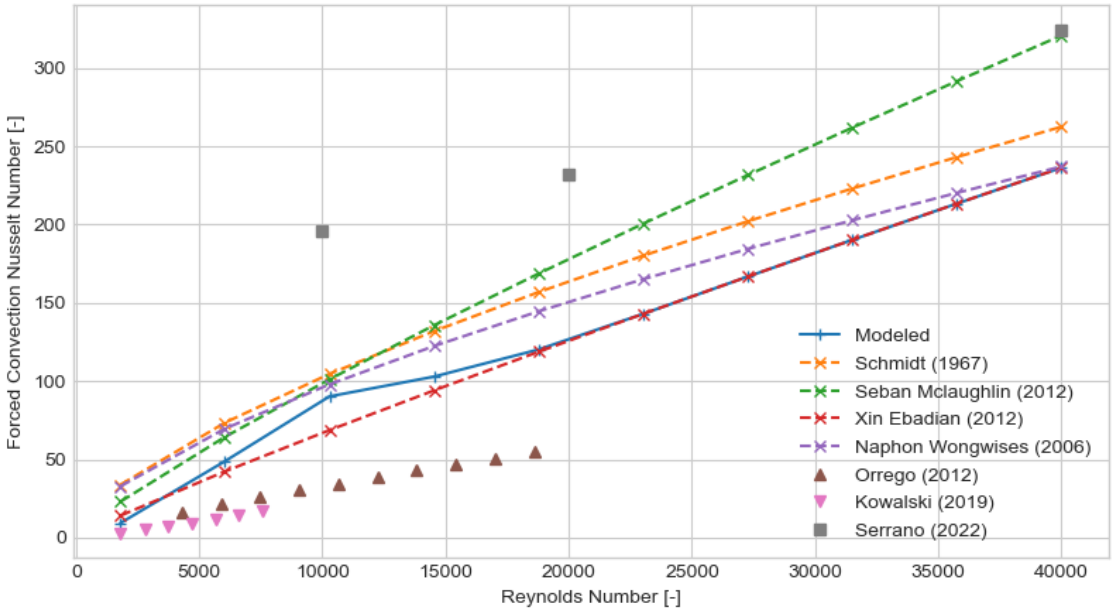

Figure 3.11: Validation data for forced convection Nusselt number models[11, 7, 14].

In efforts to improve accuracy of `T-rHEX.py`, a validation process for both the friction and forced convective heat transfer coefficient models is performed. Kowalski and Downarowicz investigated the heat transfer of a helicoidal heat exchanger where the coolant channel is inside the diffuser [7]. Their work focused on comparison between their experimental data to existing Nusselt number models. Orrego et al. investigated a cone-shaped helicoidal channel with perpendicular heating flow to measure the effects of heating on a cone-shaped helicoidal channel[11]. Additionally Serrano et al. conducted an experiment to measure the convective heat transfer coefficient of a pipe[14]. The work from Serrano et al. is used with the purpose of comparison between helicoidal channels and straight pipes.

As seen in Figure 3.11, both helicoidal channel models and helicoidal channel experimental data achieve much lower Nusselt numbers than for straight pipe experimental data. As helicoidal channel flows exhibit centrifugal forces, radial pressure gradients are generated, leading to shift in fluid towards the furthest wall from the axis of rotation. This reduces the flow velocity near the closest wall from the axis of rotation, which reduces convection. Kowalski's results show how the effect is dependent both on averaged Reynolds number, Prandtl number and curvature ratio. Orrego's results are slightly higher than Kowalski's due to the beneficial effect of convection at the wall furthest from the axis of rotation. Overall Kowalski concludes that all convection models overpredict convection heat transfer, however, the model provided by Xin and Ebadian follows best their expected trend for convection within helicoidal channels[7]. For this reason, the used convection model was tuned to better fit the existing model by Xin Ebadian. In conclusion, all tested forced convection models overpredict Nusselt number of helicoidal paths. There can be a variety of reason for this inconsistency. However, since Kowalski concluded that all models overestimated heat transfer, it is expected that the T-rHEX low fidelity model to overpredict heat transfer compared to experimental results.

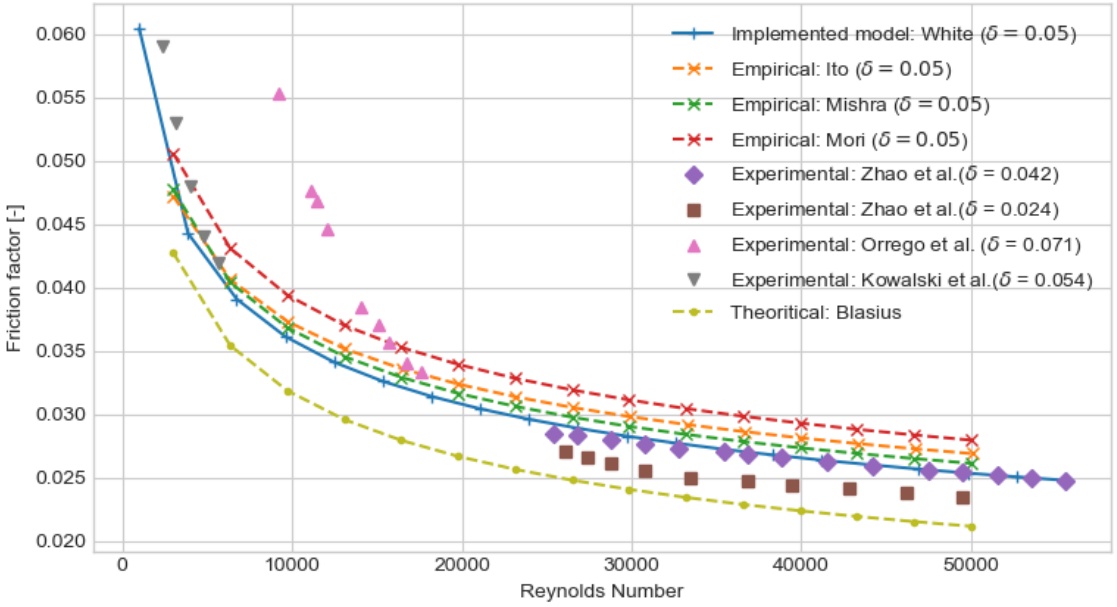

Figure 3.12: Validation data for friction factor models for a given curvature ratio ($\delta_{curvature}$)[11, 7, 17].

Validation of the friction model is as important as validating the convection model due to the frictional losses in both the diffuser and coolant. Both Kowalski's and Orrego's experimental data are valid for frictional model validation[7, 11]. Additionally Zhou et al. performed experiments on helicoidal channels using different curvature ratios. For this validation procedure, a curvature ratio of 0.05 is chosen since validation data is available. Figure 3.12 shows empirical models following similar trends, with Blasius (simplest laminar flow friction model) resulting in the lowest friction. Turbulent models are found to slightly overpredict friction at high Reynolds number flows while under predicting friction at low Reynolds number flows. The implemented pipe model uses White's equation to improve effects of turbulent flows and to account for centrifugal effects. This model is found to be robust even at higher curvature ratios.

Zhou shows that an increase in curvature ratio leads to an increase in friction[17]. Similarly, the implemented model follows the same trend, however the sensibility to curvature is reduced compared to experimental data. This leads to a under prediction of friction for high curvature ratios. For low Reynolds number flows, Orrego's data suggest values which are higher than all empirical models. This shows that for high curvature ratios, friction is under predicted for low Reynolds number flows in general, and the effect of curvature increase leads to a stronger under prediction of friction. In conclusion, the friction model works well for high Reynolds number flows, and acceptable results are obtained for low Reynolds number flows if the curvature ratio is close to 0.05. In conclusion, both the convective heat transfer models and the friction models should be calibrated to the specific geometry and operating conditions, as their predictive accuracy is strongly case dependent.

3.3. Results: Converting the existing turbine diffuser into a recuperator for the ORCHID WHR cycle

This study considers two scenarios. Firstly, the effect of implementing the conical axial diffuser of the ORCHID turbine as a recuperator is investigated. This setup is named the original or existing ORCHID with recuperation. Later, in section 3.4, the geometry of the existing ORCHID diffuser is optimized. This setup is named the optimized T-rHEX.

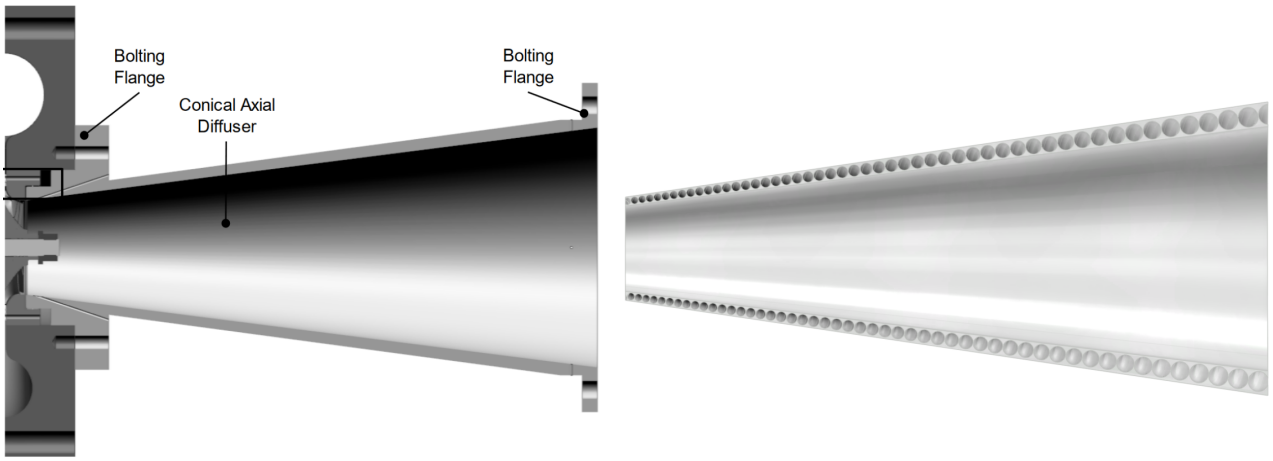

(a) The ORCHID turbine diffuser.

(b) The ORCHID turbine diffuser with recuperation.

The current ORCHID turbine is coupled to an adiabatic diffuser as shown in Figure 3.13a,implementing MM (hexamethyldisiloxane) as the organic working fluid of the system. The inlet thermodynamic state of the diffuser is defined by the turbine exit conditions. The ORCHID ORC with the given adiabatic diffuser geometry operates with a thermal efficiency of 12.11%, enabling a total ORCHID turbine work extraction of $9940\,\mathrm{W}$. This chapter implements the effects of implementing the diffuser as a recuperator, where coolant is passed along helicoidal channels passing along the exterior surface area of the diffuser as seen in Figure 3.13b.

Fluid	MM
Mass flow rate	0.149 [kg/s]
Inlet temperature	520.6 [K]
Inlet pressure	40000 [Pa]
Inlet Mach	0.53 [-]
Inlet radius	18.9 [mm]
Outlet radius	53.7 [mm]
Semi-opening angle	7° [deg]
Length	283.8 [mm]

Table 3.2: ORCHID turbine diffuser fluid and geometrical properties.

To reduce the number of design variables, a maximum curvature ratio of 0.1 is imposed on the coolant channels. Consequently, each coolant channel diameter must be less than or equal to one tenth of the local diffuser diameter, with the final diameter obtained by rounding up the number of coolant channels required to satisfy this constraint. This ensures that the resulting curvature ratios remain consistent with values reported in experimental studies[11, 7, 17]. Once determined the number of coolant channels, the value is fixed while the coolant channel diameter varies along the length of the recuperator (subsection 3.1.3). The coolant enters the helicoidal channel at the end side of the diffuser and exits at the inlet side of the diffuser. This overall countercurrent arrangement allows to maximize temperature differences along the diffuser (subsection 2.2.2). To enhance heat transfer between the two streams, the coolant channels are wrapped around the diffuser with a constant twist angle. This twist angle is selected through a single design variable optimization, in which the objective is to maximize the ORC efficiency. The procedure yields an optimal constant twist angle of $82.37°$. A more comprehensive geometric optimization, based on diffuser shaping rather than coolant channel twist alone, is presented later in section 3.4.

By routing the coolant through a helicoidal channel along the diffuser surface, the ORC efficiency (η_{ORC}) increases by 0.42%. This improvement is achieved without added geometric complexity, which allows for efficiency increment without significantly increasing structural weight. The model predicts a total thermal duty of $2921\,\mathrm{W}$ and a heat exchanger effectiveness (ϵ) of 8.36%. The addition of the coolant path generates frictional losses, which in turn raises the required pump power. For the given optimal twist angle, the pump power needed to overcome these pressure losses is $22.0\,\mathrm{W}$.

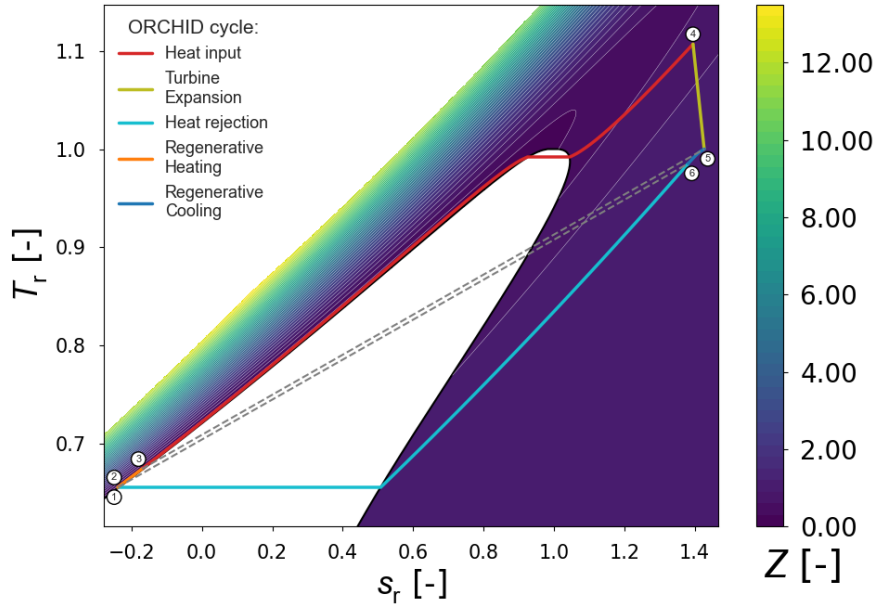

Inlet (point 5)	
Temperature [K]	518.7
Pressure [Pa]	40000
Mach number [-]	0.534
Adiabatic outlet (point 6)	
Temperature [K]	520.6
Pressure [Pa]	45840
Mach number [-]	0.058
Cooled outlet (point 6)	
Temperature [K]	511.0
Pressure [Pa]	45880
Mach number [-]	0.057

Table 3.3: Inlet and outlet thermodynamic properties of the ORCHID turbine diffuser.

Figure 3.14: Temperature–entropy diagram of the ORC with recuperation achieving a thermal efficiency of 12.53% (+Δ0.42%), showing iso-lines of the compressibility factor.

Figure 3.14 shows the ORC with regeneration, where the turbine diffuser is operated as a thermal recuperator. The turbine work remains unchanged because the inlet (point 4) and outlet (point 5) states are fixed. Downstream of the turbine, the diffuser exit state (point 6) departs from the adiabatic reference due to cooling, which lowers both temperature and entropy. The recovered heat is transferred to the coolant. After leaving the condenser, the coolant flows through the recuperator (point 2 to point 3), where it receives this heat, increasing its temperature and entropy. As a result, the working fluid requires less external heat input to reach turbine inlet conditions (point 4), thereby improving the thermal efficiency of the ORC.

To better understand the performance of the recuperator, heat transfer capabilities need to be analyzed. The heat flux along the diffuser is an indicator of how heat can be transferred between the diffuser stream and coolant channels. Figure 3.16 shows a 3D view of the diffuser with heat flux values along its exterior surface. To ease understanding, the surface is cut axially and flattened into a 2D view. This allows to directly project the coolant channel paths along the surface of the diffuser. This procedure is done for all low fidelity model results plotted in this study.

As given in Equation 3.20, heat flux is directly proportional to the difference in temperature between streams and the overall heat transfer coefficient. Firstly, to understand how temperature difference between streams and heat flux are linked along the diffuser, the thermal plots in Figure 3.15 can be analyzed.

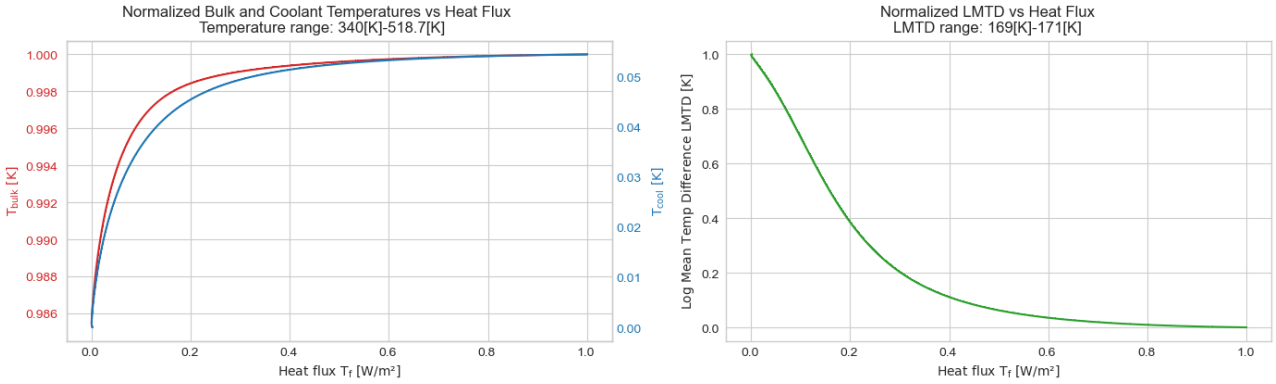

Figure 3.15: Thermal plots along the recuperator ORCHID with recuperation.

Figure 3.15 shows the temperature evolution of both the coolant and the diffuser flows. The temperature

increase of the coolant is larger than the temperature decrease of the diffuser stream. This follows directly from the difference in thermal capacitance between streams. Since the system is closed, the mass flow rates are fixed, and the difference in thermal capacitance arises from the specific heat capacities of the two fluids. Both temperature and phase influence the specific heat capacity. In the ORC using MM, the phase difference between the gaseous diffuser flow and the liquid coolant plays only a minor role, while temperature dependence is dominant. For the ORCHID with recuperator setup, the specific heat capacity of the diffuser gas remains slightly higher than that of the liquid coolant over the entire recuperator length. Consequently, the diffuser stream exhibits a smaller temperature change than the coolant.

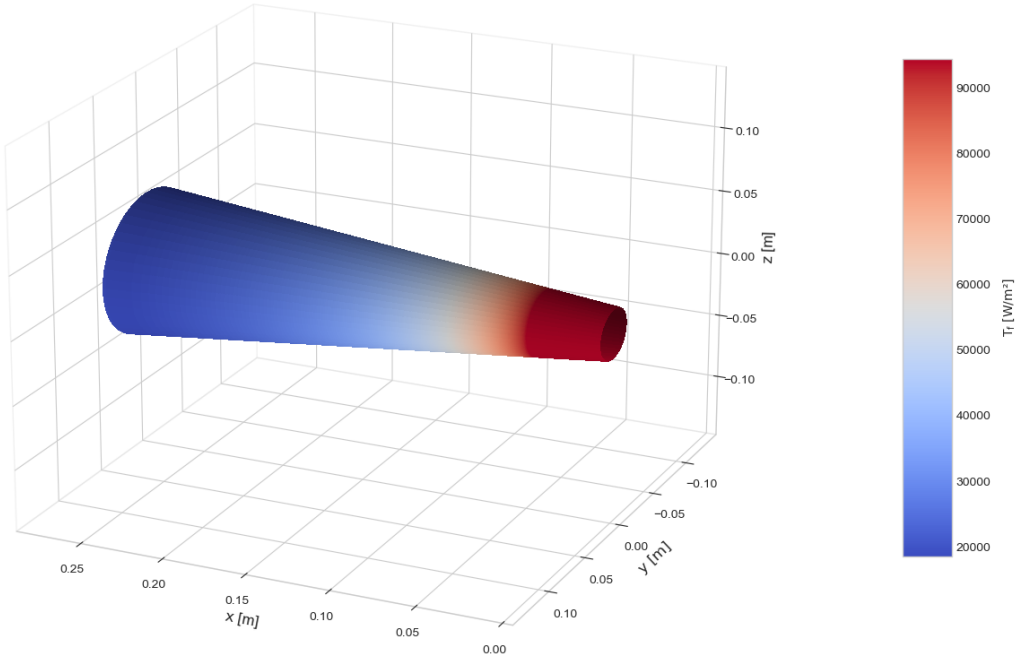

Figure 3.16: 3D view of the heat flux along the surface of the diffuser for the given ORCHID with recuperation setup

In terms of heat transfer induced, the averaged temperature difference (ΔT_{LMTD}) is largest at the lowest heat flux point, which coincides with the outlet of the diffuser (see Figure 3.17). Based on the previous thermal capacitance conclusion, the temperature difference between channels is expected to increase (as described in Figure 2.4). It can be seen in Figure 3.15 that in fact the temperature differences does increase. On the other hand, the larger temperature difference between channels does not imply a larger heat flux. Although there is a slight increment in temperature difference between channels along the diffuser, the temperature difference between streams only varies $2\,\mathrm{K}$. As seen in Figure 3.17, heat flux varies significantly along the length of the recuperator, thus temperature difference is found not to be the determining factor in heat transfer between the diffuser and coolant streams.

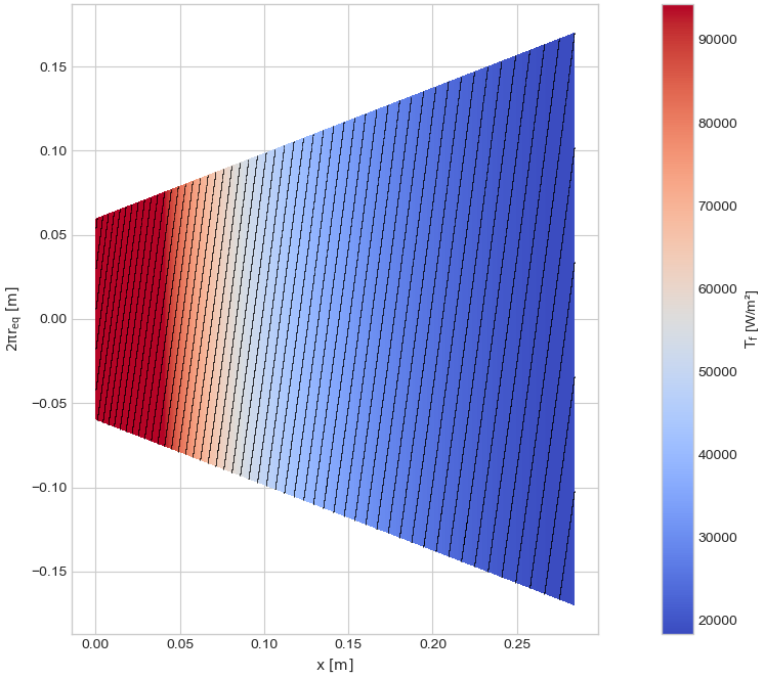

Figure 3.17: Heat flux distribution along the diffuser surface for the ORC with recuperation, including projected coolant channel boundaries.

In terms of heat transfer, Figure 3.15

shows that the largest temperature difference between streams (ΔT_{LMTD}) occurs at the point where the local heat flux is minimum, which corresponds to the diffuser outlet region seen in Figure 3.17. From the previous discussion on thermal capacitance (see Figure 2.4), the temperature difference between channels is expected to increase along the recuperator, and Figure 3.15 confirms that ΔT does indeed grow slightly towards the diffuser exit. However, this increase is modest as the temperature difference between streams changes by only about $2\,\mathrm{K}$, whereas Figure 3.17 shows that the local heat flux varies significantly along the recuperator length. This indicates that the local heat transfer rate is not simply controlled by the temperature difference, but rather by variations in local heat transfer coefficients along the recuperator.

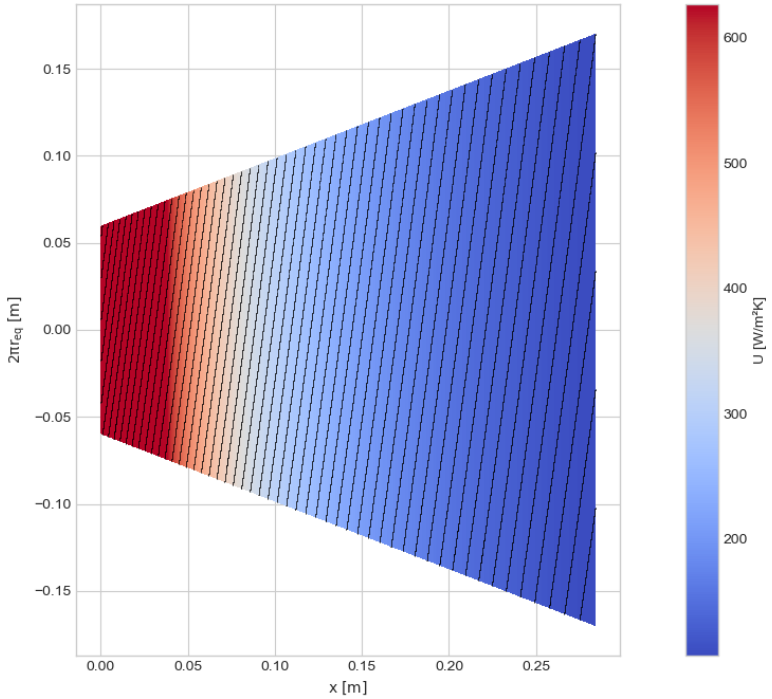

Figure 3.18: Total heat transfer coefficient distribution along the diffuser surface for the ORC with recuperation, including projected coolant channel boundaries.

Another important aspect of the recuperator performance is the variation of the total heat transfer coefficient along its length. Heat transfer in the recuperator is governed by convection on both the diffuser side and the coolant side (see subsection 3.1.4). Because the thermal resistance network treats these two convective processes in series with reference to the diffuser exterior area, the total thermal resistance is the sum of the individual convective resistances:

$$\frac{1}{U_{\text{total}}} = \frac{1}{h_{c_{\text{diffuser}}}} + \frac{1}{h_{c_{\text{coolant}}}}. \tag{3.27}$$

Comparison of Figure 3.18 with Figure 3.17 shows that the heat flux distribution along the recuperator is primarily governed by U_{total}. As illustrated in Figure 3.19, the total heat transfer coefficient reaches its maximum near the diffuser inlet, with values approaching $5000\,\mathrm{W\,m^{-2}\,K}$. Moving along the diffuser stream, U_{total} decreases following an exponential decay. To understand the origin of this behavior, the individual convection coefficients for the diffuser side (h_{c_b}) and the coolant side (h_{c_c}) are examined.

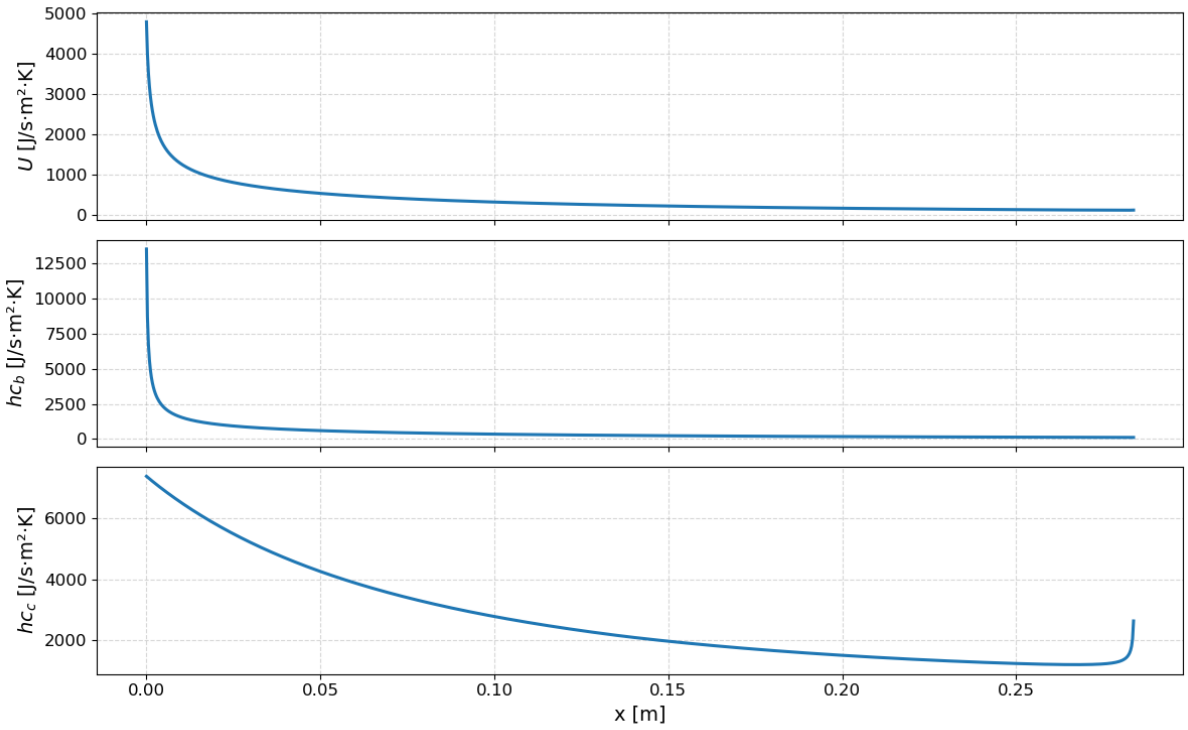

Figure 3.19: Total, diffuser and coolant heat transfer coefficients along the recuperator for the ORCHID with recuperation.

As shown in Figure 3.19, the diffuser experiences a very high convective heat transfer coefficient at the inlet, followed by a rapid decrease that also follows an exponential decay as the flow progresses downstream. This behavior is driven by the development of the thermal boundary layer along the diffuser walls. Near the inlet the thermal boundary layer is thin, which allows a high heat transfer rate. As the flow moves downstream, the thermal boundary layer thickens, which reduces the local heat transfer coefficient. In a straight pipe, turbulence development increases the Reynolds number and thus heat transfer rate. In a diffuser, however, the expanding cross section decelerates the flow and reduces the local Reynolds number, causing the thermal boundary layer to thicken more rapidly than in a constant area duct. This reduction in Reynolds number, combined with the presence of an adverse pressure gradient, suppresses turbulence close to the wall and further decreases the heat transfer rate along the diffuser.

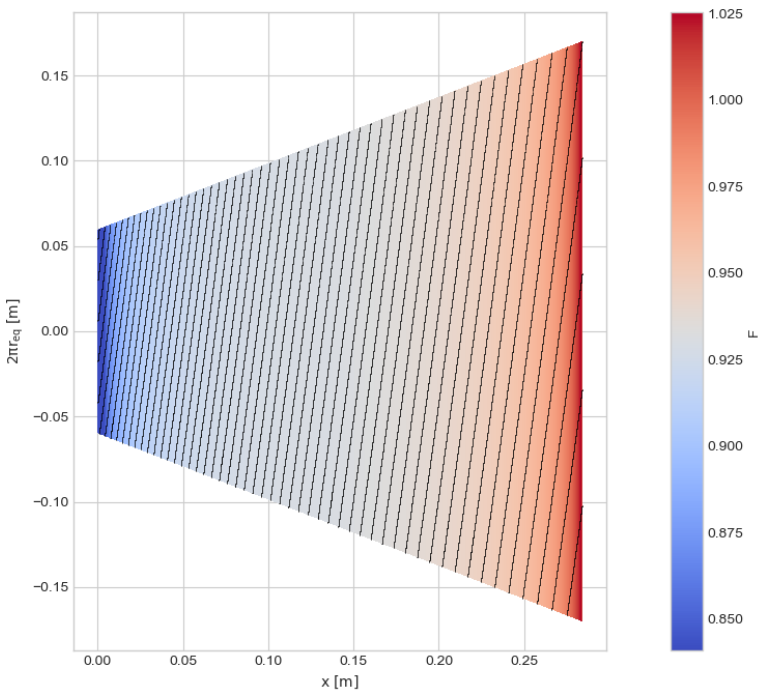

Figure 3.20: Correction factor along the diffuser surface for the ORC with recuperation, including projected coolant channel boundaries.

The coolant channel behaves similarly to internal flow in a pipe. As the exterior diffuser radius decreases, the coolant channel cross sectional area is reduced, and mass conservation causes the coolant velocity to increase. Although the coolant stream also develops a thermal boundary layer (see inlet/right most spike in Figure 3.19 since coolant flow is set as countercurrent), the acceleration of the flow increases inertial forces, which thins the thermal boundary layer and enhances heat transfer rate. Superimposing both diffuser stream and coolant channel stream effects lead to the given distribution of total heat transfer coefficient, where the highest heat transfer is at the inlet of the diffuser and the lowest heat transfer is close, but not at the diffuser outlet.

As shown in Figure 3.20, the correction factor remains close to 0.93 over most of the recuperator, consistent with typical cross flow behavior relative to an ideal countercurrent reference [5]. Near the coolant inlet, the correction factor is slightly elevated because inlet thermal boundary layer development effects increase convection in both channels, yet the countercurrent reference has a shorter flow path per cell and therefore a larger fraction of its thermal boundary layer remains undeveloped promoting heat transfer over the helicoidal channel. Toward the coolant outlet, the correction factor decreases as the coolant velocity rises. Both the effects of a shorter channel with fully a developed boundary layer and larger hydraulic diameter result in a net reduced convective heat transfer performance when comparing the helicoidal cross flow channel to the countercurrent reference. From a modeling perspective, the correction factor captures the relative heat transfer capability of coolant channels at identical thermodynamic states but with different geometries. Values greater than one near the coolant inlet are non physical and originate from discretization errors. The helicoidal channel has a longer flow path per cell, which leads to coarser axial gradients than in the pure countercurrent reference. This causes the convective heat transfer model to overpredict inlet boundary layer development effects. In reality, boundary layer development would be identical for both configurations because the inlet flow conditions are the same.

Research Sub-Question RSQ1

To what extent does integrating and optimizing the T-rHEX geometry improve the thermal efficiency of a high-temperature organic Rankine cycle waste-heat recovery system?

In conclusion, the implementation of the diffuser as a heat exchanging component (T-rHEX concept) is proven to increase cycle efficiency. By adapting the existing ORCHID turbine diffuser to implement coolant channels around the outer surface of the diffuser, the overall ORC thermal efficiency is proven to increase by 0.42%.

This improvement in ORC efficiency corresponds to a 3.56% reduction in the evaporator thermal power input from the low-grade waste heat source. As a result, both the evaporator and condenser can be proportionally downsized, reducing the overall weight of these components. In the context of a turboshaft engine equipped with an air-cooled ORC bottoming unit (Figure 1.1), this weight reduction is expected to further improve fuel economy and raise the overall thermal efficiency of the propulsion system.

3.3.1. Comparison between an adiabatic turbine diffuser and a turbine diffuser with heat transfer

To understand how the effect of heat transfer affects the flow within each stream, let us compare results with heat transfer to adiabatic results for a fixed recuperator geometry.

Heat transfer has only limited influence on the flow dynamics. The velocity field is primarily governed by the channel geometry, and thermal effects introduce only secondary modifications. To visualize the effect of heat transfer on flow dynamics, the Mach number is used, as it not only indicates the flow regime but also the variation in velocity along the streams.

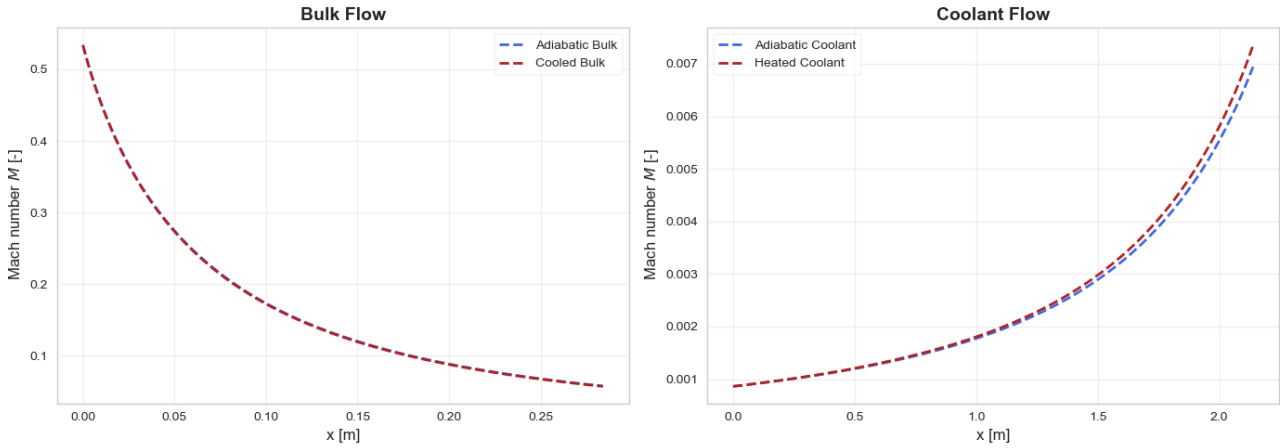

Figure 3.21: Mach number distributions comparing adiabatic and diabatic cases for the ORCHID with recuperation along the stream path.

Figure 3.21 shows that both the diffuser flow and the coolant remain fully subsonic, well below any transonic effects. The diffuser enters at Mach 0.54 ($87.5\,\mathrm{m\,s^{-1}}$) and decelerates to Mach 0.06 ($9.4\,\mathrm{m\,s^{-1}}$) at the outlet. Although most of the diffuser operates below the typical compressibility threshold of approximately Mach 0.3[3], the inlet lies above this limit, so flow compressibility effects are still relevant locally. Comparing adiabatic and diabatic diffuser cases, the diabatic flow exhibits a slightly lower exit velocity, consistent with the extraction of energy from cooling. Nevertheless, the difference is small and can be considered negligible for the present analysis.

The coolant channel shows a slightly stronger response to diabatic effects than the diffuser. Because the coolant exits the condenser as a liquid, its density is much higher than that of the gaseous diffuser flow. Mass conservation therefore requires a much lower inlet velocity for the coolant. As shown in Figure 3.21, the coolant accelerates along the channel due to the progressive reduction in cross sectional area, since the channel diameter decreases with the diffuser radius (see subsection 3.1.3). In addition, heat recuperated from the diffuser increases the coolant temperature and reduces its density, which further increases the local velocity through continuity. As a combined result, the coolant accelerates from an inlet Mach number of 8.62×10^{-4} ($0.647\,\mathrm{m\,s^{-1}}$) to an outlet Mach number of 7.40×10^{-3} ($5.32\,\mathrm{m\,s^{-1}}$).

In terms of thermodynamic parameters, temperature has the most effect on heat transfer. In an adiabatic diffuser, due to diffuser flow expansion, the static temperature rises up to $2\,\mathrm{K}$ (+0.4% with reference to inlet temperature). In contrary, for the cooled diffuser, a temperature drop of $7.5\,\mathrm{K}$ is obtained (-1.5% with reference to inlet temperature). As discussed in subsection 2.2.4, the negative temperature axial gradients contribute to a more stable boundary layer. Combining this effect with cooled walls, both viscousity gradients directly favor boundary layer stability, thus allowing for higher adverse pressure gradients before separation occurs.

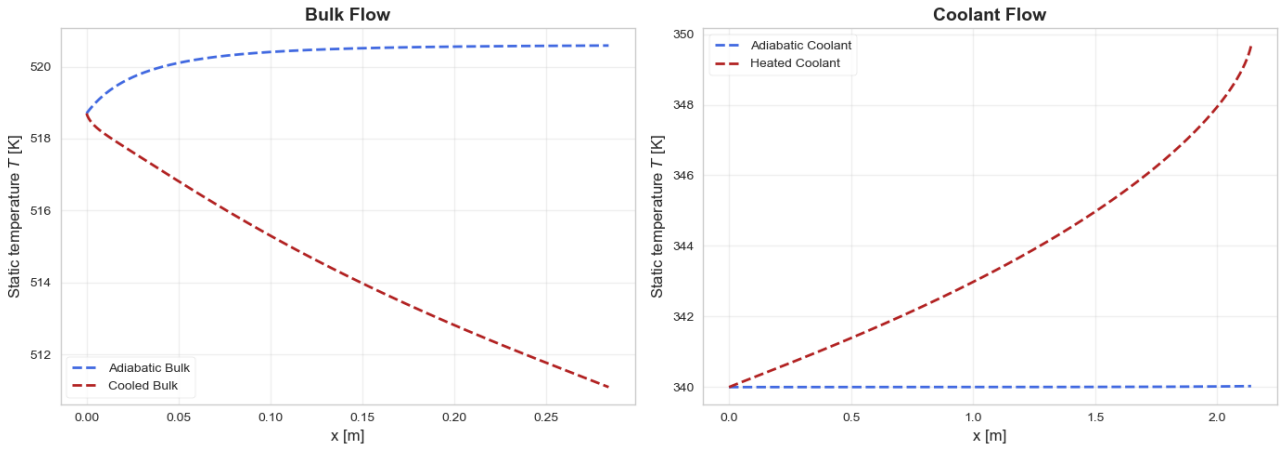

Figure 3.22: Static temperature distributions comparing adiabatic and diabatic cases for the ORCHID with recuperation along the stream path.

As the coolant channel cross sectional area decreases along its path, the flow accelerates due to geometric convergence. This produces a strong increase in coolant velocity (Figure 3.21), but the associated adiabatic temperature rise is negligible, with a static temperature increase below 0.01%. In contrast, heat addition from the diffuser produces a meaningful thermal response, raising the coolant temperature by almost $10\,\mathrm{K}$ ($+2.8\%$).

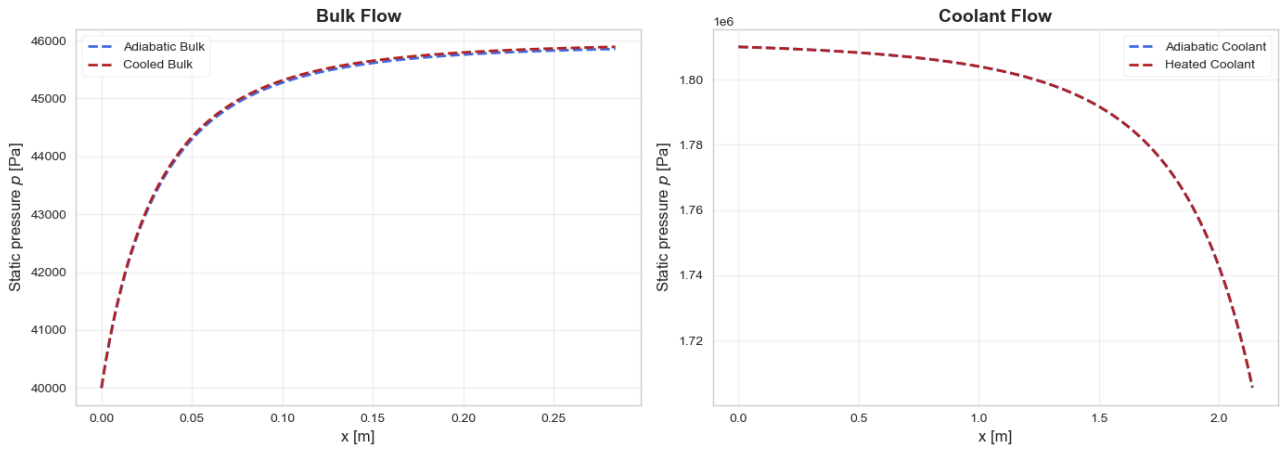

Figure 3.23: Static pressure distributions comparing adiabatic and diabatic cases for the ORCHID with recuperation along the stream path.

Another critical thermodynamic parameter to consider is the pressure. Pressure plays a secondary role in heat transfer, by means of changing thermodynamic properties of the fluid. As seen in Figure 3.23, the effect on pressure due to heat transfer is very small. Cooling the diffuser flow leads to an increase in pressure rise. This can be explained based on the total pressure increase, allowing for further expansion of the fluid for the same diffuser geometry. On the other hand, the coolant pressure exhibits a negligible pressure changes, as the static pressure drop is dominated by friction losses.

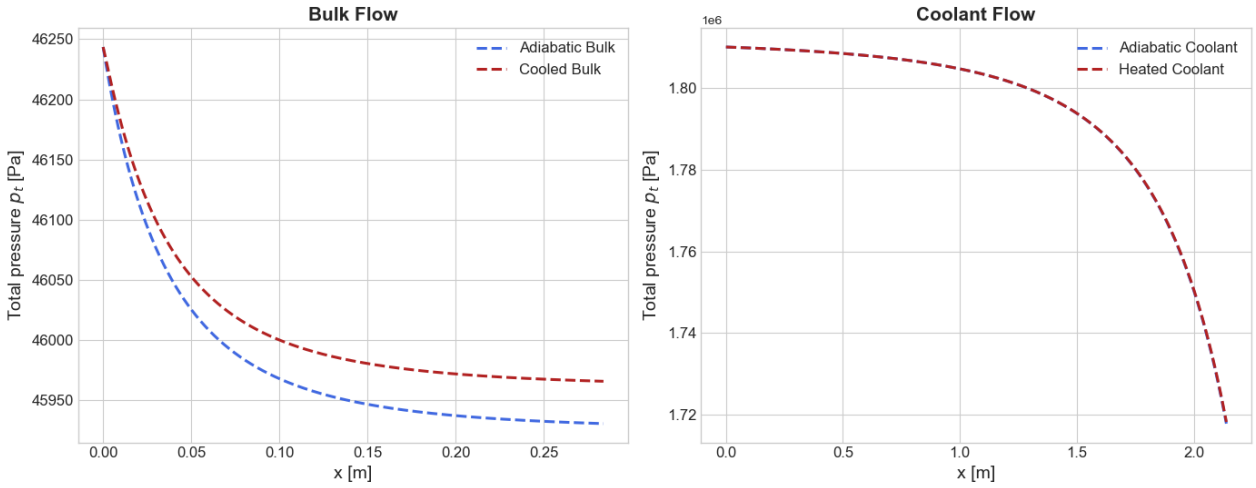

Figure 3.24: Total pressure distributions comparing adiabatic and diabatic cases for the ORCHID with recuperation along the stream path.

Total pressure is a key thermodynamic variable for assessing the combined effects of heat transfer and friction. As shown in Figure 3.24, the diffuser flow exhibits a net total pressure decrease, indicating that frictional dissipation outweighs the effect of cooling. Nonetheless, cooling partially mitigates these losses, producing a measurable total pressure recovery relative to the adiabatic case. In contrast, the liquid coolant shows almost no variation in total pressure along the channel. This behavior can be explained by evaluating the Gr"uneisen parameter (G). The coolant's G is roughly an order of magnitude higher than that of the gaseous diffuser flow, implying a much weaker sensitivity of thermodynamic state to heat addition (see subsection 2.1.2). As a result, identical heat transfer leads to noticeable total pressure changes in the gas, but negligible changes in the liquid stream.

To complete the assessment of heat transfer effects on the diffuser and coolant streams, the associated compressibility effects are examined. A useful indicator of compressibility is the density variation along the flow path, since changes in density reflect the degree of coupling between the thermodynamic and velocity fields.

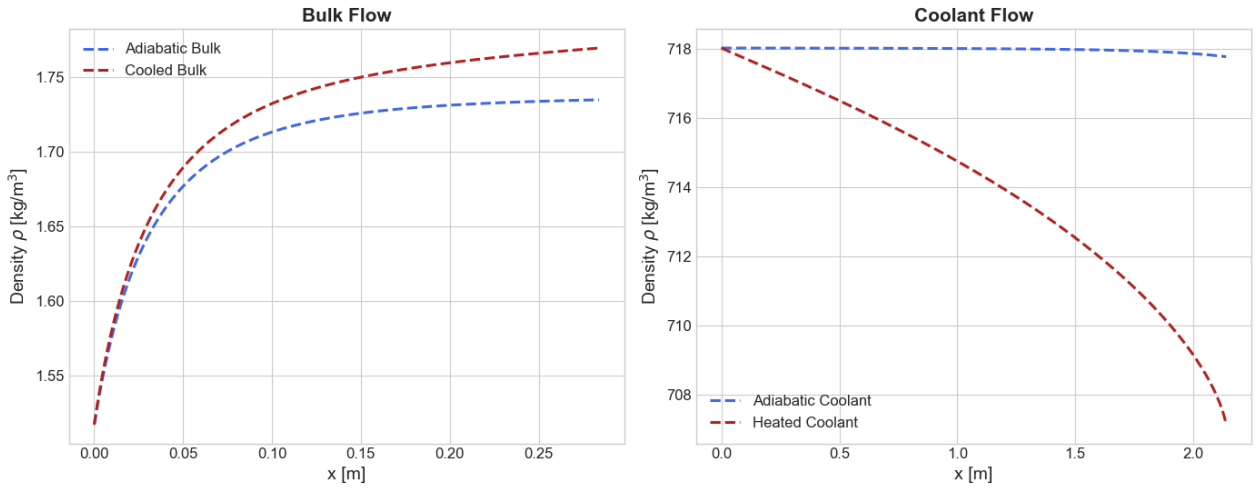

Figure 3.25: Fluid density distributions comparing adiabatic and diabatic cases for the ORCHID with recuperation along the stream path.

As seen in Figure 3.25, heat transfer plays a significant role in density changes. For the cooled diffuser flow, density increases, while for the heated coolant flow, density decreases. This is expected since density behaves inversely proportional to temperature. A more important remark is the adiabatic case. As seen in Figure 3.25, adiabatic diffuser flow undergoes a density increment along the diffuser, while the coolant flow density stays approximately constant. This has to do with flow compressibility. As the liquid coolant is well within the incompressible regime, constant density with small deviations due to static temperature are expected. On the other hand, diffuser flow experience a strong variation in density. Because the process is adiabatic, density variations arise solely from pressure changes due, meaning that thermodynamic and kinematic fields are coupled and the flow remains compressible.

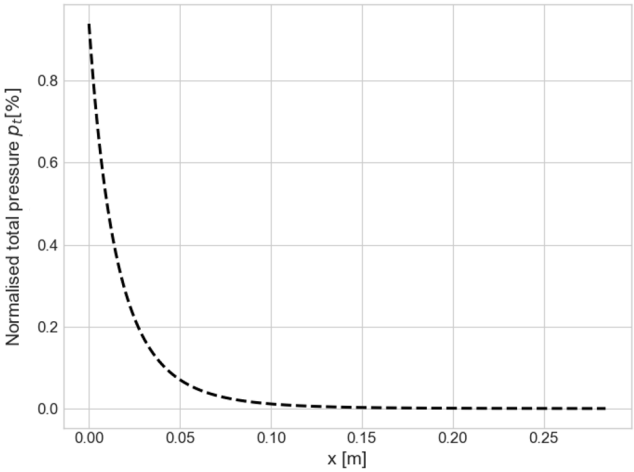

Figure 3.26: Normalized total pressure difference between Bernoulli (incompressible flow) total pressure and REFPROP total pressure prediction.

To assess compressibility effects, the total pressure predicted by REFPROP for a compressible flow is compared with the incompressible Bernoulli total pressure. As shown in Figure 3.26, regions with elevated Mach number such as the diffuser inlet exhibit a compressible total pressure that exceeds the incompressible value. Although most of the diffuser operates within an approximately incompressible regime, the inlet does not. This impacts the definition of the diffuser pressure coefficient (see Equation 3.26), which uses the incompressible inlet total pressure as a reference. Because the true (compressible) total pressure at the inlet is higher, a diffuser can yield pressure coefficient values exceeding 1 even when total pressure decreases along the flow. Overall, the effects of flow compressibility play a relevant role, thus cannot be neglected.

To understand the effects of non-ideal gasses on the diffuser flow, the compressibility factor (Z) can be analyzed.

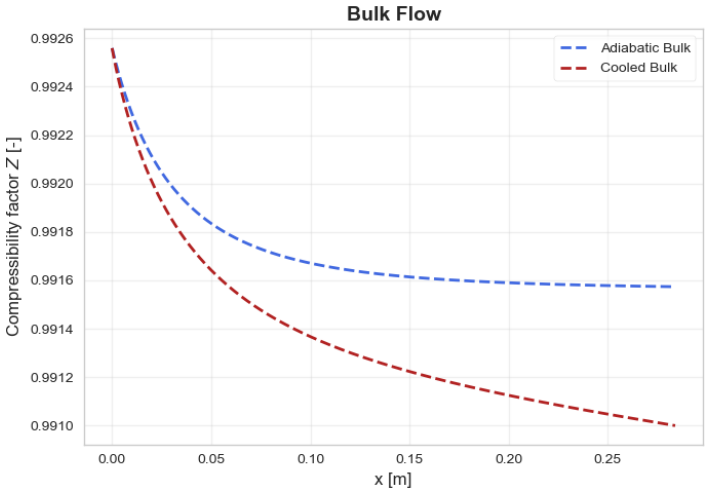

Figure 3.27: Compressibility factor distributions comparing adiabatic and diabatic cases for the ORCHID with recuperation along the stream path.

It can be seen in Figure 3.27 how most of the diffuser flow achieves compressibility factors higher than 0.99. Values close to 1 imply the gas behaves like an ideal gas. Thus given a compressibility factor of 0.99, the flow within the diffuser can be considered to behave like an ideal gas. Furthermore, Figure 3.27 shows that cooling reduces compressibility factors, leading to less ideal flows. Although Figure 3.27 exhibits a small change, higher thermal power values are predicted to have a stronger influence on compressibility. Thus better performing heat exchangers are more at risk of incorrectly assuming ideal gas flows.

3.3.2. Comparison between countercurrent and cross-flow coolant channel arrangement

To measure the performance benefits of a cross-flow heat exchanger over a pure countercurrent flow heat exchanger, both arrangements are calculated and compared.

Table 3.4: Comparison between countercurrent flow and cross-flow arrangement for the ORCHID with recuperation configuration.

	Countercurrent flow	Cross-flow	Percentage difference [%]
Coolant channel length [m]	0.284	2.14	+654%
Number of coolant channels [-]	32	5	-84.4%
Total thermal power [W]	1960	2920	+49.1%
Number of heat Transfer Units [-]	0.0375	0.0622	+65.9%
Effectiveness [%]	5.44	8.36	+53.7%
Cycle efficiency [%]	12.4	12.5	+0.13%
Required pump power [W]	0.0721	22.0	+30500%
Diffuser temperature drop [K]	4.51	7.66	+69.8%
Coolant temperature rise [K]	6.52	9.72	+49.1%
Diffuser pressure coefficient [-]	1.010	1.013	+0.29%
HEX compactness [m]	1.95	1.87	-4.40%
Total Volume [m^3]	0.00182	0.00173	-4.95%

Percentage differences in Table 3.4 are computed relative to the pure countercurrent reference. Before discussing these results, an important clarification must be made regarding the comparison between the countercurrent values in Table 3.4 and those reported by Colonna[2]. It was found that Colonna's countercurrent annular coolant predictions significantly overestimate the heat transfer rate. The zero-order LMTD approach used for preliminary analysis of the T-rHEX baseline applies the diffuser inlet velocity to evaluate the convective heat transfer coefficient. As shown in Figure 3.21, using the inlet velocity as a global reference leads to an significant overestimation of the Reynolds number and consequently of the diffuser convective heat transfer. As a result, the recuperator thermal power reported by Colonna is unphysically high. For the present study, the pure countercurrent configuration is instead constructed by imposing a zero twist angle on the coolant channels while maintaining all other geometrical properties. Although the coolant channels differs from the annular arrangement considered by Colonna, it provides a consistent and physically representative basis for comparing countercurrent and cross-flow configurations.

Table 3.4 shows how the most critical aspects of the recuperator improve when an optimized cross-flow coolant channel arrangement is used. By wrapping the coolant channel around the diffuser, the total thermal power increased by 49.1%, giving a major increase in heat transfer capabilities of the recuperator. Naturally, as the inlet conditions stay constant and the local number of heat transfer units (Ntu) increase, the heat exchanger effectiveness (ϵ) and total thermal power increases. Additionally to thermal improvements, diffuser performance also is improved. Both flow arrangements lead to pressure coefficient values larger than 1 with the cross-flow configuration having the edge over the pure countercurrent flow. This pressure effect can be directly related to the additional heat transfer in the cross-flow arrangement.

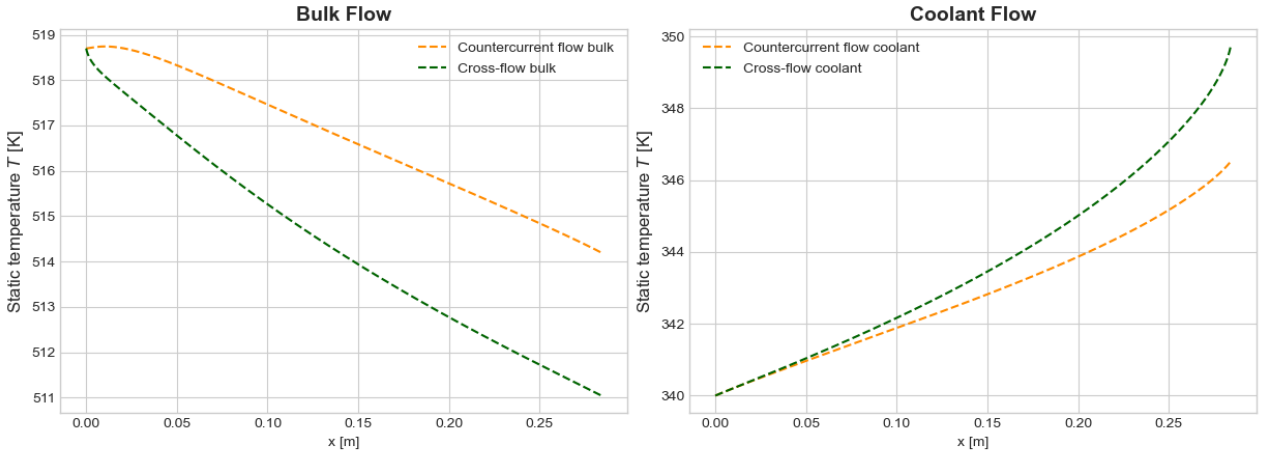

Figure 3.28: Static temperature along the recuperator comparing countercurrent flow and cross-flow arrangements for the ORCHID with recuperation setup.

The temperature distribution is a good thermodynamic indicator to understand the local effect of cross-flow arrangement over countercurrent flow arrangement. From Figure 3.28, it can be seen that the temperature drop is much greater for the cross-flow arrangement than for the countercurrent flow. This indicates that the heat flux distribution of the cross-flow arrangement is greater in magnitude to that of the countercurrent flow. On the coolant side, the temperature increase of the cross-flow arrangement is greater than the countercurrent flow arrangement. As both streams have higher temperature changes, the heat exchanger effectiveness is greater, as shown in Table 3.4

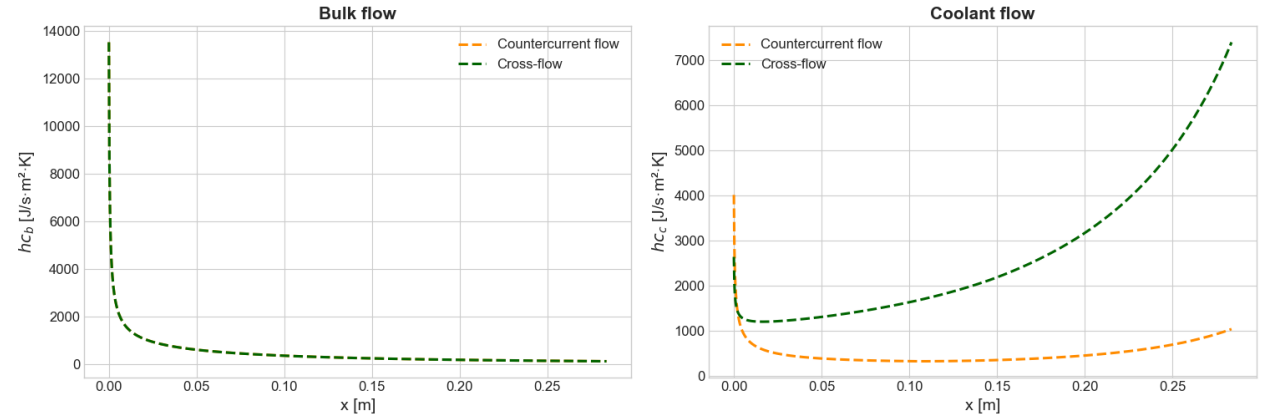

Figure 3.29: Forced convection coefficients along the recuperator comparing countercurrent flow and cross-flow arrangements for the ORCHID with recuperation setup.

Figure 3.29 shows that diffuser convection coefficient is nearly identical for both countercurrent and cross-flow arrangements, whereas coolant convection coefficient exhibits significant differences. These differences arise directly from the flow conditions imposed by the geometric discretization of the coolant passages.

To understand the differences at the coolant inlet, the geometric discretization must be considered. For a fixed curvature ratio, the cross-sectional area of each coolant channel arrangement is approximately constant (with minor adjustments due to rounding the diameter to satisfy the curvature ratio constraint). Since the coolant inlet thermodynamic state is the same, the coolant density is kept constant for both arrangements. However, as shown in subsection 4.1.1, the number of channels depends on the twist angle (α_t). Increasing the twist angle reduces the number of available channels. As a result, a pure countercurrent configuration contains more channels than a cross-flow configuration. Because the total coolant mass flow is evenly distributed among channels, the mass flow rate per channel, and therefore the inlet velocity, is lower in the countercurrent case than in the cross-flow case. The higher velocity in the cross-flow channels increases the Reynolds number, increasing turbulence effects and yielding a higher convective heat transfer coefficient.

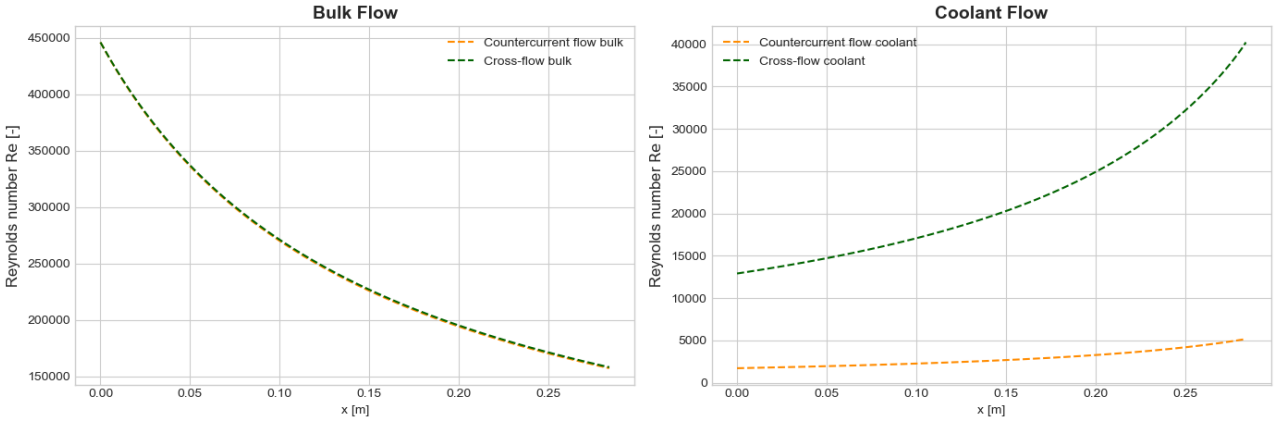

Figure 3.30: Reynolds number along the recuperator comparing countercurrent flow and cross-flow arrangements for the ORCHID with recuperation setup.

As seen in Figure 3.30, not only is the Reynolds number higher at the inlet, but also the Reynolds number increases more steeply along the channel length for cross-flow than countercurrent flow. To understand this let us rewrite the Reynolds number using mass continuity.

$$Re_D = \frac{\dot{m}\, d_H}{A_{\text{cross}}\, \mu} \tag{3.28}$$

Given that the coolant channel diameter is approximately constant, the change is Reynolds number along the stream is a function of dynamic viscosity. For fluids in liquid phase, viscosity decreases with increasing temperature. Since the cross-flow arrangement exhibits a larger temperature rise, the corresponding viscosity decrease is stronger, leading to a higher increase in Reynolds number compared to pure countercurrent case. Combining both inlet conditions and the effect of viscosity, the cross-flow arrangement experiences a significant improvement in convection performance compared to countercurrent arrangement.

Lastly, Figure 3.29 also shows the countercurrent flow with a stronger thermal boundary layer development effects at the inlet compared to cross-flow. Given that an increase in Reynolds number leads to a decrease in boundary layer thickness, the increase in inlet Reynolds number would imply higher heat transfer between the coolant flow and walls. However as seen in Figure 3.30, this is not the case. Discretization plays an important role as the cross-flow channel length per cell is much greater than the pure countercurrent flow channel. This issue can lead to the same discretization error in the convection coefficient model as presented in Figure 3.20, which reduces the inlet convection of the cross-flow compared to the countercurrent flow. Therefore the observed differences cannot be attributed reliably to physical boundary layer development alone.

Research Sub-Question RSQ2

To what extent does adopting a cross-flow heat exchanger arrangement within the T-rHEX influence its thermal performance?

In conclusion, the cross-flow arrangement provides a substantial improvement in heat transfer performance compared to the pure countercurrent arrangement. Since the helicoidal coolant arrangement contains fewer channels, each channel carries a larger share of the total mass flow rate, leading to higher local Reynolds numbers and therefore higher convective heat transfer coefficients. With a 53.7% increase in recuperator heat transfer effectiveness, the benefits of the higher convection coefficient outweigh the 2D cross-flow heat transfer effects shown in Figure 3.20. Conversely, the cross-flow arrangement also increases frictional losses in the coolant channels, requiring a higher pump power to overcome the associated pressure drop. Nevertheless, the gain in heat transfer performance dominates, as the net cycle efficiency improves by 0.13% when implementing a cross-flow arrangement over a pure countercurrent flow arrangement. For this reason, the cross-flow arrangement is implemented for both the ORCHID turbine diffuser with recuperator design and for the optimized T-rHEX design described in section 3.4.

3.4. Results: Geometry optimization of the turbine diffuser for recuperator integration in the ORCHID WHR cycle

Having demonstrated the ORC efficiency gains achievable with the T-rHEX concept, the next step is to optimize its geometry. The following section outlines the optimization setup and presents the resulting optimal design and performance.

3.4.1. Optimization setup

The current ORC with recuperation uses the original turbine diffuser geometry, which was designed for adiabatic flow conditions. To enhance recuperator performance, this geometry must be re-designed. For reference, Colonna's preliminary baseline T-rHEX study employed a conical diffuser with a larger semi-opening angle and greater length enhancing significantly heat transfer. Nevertheless, it is believed that by allowing for a more complex diffuser geometry, heat exchanger can be further improved without increasing the required heat exchanger volume. Since the goal of this work is to maximize ORC efficiency within the WHR system, the optimization problem is formulated by minimizing the inverse of the ORC efficiency (see Equation 3.29). For a fixed turbine work output, the cycle efficiency depends on the recuperated thermal power and the additional pump work required to overcome coolant stream pressure losses. In order to be consistent with the ORC, the thermodynamic inlet conditions of the diffuser and coolant remain constant. Additionally, at the diffuser inlet, the turbine exit gases must remain constant to ensure constant work done. Therefore to ensure adequate coupling between the turbine and diffuser, the inlet geometrical parameters are kept the same. This is not the case for the coolant channels as it depends on the given twist angle and the radius at the exit of the optimized diffuser.

The first design variable in the optimization problem is the diffuser length (L). Diffuser length strongly influences heat exchanger effectiveness because it directly increases the wetted surface area, but at the expense of a larger exchanger volume. It also determines the coolant channel length, which governs the associated pressure losses.

The second design variable in the optimization problem is the twist angle of the coolant channel (α_t). Similarly to section 3.3, the twist angle is constant along the diffuser, therefore the coolant channel is allowed to have a variable cross-sectional area. Other coolant channel geometrical parameters such as the curvature ratio are kept constant.

The remaining design variables are a vector of radii representing the exterior diffuser walls ($\vec{r}$). The shape of the diffuser is defined by the distribution of semi-opening angles (θ) along the diffuser. For a fixed number of discrete cells, the exterior wall is represented by the corresponding semi-opening angle, inlet and outlet radii. If each cell was to be considered in the optimization, $\vec{r}$ would be required to be of length `N_points + 1`. This raises a computational expense issue, which becomes exponentially more costly as the diffuser is further discretized. To avoid this, the diffuser walls are modeled using a spline, where a fixed number of radii are specified, and the remaining are interpolated based on the spline. The spline is constructed as a continuous line using cubic fitting between design radial coordinates, while the number of radial coordinates to define the diffuser exterior walls (`N_variables`) is selected by the user. Using this spline, the function `transform_vars_soa()` converts the generated splines into the required semi-opening angle distribution used in `T-rHEX.py`. The design vector is then given by an array of length equal to the number of selected radii coordinates plus a variable for the diffuser length and an variable for the coolant twist (see Equation 3.30). This makes the design vector independent of the discretization refinement, saving significantly computational cost of the optimization problem.

The remaining design variables are the radial coordinates defining the exterior diffuser wall ($\vec{r}$). The diffuser geometry is governed by the distribution of semi-opening angles (θ) along its length. For a fixed number of discrete cells, the exterior wall is represented by the corresponding semi-opening angle, inlet and outlet radii. However, this would require $\vec{r}$ to contain `N_points + 1` entries, which makes the optimization computationally expensive, with cost increasing rapidly as the discretization is refined. To mitigate this, the diffuser wall is parameterized using a spline. For this, a fixed number of radial coordinates is specified, and the full wall profile is obtained by cubic interpolation between these design points. The number of spline radial coordinates (`N_variables`) is chosen by the user. The resulting spline is then converted into the required semi-opening angle distribution through the function `transform_vars_soa()`, to be used to fully described the diffuser geometry in `T-rHEX.py`. The final design vector therefore consists of the selected radial coordinates, together with one variable for the diffuser length and one for the coolant twist angle (see Equation 3.30). This formulation

decouples the design vector size from the grid refinement, significantly reducing the computational cost of the optimization.

$$\textbf{Objective:} \quad \min_{\vec{\mathbf{x}}} \; f(\vec{\mathbf{x}}) = \frac{1}{\eta_{\mathrm{ORC}}} = \frac{\dot{Q}_{\mathrm{input}}}{\dot{W}_{\mathrm{net}}} = \frac{\dot{Q}_{\mathrm{input}}^{\text{no recuperator}} - \dot{Q}_{\mathrm{recuperator}}}{\dot{W}_{\mathrm{turbine}} - \dot{W}_{\mathrm{pump}}} \tag{3.29}$$

$$\textbf{Design vector:} \quad \vec{\mathbf{x}} = \{\vec{r},\, L,\, \alpha_t\} \tag{3.30}$$

$$\textbf{Constraints:} \quad C_{p_{\text{diffuser}}}(\vec{\mathbf{x}}) \;\geq\; 0.9\, C_{p_{\text{diffuser}}}^{\text{no recuperator}} \tag{3.31}$$

$$\frac{dC_p}{dx}(\vec{\mathbf{x}}) \;\leq\; \max_{x\in[0,L]} \left(\frac{dC_p}{dx}\right)^{\text{no recuperator}} \tag{3.32}$$

$$V_{\mathrm{total}}(\vec{\mathbf{x}}) \;\leq\; V_{\mathrm{total}}^{\text{baseline T}-\text{rHEX}} \tag{3.33}$$

$$\textbf{Bounds:} \quad r_i^{\min} \;\leq\; r_i \;\leq\; r_i^{\max}, \qquad i = 1, \ldots, N_{\mathrm{var}} \tag{3.34}$$

$$0.1\, L^{\text{no recuperator}} \;\leq\; L \;\leq\; 5\, L^{\text{no recuperator}} \tag{3.35}$$

$$1^\circ \;\leq\; \alpha_t \;\leq\; 89^\circ \tag{3.36}$$

To limit the optimization to realistic and feasible results, constraints are used. A total of three inequality constraints are used. Each targeting critical aspects of both diffuser performance and recuperator limitations.

- **Pressure recovery constraint:** Diffuser performance is based on the ability to recover pressure to achieve the target back pressure. In order to maintain the diffuser performance aspect, the recuperator may not achieve lower pressure recovery coefficients ($C_{p_{\text{diffuser}}}$) than 90% of the ORCHID turbine diffuser without recuperation (Equation 3.31).
- **Maximum pressure gradient:** Diffuser performance is strongly influenced by separation. Although one dimensional separation criteria such as the Stratford criterion can be used to detect impending separation, they are valid only for moderate adverse pressure gradients and are therefore not suitable for diffusers operating under stronger gradients. As an alternative, and given that wall cooling generally enhances boundary layer stability, separation can be assessed by comparison with the ORCHID turbine diffuser without recuperation. If the cooled diffuser exhibits local adverse pressure gradients that remain below the maximum adverse pressure gradient of the ORCHID turbine diffuser without recuperation, then the flow can be considered approximately stable (Equation 3.32). This assumes that ORCHID turbine diffuser without recuperation is fully stable, which may not be the case.
- **Total volume:** As part of optimizing the overall WHR system performance, the reduction in recuperator volume allows for a more compact heat exchanger, decreasing its weight and increasing its thermal power density. For this, the upper bound is set with respect to the baseline T-rHEX (Equation 3.33).

In addition to the imposed constraints, each design variable is bounded within predefined limits. For the radii in $\vec{r}$, the bounds were derived from a sonic flow estimate based on inlet conditions. The minimum radius corresponds to a local Mach number of 0.8 (lower bound), while the maximum radius corresponds to a Mach number of 0.001 (upper bound), as shown in Equation 3.34. Since these bounds are obtained using as reference inlet conditions, they approximate rather than reproduce the true local Mach number inside the diffuser. In the unlikely event that the flow approaches sonic conditions within the domain, `N1D-Flow` returns a value used to penalize the optimization result. For the diffuser length, broad bounds are imposed to avoid restricting the search space, ranging from 10% to 500% of the original ORCHID turbine diffuser length. Finally, the twist angle is geometrically restricted between pure countercurrent flow (0°) and pure cross-flow (90°). In practice, a pure cross-flow configuration is not physically realizable, as the coolant channel requires an inlet and an outlet. Additionally, due to numerical function asymptotes, a value of zero twist is not accepted. Therefore, the admissible range is limited to 1° to 89°.

The optimizer uses the Python library `Scipy.optimize`, in order to set up a optimization problem. The objective function is minimized using SLSQP optimization method. The maximum iterations are set to 300, while

objection function stopping criterion is set at 1×10^{-6}. The eXtended Design Structure Matrix (XDSM) diagram showing an overview of the spline interpolation, T-rHEX solver, constraints and objective function is shown in Figure 3.31.

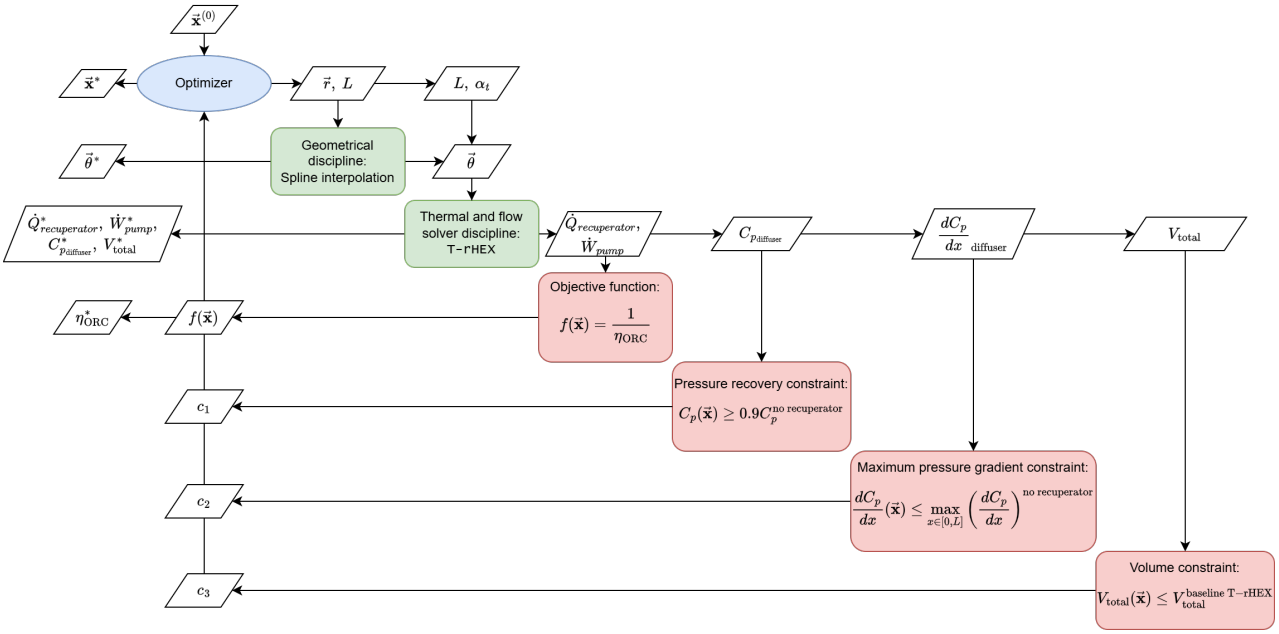

Figure 3.31: XDSM diagram for optimization of the T-rHEX geometry.

To complete the optimization setup, the numerical settings must be defined. The number of grid points is important as it determines the accuracy of the T-rHEX results as well as the computational cost. Gradient-based methods such as SLSQP require one evaluation of the T-rHEX solver per design variable and per constraint at each iteration, making the total runtime strongly dependent on discretization implemented. Since the number of iterations depends on the stopping criterion and the Jacobian step size, the computational cost cannot be predicted a priori. It is therefore essential to select a discretization that offers an acceptable compromise between accuracy and runtime. Based on the results in Table 3.1, numerical error in energy conservation critical. To ensure sufficient results accuracy without excessive runtime, a resolution of 10000 grid points was selected as it maintains mass and energy errors close to 1%. The iterative thermal solver convergence tolerance is kept at 0.1%, consistent with simulations in section 3.3. A value of `N_variables=7` was chosen to parameterize the diffuser geometry, as spline representations provided minimal error (maximum semi-opening angles error$\approx 2.0 \times 10^{-6}{}^\circ$). The Jacobian step size is set to 1.0×10^{-3}, since smaller values lead to sensitivity issues with twist angle (α_t). To complete the optimization configuration, the optimizer stopping criterion follows typical recommendations, set to 1.0×10^{-6}.

3.4.2. Full geometry optimization of the ORCHID turbine diffuser

The optimization resulted in a total of 28 iterations, with a total runtime of 16.8 hours. The true runtime turned out to be higher than expected. It is believed that the cause of this discrepancy was running the optimization at limited CPU capacity, caused by the host when running a process for a long time. This resulted in approximately doubling the expected runtime of the simulation.

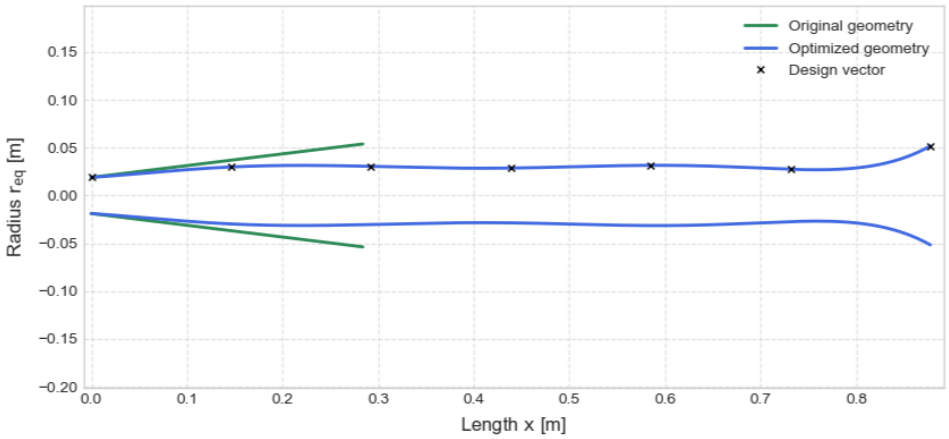

Figure 3.32: Diffuser geometry comparison between the original turbine diffuser geometry and the optimized T-rHEX recuperator geometry.

Figure 3.32 shows that the optimized configuration leads to a substantially elongated diffuser. The diffuser length increases by approximately 300%, reaching $0.878\,\mathrm{m}$. The optimized geometry exhibits three distinct regions: an inlet expansion, a mid-section of nearly constant radius, and an outlet expansion. The outlet radius decreases to $0.0517\,\mathrm{m}$, corresponding to a 3.9% reduction relative to the original ORCHID diffuser, while the mid-section radius narrows to roughly $0.03\,\mathrm{m}$. Overall recuperator volume increases by 94.2% relative to the original ORCHID diffuser. However, when compared to Colonna's baseline T-rHEX design, the optimized configuration remains significantly more compact, with a volume reduction by a factor of approximately 2.8. In addition, the coolant channel twist remained approximately constant to its initial conditions, giving an optimal value of $82.26°$.

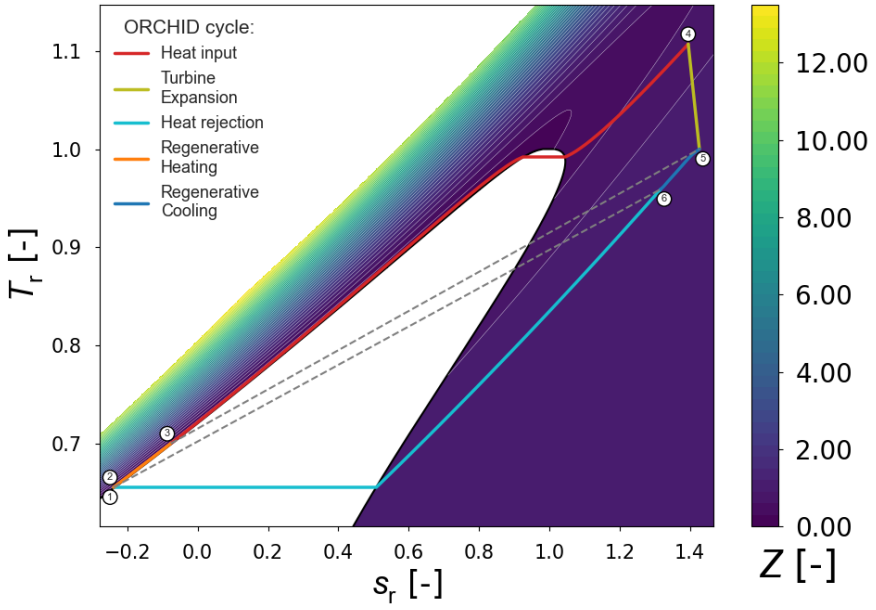

Figure 3.33: Temperature–entropy diagram of the ORC with optimized recuperation achieving a thermal efficiency of 13.16% (+Δ1.05%), showing iso-lines of the compressibility factor.

The optimized shape of the T-rHEX diffuser and coolant channels leads to a significant increase in heat transfer rate between the diffuser stream and the coolant streams. This significant thermal power increase leads to a significant increase in cycle efficiency. In comparison, the frictionless cycle efficiency, which does not consider the required pump power to overcome coolant pressure losses, is 13.25%. Accounting for coolant channel pressure losses the cycle efficiency drops to 13.16%. By optimizing the shape of the diffuser, a net 1.05% increase is achieved on the ORC efficiency. Such increase in efficiency leads to a decrease in evaporator duty, allowing to decrease size of evaporator and condenser heat exchanger, thus reducing weight. On the other

hand, the long coolant channel requires additional power to overcome these new pressure losses. The new required power by the pump reduces the efficiency of the cycle. In order to evaluate the optimized T-rHEX, the results are compared to previous relevant setups in Table 3.5. These consist of the original ORCHID turbine diffuser without recuperation, the original ORCHID turbine with recuperation, the baseline T-rHEX presented by Colonna, and the optimized T-rHEX.

Table 3.5: Comparison between the ORCHID original diffuser without recuperation, the ORCHID original diffuser with recuperation, the baseline T-rHEX and the optimized T-rHEX.

	ORCHID without recuperation	ORCHID with recuperation	Baseline T-rHEX	Optimized T-rHEX
Coolant channel length [m]	-	2.140	0.517	6.54
Number of coolant channels [-]	-	5	210	5
Total thermal power [W]	0	2920	3744	7017
Number of heat Transfer Units [-]	0	0.0622	0.0739	0.157
Effectiveness [%]	0	8.36	10.86	22.2
Cycle efficiency [%]	**12.1**	**12.5**	**12.7**	**13.2**
Efficiency rise [Δ%]	0	0.42	0.57	1.05
Required pump power [W]	0	22.0	10.6	65.8
Diffuser temperature difference [K]	+1.88	-7.66	-10.4	-21.2
Coolant temperature difference [K]	-	+9.72	+12.4	+23.1
Diffuser pressure coefficient [-]	1.00	1.01	1.03	0.91
HEX compactness [m]	-	1849	2744	1240
Total Volume [m3]	0.00127	0.00173	0.00714	0.00336

All configurations exhibit weak thermal performance. For every design, the heat exchanger effectiveness remains below $25\,\%$, indicating that only a small portion of the maximum recoverable thermal duty is achieved. This weak performance is consistent with the low number of heat transfer units (Ntu), which indicates limited convective capacity relative to the thermal capacitance rates of the streams, and with the large compactness values (P_V), which signify poor volumetric utilization of the heat transfer surface. Nevertheless, for the given configurations in Table 3.5, the optimized T-rHEX clearly outperforms. The cycle efficiency implementing the optimized T-rHEX as a recuperator doubles efficiency gain when compared to both the ORCHID with recuperation setup and the baseline T-rHEX. The optimized heat exchanger is capable of recuperating $7\,\mathrm{kW}$ of heat, that being 8.5% of the total thermal input of the ORC system. The improvement in heat transfer rate allows the optimized T-rHEX to more than double the heat exchanger effectiveness compared to other models.

In contrary, to reach such improvements in cycle efficiency, the pressure recovery of the diffuser is reduced. The optimized T-rHEX is able to achieve a pressure coefficient of 0.906, this being 9.9% less than the pressure coefficient achieved by the original ORCHID diffuser without recuperation and 12.5% less than the baseline T-rHEX. Consequently, the reduction of pressure has a small benefit in terms of flow separation. The maximum pressure gradient was limited by the optimization constraint in order to avoid high values of localized adverse pressure gradients that can potentially lead to separation. The reduction in diffuser back pressure has an effect in cycle efficiency. These effects are discussed in subsection 3.4.3.

A final remark concerns the recuperator volume shown in Table 3.5. The optimized T-rHEX occupies less than half the volume of Colonna's baseline T-rHEX. Since recuperator design must minimize volume to reduce required space and structural mass, the slimmer and elongated diffuser geometry is beneficial as it enhances heat transfer while also reducing overall volume, allowing integration within tighter space constraints. The compactness values reflect this trend. Among the three configurations, the optimized T-rHEX exhibits the most favorable compactness, with the ORCHID with recuperation close behind, whereas the baseline T-rHEX performs poorest. In summary, each configuration presents distinct advantages. The ORCHID with recuperation yields modest efficiency gains but requires the least volume. The baseline T-rHEX delivers the highest pressure recovery, which benefits downstream components. The optimized T-rHEX achieves the best heat-exchanger performance and the largest cycle efficiency improvement, at the expense of slightly reduced pressure recovery and a larger volume than the original ORCHID diffuser.

To better understand the flow physics within the optimized T-rHEX, let us look at the heat flux and temperature distributions.

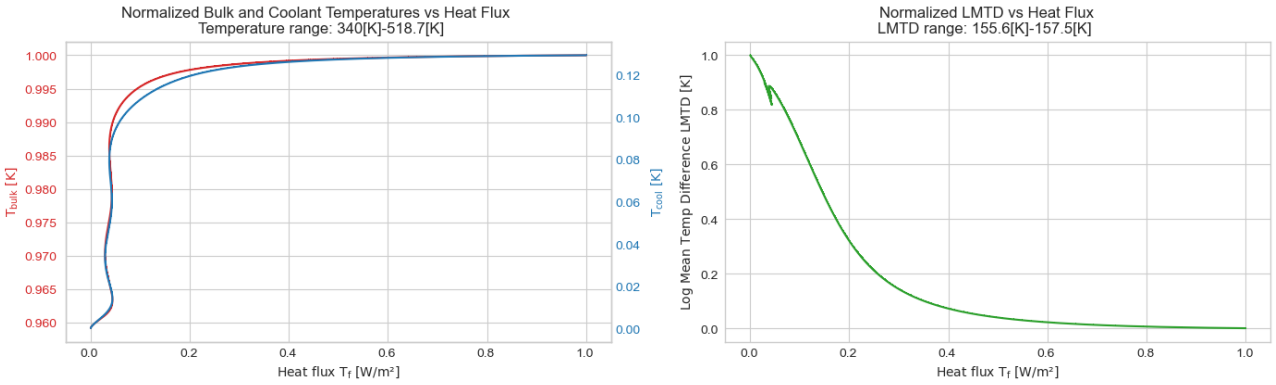

Figure 3.34: Thermal plots along the recuperator for the given optimized T-rHEX.

Similarly to the original ORCHID turbine diffuser with recuperation, Figure 3.34 also experiences a higher temperature change in the coolant channel over the diffuser. This is once again due to the heat capacitance of the diffuser flow being larger than the coolant flow. However, this time the temperature difference between streams is smaller compared to Figure 3.15. This is expected as both channels undergo a higher temperature change, thus the temperature difference between streams is reduced. Once again, the peak heat flux is found at the lowest temperature difference between channels. This shows that temperature difference was not the critical aspect of heat transfer.

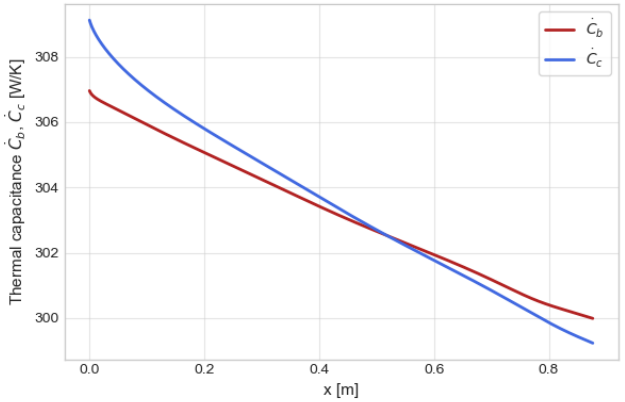

(a) Thermal capacitance of both diffuser and coolant flows for the optimized T-rHEX.

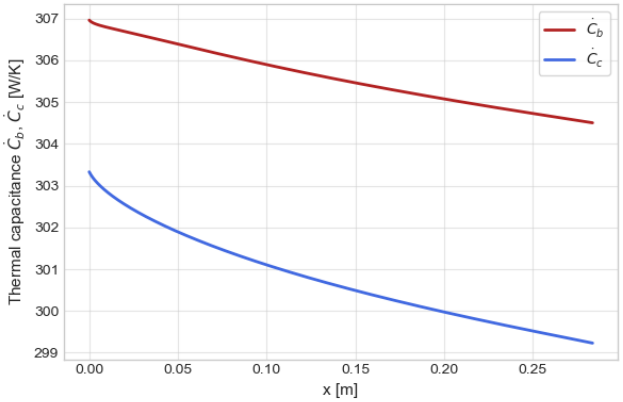

(b) Thermal capacitance of both diffuser and coolant flows for the original ORCHID turbine diffuser with recuperation.

The logarithmic mean temperature difference (ΔT_{LMTD}) in Figure 3.34 shows a non-uniform profile. Variations in static temperature caused by the changing cross-sectional area are large enough to influence the overall temperature trends, so identifying the thermally limiting stream requires examining the thermal capacitance of each stream. In the original ORCHID diffuser with recuperation, the diffuser stream was the limiting side (see Figure 3.35b). In contrast, Figure 3.35a indicates that, in the optimized T-rHEX, the coolant thermal capacitance exceeds that of the diffuser near the diffuser inlet. Because the coolant experiences a larger temperature rise than the diffuser, its specific heat increases, thereby increasing its thermal capacitance. Once the coolant becomes the limiting stream, the diffuser flow undergoes a larger temperature change. As a result, the optimized T-rHEX exhibits more balanced temperature changes between the two streams than the original ORCHID configuration with recuperation (see Table 3.5).

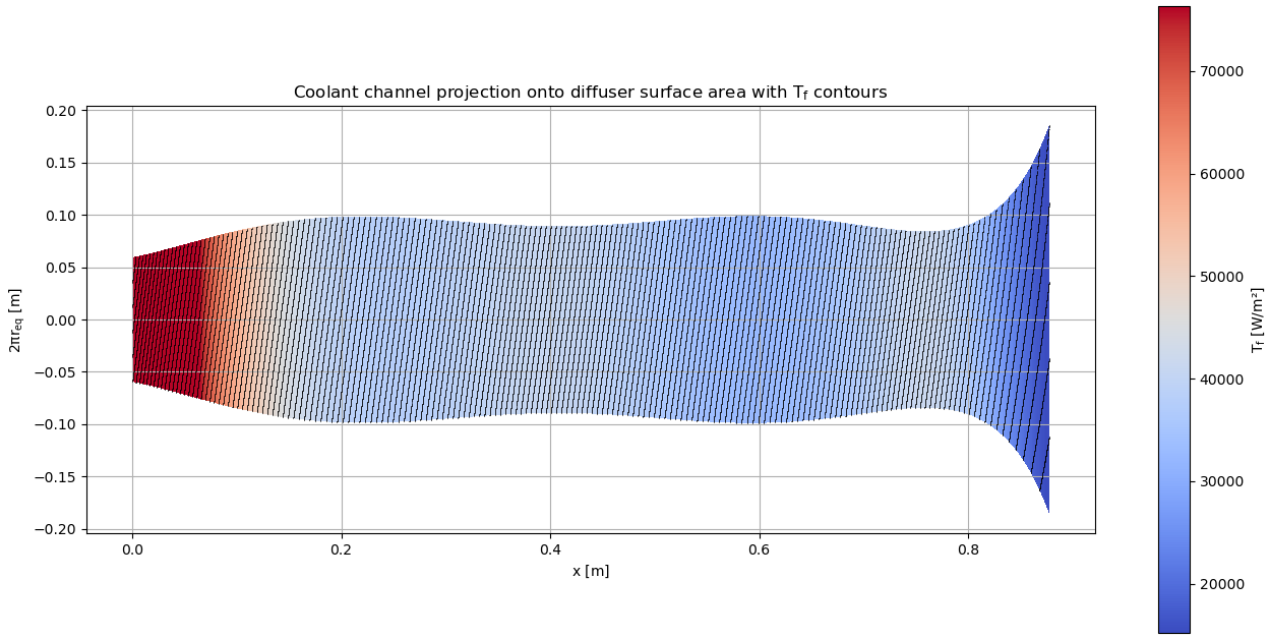

Figure 3.36: heat flux along the surface of the diffuser for the given optimized T-rHEX.

As seen in Figure 3.36, heat flux distribution shares similarities with Figure 3.17, where the peak heat flux is at the diffuser inlet and the lowest heat flux is at the diffuser outlet. The inlet heat flux peak reaches values of approximately $600\,000\,\mathrm{W\,m^{-2}}$), while showing a maintained averaged heat transfer for the middle section of the diffuser of approximately $40\,000\,\mathrm{W\,m^{-2}}$). By increasing the averaged heat flux, the heat exchanger not only is improved by increasing the wetted area of the diffuser, but also by increasing the efficiency.

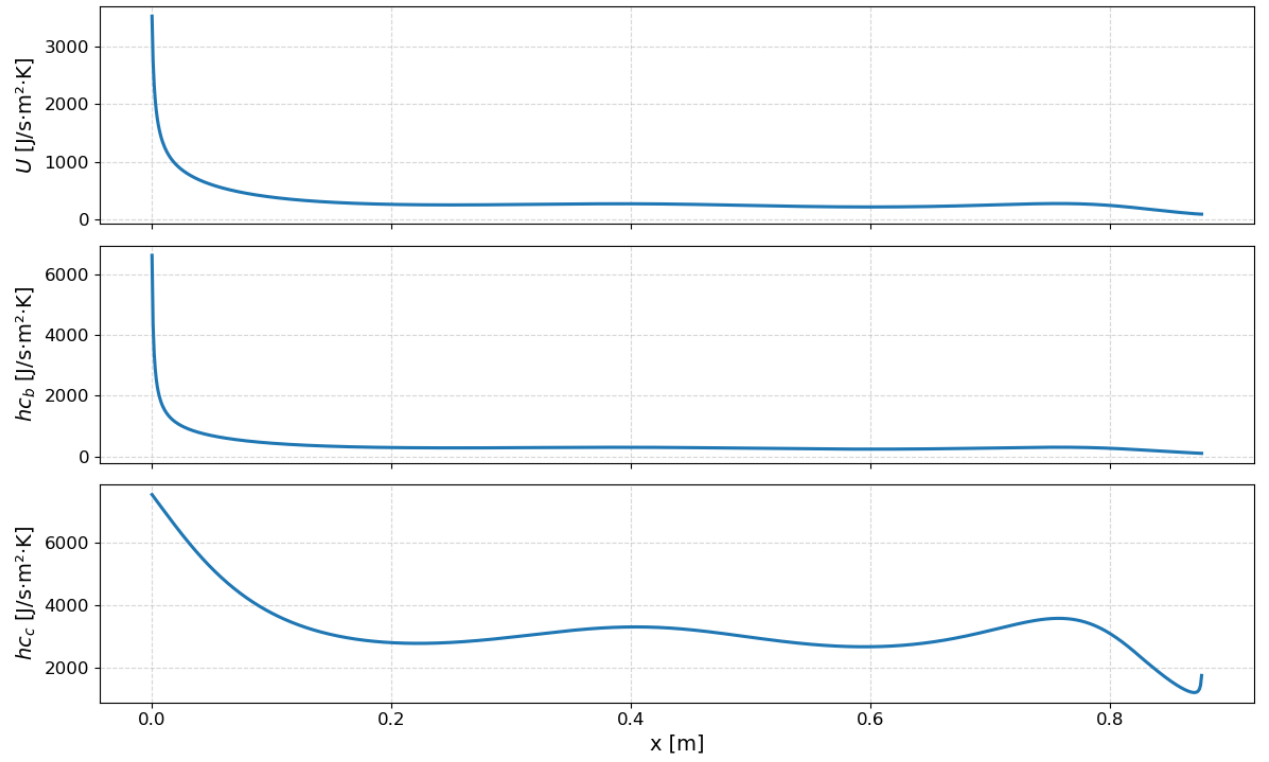

Figure 3.37: Total, diffuser and coolant heat transfer coefficients along the recuperator for the optimized T-rHEX.

In terms of convection heat transfer coefficients, as expected, the overall heat transfer coefficient influences strongly the distribution of heat flux along the recuperator. The diffuser convective heat transfer distribution is similar to that of the original ORCHID diffuser with recuperation, where inlet effects due to boundary layer development lead to a spike in heat transfer rate. However, past the inlet section, the optimized T-rHEX is able to maintain a higher convective heat transfer coefficient, unlike the original ORCHID diffuser, where convective heat transfer coefficient constantly decreases.

The coolant channel shows convection coefficients on average higher than $3000\,\mathrm{J\,s^{-1}\,m^{-2}\,K^{-1}}$, which is a major improvement as compared to the original ORCHID diffuser with recuperation. Such improvement causes an increase in total heat transfer coefficient (U_{total}), specially at the mid-section and close to the outlet. This improves the heat transfer rate of the recuperator, allowing for a significant increase in thermal power.

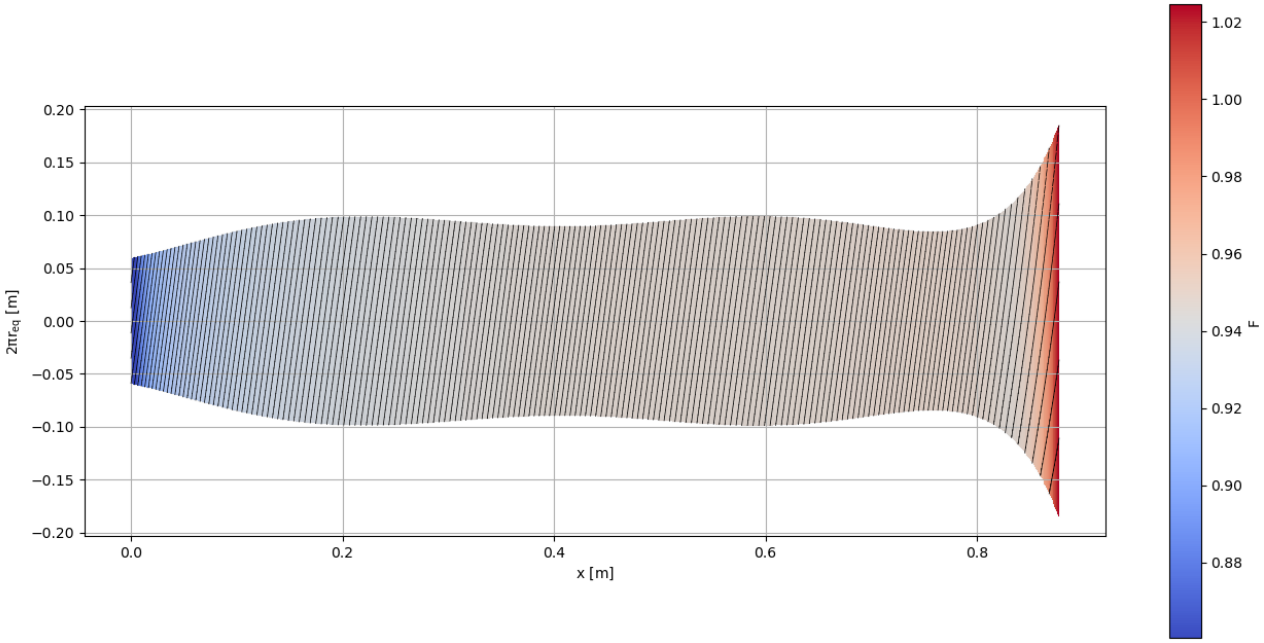

Figure 3.38: Correction factor along the surface of the diffuser for the given optimized T-rHEX, including projected coolant channel boundaries.

In terms of the correction factor due to cross-flow effects, the results are similar to Figure 3.20. Most of the diffuser achieves an average correction factor of 0.94. At the inlet of the diffuser, a slight worse cross-flow performance is observed by the optimized T-rHEX. However, the overall effect of cross-flow remains similar. This is expected since the twist angle remained close to the value of the original ORCHID diffuser with recuperation. In conclusion, the effect of cross-flow remained similar to the ORCHID diffuser as a recuperator, while the convection heat transfer improved. Therefore the optimized has primarily increased the heat transfer rate by improving convection within the coolant.

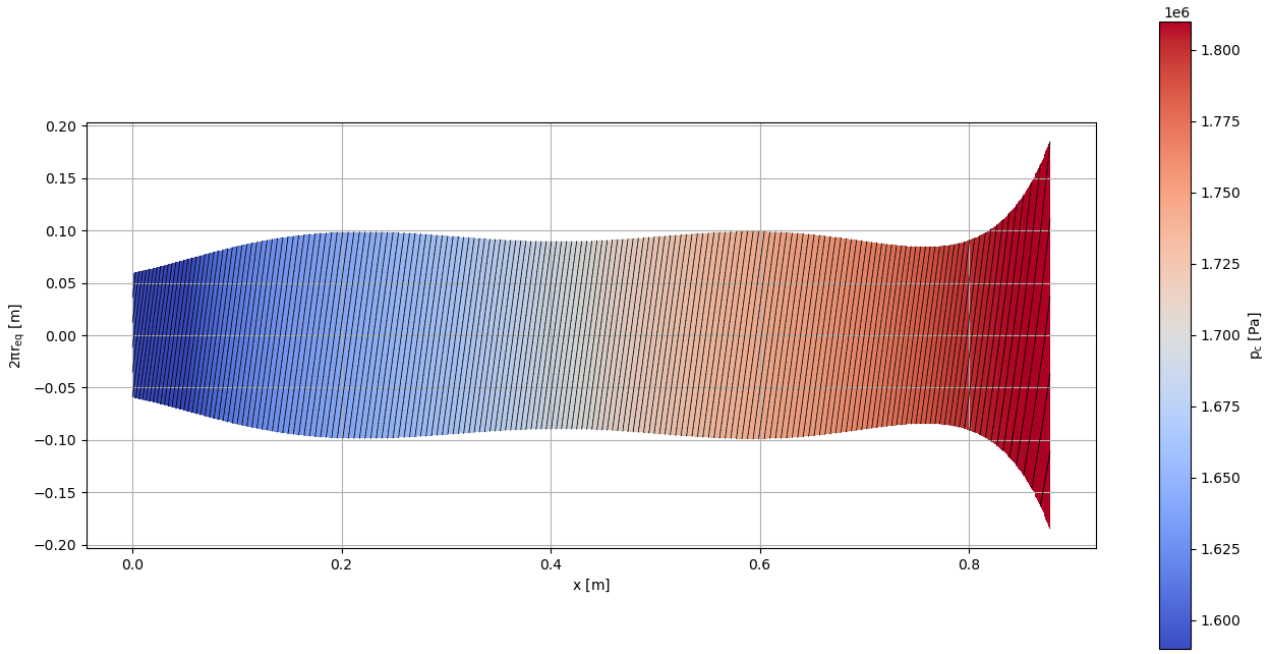

Figure 3.39: Coolant channel static pressure along the recuperator for the given optimized T-rHEX, including projected coolant channel boundaries.

Friction plays a major role in pressure losses. As expected, the coolant channel pressure losses for the optimized T-rHEX configuration are greater than for the original ORCHID diffuser with recuperator, since the coolant channel approximately three times longer. As seen in Figure 3.39, the static pressure decreases along the coolant channel. At the inlet of the coolant channel (diffuser outlet) and along the middle of the diffuser, a steady pressure loss is present due to the effects of friction and heating. However, at the exit of the coolant channel (diffuser inlet), the coolant channel cross sectional area decreases, leading to flow acceleration and therefore additional pressure losses due to friction. Therefore, superimposing the effects of pressure reduction due to heating and additional frictional losses, the coolant channel experiences a higher pressure drop, thus requiring more pump power to overcome such pressure drop.

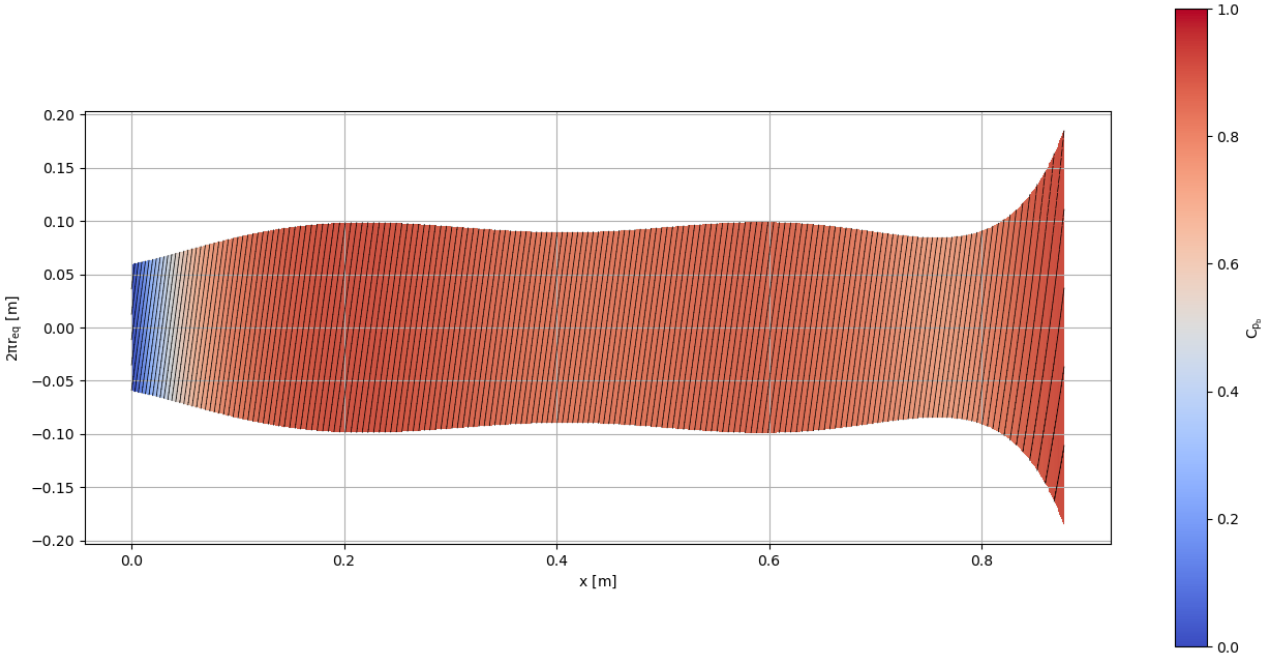

Figure 3.40: Diffuser static pressure coefficient along the recuperator for the given optimized T-rHEX, including projected coolant channel boundaries.

The pressure coefficient indicates the local pressure with relation to inlet conditions. Therefore, an increase in pressure coefficient is directly proportional to a static pressure rise. It can be seen in Figure 3.40 how the diffuser builds most of its pressure at the initial section of the diffuser, while maintaining pressure through the middle section and regaining more pressure at the outlet of the diffuser. As the middle section of the recuperator is elongated to benefit from improved heat exchanger performance capabilities, additional frictional losses lead to a decrease in pressure within the diffuser. As the diffuser pressure coefficient is constrained by the optimization problem, the middle section of the length is optimized to the given length, in order to minimize pressure losses in the diffuser and maximize heat transfer. At the outlet of the diffuser, another expansion procedure is performed with the goal to recover the pressure lost due to friction in the middle section of the diffuser. If a higher pressure coefficient is to be imposed as a constraint, it is believed that the middle section would be shortened to compensate, causing a significant decrease in heat transfer capabilities.

3.4.3. Effect of diffuser back pressure on ORC efficiency

So far, the effects of changing the diffuser back pressure have been neglected. Changes in back pressure lead to changes in condenser pressure, which shifts the operational conditions of the condenser and thus efficiency of the cycle. For a reduction in diffuser back pressure, the saturation temperature of MM siloxane decreases with respect to the original saturation temperature, leading to an increase in phase change entropy between gaseous and liquid state. This is reflected in a T-s diagram by a downwards shift in the condensation line. In ideal Rankine cycle calculations, a decrease in condensation temperature would implement an increase in net heat input into the system ($\dot{Q}_{\text{net}} = \dot{Q}_{\text{input}} - \dot{Q}_{\text{reject}} = \dot{W}_{\text{turbine}} - \dot{W}_{\text{pump}}$), which due to conservation of energy would imply an increase in turbine work extraction. In reality, the changes in diffuser performance does not affect the fixed turbine work extraction, but affect downstream components such as the ORCHID condenser. Due to conservation of energy and neglecting the small contribution of the pump, the changes in heat rejection are compensated with changes in heat input. Therefore, for an increase in heat rejection, the ORC efficiency decreases.

$$\eta_{\text{rankine}} = \frac{\dot{W}_{\text{net}}}{\dot{Q}_{\text{input}}} = \frac{\dot{W}_{\text{turbine}} - \cancel{\dot{W}_{\text{pump}}}}{\dot{W}_{\text{turbine}} - \cancel{\dot{W}_{\text{pump}}} + \dot{Q}_{\text{reject}}} \tag{3.37}$$

For a reduced back pressure, as in the optimized T-rHEX setup, the condenser operates at a lower saturation temperature than the original saturation temperature. At this lower temperature, the entropy of condensation and the latent heat of vaporization increase. Consequently, to remove the additional latent heat, the total heat rejected by the condenser must increase. To quantify this effect, the following 3 scenarios are considered:

1. Comparison at constant pressure for 2 different diffuser exit temperatures.
2. Comparison at constant temperature for 2 different diffuser exit pressures.
3. Comparison between original ORCHID turbine diffuser with recuperation and optimized T-rHEX.

Using numerical integration, the heat rejection is approximated by integrating temperature and entropy (Equation 2.15) from the diffuser exit conditions to the inlet coolant conditions, accounting for both sensible heat and latent heat of vaporization.

For the first scenario, the results are analogous to the original ORCHID diffuser with recuperation setup, since the difference in pressure is almost negligible. Constant diffuser exit pressure implies that the saturation temperature remains constant, thus the latent heat of vaporization stays the same. The difference in heat rejection is therefore purely due to difference in sensible heat. This difference in sensible heat is already accounted for in cycle efficiency by the recuperated thermal power.

In the second scenario, a reduction in pressure causes a reduction in the saturation temperature, which in turn increases the latent heat of vaporization. Additionally, the decrease in saturation temperature leads to an increase in sensible heat. To quantify this effect, the exit temperature was held constant, and the exit pressures of the ORCHID and optimized T-rHEX were compared, showing a 1.43% pressure reduction. As a result, the latent heat of vaporization increased by 0.1%, while the sensible heat rose by 0.24%, yielding an overall increase in heat rejection of 0.18%. This increase is marginal, nevertheless, for larger pressure drops, this effect may become significant, which highlights the importance of accounting for condenser saturation pressure in ORC calculations.

In the last scenario, the direct comparison between the different diffuser exit conditions is performed. This accounts for both pressure and temperature changes, which represents a more realistic comparison. Given the higher exit pressure of the original ORCHID diffuser with recuperation, the latent heat of vaporization increases by 0.1%, as expected from the second scenario. On the other hand, the higher exit temperature of the original ORCHID diffuser with recuperation leads to a 9.7% increase in sensible heat. Therefore, the overall heat rejected of the original ORCHID diffuser with recuperation setup is 5.5% larger than the optimized T-rHEX. As the effects of sensible heat are already considered in the definition of recuperated thermal power, only the effect of diffuser back pressure changes to the ORC efficiency are required to be quantified. These effects are not captured in the low fidelity model (`T-rHEX.py`). Although the associated pressure variations are small, the ORC efficiencies reported in chapter 4 have been adjusted accordingly to reflect the true estimated cycle performance.

Research Sub-Question RSQ1

To what extent does integrating and optimizing the T-rHEX geometry improve the thermal efficiency of a high-temperature organic Rankine cycle waste-heat recovery system?

Integrating and optimizing the T-rHEX geometry for the representative high-temperature ORC system leads to a substantial improvement in ORC thermal efficiency. The optimized T-rHEX increases the recuperated thermal power sufficiently to raise the overall cycle efficiency by approximately 1.05%, while requiring less than half the volume of the baseline T-rHEX and only a modest increase in volume relative to the original ORCHID diffuser. While the optimized T-rHEX increases ORC thermal efficiency and heat exchanger compactness, the associated reduction in diffuser back pressure lowers the achievable diffuser expansion ratio and therefore limits kinetic energy recovery from the turbine exhaust. Additionally, the reduction in back pressure increases condenser heat rejection, lowering ORC efficiency by only 0.019%, a negligible fraction compared to the efficiency gained through enhanced recuperation. To improve pressure recovery, it is believed that implementing a more suitable separation criterion as optimization constraints can yield to improved pressure recovery results.

In summary, the T-rHEX concept provides a significant performance enhancement for high-temperature Organic Rankine Cycle waste heat recovery systems. By implementing the T-rHEX into the WHR cycle, thermal duty of the evaporator and condenser can be reduced, allowing for a downsize in heat exchangers, and thus reducing the overall weight of the waste heat recovery systems for airborne propulsion system applications. Similarly, other industrial heat recovery applications can implement the T-rHEX concept to simply increase thermal efficiency, or to potentially increase the total heat input to the cycle in order to increase turbine work.

4

High fidelity modeling of the T-rHEX

The existing low fidelity model is limited to low fidelity (1D) modeling assumptions, where 3D effects are not considered. To further improve the understanding of heat transfer and fluid dynamics phenomena within the T-rHEX design, a high fidelity (3D) model is to be built order to obtain improved results of both the ORCHID diffuser with recuperation and the optimized T-rHEX setups. To do so, the high fidelity (3D) model consist of a Conjugate Heat Transfer (CHT) simulation using Siemmens' commercial software StarCCM+. The Computer Aided Design (CAD) model are obtained using Dassault Systèmes' 3DEXPERIENCE/CATIA. The geometry of the diffuser and coolant channels is dictated by the low fidelity (1D) model, thus consistent with the low fidelity model results. This chapter consists of a description of the high fidelity model setup, following by the original ORCHID diffuser with recuperation results and lastly the optimized T-rHEX results.

4.1. Model methodology

This section describes the high fidelity model setup, starting with the CAD model implications, followed by the CHT implications to accurate model the fluid flow and heat transfer within the recuperator.

4.1.1. Geometrical modeling

To ensure consistency between the low and high fidelity models, the three dimensional geometry must accurately reflect the one dimensional formulation. The CAD models are constructed by importing the diffuser radial coordinates from the 1D solution and generating the 3D diffuser surface through axial revolution. In contrast, the coolant channel layout in the low fidelity (1D) model relies on the simplifying assumptions described in subsection 3.1.3, including the "tightly packed"channel arrangement, which is not physically realizable in a 3D solid. To generate a geometry, the curvature ratio is artificially reduced by introducing a finite structural wall thickness. Specifically, the minimum gap between the diffuser wall and the nearest coolant channel wall is set to ten percent of the local channel diameter. This radial outward shift of the channels also introduces a gap between adjacent coolant passages, ensuring each channel is structurally isolated. The recuperator solid core is obtained by subtracting the diffuser volume and all coolant channel volumes from a common outer block, thereby preserving geometric consistency while maintaining the physical constraints required for high fidelity (3D) modeling.

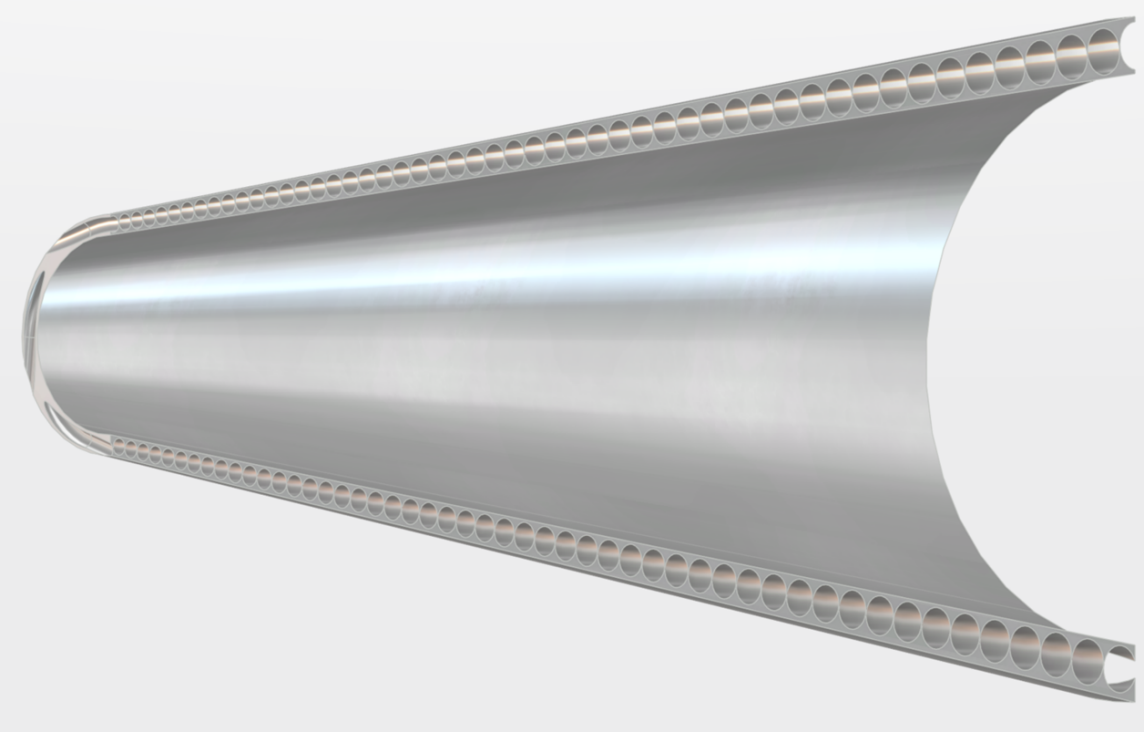

Figure 4.1: 3D isometric view of the original ORCHID turbine diffuser geometry with recuperation, presented with a radial-axial section cut to expose internal features.

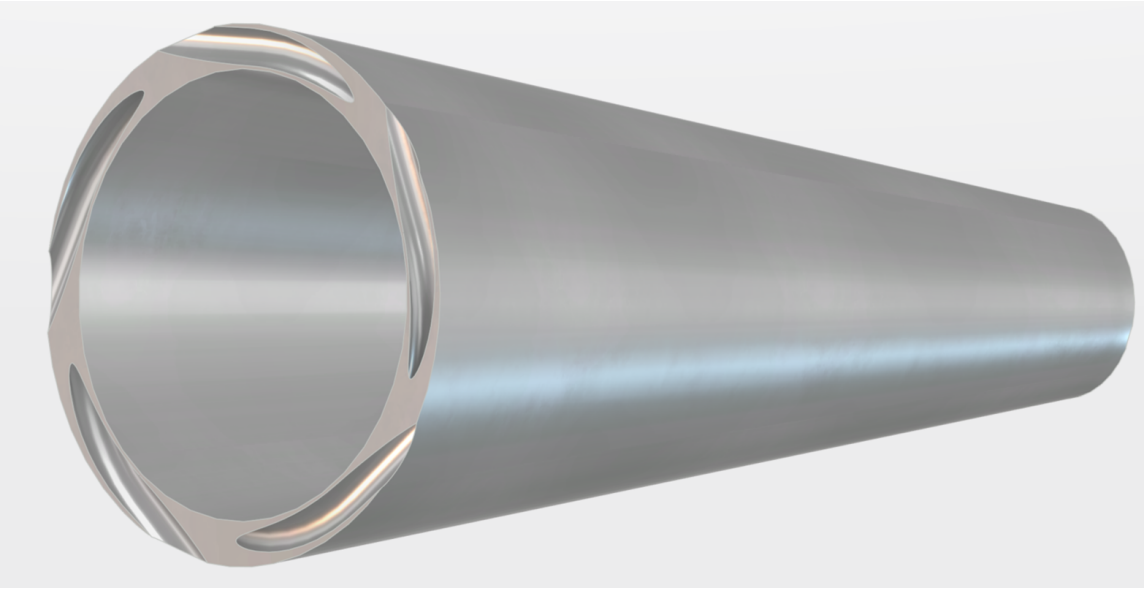

Figure 4.2: Full 3D isometric view of the original ORCHID turbine diffuser geometry with recuperation.

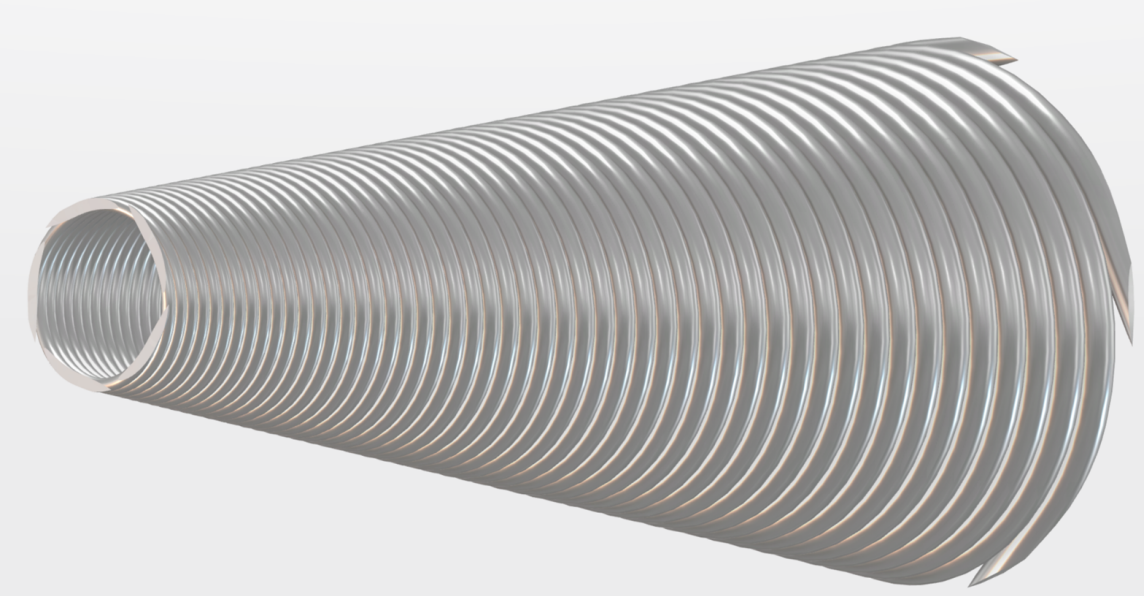

Figure 4.3: 3D isometric view of the isolated coolant channels from the original ORCHID turbine diffuser with recuperation setup.

From a structural standpoint, the high fidelity (3D) model presents certain uncertainties. First, the pressure difference between channels may lead to structural failure due to the implementation of thin walls. This aspect is considered outside the scope of this study. Additionally, the thin geometry imposes stringent mesh resolution requirements for the solid region, significantly increasing the computational cost. This is one of the main limitations of the high fidelity (3D) model.

From a fluid dynamics perspective, reducing the curvature ratio introduces a discrepancy in the coolant channel representation of the three dimensional model. Although the imposed curvature ratio does not alter the channel length, it decreases the geometric curvature of the flow path. Because the coolant path is displaced farther from the axis of rotation while the fluid velocity is preserved, the centrifugal effects acting on the coolant are slightly smaller than the effects present by the low fidelity model. Nonetheless, the channel length and diameter remain consistent with the one dimensional model, ensuring that the primary geometrical constraints of the recuperator design are retained.

In terms of heat transfer, the assumption that each coolant channel is thermally insulated from neighboring channels is no longer valid in the high fidelity (3D) model. Thermal interaction between adjacent coolant channels arises from the temperature gradient that develops along the flow path, where the coolant temperature increases progressively toward the outlet. This temperature difference induces lateral heat transfer between channels, causing heat to flow from warmer downstream regions to cooler upstream regions. As a result, the downstream coolant temperature decreases while the upstream temperature increases, leading to a partial thermal homogenization among channels. As previously described in Figure 3.8, it is believed that this effect is significantly inferior to the heat transfer between diffuser and coolant streams. The effect is further elaborated upon in subsection 4.2.6.

Figure 4.4: 3D isometric view of the optimized T-rHEX geometry, presented with a radial-axial section cut to expose internal features.

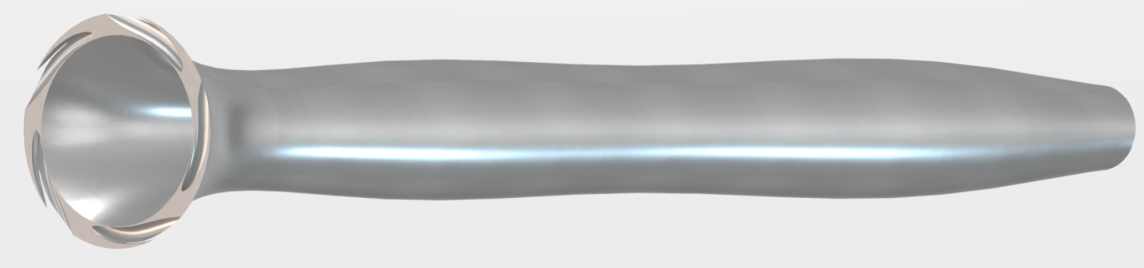

Figure 4.5: Full 3D isometric view of the optimized T-rHEX geometry.

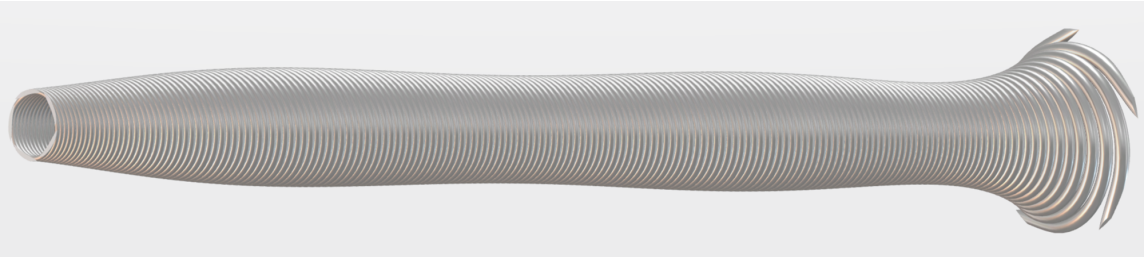

Figure 4.6: 3D isometric view of the isolated coolant channels from the T-rHEX optimized setup.

The optimized T-rHEX CAD model was built with the same approach to the original ORCHID diffuser with recuperation CAD model. As shown in the CAD reconstruction, the elongated geometry of the optimized T-rHEX results in an increase in heat exchanger volume compared to the original ORCHID turbine diffuser with recuperation. Therefore, it is expected that the computational cost of the optimized T-rHEX to be greater than the ORCHID diffuser with recuperation.

4.1.2. Conjugate heat transfer solver

Conjugate heat transfer (CHT) simulations resolve fluid convection and solid conduction in a fully coupled manner by solving the continuity, momentum, and energy equations in the fluid regions and the energy equation in the solid. In the present setup, three regions are solved simultaneously.

The first region is the diffuser, where the organic gaseous fluid is modeled as a compressible non-ideal gas. To do so, a steady coupled flow RANS solver is combined with the coupled energy model from StarCCM+[15]. To account for possible non-ideal gas effects, an EoS model is implemented. Unlike for low fidelity (1D) modeling, the implementation of REFPROP would require millions of function calls per iteration, deeming this method computationally excessive. Instead, since low fidelity (1D) model results concluded that non-ideal gas effects are small, a simple but effective Van der Waals EoS model is used (Equation 2.6). The implementation of the Van der Waals model in this CHT is based directly on a REFPROP property map to generate a single EoS, where coefficients are based on the critical pressure and temperature for the organic dense vapor. Additionally, to account for buoyancy effects due to density changes, a gravity model is implemented based on the Boussinesq model[15].

$$\vec{f}_{\text{body}} = \rho \vec{g} \beta_{TE} \left(T_{ref} - T \right) \tag{4.1}$$

This additional model allows the introduction of additional body forces ($\vec{f}_{\text{body}}$) to the momentum equations due to the effect of buoyancy.

The second region is the coolant, which utilizes a steady coupled flow RANS solver combined with the coupled energy model. However, due to negligible flow compressibility effects of liquids, the coolant is modeled as incompressible. Thermophysical properties such as viscosity, density, and specific heat are therefore prescribed as functions of temperature only.

The third region is the solid structure. This region implements constant thermal properties based on the properties of pure aluminium. Aluminium is chosen due to its excellent thermal properties as well as ease to mill, the later for ease to manufacture the complex recuperator geometry. To couple energy models with the fluid regions, a coupled solid energy solver is implemented, allowing to model steady state conduction within

the material. The goal of the solid region within this CHT simulation is to act as a realistic thermal bridge between the diffuser and coolant flows.

Coupled implicit solver

With the coupled implicit solver, the continuity, momentum, energy, and species equations are solved simultaneously as a single vector system. The velocity field follows from the momentum equations, while pressure is obtained from the continuity constraint and density is evaluated through the equation of state. Solving the governing equations in a fully coupled manner improves variable coupling and numerical robustness[15]. The vector system is discretized in space and time using an implicit Euler scheme combined with a Newton linearization of the fluxes, yielding a linear system at each iteration. To remove both high and low frequency error components from iterative solver methods, StarCCM+ employs an Algebraic Multigrid (AMG) method, which constructs a hierarchy of algebraically coarsened systems. Residuals are restricted to the coarse levels and corrections are prolonged back to the fine grid, providing fast multilevel convergence at modest computational overhead[15]. Relaxation factors also play a central role in solver stability. High relaxation values accelerate convergence but increase the risk of divergence, whereas lower values improve stability at the cost of additional iterations.

For the present CHT simulations, the coupled implicit formulation was found to be more accurate and stable than segregated approaches. Preliminary tests confirmed that the coupled solver reduced nonphysical pressure oscillations near the coolant inlet. In terms of convergence, the current AMG setup is found to provide sufficient numerical stability. Instead, convergence was found to be limited by the turbulence model. Therefore, the default AMG settings were selected.

Turbulence model

To model turbulence reliably in the conjugate heat transfer simulation, the turbulence model must handle viscosity variations and remain sufficiently robust to achieve convergence. As outlined in subsection 2.3.2, LES is not considered due to the limited simulation time, and restricted random access memory. Instead, a steady RANS turbulence model is implemented.

For diffuser flows, accurate prediction of pressure gradient effects within the boundary layer is essential. The most rigorous RANS approach is the Reynolds Stress Model, which resolves all components of the Reynolds stress tensor and thus accounts for turbulence anisotropy[13]. However, the added nonlinearity and computational expense of RSM produced poor convergence in the present CHT configuration, specially in the coolant channel stream due to the coarse mesh quality. For this reason, a choice to pursue another turbulence model was taken. Future work can be performed either by implementing a finer coolant mesh to implement two different turbulence models for each stream.

The next most appropriate choice is the eddy viscosity based SST $k-\omega$model, which blends near wall $k-\omega$ behavior with free stream $k-\epsilon$ characteristics and generally performs well in flows with strong pressure gradients and attached or mildly separated boundary layers in comparison to other EVMs. Although the coolant channel exhibits streamline curvature for which linear eddy viscosity models are not ideal, the SST $k-\omega$ model showed stable convergence and produced results consistent with expectations. Studies of dense vapor flows also report good agreement between DNS and RANS predictions using SST $k-\omega$[16], supporting its suitability for wall bounded turbulence with significant thermophysical property variations. For these reasons, SST $k-\omega$ is selected for verifying the one dimensional model against the three dimensional CHT simulations.

Boundary conditions

Boundary conditions are critical to obtaining valid and physically consistent results. They ensure the existence of unique solutions to the Navier–Stokes equations solved by the numerical solver. Unrealistic or poorly defined boundary conditions can lead to numerical instability or non-physical flow behavior, potentially causing divergence or convergence toward meaningless solutions. Therefore, defining consistent and adequately constrained boundary conditions is essential to ensure that the computed flow field accurately represents the intended operating conditions.

Due to the optimized T-rHEX configuration yielding a similar optimum twist angle, the number of coolant channels remains constant. Consequently, except for the outlet conditions, the fluid dynamics solver setup is largely consistent between the original ORCHID turbine diffuser and optimized T-rHEX setups. Interfaces between the solid structure and fluid regions are modeled as heat transferring walls, while the outer surface of the recuperator is modeled as an adiabatic wall. Since the flow remains fully subsonic in both the diffuser and coolant channels, appropriate boundary conditions must specify both dynamic and static components.

At the inlet, five Dirichlet boundary conditions are imposed. The mass flow rate at the inlets of both the coolant channels and the diffuser is fixed to match the low fidelity model inlet specifications, enabling direct comparison. The velocity vector components and total temperature are also prescribed. StarCCM+ determines density and velocity components by solving the mass flux and total enthalpy equations [15].

At the outlet, additional Dirichlet boundary conditions are required to obtain a well-posed subsonic flow problem. This is achieved by imposing a constant target static pressure and temperature, consistent with the low fidelity (1D) model results. Numerically, this means that the gradient based solution is scaled with respect to the outlet reference conditions, obtaining a unique solution. As is shown later in subsection 4.3.4, this leads to possible discrepancies between the high fidelity and low fidelity inlet static conditions. Nevertheless, all pressure field results remain suitable for qualitative comparison.

4.2. Results: Existing ORCHID turbine diffuser as a recuperator

This section covers all of the results related to the ORCHID with an optimized coolant channel setup. The mesh refinement and convergence are discussed, followed by CHT results for the original turbine diffuser integrated as a recuperator in the ORC. These results are to be discussed on their own before comparing them to the low fidelity model (1D) results.

4.2.1. Mesh refinement and convergence

In order to run these complex CHT simulations with sufficient mesh refinement, the DelftBlue High Performance Computing (HPC) cluster is used. The accessible innovation partition imposes a memory limit of 250 GB per job and allows the use of up to 64 CPU cores, with a maximum wall time of 24 hours. This imposes a limit both in the mesh resolution and in the convergence rate.

To establish a baseline, fully resolved grid to perform DNS would require approximately 23×10^9 coolant channel cells and 5.2×10^{12} diffuser cells. These numbers are outside reach for the given resources available for research, thus the reason for the implementation of the turbulence modeling. The implemented mesh consists of 3 individual meshes coupled with contact in-place interfaces. These interfaces update wall temperature boundary conditions for all heat transferring surfaces. Information at the interface is interpolated based on cell area to cells in contact with such surface. Although this process should obey conservation of energy, numerical errors may lead to inconsistencies. For the current setup, accuracies of 99.6% are achieved across all interfaces.

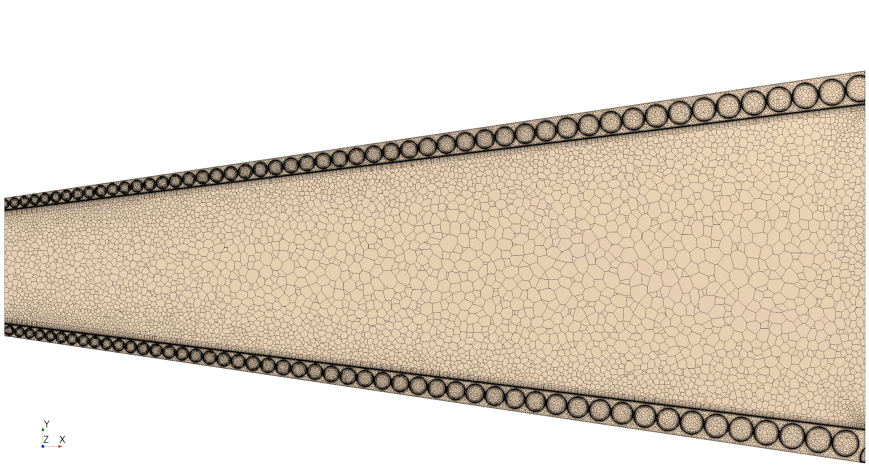

(a) Cross section view of the mesh along the axial-radial plane.

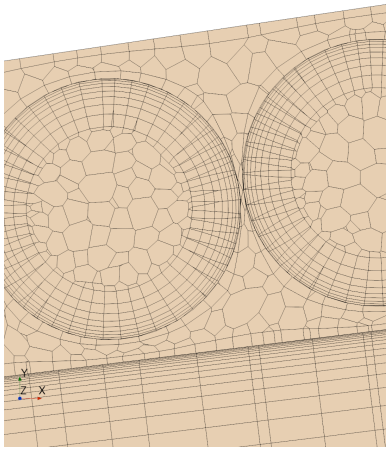

(b) Zoomed view of the cross section view at the coolant-structure and diffuser-structure interfaces.

Figure 4.7: Cross-sectional view of the mesh for the existing ORCHID turbine diffuser with recuperation.

The diffuser and coolant meshes are designed with refined wall treatments to accurately capture near wall turbulence. In the diffuser region, the mesh density is progressively increased towards the walls, with a prism layer implemented to resolve high perpendicular flow gradients. These prism layer cells typically possess high aspect ratios and are aligned tangentially to the wall in a structured manner, to ensure proper resolution of

wall bounded turbulence. To ensure adequate wall treatment without excessively increasing computational cost, the prism layer is finely resolved to achieve y_+ within viscous sublayer ($y_+ < 5$). For the diffuser mesh, over 55% of wall bounded cells are within $y_+ < 1$, 93% within $y_+ < 1.5$, and 99.8% within $y_+ < 5$. This low y_+ approach allows for the viscous region to be solved in a laminar manner ($u^+ = y^+$) and for direct computation for wall conduction. Nevertheless, commercial CFD software add wall treatment functions for numerical robustness[15].

The coolant mesh is implemented where prism layers occupy a significant portion of the cross section of the mesh (Figure 4.7b). This is done as the Reynolds number within the coolant channel is an order of magnitude lower than the diffuser thus a more predominantly laminar regime is expected. Due to the nature of smaller characteristic length scales and the curvature of the channels, the spatial resolution required is higher than the diffuser. In order to reduce cost, near wall mesh refinement is relaxed by imposing no y_+ limit. In order to capture near wall momentum and thermal gradients, StarCCM+ all y_+ hybrid wall treatment is selected. This wall model simply interpolates between the low y_+ and high y_+ models depending on the value of y_+. As used in the diffuser, the low y_+ model only implements wall treatment functions for robustness. Meanwhile for high y_+, wall shear stress, turbulent production and turbulent dissipation are derived from equilibrium log-layer assumptions[15]. This assumes that the near wall cells lie within the logarithmic region of the boundary layer, thus implementing a log-law region model for $y_+ > 30$. As the coolant channel does not implement a y_+ limit, results give y_+ values ranging from below 1 close to the coolant inlet to values greater than 30 approaching the outlet. Blending of low and high y_+ wall treatment models improves code robustness but may result in numerical inconsistencies when predicting wall bounded properties such as shear stress or heat transfer.

To conclude the discussion on mesh refinement, the solid structure region was discretized using a relatively coarse mesh. The primary consideration in this region is the smallest characteristic length scales, corresponding to the gaps in between coolant channels. As described in subsection 4.1.1, these gaps are small, which results in locally increased cell density. However, unlike the fluid regions, the primary purpose of the solid mesh is to provide a thermal path between the diffuser and the coolant. Consequently, the mesh was designed to be as coarse as possible while retaining sufficient resolution to capture temperature gradients in the solid, and with acceptable mesh quality properties to ensure numerical stability.

Table 4.1: Mesh cell count for each individual region for both CHT simulations.

	Diffuser cell count [-]	Coolant channels cell count [-]	Structure cell count [-]
ORCHID diffuser as a recuperator	1.3×10^6	18.7×10^6	5.1×10^6
Optimized T-rHEX	4.4×10^6	3.6×10^6	24.7×10^6

The quality of all meshes is assessed based on specific cell properties. Firstly, all cells are verified to have positive volumes. Secondly, cell skewness is used as an indicator of connectivity, as high skewness angles ($\theta_{skewness} > 85°$) can induce errors in gradient-based (diffusive) fluxes and cause convergence issues. While skewness was generally not problematic in the fluid regions, some cells in the solid region, particularly within the gaps between coolant channels, exhibited skewness angles exceeding this threshold. This could locally reduce thermal conductivity due to numerical dissipation. Lastly, cell quality was also evaluated based on cell shape, as elongated or warped cells produce errors in transport-based (convective) fluxes, also leading to numerical diffusion[15]. As seen in Figure 4.8, the average cell quality does not approach 1. This is to be expected due to the implementation of unstructured meshes. Such meshes produce approximately uniform numerical errors independent of flow direction, making them well suited for complex flows characterized by high vorticity or helicoidal motion. Figure 4.8 also shows how both fluid region's cell quality are within acceptable values[15]. In contrast, the solid region mesh reaches values lower than 0.2, once again highlighting the coarseness of the solid region. For the purposes of this study, the coarseness of the solid region mesh is deemed acceptable, this way the introduced numerical error is treated as additional conductive resistance of the structure.

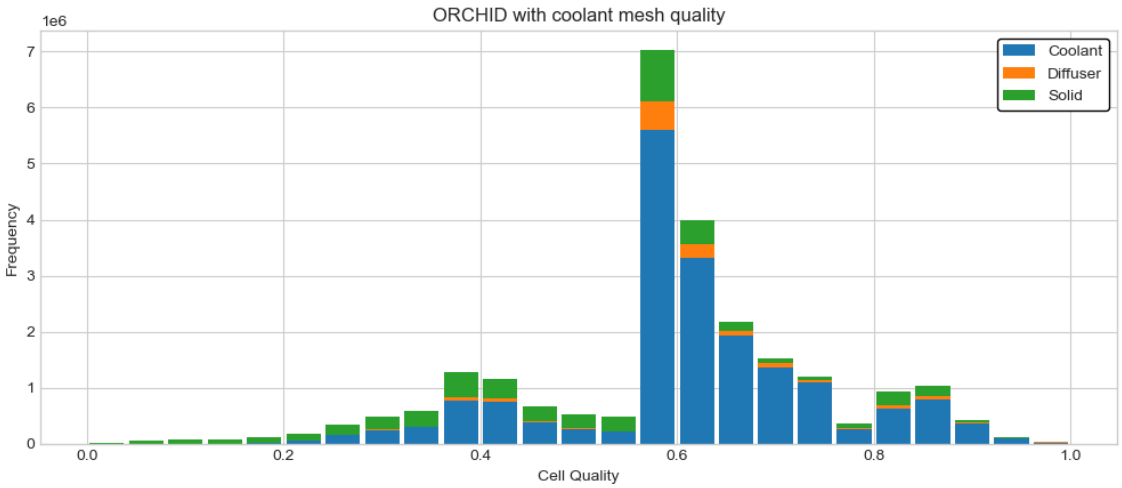

Figure 4.8: Cell quality histogram for the ORCHID diffuser as a recuperator mesh.

In terms of convergence behavior, using a two-equation RANS eddy-viscosity model (EVM) is deemed necessary to achieve satisfying convergence, thereby minimizing both the residuals and the overall solution error. This modification enabled stable residual levels of the order of 10^{-6}, with the exception of the energy and specific dissipation rate (Sdr), which converged only to approximately 10^{-2}. Poor Sdr convergence is believed to be caused by inlet boundary conditions. Cells bounding both a wall and an inlet boundary tend to have numerical error, this also propagates into the turbulence transport equations. Verification successfully confirmed that this is the case, thus a physically consistent inflow profile would improve both flow field prediction and convergence robustness. Moreover, poor energy residual convergence is likely due to insufficient mesh resolution of the solid region, causing numerical instabilities in conductive fluxes between cells of the solid domain.

4.2.2. Diffuser Velocity

One of the most significant differences between low fidelity and high fidelity models implemented are the velocity profiles. Low fidelity model assume a 1D bulk velocity, where effect of radial gradients are approximated based on parameters such as Reynolds number, Mach number or Prandtl number. Although these parameters are good indicators of the flow state, they do not account for 3D effects such as turbulence or separation.

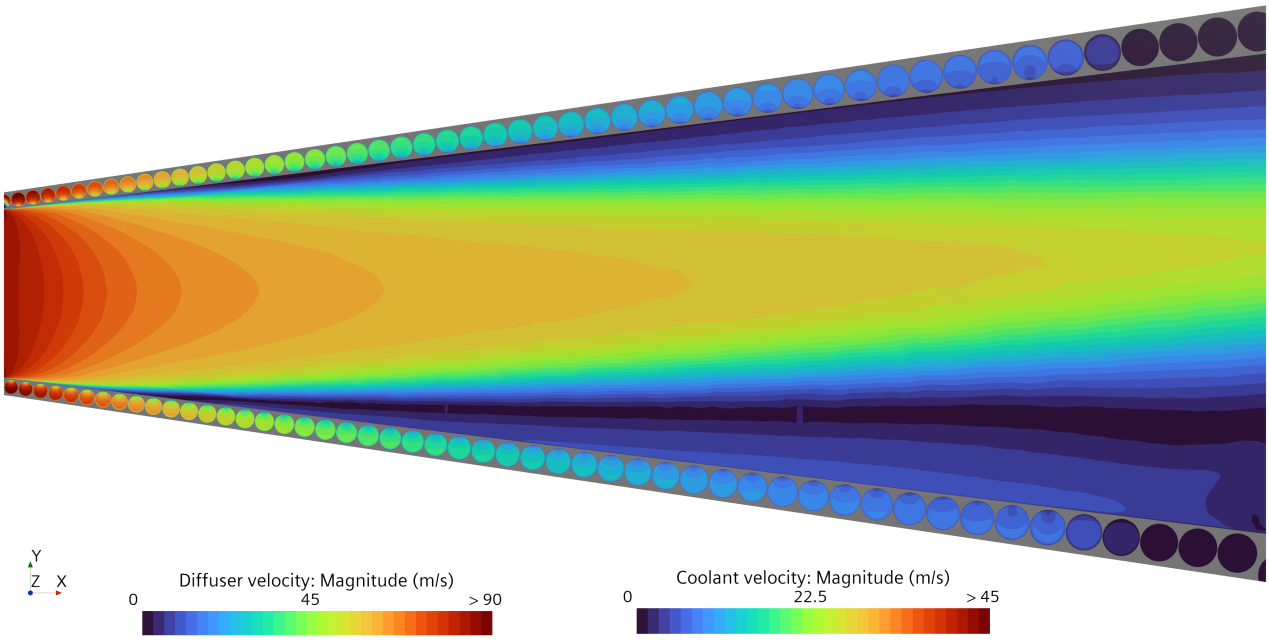

Figure 4.9: Velocity magnitude contours of the existing ORCHID turbine diffuser with recuperation.

To examine the three-dimensional flow field, an axial–radial planar cut is used. Since the diffuser is axisymmetric, this view captures both axial and radial variations effectively. As shown in Figure 4.9, the diffuser flow decelerates progressively as the cross-sectional area increases. The no-slip condition causes boundary layer growth along the walls, producing pronounced radial gradient of velocity. The velocity field is fount to not be fully axisymmetric. Separation forms along the bottom wall shortly downstream of the inlet and expands as the flow progresses downstream. This localized separation suggests a potential influence of heat transfer on boundary layer stability. To further investigate the effects of heat transfer on separation, the adiabatic existing ORCHID turbine diffuser is simulated.

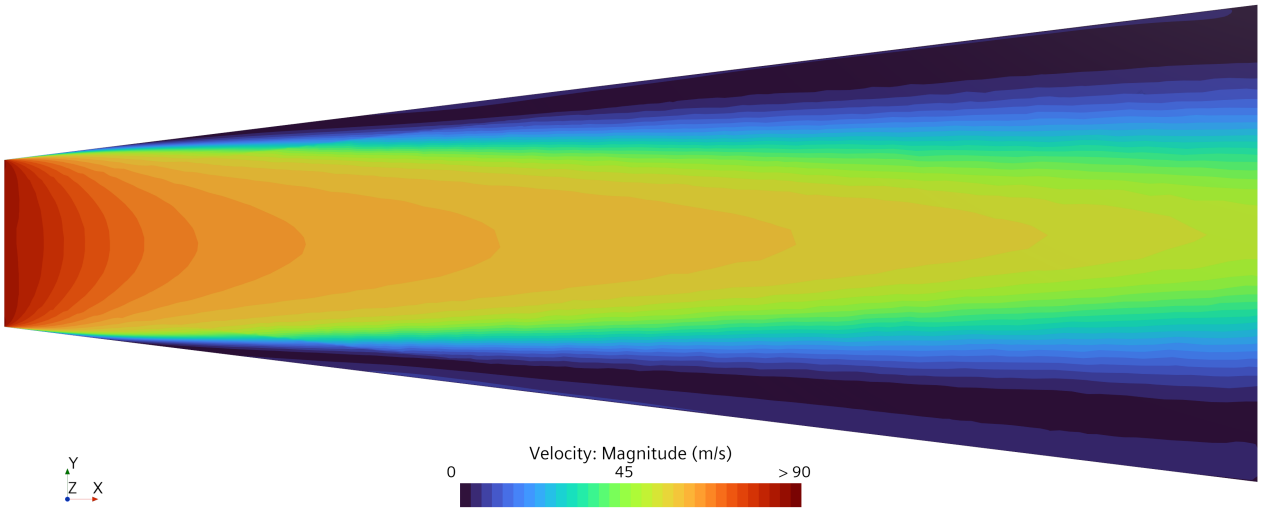

Figure 4.10: Velocity magnitude contours of the adiabatic existing ORCHID turbine diffuser.

As seen in Figure 4.10, the velocity profiles are similar to Figure 4.9, both with strong radial gradient of velocity due to boundary layer growth. However, the adiabatic case shows a more axisymmetric velocity profile. To visualize the size of the separation bubble within the diffuser, axial flow reversal plots can be compared. Furthermore, in addition to the cooled and adiabatic diffusers, a third case is simulated using a constant heat flux distribution to remove heat transfer variation effects.

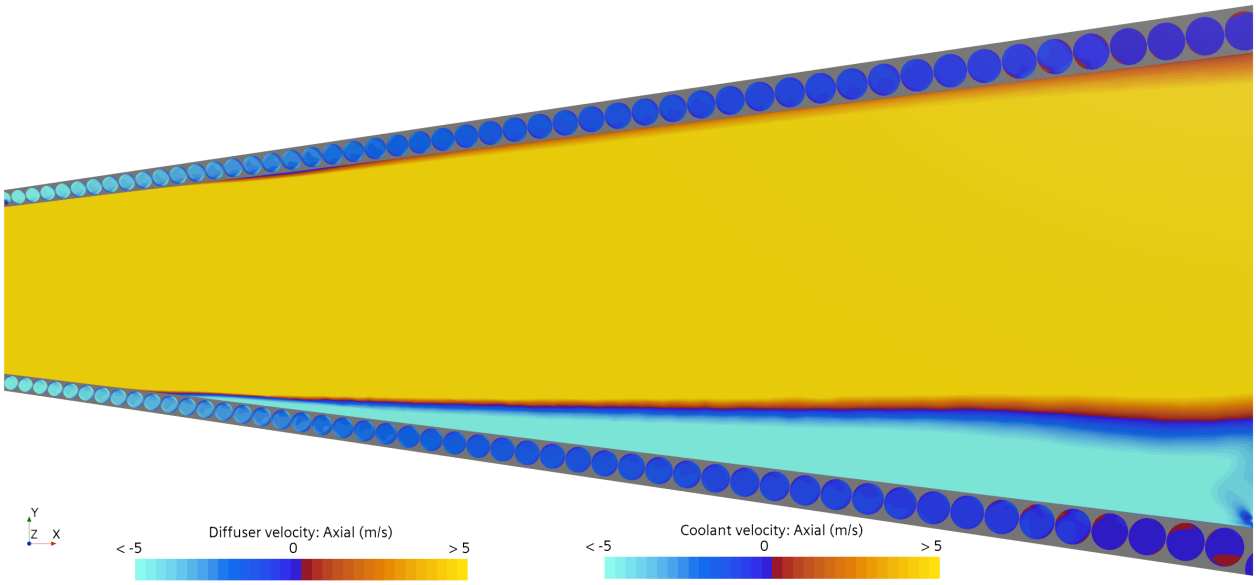

Figure 4.11: Axial velocity contours indicating separation bubbles for the existing ORCHID turbine diffuser with recuperation.

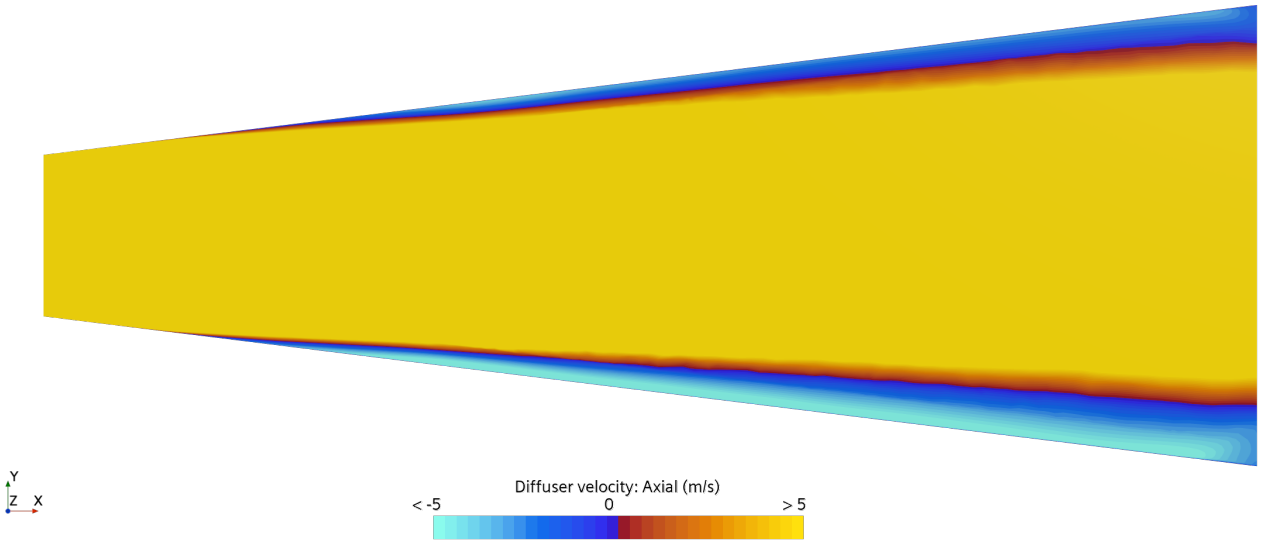

Figure 4.12: Axial velocity contours indicating separation bubbles for the adiabatic existing ORCHID turbine diffuser.

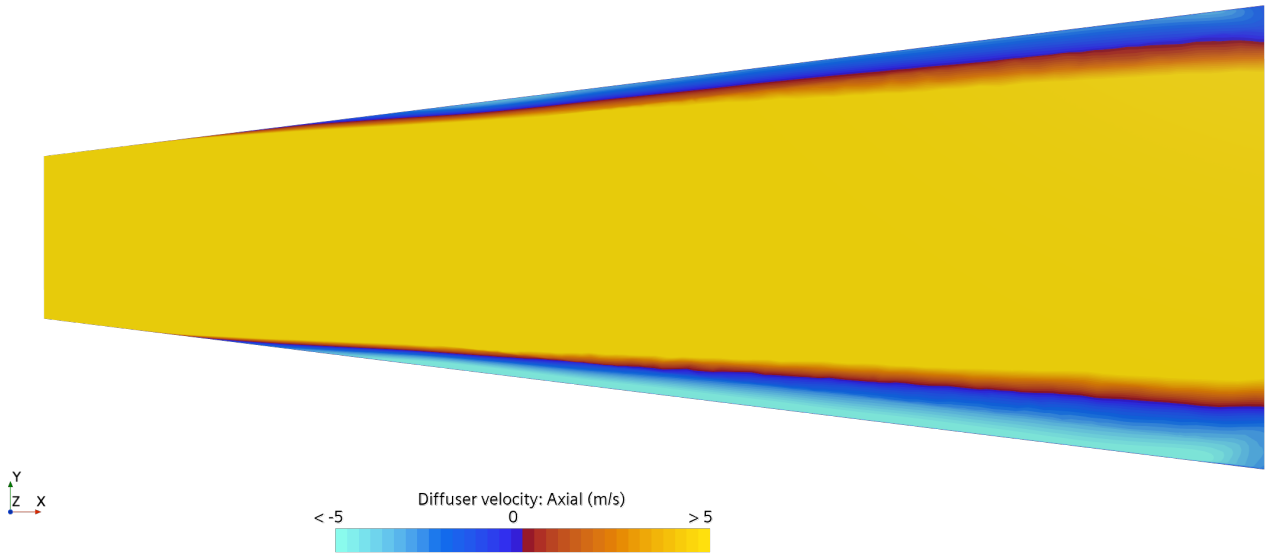

Figure 4.13: Axial velocity contours indicating separation bubbles for the existing ORCHID turbine diffuser under constant heat flux.

Figure 4.12 shows that the adiabatic diffuser exhibits separation uniformly along all walls in an axisymmetric manner, whereas the cooled diffuser in Figure 4.11 experiences separation only along the bottom surface. As shown earlier in Equation 2.28, wall cooling increases boundary layer stability through viscosity gradients induced by heat transfer. Although cooling can delay or weaken the onset of separation, it does not guarantee boundary layer stability once separation has initiated. This is evident from Figure 4.13, which even under constant heat flux, the size of the separation bubble remains almost identical to the adiabatic case. A closer comparison between Figure 4.13 and Figure 4.12 shows that cooling slightly delays the point of initial separation, but this effect is small relative to other mechanisms such as thermal mixing due to buoyancy and baroclinic instabilities.

In this study, two primary heat transfer mechanisms are found that shape the separation bubble. Firstly, buoyancy effects caused by heat transfer before separation have an effect on the core flow interaction with the separation region through thermal mixing. Due to cooling, buoyancy effects are expected to disrupt the axisymmetry of the flow, as the gravity model implemented (Equation 4.1) acts as a body force only acting along the vertical direction. Buoyancy effects are limited in gaseous fluids due to limited density changes. Nevertheless, their effects may contribute to differentiate in separation effects between the top and bottom surfaces of the diffuser. At the top surface, the boundary layer is cooled. The denser fluid then tends to shift downwards, mixing with the high energy core flow of the diffuser. This thermal mixing process introduces high energy flow into the boundary layer which increases kinetic energy allowing for separation to be postponed, or avoided. The bottom surface has the opposite effect as the top surface. The low energy boundary layer flow remains at the bottom, which limits the kinetic energy of the boundary layer flow. As the heat flux is much greater near the inlet than the averaged value, Figure 4.11 experiences higher thermal mixing effects due to buoyancy than Figure 4.13. Downstream after separation, the recirculation region acts as an insulation layer, limiting cooling effects on the core diffuser flow.

The second mechanism found is baroclinic torque. As described in section 2.3, misalignment of density and pressure gradients leads to generation of vorticity instabilities. As seen in subsection 4.2.3, radial temperature gradients, leading to density gradients are high close to the separation point. Additionally, in subsection 4.2.4, axial pressure gradients are highest close to the inlet. Superimposing both fields leads to strong baroclinic torque close to the wall in between the inlet and the separation point.

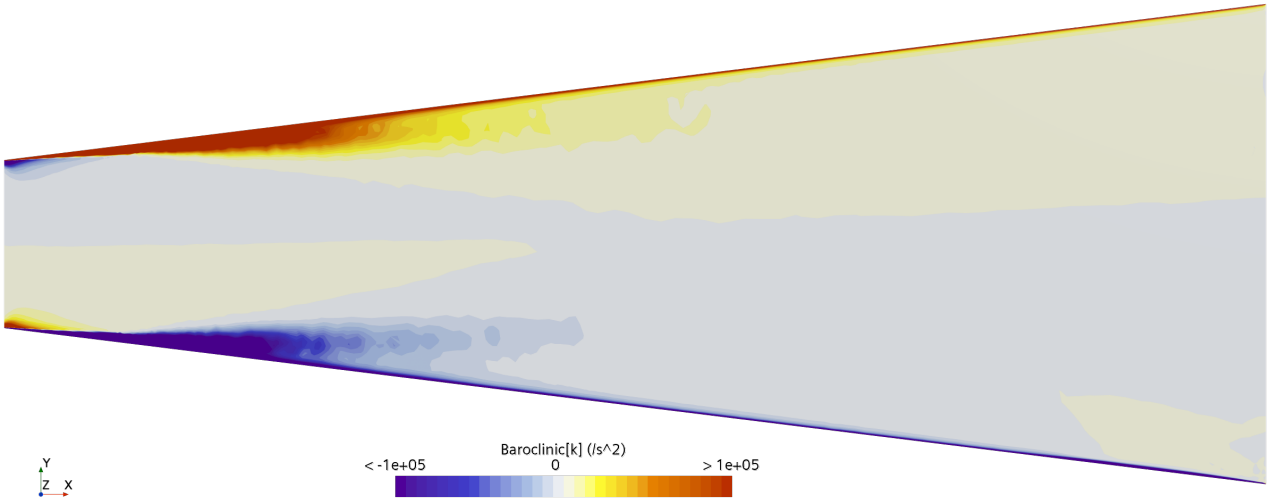

Figure 4.14: Baroclinic torque contours of the existing ORCHID turbine diffuser with recuperation.

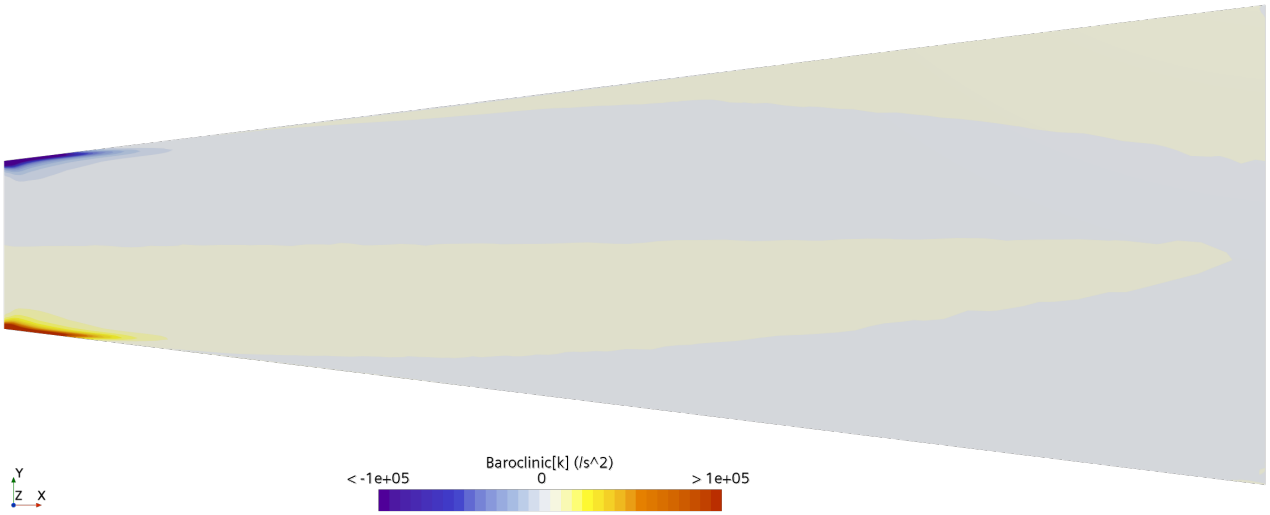

Figure 4.15: Baroclinic torque contours of the adiabatic existing ORCHID turbine diffuser

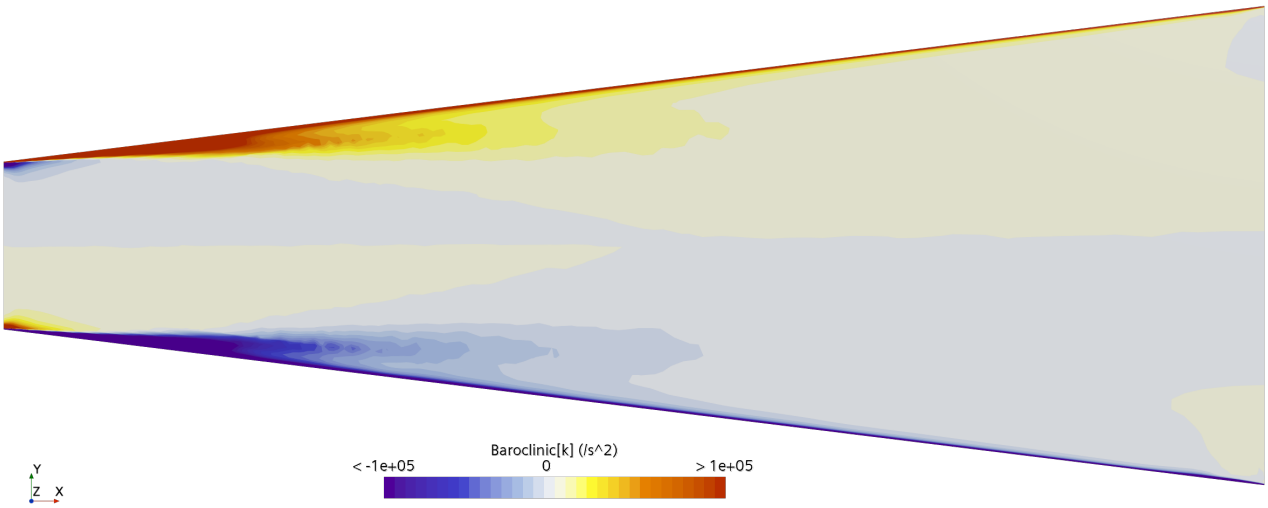

Figure 4.16: Baroclinic torque contours of the existing ORCHID turbine diffuser under constant heat flux.

As expected, in the adiabatic diffuser, no baroclinic instabilities are observed since there is no heat transfer to generate density gradients. The results shown in Figure 4.15 indicate that the only observed fluctuations are numerical artifacts originating from inlet pressure field instabilities (see Figure 4.24). Comparing the existing ORCHID diffuser with recuperation to the constant heat flux case, similar baroclinic patterns are observed. However, the existing ORCHID diffuser with recuperation exhibits baroclinic instabilities of greater magnitude over a larger area, particularly near the separation region. This is expected due to the higher heat flux at the inlet region compared to the constant heat flux case, leading to stronger density gradients interacting with the existing pressure gradients.

Baroclinic instabilities interact with the boundary layer before, during and after separation. Given the adiabatic diffuser, the pre-existing vorticity is enhanced with the addition of the baroclinic instabilities. Considering the alignment of the density gradients due to cooling and the adverse pressure gradients as seen in Figure 4.17, the baroclinic torque generated adds on to the pre-existing vorticity production due to viscous effects and vortex stretching. This in effect generates a velocity profile with higher radial gradient of velocity, which leads to a reduction in boundary layer thickness. This results have been previously demonstrated for flat plates[6]. A thinner boundary layer, in turn, increases the magnitude of radial gradient of velocity, thereby increasing boundary layer stability (see Equation 2.28). As baroclinic torque effects are greater for higher cooling rates, the existing ORCHID turbine diffuser with recuperator undergoes higher heat transfer effects near the inlet than the constant flux setup, leading to stronger baroclinic instabilities, and therefore improvement of the boundary layer stability.

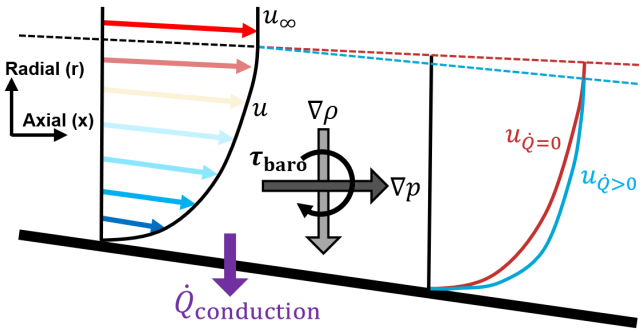

Figure 4.17: Comparison between an adiabatic (red) boundary layer and the cooled (blue) boundary layer subjected to baroclinic torque (τ_{baro}).

To conclude on heat transfer effect on separation, both baroclinic torque and buoyancy thermal mixing effects are considered simultaneously. As previously discussed, the constant heat flux case shows little effect on separation prevention compared to the adiabatic case. On one hand, both the baroclinic instabilities and the viscosity gradient effect present provide a limited but symmetric improvement over pure adiabatic separation by means of separation delay. On the other hand, the reduced heat flux at the inlet provides reduced cooling benefits. The combination of reduced thermal mixing due to buoyancy effects, reduced baroclinic torque effects and reduced viscosity gradients are found to be insufficient to prevent separation due to the present adverse pressure gradients. Considering the existing ORCHID turbine diffuser with recuperation, the inlet region provides a much higher heat flux compared to the constant averaged value. Baroclinic torque contours shown in Figure 4.14 display a much stronger effect compared to the constant heat flux case, thus it is expected that the boundary layer of the existing diffuser to be reduced compared to the constant heat flux case. The combination of higher radial gradient of velocity and higher radial gradient of viscosity lead to a more stable boundary layer as given in Equation 2.28. In addition, the enhanced thermal mixing at the top surface leads to an improved boundary layer stability, while the opposite effects occurs at the bottom surface. It is believed that superimposing both effects lead to a significantly improved boundary layer stability at the top surface, which leads to little to no separation at the top surface, while the bottom surface undergoes severe separation. Once the flow has separated, the flow shifts upwards due to the flow asymmetry, which leads to a significant growth in the separated bubble. Future studies could validate this conclusion by employing a more advanced turbulence model, such as the Reynolds Stress Models (RSM), or by using a higher-fidelity solver, for instance through Large Eddy Simulation (LES), in order to properly model the effects of baroclinic instabilities.

In order to better understand the flows within the diffuser, a radial segmentation procedure can be performed, where properties are averaged per section. There are multiple methods for averaging properties. The most simplest one, area averaging, is the simple arithmetic mean of a flow property over a cross-section, where each measurement is weighted only by its corresponding area fraction. It represents a purely geometric average.

$$\bar{\phi}^A = \frac{1}{A}\int \phi dA \tag{4.2}$$

Area averaging preserves pressure forces and volumetric flow but not mass or energy. Using an area aver-

aging technique can overemphasize large regions with low flux, making it physically unrepresentative[3][9].

$$\bar{\phi}^M = \frac{1}{\dot{m}} \int \phi d\dot{m} \tag{4.3}$$

Mass-flow averaging weights properties by their local mass flux, which better reflects the convective transport of fluid properties and conserves total energy flow. It is widely used because it tracks how the flow carries energy and momentum, although it does not accurately capture pressure forces[3][9].

Mixed-out averaging is not a direct averaging method. Instead, it determines the uniform flow state that would result if all non-uniformities were perfectly mixed at constant area, while conserving mass, energy, and momentum. This approach provides the most physically consistent representation of a possible end state, but it also reflects the performance degradation associated with irreversible mixing losses [3]. Consequently, mixed-out averaging is the most meaningful measure of the flow conditions that would interact with downstream components [9]. However, in flows with heat transfer as well as with changes in cross-sectional area, the mixed-out end state represents a theoretical equilibrium that cannot actually be reached. Comparison between end states would introduce bias depending on the local entropy of the flow due to heat transfer. For this reason, mass-flow averaging is preferred over mixed-out averaging. Although not accounting for irreversible mixing effects, it provides the most representative instantaneous averaged values of the flow.

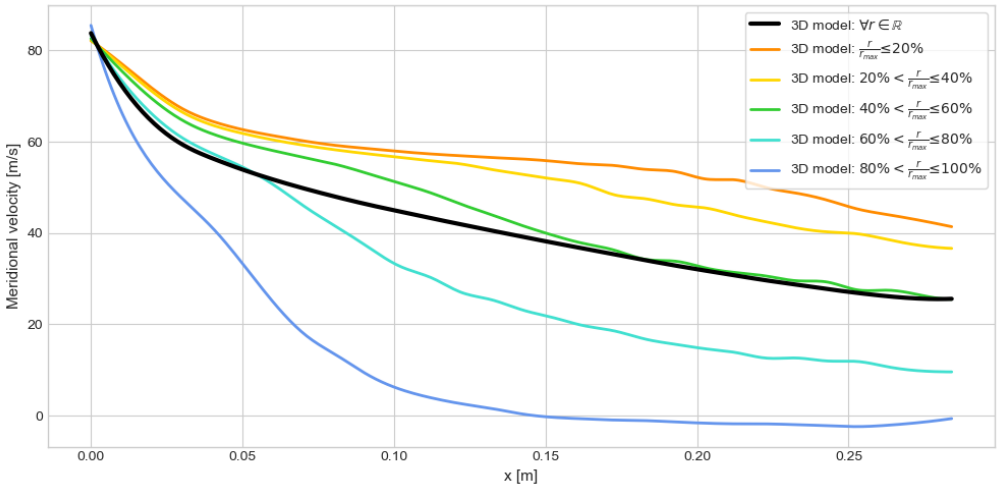

Figure 4.18: 3D meridional velocity variations per radial segment for the existing ORCHID turbine diffuser with recuperation.

As expected, Figure 4.18 shows how the meridional velocity (or axial velocity as for the case of the diffuser) decreases the closer to the wall. Additionally, a clear change in the velocity gradient can be noticed for all segments after separation occurs. While flow closed to the wall reaches negative values, centered flow behaves as if the flow expansion effect is reduced, thus the decrease in overall velocity is reduced.

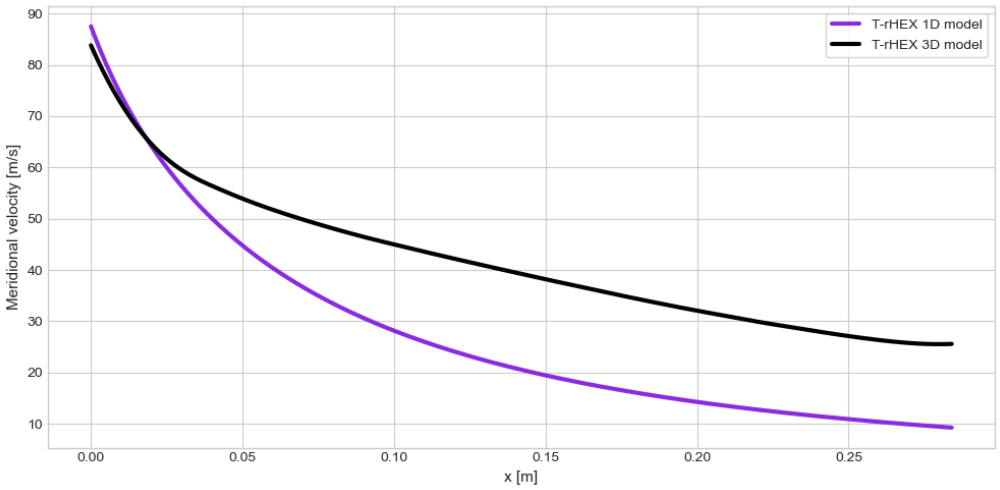

Figure 4.19: Meridional velocity comparison between 1D and 3D diffuser models along the existing ORCHID turbine diffuser with recuperation.

Comparing the 1D and 3D results shows similarities in flow expansion at the inlet before separation effects start to play a role. Once the flow separates, it is clear that the effect of flow expansion is reduced, leading to a higher exit velocity. While the low fidelity (1D) model predicts a 89.5% velocity reduction, the high fidelity (3D) model only predicts 68.5% velocity reduction. Similarly, in the case of adiabatic diffuser flows, the low fidelity (1D) model predicts a 89.3% velocity reduction, while the high fidelity (3D) model predicts a 67.2% velocity reduction. Overall, diffuser velocity characteristics can be summarized by the importance of separation on flow characteristics, for this reason the low fidelity model overpredict velocity reduction across the diffuser.

4.2.3. Diffuser Temperature

Temperature is the main drive of heat exchange. In order to ensure precision, both fluid streams bulk temperature need to be estimated with good accuracy. The high fidelity model (high fidelity (3D) model) results present radial variations within the temperature field. These are not available in the low fidelity (1D) model.

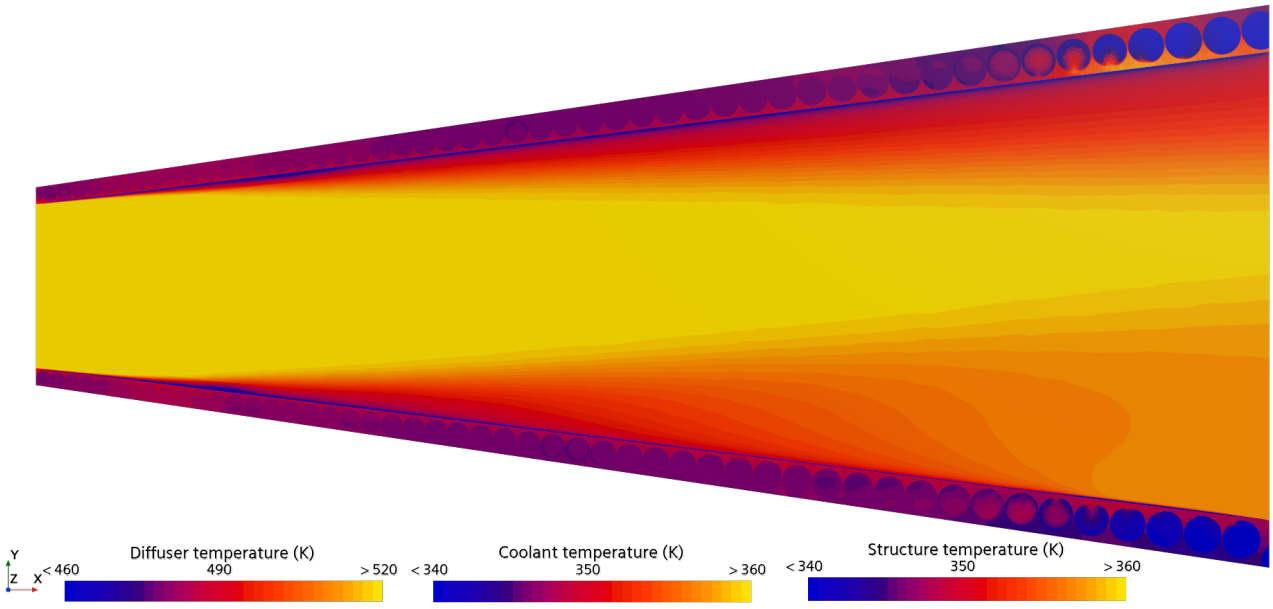

Figure 4.20: Temperature contours of the existing ORCHID turbine diffuser with recuperation.

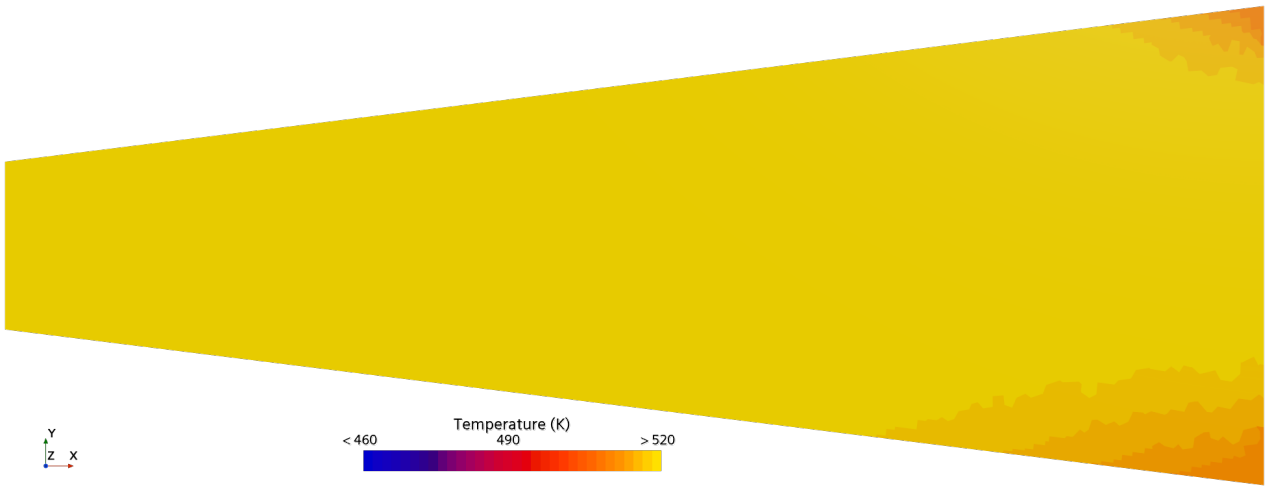

Figure 4.21: Temperature contours of the adiabatic existing ORCHID turbine diffuser.

As seen in Figure 4.20, the main core of the diffuser flow remains constant in temperature while close to the walls, temperature is significantly decreased. This effect is referred to the development of a thermal boundary layer. While the top surface resembles similarities to the momentum boundary layer, the bottom surface shows strong dissimilarities due to the separation bubble. The separation bubble acts as an insulation layer, preventing cooling between the bulk diffuser flow. This is reflected in the temperature field by a decrease in radial temperature gradients within the separation region. In terms of heat transfer, reduced temperature gradients are an indicator of poor heat transfer between the structure and the diffuser flow.

In comparison, the temperature field for the adiabatic diffuser is more uniform. While static temperature rise is small, Figure 4.21 only shows decreasing temperature close to the exit at regions of lowest momentum. These are likely due to the numerical error introduced by the outlet boundary condition. Overall, it is clear that the adiabatic diffuser can be represented by an approximately uniform temperature gradient while the cooled diffuser must account for the strong radial temperature gradients.

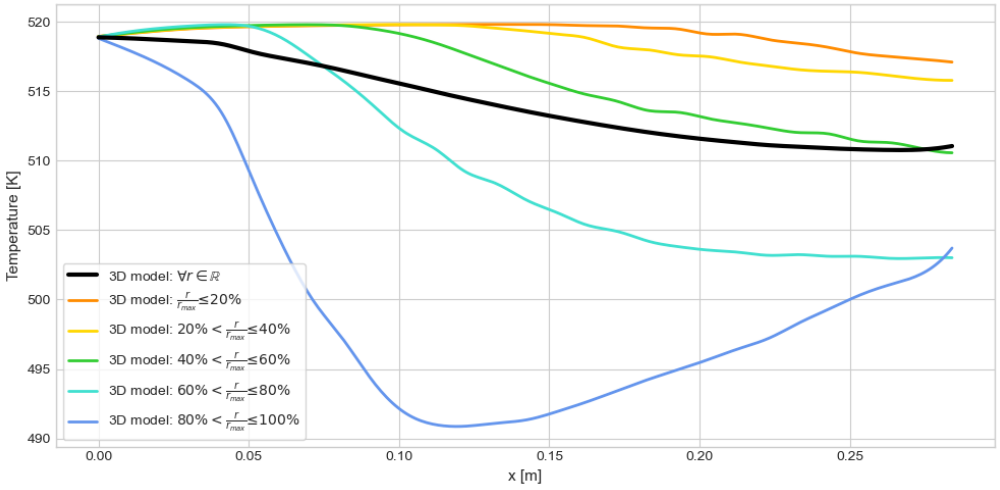

Figure 4.22: 3D temperature variations per radial segment for the existing ORCHID turbine diffuser with recuperation.

Temperature gradients can also be analyzed by means of segmenting the domain into radial segments. Temperature values are averaged using a mass flow averaging technique (as described for Figure 4.18). As seen in Figure 4.22, while segments close to the axial (center) axis of the diffuser gain slightly static temperature due to flow expansion, the wall bounded flow sees a significant decrease in temperature due to cooling. As flow progresses along the diffuser, cooling starts to propagate towards flows near the center axis. In addition, the separation bubble effects are also reflected on Figure 4.22, as the wall bounded flows sees a net increase

in temperature once the flow has separated. This matches the temperature contours shown in Figure 4.20.

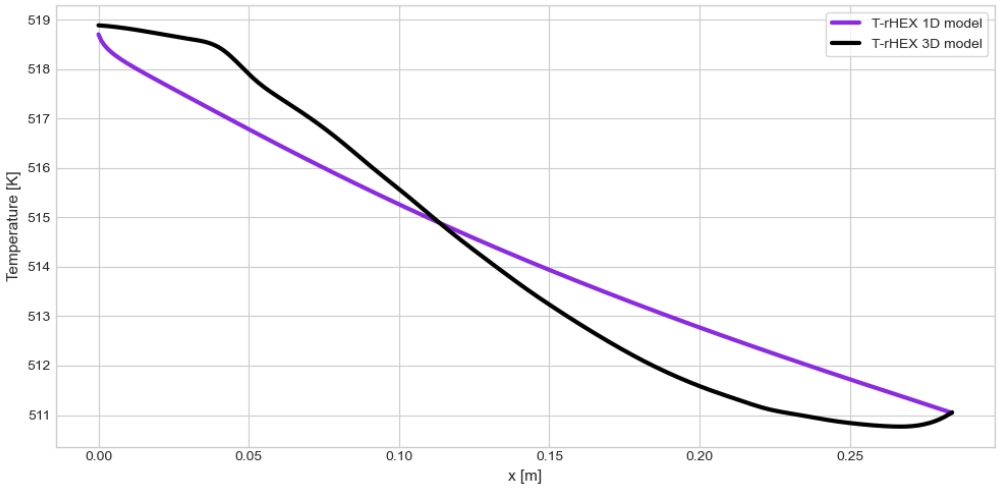

Figure 4.23: Temperature comparison between 1D and 3D diffuser models along the existing ORCHID turbine diffuser with recuperation.

Comparing the low fidelity (1D) model diffuser flow to the high fidelity (3D) model, diffuser flow shows similarities and differences. While the low fidelity (1D) model does predict well inlet and outlet conditions, the temperature gradients differ. Firstly, the low fidelity model overpredict inlet heat transfer as the temperature gradient is steeper. After the inlet effects, temperature drop of the high fidelity model is greater than the low fidelity model, likely due to underestimation of heat transfer. At the outlet, separation reduces heat transfer rate, thus temperature stalls. Overall, the low fidelity (1D) model and the high fidelity (3D) model exhibit similar temperature decrements, these being 1.5% and 1.6% respectively. However, Figure 4.23 shows that further improvement can be done in order to increase accuracy of the ow fidelity model.

4.2.4. Diffuser Pressure

Pressure is an important parameter for diffuser performance. For this high fidelity model, pressure is no longer assumed to be axisymmetric, and therefore solved in a 3D field alongside the previously discussed variables.

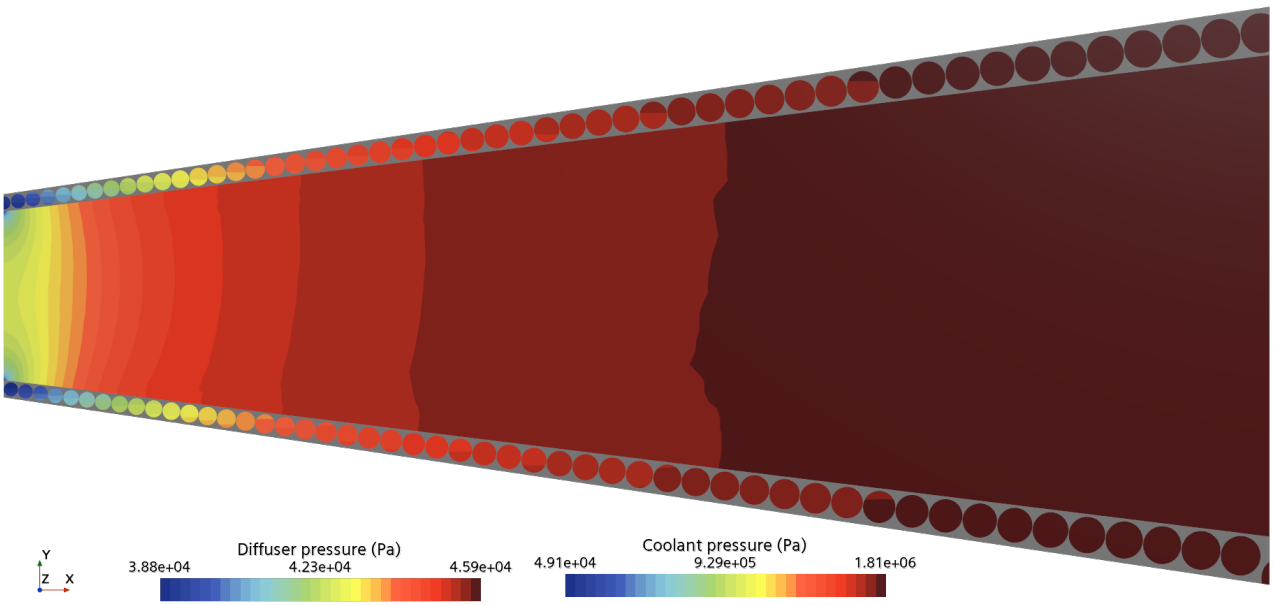

Figure 4.24: Pressure contours of the existing ORCHID turbine diffuser with recuperation.

Pressure results given in Figure 4.24 show how most of the pressure recovery occurs early on near the inlet of the diffuser. Additionally, radial pressure gradients are null, with the exception at the separation bubble, where isobar contours can be seen to shift. This is expected due to the local curvature of the streamlines within the recirculation region. However, the overall effect is small compared to the dominant axial pressure gradients.

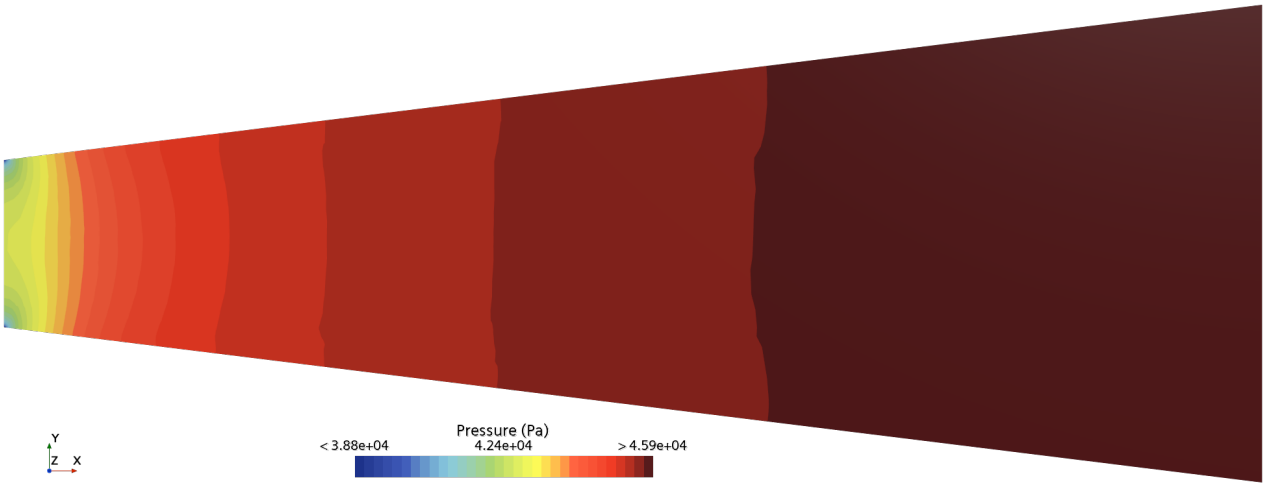

Figure 4.25: Pressure contours of the adiabatic existing ORCHID turbine diffuser.

Comparing adiabatic and cooled diffusers shows how pressure fields are almost identical, both fields showing almost no radial pressure variation. Figure 4.25 shows how the pressure field has higher symmetry compared to Figure 4.24 due to the interaction of the flow with the separated flow. However, the overall pressure recovery for the cooled diffuser is higher than for the adiabatic diffuser. The diffuser pressure coefficients for the high fidelity (3D) model with coolant resulted in 0.737, while for the adiabatic high fidelity (3D) model resulted in 0.706. This increase in pressure recovery is associated both by the increase in total pressure due to cooling and by the improvements in stability of the boundary layer, reducing the effects of separation.

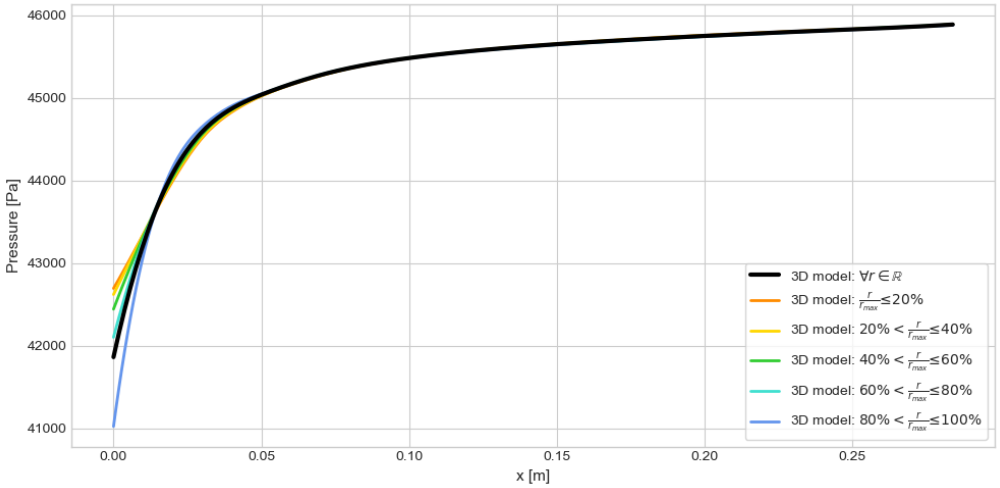

Figure 4.26: 3D meridional velocity variations per radial segment for the existing ORCHID turbine diffuser with recuperation.

Figure 4.26 shows that radial pressure gradients in the diffuser are negligible. The small variations at the inlet arise from numerical adjustments in the boundary condition to enforce the prescribed mass flow rate. Overall, the pressure field is dominated by axial gradients.

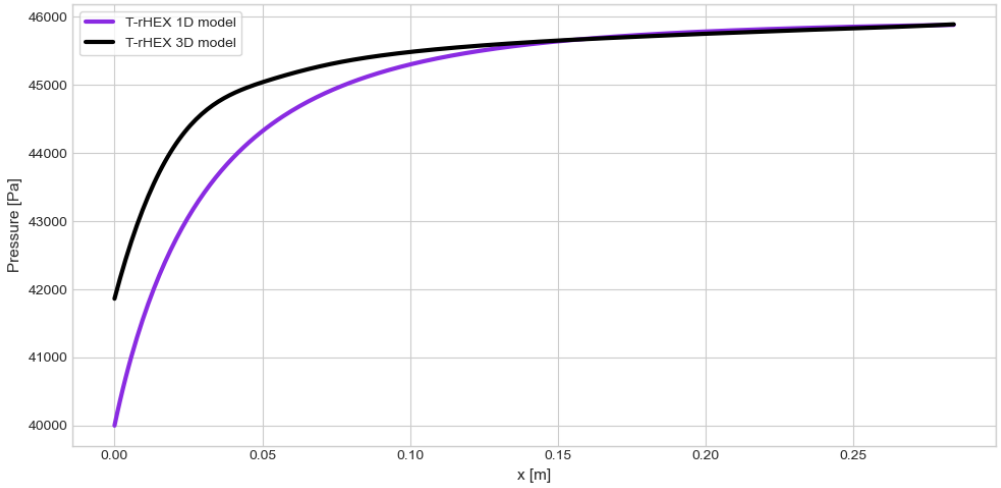

Figure 4.27: Meridional velocity comparison between 1D and 3D diffuser models along the existing ORCHID turbine diffuser with recuperation.

The comparison of low fidelity (1D) model and high fidelity (3D) model results shown in Figure 4.27 shows an important deviation. The initial pressure difference is to do with the scaling of the pressure field when solving the Navier Stokes equation. In order to specify pressure, the outlet condition is specified (see subsection 4.1.2). This leads to inconsistent initial conditions between the low fidelity (1D) and high fidelity (3D) models. Instead, results can be analyses from a qualitative point of view. Comparing the pressure gradients near the inlet, it can be seen that the low fidelity (1D) model solver predicts well changes of pressure due to area change with both friction and heat transfer. However, once the flow is separated, the pressure recovery for the diffuser for the high fidelity (3D) model is reduced. This results in a static pressure rise of 9.9% compared to 14.7% from the low fidelity (1D) model. Considering adiabatic results, the low and high fidelity model results predict static pressure rise of 9.3% and 14.6% respectively. This comparison leads to once again cooling providing a small but consistent pressure recovery benefit regardless of the flow conditions of the diffuser.

The dominant total pressure gradients are in the radial direction (see Figure 4.28). This is to be expected due to the influence of friction and heat transfer at the walls. Close to the inlet, the friction is the highest due to the high inlet velocity, leading to total pressure losses. As the flow decelerates, frictional effects diminish, and heat transfer effects become increasingly dominant in determining the total pressure variation.

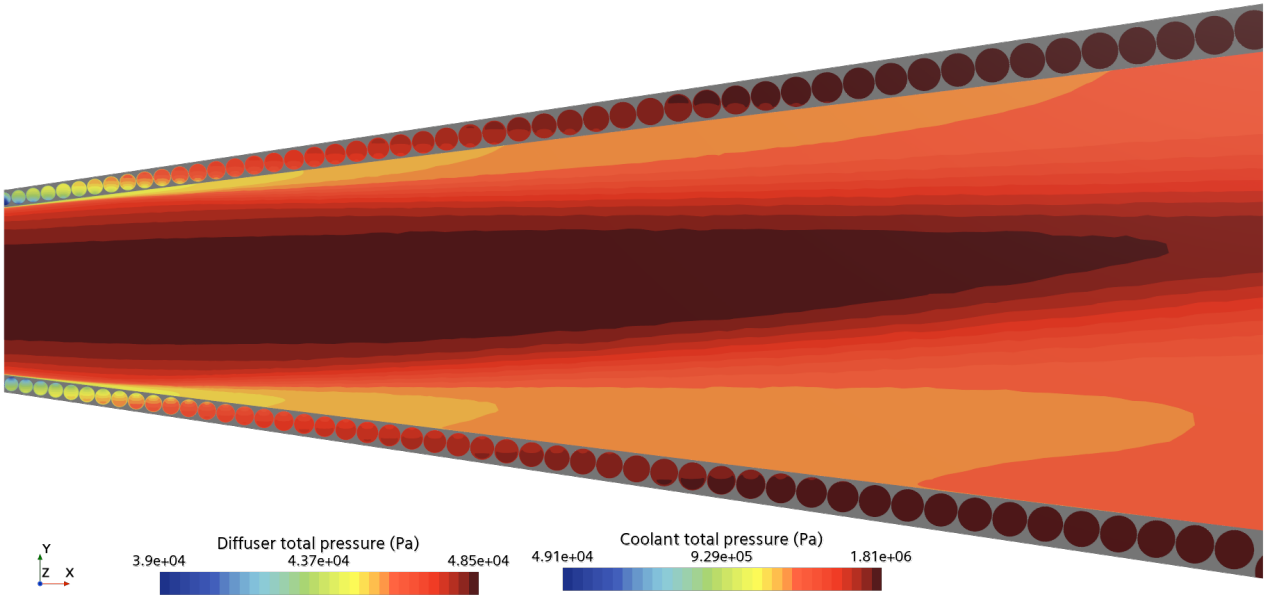

Figure 4.28: Total pressure contours of the existing ORCHID turbine diffuser with recuperation.

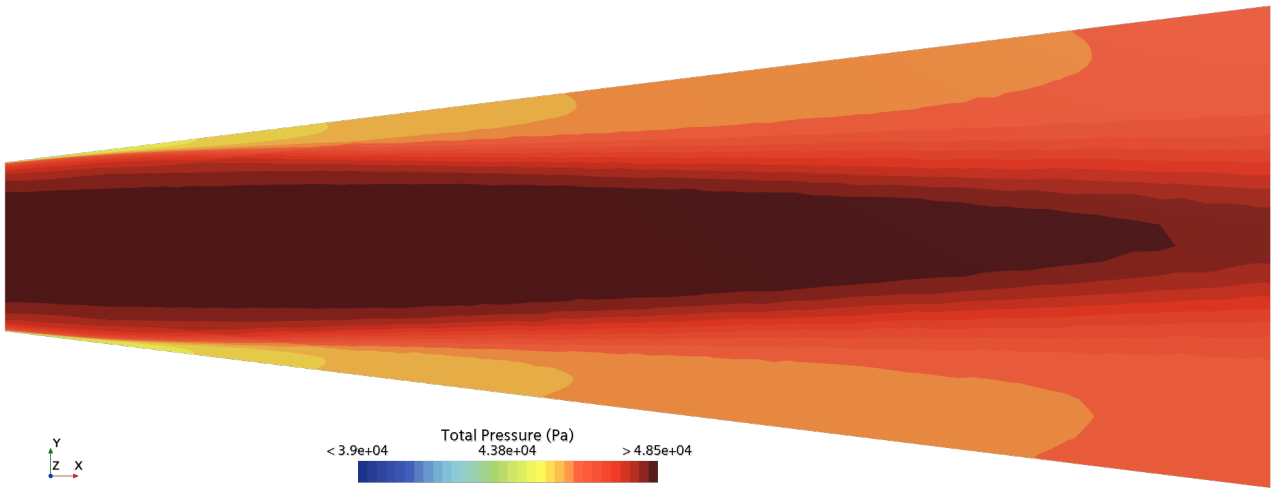

Figure 4.29: Total pressure contours of the existing adiabatic ORCHID turbine diffuser.

As shown by the comparison between Figure 4.28 and Figure 4.29, the total-pressure contours are nearly identical. Near the wall, the adiabatic case exhibits slightly lower total pressure than the cooled wall case, consistent with the expected total pressure increase due to cooling. Overall, the cooled diffuser shows a 2.0% total pressure reduction, compared to 2.4% for the adiabatic case, indicating that heat transfer has a small but measurable effect in increasing total pressure across the diffuser.

4.2.5. Coolant Velocity

The coolant channel flow undergoes a significant acceleration as a result of the decreasing cross sectional area. However, the effect of flow convergence is limited, while other external factors may play a role. Figure 4.9 shows that meridional and radial velocity variations are both relevant, with variations increasing at higher coolant bulk velocities.

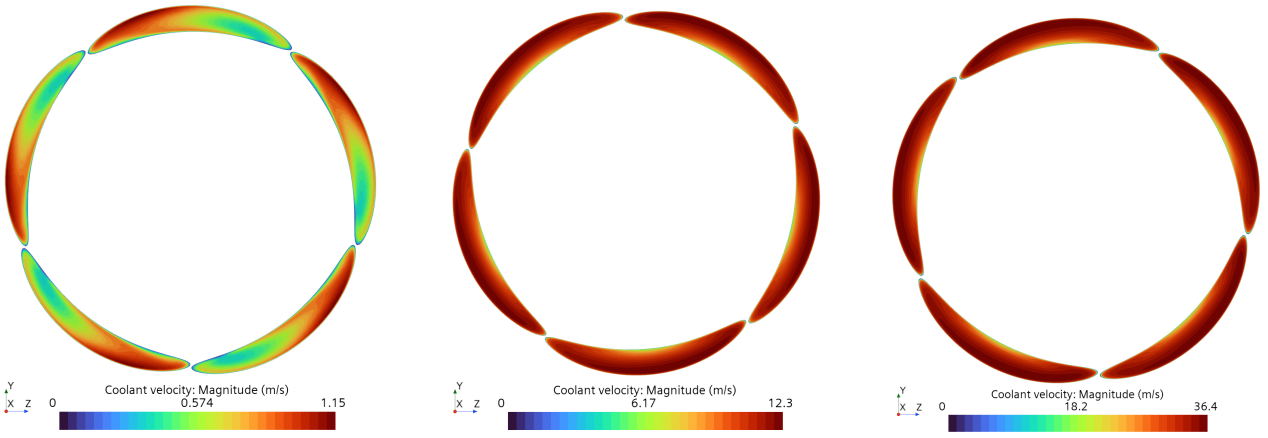

(a) Radial plane view at 5% coolant length. **(b)** Radial plane view at 50% coolant length. **(c)** Radial plane view at 95% coolant length.

Figure 4.30: Comparison between coolant channel velocities contours at different axial locations of the existing ORCHID turbine diffuser with recuperation.

Figure 4.30, illustrates radial variation of velocity within the channel as well as the bulk velocity increases as the coolant approaches the channel exit. Near the inlet, the velocity profile is undeveloped, showing a transition between the uniform flow from inlet conditions to the helicoidal path. As the flow progresses, viscous effects near the walls and by curvature induced centrifugal forces develop a velocity profile within the coolant, maintained along its complete length. The centrifugal effects due to helicoidal motion shifts the fluid toward the outer wall. This leads to two main consequences: the velocity profile no longer counterbalances the radial

pressure gradient, and curvature driven secondary flows, such as Dean vortices, are generated.

To analyze radial variations within the coolant channel the domain is divided in the radial direction. Unlike the diffuser where the division is based on the central axis to capture axisymmetric flow behavior, the coolant channel is divided according to radial position to distinguish between flow characteristics near the inner and outer walls. This approach is necessary because the coolant channel does not exhibit axisymmetric behavior due to its helicoidal path and the strong differences in heat transfer between the inner and outer walls.

Additionally, as in coolant results displayed in chapter 3, the results are displayed with respect to the recuperator length. This implies that the coolant flow travels from right (exit of the diffuser) to left (inlet of the diffuser).

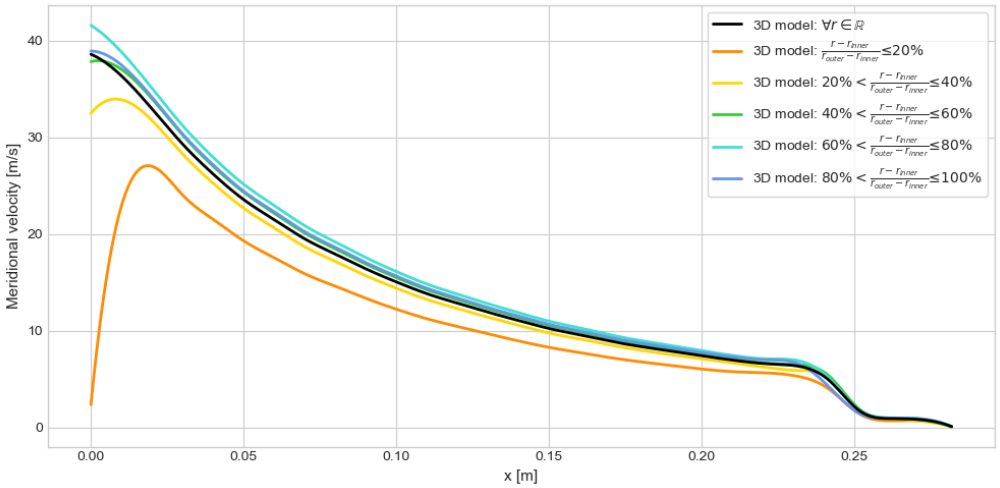

Figure 4.31: 3D meridional velocity variations per radial segment for the coolant flow of the existing ORCHID turbine diffuser with recuperation.

Radial gradient of velocity can be analyzed in Figure 4.31. Globally, flows closer to the outer wall experience a higher velocity than flows closer to the inner wall due to the outwards shift in momentum. In addition, viscous effect due to friction can also be noticed as the velocity decreases with respect to neighboring radial segments. Overall, the coolant flow increases in velocity due to the reduction in cross-sectional area. Furthermore, since the curvature ratio is fixed while the bulk flow Reynolds numbers increases, the effect of centripetal forces on coolant secondary flows increases.

In order to quantify the secondary flows present due to helicoidal motion, a non-dimensional Dean number (De) can be used as an indicator of inertial and centrifugal forces compared to viscous forces. This allows to quantify the effect on centrifugal forces on the flow, and measure the effect of secondary flows due to centrifugal forces. As the flow shifts towards the outer wall of the coolant channel, the vacant gaps are filled by fluid recirculating through the slower moving boundary layers. This results in two counter-rotating vortices known as the Dean vortices.

$$De = Re\sqrt{\frac{d_{\text{channel}}}{d_{\text{curvature}}}} = Re\sqrt{\delta_{\text{curvature}}} \tag{4.4}$$

As the low fidelity (1D) model predicts a Dean number across the complete coolant channel higher than the fully turbulent threshold (De>400), secondary flows in the coolant channel can be considered to be relevant. As the centrifugal force in Figure 4.32 pushes the fluid downwards towards the outer wall, fluid recirculates through the side walls upwards, creating two counter-rotating vortices. This secondary flow redistributes meridional momentum into tangential momentum (swirl). The swirl component may benefit heat transfer between the coolant flow and the solid structure. This is investigated in subsection 4.2.8.

In terms of radial variations, the effect of secondary flows increases proportionally with Reynolds number (given the fixed curvature ratio). As the velocity increases, the centrifugal effects play a larger role, leading to higher radial variations in velocity between the inner and outer coolant channel walls.

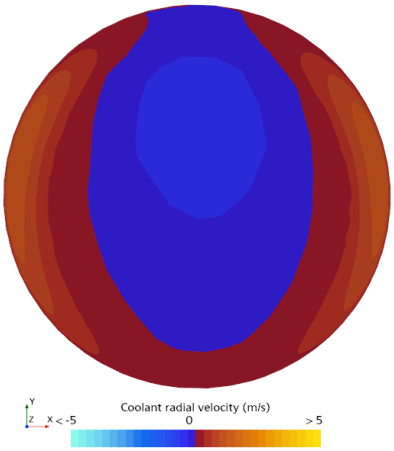

(a) Coolant channel radial velocity (u_r) contours due to centrifugal forces.
Orientation: Centrifugal forces act downwards. The blue contours indicates flow towards outer wall while the yellow/red indicates recirculated flow away from the outer wall.

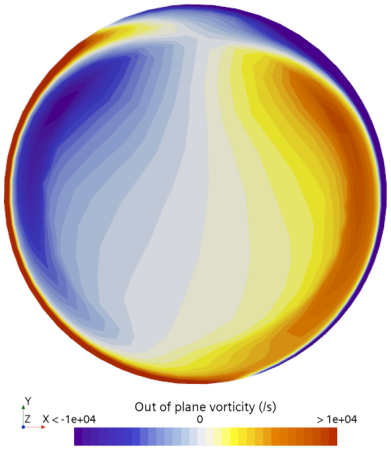

(b) Coolant channel vorticity contours due to centrifugal forces.
Orientation: Centrifugal forces act downwards. Out of plane vorticity is positive, while into the plane vorticity is negative.

Figure 4.32: Secondary flows within the coolant channel due to the effects of centrifugal forces.

In terms of bulk velocity of the coolant, the averaging based on mass flow puts more weight on regions with higher momentum flux more towards the average. This leads to a bulk velocity higher than the area averaged velocity, which could include a slight overestimation. For comparison, the low fidelity results are compared to the high fidelity results in Figure 4.33.

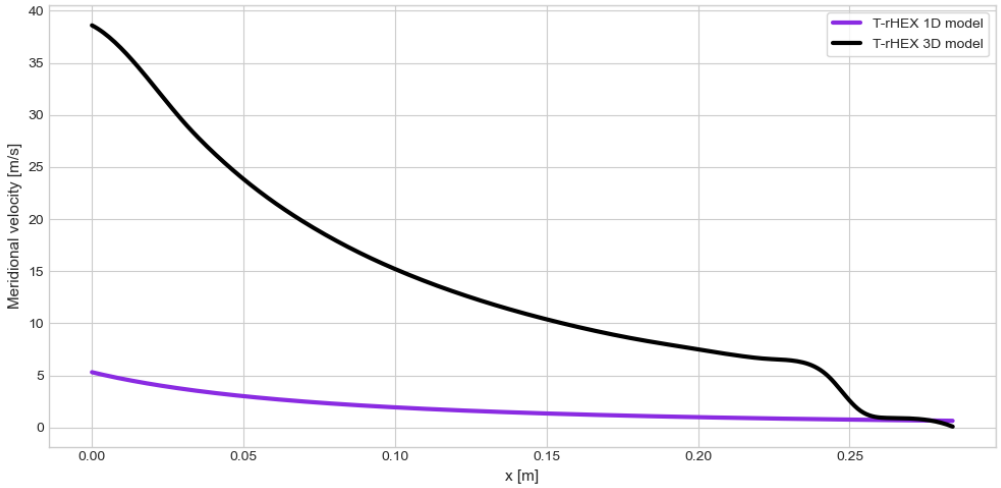

Figure 4.33: Meridional velocity comparison between 1D and 3D coolant models along the existing ORCHID turbine diffuser with recuperation.

Comparing the low fidelity (1D) model with the high fidelity (3D) model reveals a clear discrepancy. While the 1D model predicts only a modest increase in meridional velocity, the 3D model results show a much stronger flow acceleration. Such a pronounced difference cannot be fully attributed to averaging method bias and therefore indicates a more fundamental modeling issue.

Centrifugal forces play a role in shaping the velocity distribution, however the bulk velocity must be the same as for the low fidelity (1D) model due to mass conservation. Considering mass continuity, the change in velocity is proportional to changes in density and cross-sectional area. One of the possible discrepancies can be the geometry adaptation of the 1D model to the 3D model. However, as described in subsection 4.1.1, the geometrical error is minimal as coolant geometrical properties were directly derived from the low fidelity

model. Alternative, changes to density are derived from temperature. As is shown in subsection 4.2.6, these deviate from the low fidelity model but not enough to provide such a significant increase. The last possibility is numerical error being introduced, which leads to mass conservation imbalance.

To consider numerical error, the quality of the setup needs to be reconsidered. The coolant channel boundaries are on the same plane as the diffuser boundaries (see Figure 4.3). Having an outlet boundary at an angle far from orthogonal with respect to the coolant exiting flow direction can cause severe numerical error. While the software implemented has shown to be capable of handling well numerical instabilities, the results may converge to non-physical solutions. Looking at the coolant exit boundary in Figure 4.31, the velocity unexpectedly decreases. This non-physical phenomena shows that the quality of the coolant channel boundary conditions introduces numerical error into the solution.

The combination of boundary condition errors with the poorly refined coolant channel mesh lead to inconsistencies in mass continuity. Mass imbalance in CFD can arise from poor convergence, numerical instabilities, mesh quality, inconsistent boundary conditions, or non-physical initial conditions [15]. As described in subsection 4.2.1, continuity convergence is considered sufficient. Furthermore, the domain is initialized with the results from the low fidelity (1D) model, thus cannot be considered to be non-physical. Some small numerical instabilities are found close to the coolant outlet boundaries. However, it is believed that the source of the mass imbalance is the combination of poor inlet and outlet boundary conditions, combined with the use of a poorly refined mesh. As a result, the inlet undergoes an increase in convective flux, leading to higher mass flow rate than original, which leads to an over prediction of coolant velocity. Unfortunately, this discovery was found late during postprocessing, thus no additional modifications to the simulation could be performed given the time limitations of the thesis study. This includes the coolant results for the optimized T-rHEX as well.

Overall, although the absolute value of the high fidelity (3D) model results cannot be considered more accurate than the low fidelity, the general characteristics of the flow can be useful to understand flow behavior that is not captured within the low fidelity (1D) model.

4.2.6. Coolant Temperature

The coolant bulk temperature increases along its path. Figure 4.20 as shows how the temperature of the structure follows closely the temperature of the coolant channel. The structural interface between the diffuser wall and coolant walls shows an intermediate temperature between diffuser flow temperature and coolant temperature, closer to the coolant temperature than diffuser temperature. This indicates the heat transfer coefficient of the coolant to be much bigger than the diffuser heat transfer coefficient, allowing for small temperature differences between the coolant and the structure compared to diffuser and structure. This matches the results of the low fidelity (1D) model (see Figure 3.19) as well as the heat transfer coefficients of the high fidelity (3D) model (see subsection 4.2.8).

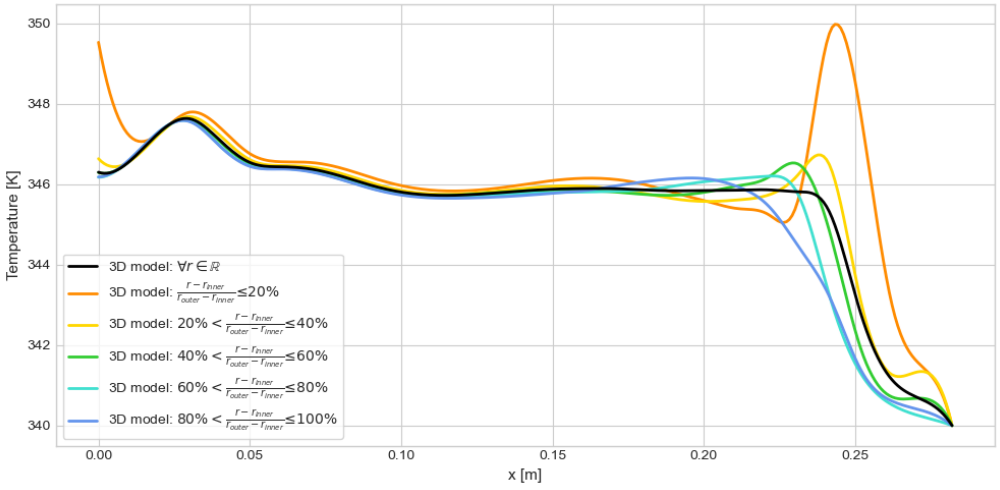

Figure 4.34: 3D temperature variations per radial segment for the coolant flow of the existing ORCHID turbine diffuser with recuperation.

Once again, segmenting the coolant channel radially allows us to compare different layers of the coolant chan-

nel in order to better understand heat transfer and centrifugal effects. Apart from the expected temperature increase, Figure 4.34 shows a unexpected temperature trend. As given in Figure 4.36, the low fidelity (1D) model predicts a more or less linear temperature gradient. However, this is not the case for the high fidelity (3D) model. Firstly, it can be seen in Figure 4.34 how radial temperature gradients are small. Temperature is almost always higher closer to the inner wall than to the outer wall. This is expected as heat flux enters through the inner wall into the coolant flow. Secondly, the complete coolant flow temperature profile results in a rapid temperature increase, followed by a slow temperature increase, and at the outlet a small temperature decrement. This unorthodox temperature distribution is also non-physical, specifically due to the rapid temperature spike at the inlet and the small decrement at the outlet.

Thermal inertia dissipates the temperature spike into other neighboring regions, damping out the thermal instability. To understand this spike, the mechanism of heat flux between the coolant flow and the structure surface needs to be considered. Conduction is dominated by temperature difference between the solid interface and the temperature of the closest cell belonging to the coolant fluid. While the temperature of the solid interface is determined by the solid coupled energy solver, the temperature closest to the solid interface is determined by the wall treatment model. As discussed in subsection 4.2.1, wall treatment is strongly dependent on mesh refinement. Since the coolant channel mesh is not specifically refined to a fixed y_+, the wall treatment model changes along the coolant channel.

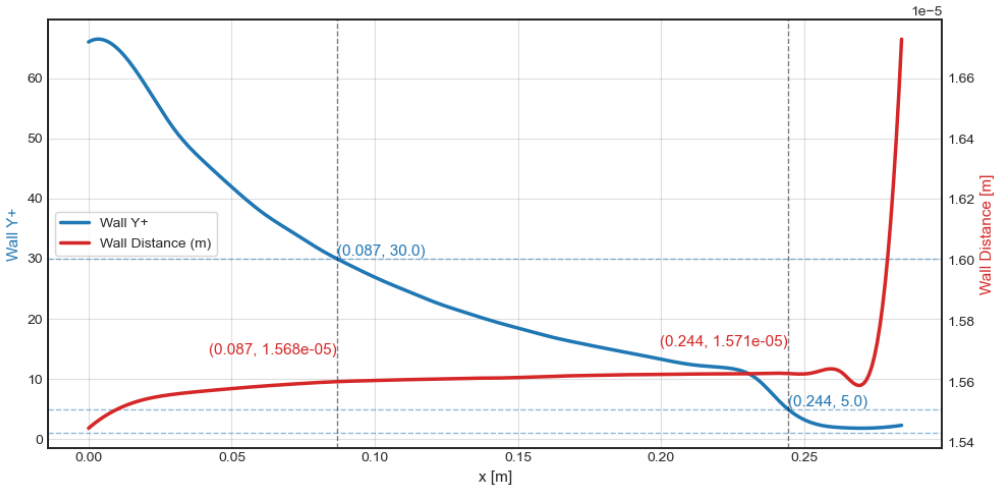

Figure 4.35: Comparison between wall y_+ and wall distance along the coolant channel of the existing ORCHID turbine diffuser with recuperation.

As seen in Figure 4.35, the wall distance decreases rapidly. This is because local y_+ values are small but vary, leading to fluctuations in wall distance prediction by the wall treatment model. Along the channel, as velocity increases, wall y_+ increases, thus the wall treatment model switches to a fully empirical model (high y_+ treatment). This fluctuation coincides with Figure 4.31 coolant velocity fluctuation, as well as Figure 4.34 coolant temperature fluctuations. Apriori, the temperature spike was linked to the change in wall treatment model, which has an effect in the local heat flux and shear stress predictions by the solver. However, after the conclusion on mass conservation imbalance close to the inlet, it can be concluded that both effects lead to a local increase in thermal inertia, leading to the given temperature spike. As the issue was previously linked to the wall treatment model, a decision to implement a more consistent wall treatment model is recommended. In Figure 4.77 (see section 4.3), it can be seen how the use of a constant wall treatment along the full length of the coolant channel allows for a more accurate heat transfer model between the solid and liquid interface.

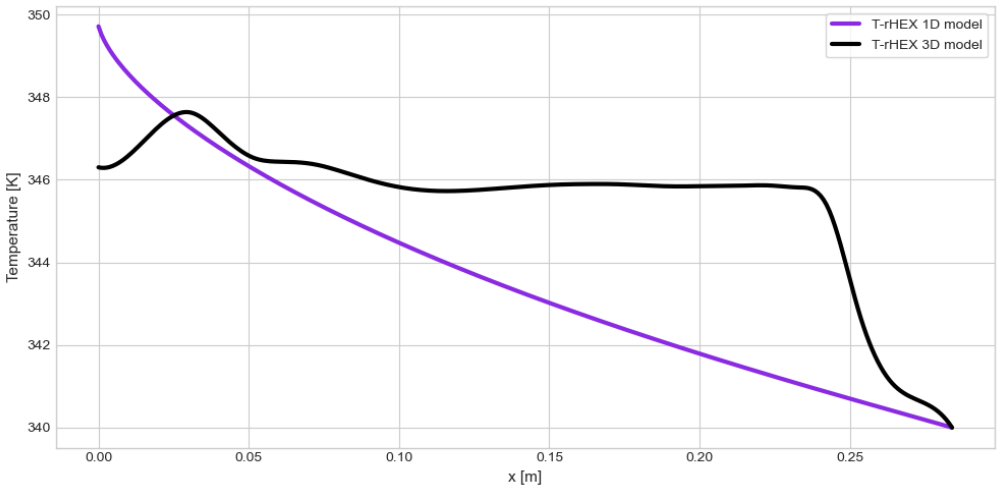

Figure 4.36: Temperature comparison between 1D and 3D coolant models along the coolant flow of the existing ORCHID turbine diffuser with recuperation..

Overall, the prediction of the coolant temperature is compromised. Comparing the low fidelity (1D) and high fidelity (3D) models in Figure 4.36 shows how temperature trends differ. Nevertheless, the global performance comparison in temperatures shows similarities. While the low fidelity (1D) model predicts a static temperature rise of 2.8%, the high fidelity (3D) model predicts a static temperature rise of 1.8%.

4.2.7. Coolant Pressure

The coolant channel experiences both a decrease in pressure along the meridional flow path as well as significant radial pressure gradients due to the strong curvature. Due to the arrangement of the recuperator in countercurrent flow, the coolant channel inlet has highest curvature radius, meanwhile the close to the outlet, the curvature radius is the smallest. Since radial pressure gradients are dependent on both curvature radius and bulk velocity ($\frac{\mathrm{d}p}{\mathrm{d}r} \approx \rho u_{bulk}^2 r^{-1}$), the radial pressure gradients increase along the coolant both due to velocity increase and due to the smaller curvature radius.

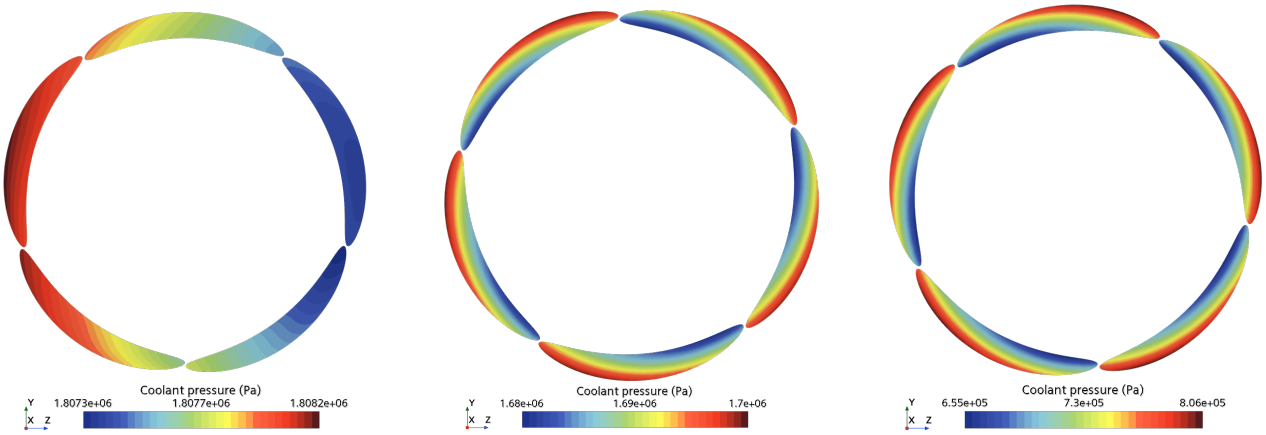

(a) Radial plane view at 5% coolant length. **(b)** Radial plane view at 50% coolant length. **(c)** Radial plane view at 95% coolant length.

Figure 4.37: Comparison between coolant channel pressure contours at different axial locations of the existing ORCHID turbine diffuser with recuperation.

With the exception of the inlet, where pressure is approximately constant, Figure 4.37 shows flows closer to the outer walls have higher pressure than flows closer to the inner wall due to centrifugal effects. Moreover, comparing the magnitude of radial pressure differences along the coolant displays how radial pressure gradients increase along the coolant channel. In addition, pressure gradients are also shown not to be perfectly radial. As the coolant channel travels counterclockwise around the diffuser, the effect of pressure losses due

to friction can be noticed by the shift in pressure contours.

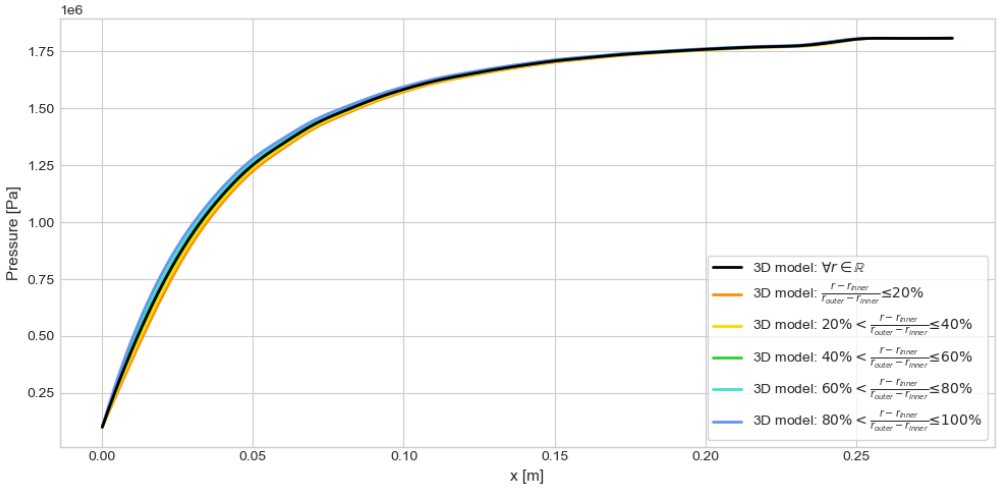

Figure 4.38: 3D pressure variations per radial segment for the coolant flow of the existing ORCHID turbine diffuser with recuperation.

Figure 4.38 confirms how radial pressure gradients increase along the coolant channel. Nevertheless, their effect can be considered negligible compared to the meridional pressure gradients. In terms of numerical error, the coolant pressure is specified by means of prescription of static pressure at the outlet. For this reason, the radial pressure difference decreases close to the outlet.

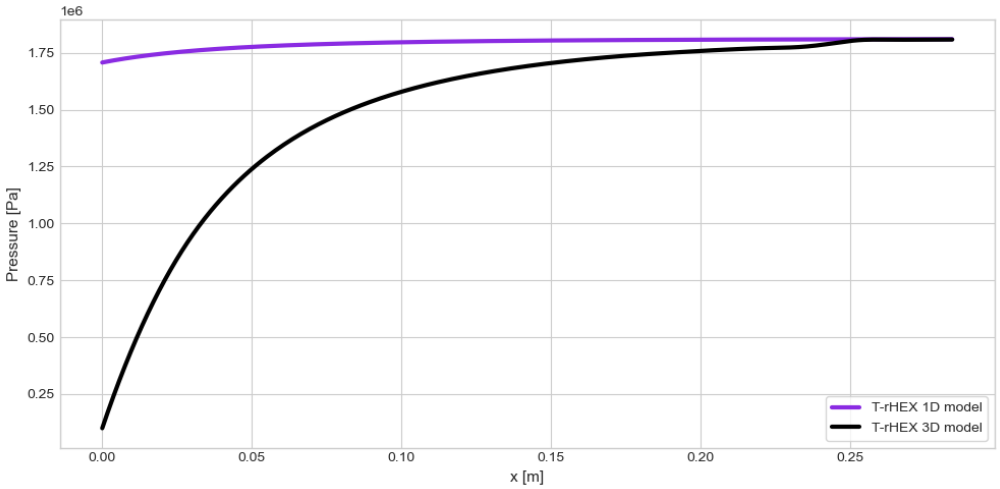

Figure 4.39: Pressure comparison between 1D and 3D coolant models along the coolant flow of the existing ORCHID turbine diffuser with recuperation.

Comparing low fidelity (1D) and high fidelity (3D) model shows how the 3D coolant channel experiences a larger pressure drop compared to the low fidelity (1D) model. Larger pressure drops imply that the pump power required increases in order to overcome such pressure drop. Pressure drops are to be avoided, as they reduce cycle efficiency by increasing pump power. As velocity increases significantly along the coolant channel, the dynamic pressure also increases, causing the static pressure to decrease. When this effect is combined with higher friction losses, the pressure drop difference between the models becomes larger. While the low fidelity (1D) model predicts a coolant channel pressure drop of 5.6%, the high fidelity (3D) model predicts a pressure drop of 94.5%.

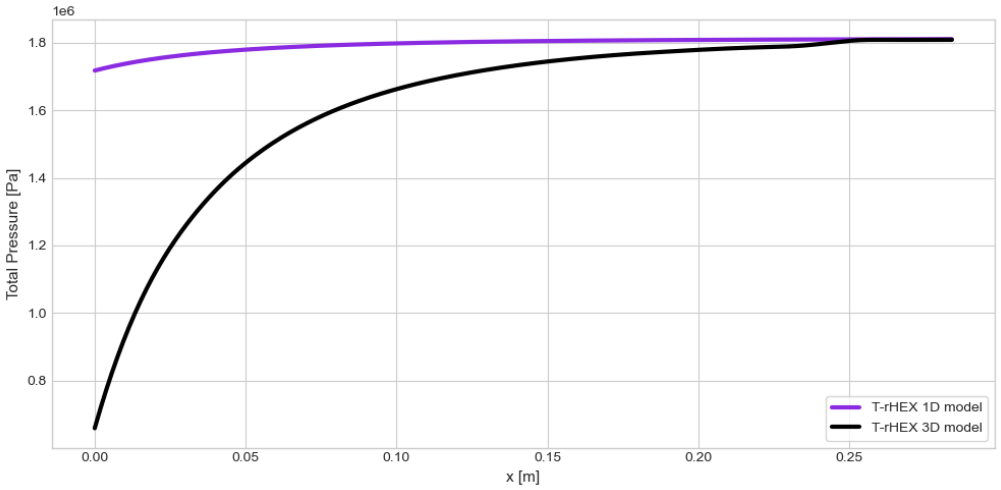

Figure 4.40: Total pressure comparison between 1D and 3D coolant models along the coolant flow of the existing ORCHID turbine diffuser with recuperation.

To better understand the causes of the high pressure losses, total pressure results are examined. Total pressure is influenced by both friction and heating, each contributing to a decrease in total pressure. Although the thermal power is found to be similar between the low fidelity (1D) and high fidelity (3D) models (see Table 4.2), the frictional effects differ significantly. As shown in Figure 4.40, the high fidelity (3D) model predicts a much larger total pressure drop compared to the low fidelity (1D) model. As the bulk velocity of the coolant increases, friction also rises, resulting in greater total pressure losses. While the low fidelity (1D) model predicts only a 5.1% total pressure drop, the high fidelity (3D) model predicts a 52.1% drop. The combination of such a large total pressure loss and the increase in dynamic pressure leads to a substantial static pressure drop as shown in Figure 4.39.

4.2.8. Heat transfer

Having examined the performance of each individual component, the overall performance of the recuperator is now evaluated. The transport of heat in a 3D heat transfer problem is driven by conduction and radiation. Convection instead is a concept accounting for the ability of the fluid to transfer heat within a fluid. Convection is then measured based on the heat flux and the fluid dynamics solution provided. At low temperatures such as for this case, radiation is negligible. Thus conduction between the fluid and solid walls becomes the primary heat transfer mechanism. Conduction models implemented are based on a finite volume diffusive flux equation, accounting for temperature difference between wall and neighboring cells as well as distance between cells and the wall[15]. The simplified steady wall bounded heat transport equation is solved in cells near the wall, where a source term is added in order to account for heat transfer from the wall. Naturally, heat introduced locally is then transferred to neighboring cells by convective and diffusive transport.

Comparing the boundary heat flux of the higher fidelity (3D) model with that of the lower fidelity (1D) model, the overall profiles appear similar. While at the inlet of the diffuser, the low fidelity model overestimates heat transfer, the second half of the diffuser achieves higher heat transfer than predicted by the low fidelity model.

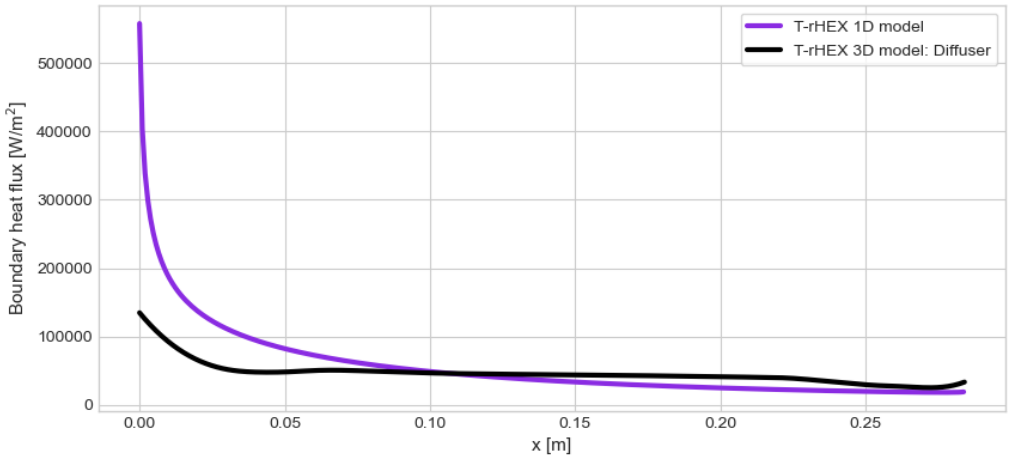

Figure 4.41: Comparison of the heat flux across the diffuser wall between low fidelity (1D) and high fidelity (3D) models along the existing ORCHID turbine diffuser with recuperation.

Comparing Figure 4.41 to the separation bubble seen in Figure 4.9, shows that the separation bubble, did not decrease significantly heat exchanger performance. Instead, as the separation bubble only insulates the bottom region, the top region sees a net increase of flow velocity close to the walls due to the upward shift of the flow (as seen by the flattening of the velocity profile in Figure 4.18). This increases local convective transport term of the flow at the top wall where flow remains attached, yielding to a higher heat exchange rate compared to the case with no separation bubble, and to comparable results between the low and high fidelity models.

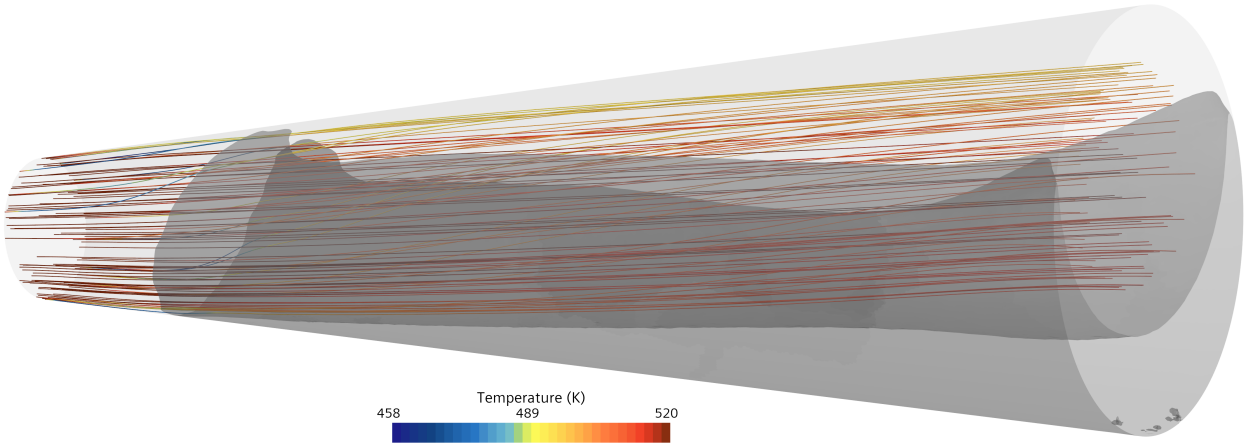

Figure 4.42: 3D visualization of the existing ORCHID turbine diffuser with recuperation displaying both temperature field on streamlines and the separation bubble contour.

By computing the streamlines of the diffuser flow, Figure 4.42 shows how there is an upwards shift in flow momentum towards the top surface. This effect is also seen in Figure 4.20 as the flow becomes less axisymmetric. The separation bubble generates a large region of recirculated flow, which limits diffuser flow expansion and acts as an insulating layer between the high temperature central bulk flow and the cooled walls.

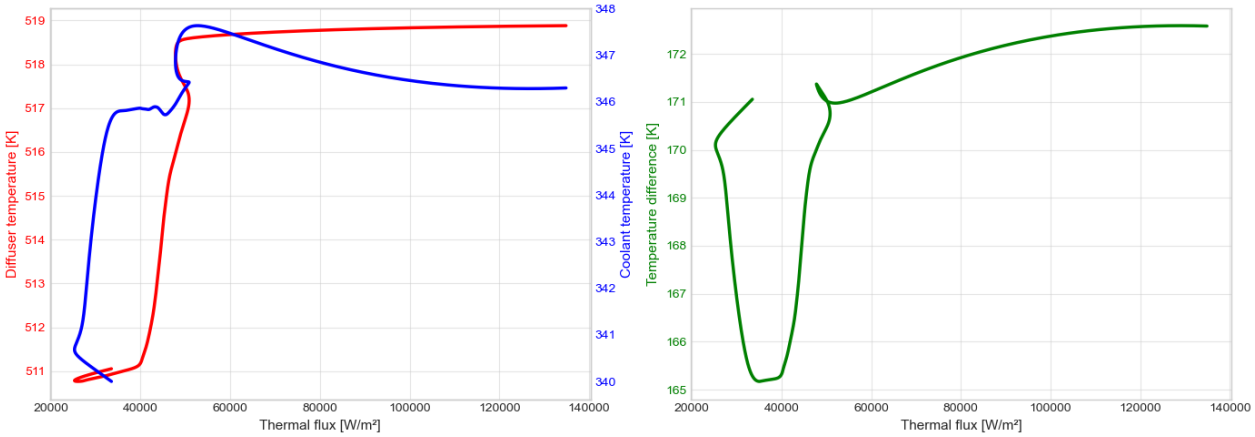

Figure 4.43: Thermal plots along the recuperator for the given existing ORCHID turbine diffuser with recuperation.

The temperature fields provide insight into how the temperature distribution drives the thermal gradient. In the low fidelity model the temperature difference between the two streams was found to be approximately constant with a range of$2\,\mathrm{K}$ (see Figure 3.15). In the high fidelity model, the range in temperature difference increases to about $7\,\mathrm{K}$, as shown in Figure 4.43. Despite this difference, the temperature variation along the channel can be once again approximated to a uniform value. Apart from the irregular temperature profiles in Figure 4.43 which arise from the coolant temperature spike near the inlet, the overall trends remains consistent with the low fidelity prediction. The highest heat flux occurs at the diffuser inlet, while the lowest values occur close to the diffuser outlet.

In order to compare convective heat transfer predictions between models, the convective heat transfer coefficient must be computed for the high fidelity (3D) model.

$$h_{c_{diffuser}} = \frac{< \dot{q}_{cond_{diffuser}} >}{< T_{diffuser} > - T_{wall}} \tag{4.5}$$

$$h_{c_{coolant}} = \frac{< \dot{q}_{cond_{coolant}} >}{T_{wall} - < T_{coolant} >} \tag{4.6}$$

To compute the convective heat transfer coefficients, the domain is divided into axial intervals. Within each interval, flow and thermal properties are averaged using either mass flow weighting or area weighting depending on the quantity. The conductive heat flux is averaged over the local wetted area to obtain the sectional mean conductive flux ($< \dot{q}_{cond} >$). In contrast the bulk temperature is defined as the mass flow averaged fluid temperature ($< T >$).

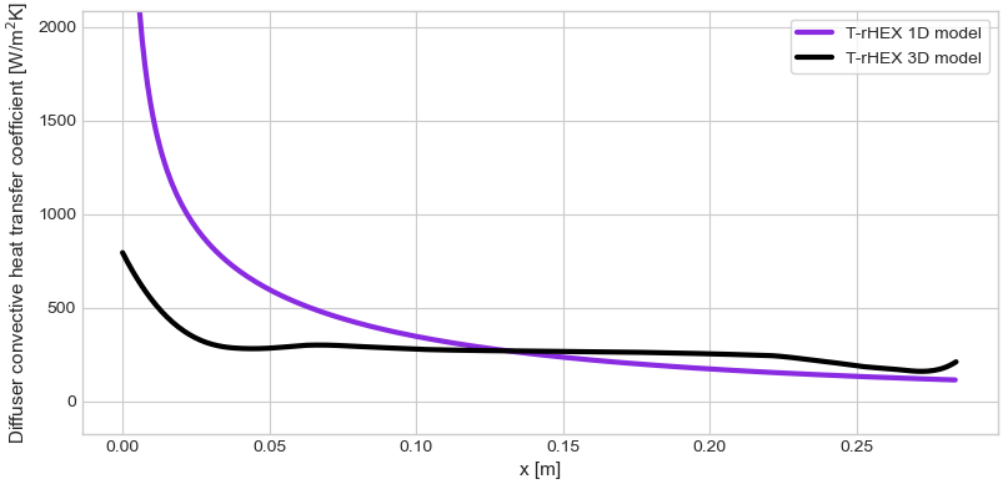

Figure 4.44: Comparison of the convective heat transfer coefficients between 1D and 3D diffuser models along the existing ORCHID turbine diffuser with recuperation.

As seen in Figure 4.44, the trend of convective heat transfer along the diffuser is similar between the low fidelity (1D) and high fidelity (3D) model. The boundary layer development effects at the inlet differ substantianlly, as the low fidelity (1D) model results overpredict convective heat transfer. The low fidelity (1D) model inlet spike is deemed unrealistic, likely caused by how the low fidelity (1D) model implements diffuser length to account for developing effects within the diffuser. Past the inlet, the high fidelity results predict a more constant convective heat transfer coefficient. This expected as, due to separation, the exposed surface (diffuser surface outside the separation bubble) sees a flow velocity higher than for the attached flow case. This creates a higher convective heat transfer rate at the top surface of the diffuser while the bottom surface sees a reduced heat transfer rate. Overall, the high fidelity model shows how inlet effects are over predicted by the low fidelity model, while 3D effects such as separation can indirectly lead to favorable heat transfer conditions.

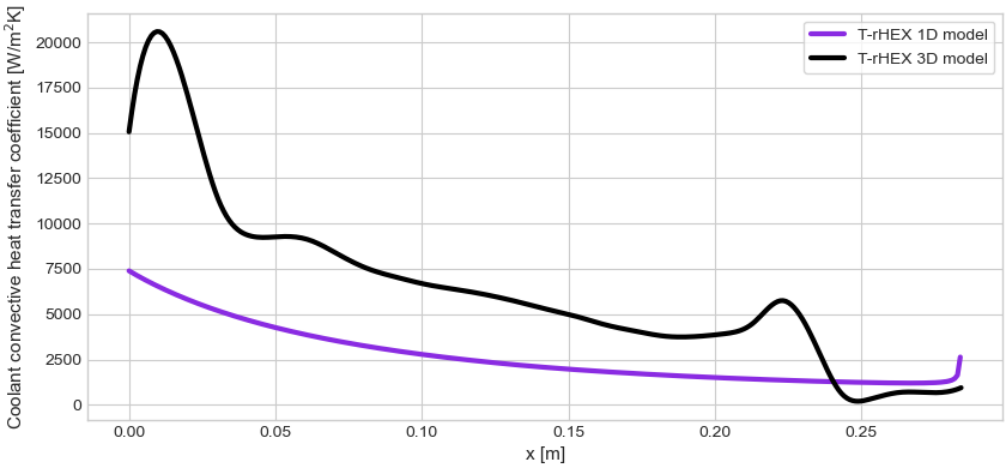

Figure 4.45: Comparison of the convective heat transfer coefficients between 1D and 3D coolant models along the the existing ORCHID turbine diffuser with recuperation.

Given that the coolant channel predicts non-physical temperature spikes and mass continuity imbalance, the accuracy of the convective heat transfer coefficient is compromised. As seen in Figure 4.45, the trend does not follow a smooth line such as the low fidelity (1D) model. Instead, the high fidelity (3D) model follows closely the shape of the coolant velocity trend (see Figure 4.31). This is expected as the convective heat transfer is directly proportional to the Reynolds number, itself dependent on the fluid velocity.

Overall, the low fidelity diffuser convective heat transfer model performs reasonably well, although the model require improvements to reduce the influence of boundary layer development effects at the inlet. Three dimensional phenomena such as separation cannot be captured by the low fidelity model, and the introduction of a separation criterion would allow assessment of when quasi-1D predictions remain valid and when heat transfer results would vary in comparison to higher fidelity models. Due to coolant channel mesh limitations, a quantitative comparison of convection between models is not meaningful. A qualitative comparison nevertheless shows a strong correlation between local velocity and heat transfer. The elevated bulk velocity and resulting secondary flows in the high fidelity model likely lead to an over prediction of convection relative to the true behavior. This would explain the increase in coolant convective heat transfer with respect to the low fidelity model.

4.2.9. Friction

Another major aspect of recuperator modeling is friction. As previously discussed in subsection 4.2.7, friction plays an important factor in fluid modeling. It is therefore of relevance to improve the friction low fidelity (1D) models to obtain results with higher accuracy.

To compare low fidelity (1D) model results to high fidelity (3D) model results, the Fanning friction coefficient (Equation 3.1) is computed. The wall shear stress in averaged using a wall surface area as weight for the averaging technique. This method allows for conservation of shear friction forces. On the other hand, both density and velocity are calculated using mass flow averaging.

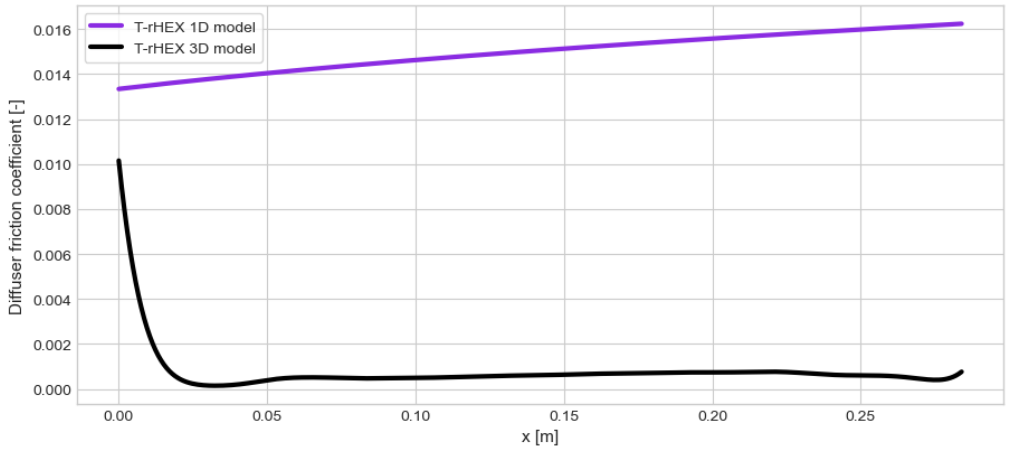

Figure 4.46: Comparison of the Fanning friction coefficient between 1D and 3D diffuser models along the existing ORCHID turbine diffuser with recuperation.

Figure 4.46 shows the low fidelity (1D) model overpredict diffuser friction compared to the high fidelity (3D) model. At the diffuser inlet, where fluid conditions are identical, the friction predicted by the low fidelity (1D) model is higher, showing the clear bias towards friction over prediction. Osnaghi's diffuser friction model implemented in the low fidelity model accounts for both skin friction and separation losses (Appendix B). Meanwhile, the high fidelity mode only predicts skin friction losses, neglecting the effects of separation or mixing. Given that the diffuser flow separates, the wall shear stress decreases significantly, thus resulting in low Fanning friction coefficient values.

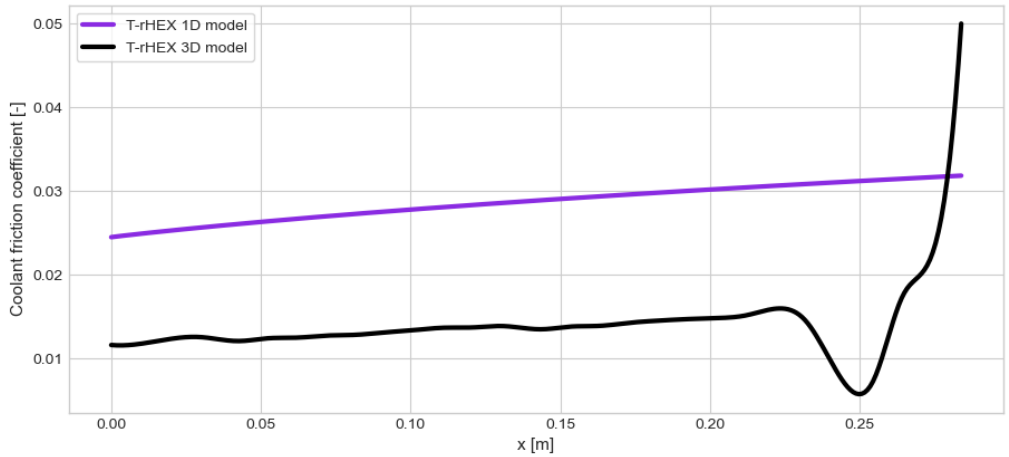

Figure 4.47: Comparison of the Fanning friction coefficient between 1D and 3D coolant models along the existing ORCHID turbine diffuser with recuperation.

The coolant channel friction follows the same general trend as the pipe-flow friction model used in the low fidelity model. Near the inlet, the choice of wall treatment strongly influences the predicted wall shear. Given the transition to a high y_+ wall treatment, the wall shear stress to be modeled rather than resolved. The modeled values show behavior qualitatively similar to the low fidelity predictions. The friction underprediction in the high fidelity model arises from two primary causes. Firstly, the geometric discretization artificially reduces curvature ratio, which reduces centrifugal effects and therefore weakens the secondary flows that would otherwise enhance wall shear for a given bulk velocity. Secondly, the artificial increase in coolant velocity raises the Reynolds number, which reduces the friction coefficient. The friction coefficient characterizes how wall shear scales with flow conditions, not the absolute magnitude of the shear. A lower friction factor does not mean the wall shear decreases, as the actual shear always increases with velocity increments.

Research Sub-Question RSQ3

How accurately does the low fidelity (1D) model predict the heat transfer performance of the T-rHEX recuperator compared to the high fidelity (3D) model?

To conclude the high fidelity modeling of the ORCHID diffuser as a recuperator, an overview table is given. Table 4.2 displays a comparison between adiabatic and regenerative cases, for both low fidelity (1D) and high fidelity (3D) models.

Table 4.2: Results comparison between low fidelity (1D) and high fidelity (3D) models for the existing ORCHID turbine diffuser with recuperation.

	Low fidelity (1D) model: adiabatic	Low fidelity (1D) model: recuperation	High fidelity (3D) model: adiabatic	High fidelity (3D) model: recuperation
Diffuser pressure coefficient [-]	1.007	1.014	0.706	0.737
Thermal power [W]	0	2921	0	2816
Required pump power [W]	0	21.5	0	345.9
Effectiveness [%]	0	8.36	0	7.89
Cycle efficiency [%]	12.11	12.53	12.06[1]	12.06[2]
Total volume [m^3]	0.00127	0.00173	0.00128	0.00184

In terms of diffuser performance, cooling is proven to increase pressure recovery for both low fidelity (1D) and high fidelity (3D) models. When accounting for 3D flow effects such as separation, pressure recovery decreases. While cooling also helps improve boundary layer stability and separation, it does not completely avoid it. The presented high fidelity (3D) model work assumed axial, turbulent free inlet conditions. However, addition of turbulent structure, such as rotor tip vortices can aid boundary layer stabilization [9]. To improve the low fidelity model, a separation criteria can be implemented to indicate when low fidelity (1D) model results may not be valid.

In terms of recuperator thermal performance, the low fidelity (1D) model slightly overpredicts heat transfer compared to the high fidelity (3D) model. Given the separation in the diffuser and the artificial temperature spike which reduced local heat flux (reduced temperature difference), the high fidelity (3D) model still provides good results. This shows that the concept of the T-rHEX is a beneficial design modification to the ORC WHR system. On the other hand, the coolant pressure losses differ significantly, as the high fidelity (3D) model predicts results an order of magnitude greater than low fidelity (1D) model results. In conclusion, while setting the original ORCHID turbine diffuser as a recuperator increases the cycle efficiency of the ORC, the coolant requires higher pump power to overcome pressure loses. It is believed that an improved low fidelity friction model together with an improved coolant channel mesh setup would enable a more realistic and optimized coolant channel design that could reduce pump power requirements while maintaining recuperated thermal power.

4.3. Results: Optimized ORCHID turbine diffuser as a recuperator

This section covers all results related to the optimized T-rHEX concept. Similarly to the ORCHID diffuser as a recuperator, the low fidelity (1D) results are used to build the geometry, and the same CHT setup is then applied to obtain the high fidelity model results. These results are to be discussed on their own before comparing them to the low fidelity model results.

4.3.1. Mesh refinement and convergence

The optimized T-rHEX implements 3 different regions, each with their individual mesh connected through in-place contact interfaces. These interfaces act as a static bound, transferring thermal properties from the

[1] This efficiency value does accounts for reduced back pressure effects. Without effects, value is 12.11%.

[2] This efficiency value is 12.061%, which is slightly reduced compared to the adiabatic efficiency of 12.058%. Also, these values accounts for reduced back pressure effects. Without effects, values are 12.107% and 12.113% respectively.

fluid regions to the solid and vice versa. For the given setup, the interface accuracies vary between the coolant-structure and diffuser structure interfaces, these being 98.5% and 99.9% respectively. The difference in accuracy is due to changes in mesh quality required to accommodate the higher overall cell count.

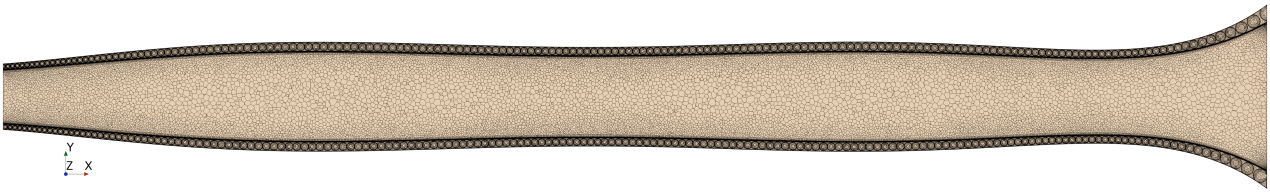

Figure 4.48: Cross-sectional view of the optimized T-rHEX mesh.

Given the same computational limitations of the available partition within the HPC, adaptations to the current setup are required. Since the optimized T-rHEX has a larger volume compared to the ORCHID with respect to the coolant channels, the optimized T-rHEX mesh is expected to have a higher cell count. Given the maximum RAM, certain mesh adaptations are necessary to accommodate the computational limitations.

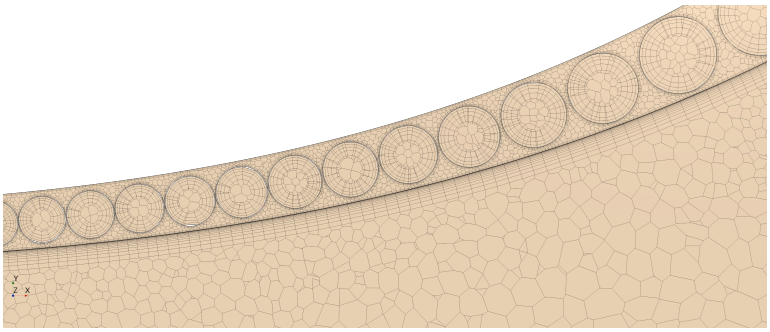

Figure 4.49: Zoomed view of the cross-section view at the coolant-structure and diffuser structure interfaces.

To ensure accurate diffuser flow results, the same mesh controls were left from the ORCHID diffuser as a recuperator setup. However, for this case, since diffuser semi-opening angles are reduced, the effect of flow expansion is smaller. This implies that for the given mesh resolution, flow close to the walls has higher velocity than for the ORCHID diffuser as a recuperator case, resulting in slightly higher y_+. In this case, only 33% of wall bounded cells are within $y_+ < 1$, 74% within $y_+ < 1.5$, 95% within $y_+ < 2$ and 99.9% within $y_+ < 5$. Since approximately all cells are resolved to within the viscous sub-layer (inner boundary layer) region, the accuracy of the wall bounded flows can be considered sufficient. Additionally, by maintaining all cells to low y_+, consistency is maintained in terms of wall treatment models, allowing for a fair comparison along the channel in terms of friction and heat transfer.

In terms of the solid structure, the ORCHID previously implemented a coarse mesh. This was found to be quite limiting in terms of thermal conduction accuracy within the solid. Nevertheless, the overall result was satisfactory, thus the same setup was maintained. Given the increase in the length of the recuperator, the number of coolant channel revolutions has increased. Since the most limiting aspect of the solid region was the resolution of the gap between the coolant channels, the increase in the length of the recuperator leads to a significant increase in cell count for the solid structure region. This cell count increase also does not provide further accuracy improvements as the same prism layer setup is maintained.

As cell count has increased for both the diffuser and the solid structure regions, due to the RAM limitations, the coolant channel must implement a reduction in cells. Naturally, this cell reduction leads to a reduction in accuracy in both turbulence predictions and wall related properties, such as friction and heat transfer. This is a major implication of the setup that can only be solved by increasing the maximum RAM limit of the CHT or by solving separately the coolant channels and diffuser in a coupled manner. On one hand, the effect of mass conservation imbalance remains present. On the other hand, the coarsening of the coolant channel leads to a consistent wall treatment model, thereby preventing fast changes in wall distance that affect both wall shear and heat transfer models. The coarsening of the coolant mesh ensures that all wall bounded effect are treated using StarCCM+ high y_+ wall treatment model.

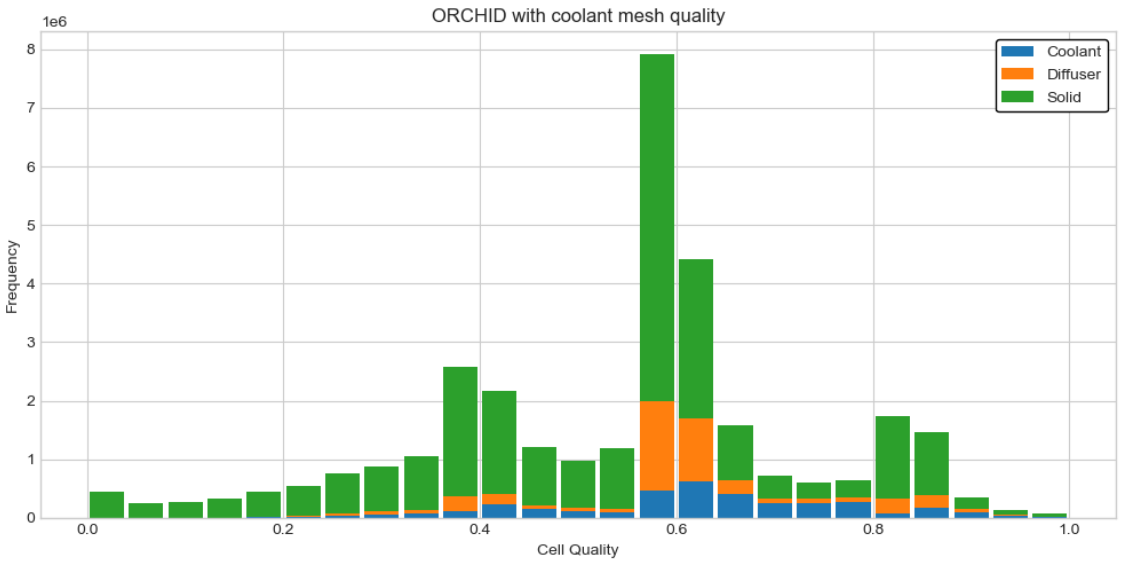

Figure 4.50: Cell quality histogram for the optimized T-rHEX.

A reassessment of the mesh cell properties confirms that no cells exhibit negative volumes. Regarding cell skewness, poor orthogonality is again observed in the solid regions, particularly in between the coolant channel gaps. Figure 4.50 illustrates the increase in the number of cells required for the solid structure results in a higher proportion of low quality cells. This outcome is expected, as the mesh configuration for the solid region is kept constant, thereby preserving its inherent coarseness. Although low quality cells may introduce numerical errors in the evaluation of boundary fluxes, further refinement of the solid mesh is not feasible, since doing so would require reducing the mesh resolution in the fluid regions, which is undesirable for the objectives of this study.

In terms of convergence, the optimized T-rHEX setup shared similar convergence behavior to the ORCHID diffuser with recuperator case. While mass, momentum and turbulent kinetic energy (Tke) residuals stabilize at around 10^{-6}, the energy and specific dissipation rate (Sdr) once again only converge to 10^{-2}. This is to be expected as the CHT setup is consistent.

4.3.2. Diffuser velocity

The elongation of the diffuser leads to a reduction of peak pressure gradients that not only reduces flow separation but also maximizes heat transfer by increasing the diffuser wetted area. Due to the effect of elongation, the diffuser undergoes a more gradual expansion process.

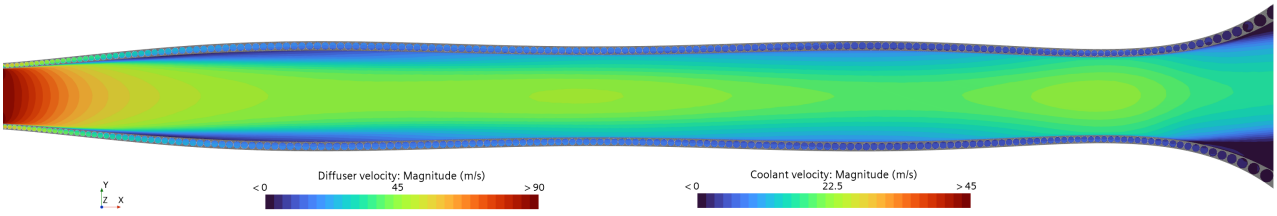

Figure 4.51: Velocity magnitude contours of the optimized T-rHEX.

Figure 4.51 shows that the optimized elongated diffuser reduces both the rate of flow expansion and the radial gradient of velocity, which has a pronounced effect on separation behavior. The shape obtained from the optimization in section 4.3 is driven by heat transfer maximization, resulting in a slight converging section near the diffuser end followed by a final expansion to maximize pressure recovery. Whereas the original ORCHID diffuser separates almost immediately, the optimized geometry exhibits only a small separation region near the outlet. This shows that adverse pressure gradients are not the sole criterion for separation, thus the potential benefit to implement a separation criteria in the low fidelity model. In terms of the velocity field, the growth of the boundary layer is moderate. In contrast to the existing ORCHID diffuser (see Figure 4.9), the central

diffuser flow is not as segregated from the wall bounded flow, allowing for higher thermal exchange between the walls and the core flow.

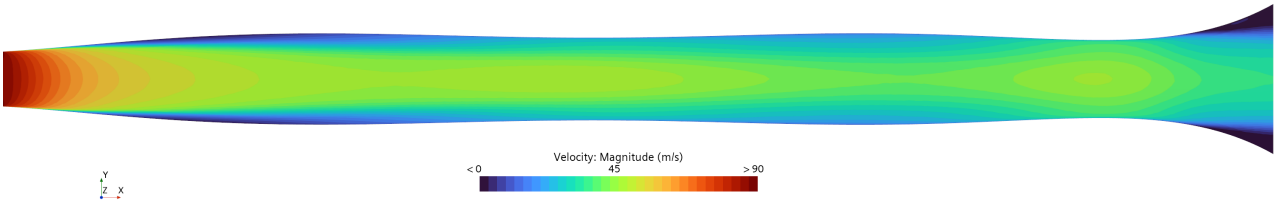

Figure 4.52: Velocity magnitude contours of the adiabatic optimized T-rHEX diffuser.

A comparison of Figure 4.51 to the adiabatic diffuser case (Figure 4.52) reveals the close similarity between the velocity profiles. Both flows follow an axi-symmetric flow behavior for the majority of the diffuser length. However, separation is once again found to be non axi-symmetric for the cooled case, where the top surface delays separation compared to the bottom surface.

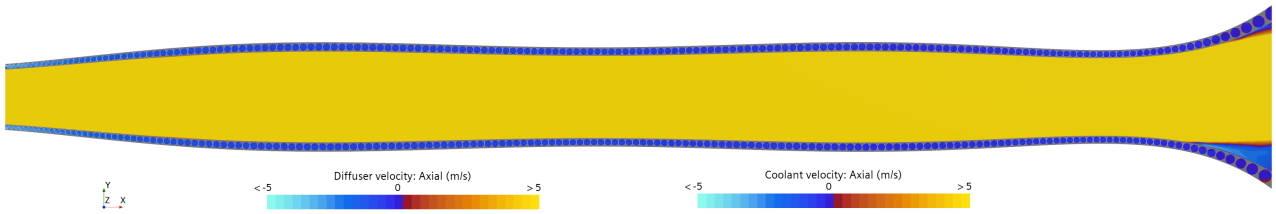

Figure 4.53: Axial velocity contours indicating separation bubbles for the optimized T-rHEX diffuser.

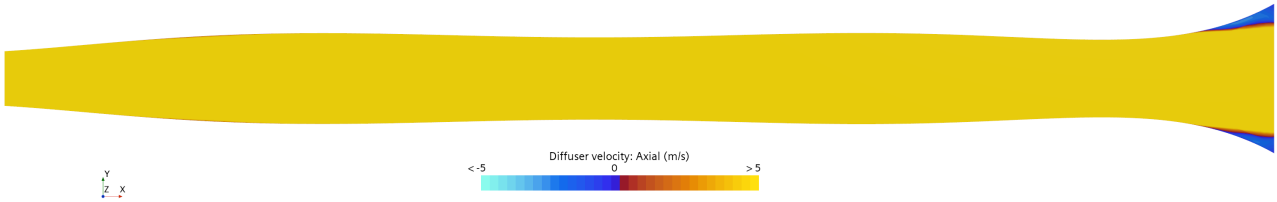

Figure 4.54: Axial velocity contours indicating separation bubbles for the adiabatic optimized T-rHEX diffuser.

The comparison between separation bubbles once again leads to the conclusion that diffuser cooling postpones separation on the top surface of the diffuser, while no benefits are found at the bottom surface of the diffuser. Once again it is believed that thermal mixing (buoyancy) improves boundary layer stability on the top surface, causing a delay separation, while the contrary occurs at the bottom surface. To consider cooling effects in more detail, the baroclinic instabilities are computed.

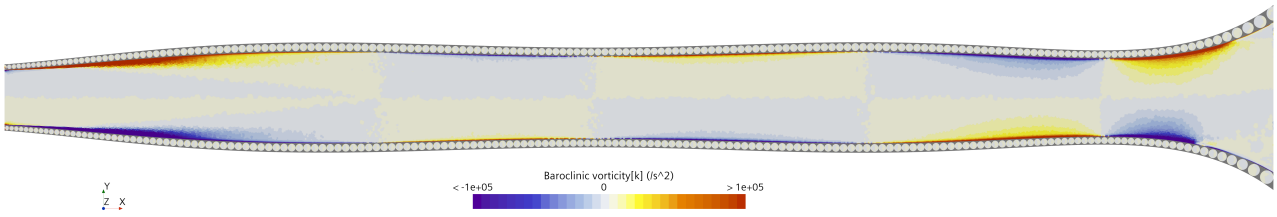

Figure 4.55: Baroclinic torque contours of the optimized T-rHEX diffuser.

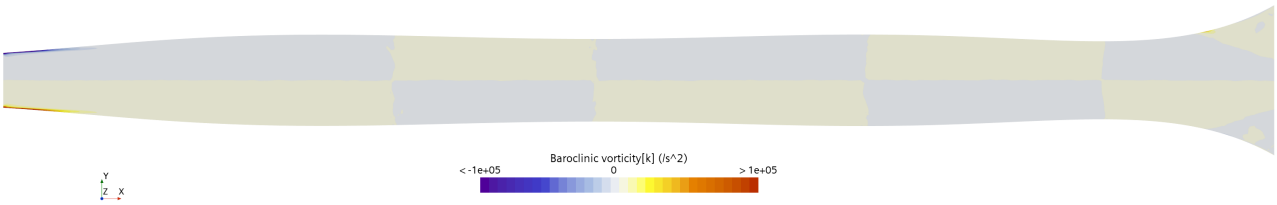

Figure 4.56: Baroclinic torque contours of the adiabatic optimized T-rHEX diffuser.

Once again, the adiabatic diffuser has no relevant baroclinic instabilities due to the lack of radial density gradients. While the inlet maintains some baroclinic instabilities due to numerical artifacts from inlet pressure field instabilities, the rest of the domain does not encounter any baroclinic instabilities. On the other hand, Figure 4.55 shows similar trends of baroclinic instabilities to the existing ORCHID turbine diffuser in Figure 4.14. The regions of baroclinic instabilities coincide with regions exhibiting high axial pressure gradients, such as the first expansion section, and the second expansion section close to the outlet. These regions contribute to the generation of vorticity which coincides with regions prone to separation. Given the adverse pressure gradients are reduced for the elongated diffuser, the effect of baroclinic torque is smaller. Nevertheless, their localized effect combined with viscosity gradients and favorable thermal mixing lead to postponing separation in the top surface significantly.

In contrast, at the bottom surface the cooled diffuser exhibits earlier separation than the adiabatic case, even tho favorable baroclinic effects and viscosity gradients are present. Along the diffuser, buoyancy effects at the bottom wall lead to lack of thermal mixing which progressively weakens the near wall momentum, making the boundary layer more susceptible to separation for a given adverse pressure gradient. By the time the flow reaches the second expansion section, the local beneficial effects of cooling are not sufficient to improve boundary layer stability.

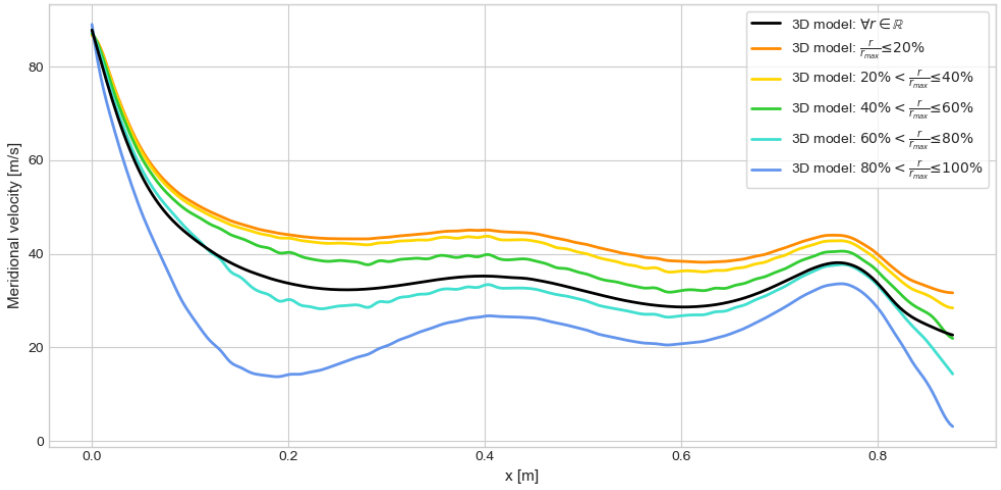

Figure 4.57: 3D meridional velocity variations per radial segment for the optimized T-rHEX diffuser.

In terms of meridional velocities along the diffuser, Figure 4.57 illustrates how flow closer to the walls experiences viscous momentum losses, reducing the velocity compared to more centralized flow. In comparison to the existing ORCHID diffuser (Figure 4.18), the difference between wall bounded flows ($\frac{r}{r_{max}} > 0.8$) and central bulk flows ($\frac{r}{r_{max}} < 0.2$) is much smaller. This can be seen as a diffuser performance increase as there are less radial variations in the velocity profile within the diffuser. However, close to the outlet of the diffuser, due to separation, large radial variations of velocity are generated.

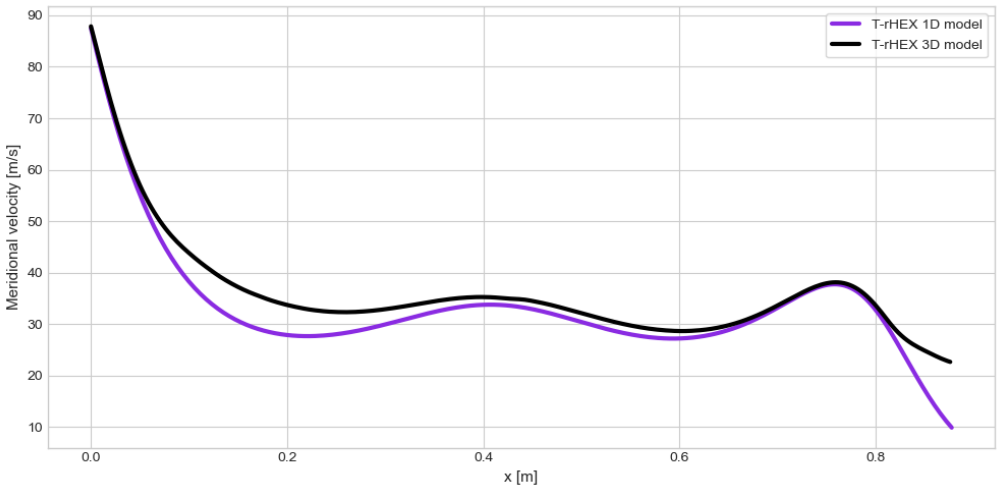

Figure 4.58: Meridional velocity comparison between 1D and 3D diffuser models along the optimized T-rHEX.

Figure 4.58 illustrates the improved prediction of the low fidelity (1D) model compared to the high fidelity (3D) model. The low fidelity (1D) model overpredicts velocity decrement at both flow expansion sections while also overpredicting velocity increments due to the oscillatory behavior of the optimized T-rHEX diffuser geometry. Once again, if separation is present, the 1D results start to differ significantly from the 3D results. Overall, the low fidelity (1D) model predicted an 88.7% velocity reduction, while the high fidelity (3D) model predicted a 74.3% velocity reduction. Adiabatic results are similar, these being 88.1% and 73.3% respectively. Similar trends are found, where the high fidelity (3D) model predicts a higher exit velocity due to the effect of flow separation, and that cooling consistently increases flow expansion to lower exit velocities for both models.

4.3.3. Diffuser temperature

Diffuser temperature plays a critical role in heat transfer performance. As discussed previously in subsection 4.2.8, wall bounded temperature results and heat transport are directly impacting the heat transfer through the solid structure interface between fluid channels.

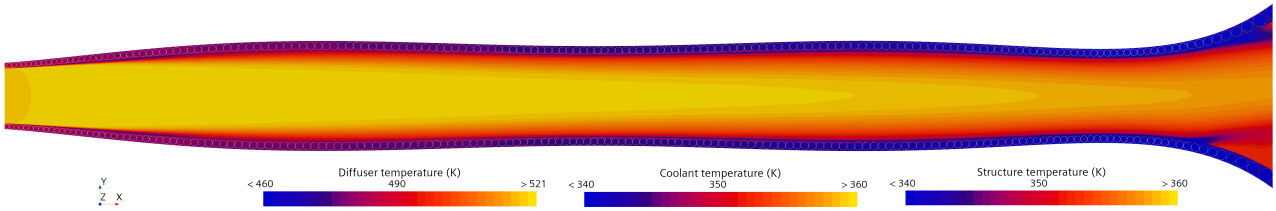

Figure 4.59: Temperature contours of the optimized T-rHEX diffuser.

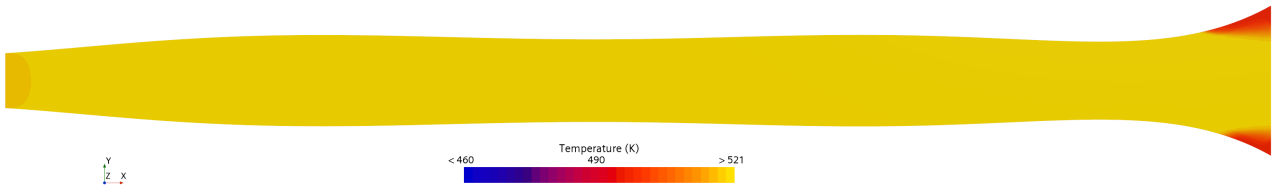

Figure 4.60: Temperature contours of the adiabatic optimized T-rHEX diffuser.

When the optimized T-rHEX is compared to the existing ORCHID diffuser, for both adiabatic and cooled case, the static temperature increases noticeably within the T-rHEX diffuser, due to the improvement in flow expansion, leading to lower velocities, which increase static temperature. Additionally, comparing Figure 4.20 and Figure 4.59, it can be seen that the central bulk flow for the optimized T-rHEX sees a net reduction in temperature before reaching the end of the recuperator. As the thermal boundary layer develops, radial gradients in temperature are formed. These are once again found to be much greater than the axial temperature gradients.

In terms of separation regions, the optimized T-rHEX sees a small temperature insulation bubble on the bottom surface of the diffuser. The effect however is limited, reflected by the lower temperature of such bubble. Another important aspect of separation is the pockets of localized low temperature at the point of separation. These are more pronounced in the optimized T-rHEX diffuser than in the existing ORCHID diffuser. Although one might be tempted to infer that the observed low temperature indicates enhanced heat transfer, this is not necessarily the case. The cause of this low temperature pocket is driven by the interaction of the main diffuser boundary layer and the reversed flow boundary layer, lifting the wall attached flow above the separation bubble, which causes low temperature fluid to mix with the general flow. This actually has a reversed effect on heat transfer, since the low fluid temperature region creates a smaller temperature gradient between the diffuser fluid and the structure, which reduces heat transfer locally.

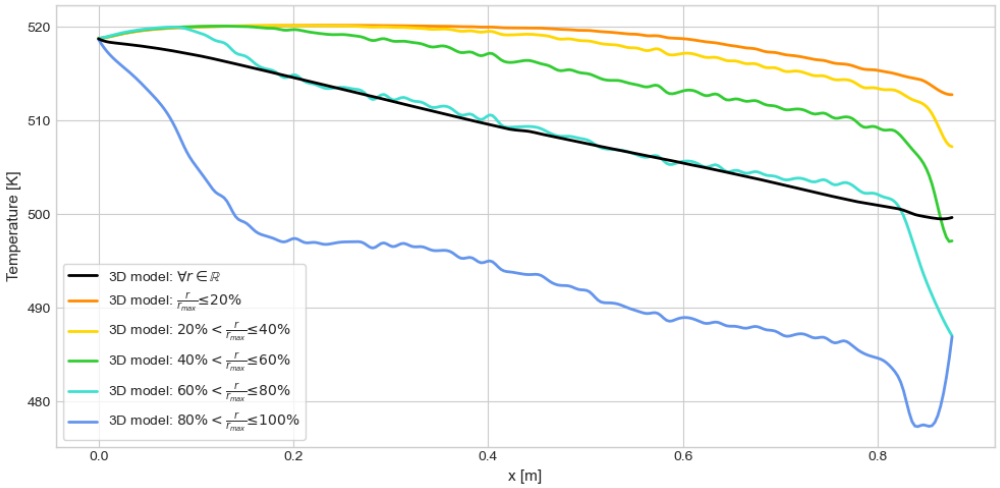

Figure 4.61: 3D temperature variations per radial segment for the optimized T-rHEX diffuser.

Looking at radial temperature gradients in more detail, Figure 4.61 shows how once again temperature gradients dominate over axial temperature gradients. Naturally, the flow closest to the wall present the lowest temperature , while the flow closest to the center (axial) axis presents the highest temperature. Additionally, it can be seen that before cooling effects reach each radial section of the flow, temperature actually increases. This is due to the initial flow expansion, which raises static enthalpy while total enthalpy is conserved. The cooling effect progresses from the walls to the center flow, which can be seen by the postponement of temperature drops for each radial section. Once cooling has reached the center flow, all segments of the diffuser decrease in temperature approximately uniformly. Comparing the full domain profile and individual profiles, it can be seen that the initial temperature decrement from the wall bounded flow is offset by the temperature increase due to the exchange of kinetic energy to thermal energy. This results in a approximately linear profile.

Finally, once again separation can be seen in the temperature profiles due to the increase in temperature near the wall. As the flow is separated, the interaction between main and reversed boundary layers lift a section of cold fluid into the domain. This is believed to be the cause of the temperature drop in radial segments between 80% and 40% of the distance between the wall and center axis.

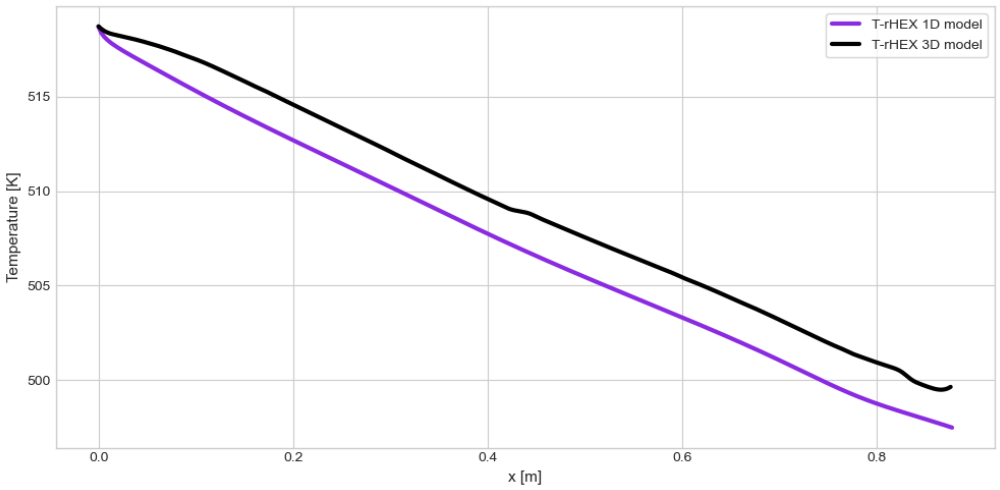

Figure 4.62: Temperature comparison between 1D and 3D diffuser models along the optimized T-rHEX.

Comparing the low fidelity (1D) model to the high fidelity (3D) model, Figure 4.62 illustrates how the profiles are similar, with an approximately constant temperature offset. This is believed to be due to the difference in heat flux between the low fidelity (1D) model and the high fidelity (3D) model (shown in Figure 4.83). Overall the low fidelity (1D) model temperature drop of 4.1% remains higher than the high fidelity (3D) model temperature of 3.7% due to the temperature offset. Considering adiabatic results, the low fidelity (1D) model predicts a net temperature increment of 0.4% while the high fidelity (3D) model shows no static temperature change.

4.3.4. Diffuser pressure

The pressure recovery capabilities of the optimized T-rHEX is one of the most important criterion considered in the design of the recuperator. The low fidelity (1D) model predicted a lower pressure recovery compared to the ORCHID diffuser as a recuperator. However, given the separation issues, this might not be the case for the high fidelity (3D) model results.

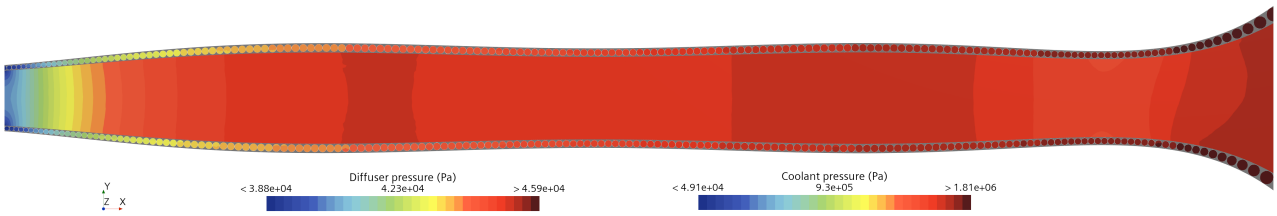

Figure 4.63: Pressure contours of the optimized T-rHEX diffuser.

Figure 4.63 shows a similar pressure rise trend to the low fidelity (1D) model (Figure 3.40), where the main pressure gain is performed at the inlet of the diffuser, then some pressure is exchanged for kinetic energy to improve convective heat transfer performance, then the final expansion is performed to gain back the pressure from the kinetic energy available at the outlet. While the main axial pressure trend is maintained, 3D effects play a role in radial pressure gradients at the end of the diffuser, due to the presence of the separation bubble.

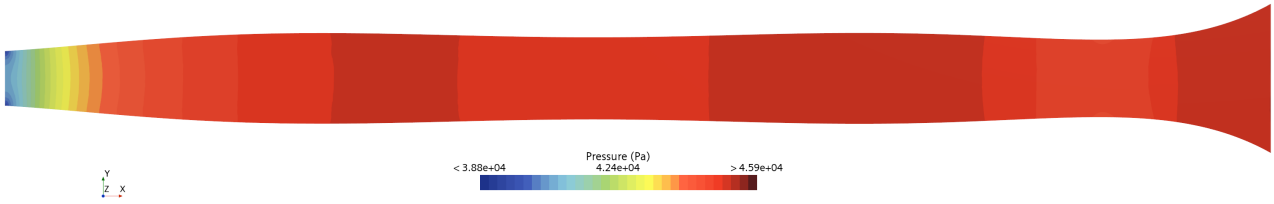

Figure 4.64: Pressure contours of the adiabatic optimized T-rHEX diffuser.

Comparing the cooled to the adiabatic case, the only major change is the axi-symmetric behaviour in pressure from the adiabatic diffuser as well as the slight increase in pressure recovery for the cooled diffuser. The diffuser pressure coefficients for the regenerative T-rHEX resulted in 0.907, while for the adiabatic T-rHEX diffuser resulted in 0.871. This makes the results the low fidelity (1D) model pressure recovery results precise as pressure recovery coefficients of 0.896 and 0.879 are obtained for the regenerative and adiabatic cases respectively.

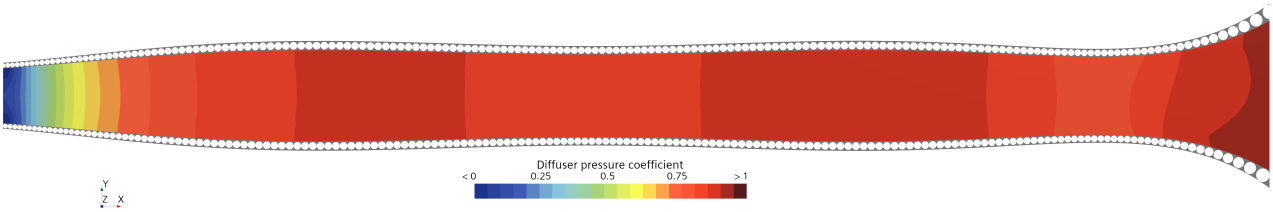

Figure 4.65: Pressure coefficient contours along the optimized T-rHEX diffuser.

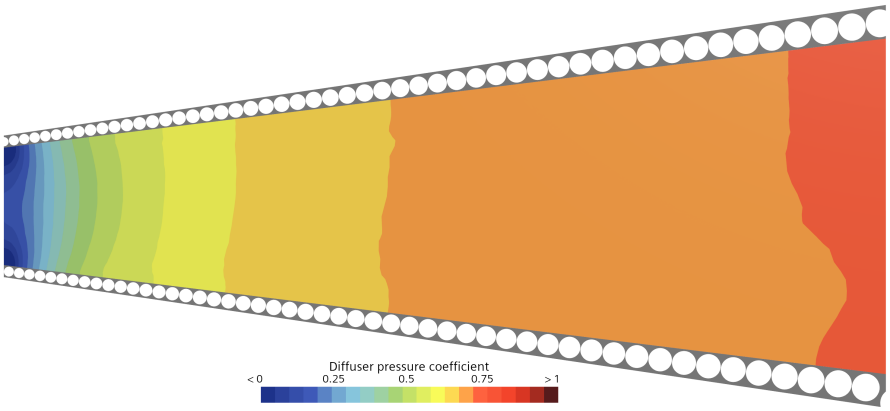

Figure 4.66: Pressure coefficient contours along the existing ORCHID turbine diffuser with recuperation.

On a separate remark, it can be seen that the existing ORCHID diffuser presents higher back pressures than the T-rHEX results in Figure 4.63. This only occurs due to the setup of the CHT boundary conditions. To prescribed the flow, the outlet pressure results from the low fidelity (1D) model were used, which implied that the existing ORCHID diffuser is capable of recovering more pressure than the optimized T-rHEX diffuser. As shown in the comparison of Figure 4.65 and Figure 4.66, the optimized T-rHEX is capable of recovering additional pressure due to avoiding separation effect, which leads to an improvement in flow expansion across the diffuser. This opposes the previous conclusion on low fidelity (1D) models, which did not account for separation.

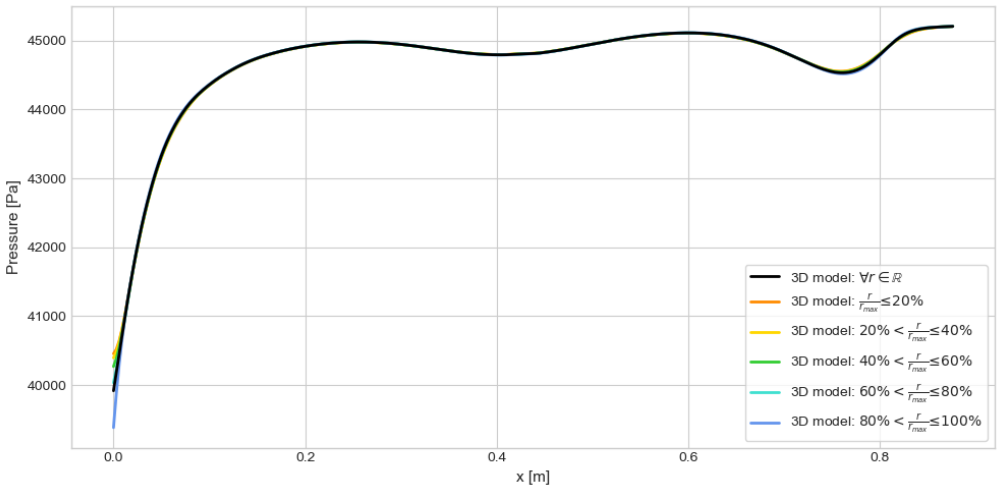

Figure 4.67: 3D pressure variations per radial segment for the optimized T-rHEX diffuser.

Similar to the existing ORCHID diffuser, radial pressure gradients are much smaller compared to axial pressure gradients. While radial pressure fluctuations may be present due to separation or streamline curvature, pressure within the diffuser remains axially dominant. The shape of the profile follows approximately the inverse of the velocity profile (see Figure 4.57), which is to be expected. Comparing the low fidelity (1D) model results to the high fidelity (3D) model results in Figure 4.68 illustrates how similar the profiles are. Once again, the low fidelity (1D) model results predict higher peaks, in this case, the pressure gain is higher than for the high fidelity (3D) model. The oscillatory behavior also shows a more or less constant pressure value for the high fidelity (3D) model, where the low fidelity (1D) model predicts a higher pressure variation. Nevertheless, the overall comparison of pressure, velocity and temperature show satisfactory low fidelity (1D) model results.

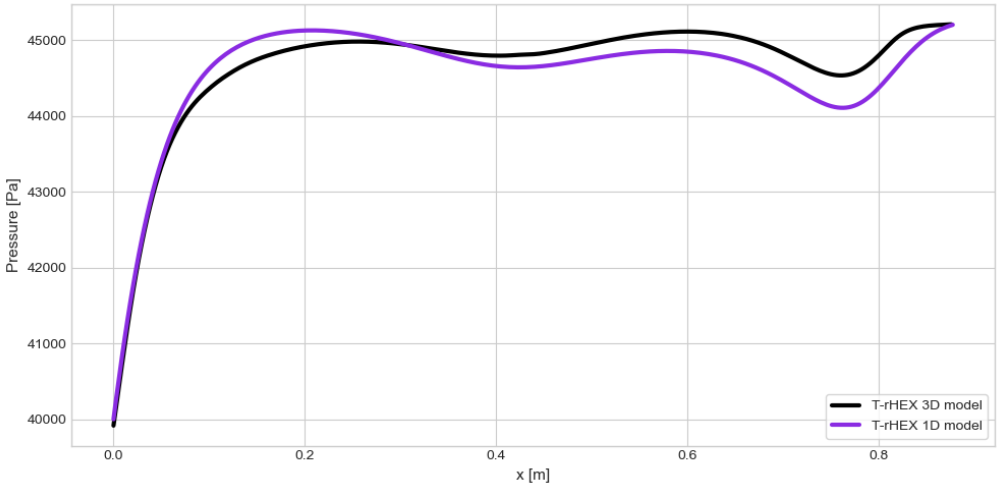

Figure 4.68: Pressure comparison between 1D and 3D diffuser models along the optimized T-rHEX.

To finalize the optimized T-rHEX diffuser section, the total pressure field is analyzed. Total pressure is a direct indication of both irreversible friction losses and reversible entropy effects due to heat transfer.

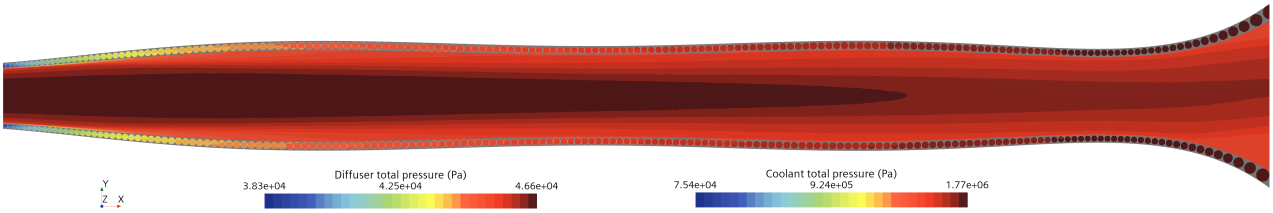

Figure 4.69: Total pressure contours of the optimized T-rHEX diffuser.

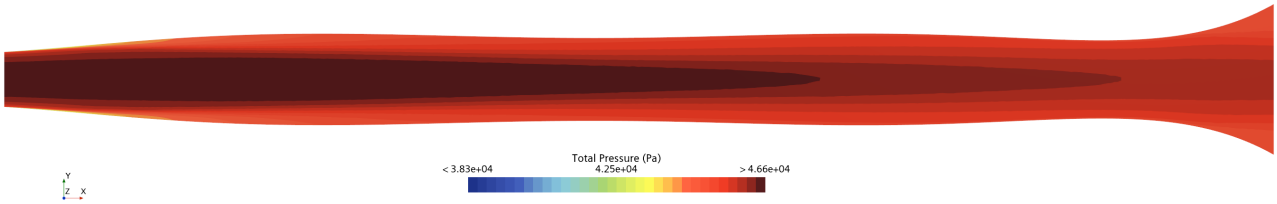

Figure 4.70: Total pressure contours of the adiabatic optimized T-rHEX diffuser.

Similarly to the existing ORCHID diffuser with recuperation, radial total pressure gradients dominate over axial gradients due to the strong influence of friction and heat transfer. When the adiabatic case is compared to the regenerative case, the regenerative case prolongs higher total pressure further downstream compared to the adiabatic case. This is due to the beneficial contribution of cooling to total pressure. While the adiabatic total pressure drop is 1.3%, the cooled diffuser total pressure drop is only 1.0%. In comparison, the low fidelity (1D) model predicted an adiabatic total pressure drop of 2.3% and a cooled diffuser pressure drop 2.1%.

In efforts to quantify losses due to friction, mixing and effects of heat transfer between the ORCHID diffuser as a recuperator and the optimized T-rHEX diffuser, the losses are quantified. In order to quantify the losses for a fair comparison between diffusers, the total pressure is compared against the initial total pressure in a non-dimensional coefficient. This coefficient is labeled the loss coefficient (k_{loss}).

$$k_{\text{loss}} = \frac{p_{t1} - p_{t2}}{p_{t1} - p_1} \tag{4.7}$$

The loss coefficient is a direct indication of the total pressure results due to both irreversible losses and heat transfer (reversible). Contours of loss coefficient are a direct indicator on viscous dissipation, flow separation, and mixing effects between inlet and outlet stations.

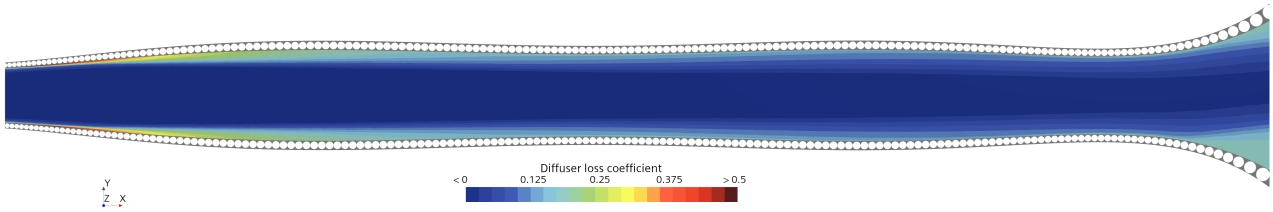

Figure 4.71: Loss coefficient contours along the optimized T-rHEX diffuser.

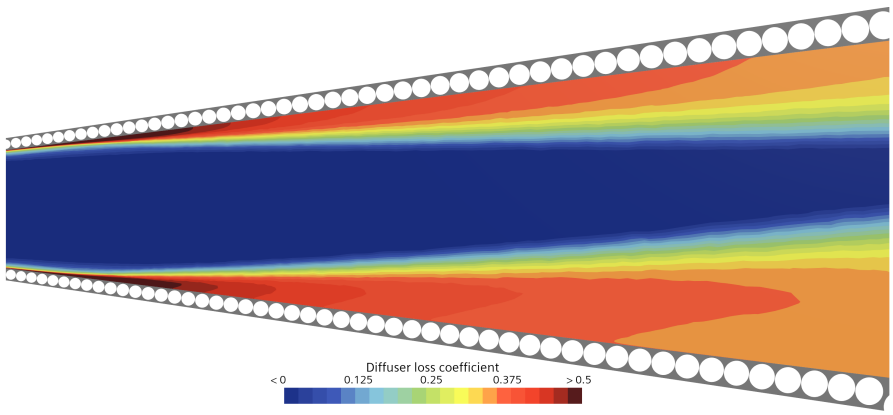

Figure 4.72: Loss coefficient contours along the ORCHID diffuser as a recuperator.

As shown in Figure 4.72, the ORCHID diffuser as a recuperator exhibits extensive regions of high loss coefficient near the diffuser walls, particularly where flow separation occurs. These losses likely originate from the combined effects of strong adverse pressure gradients, wall heat transfer, and secondary flow interactions. The near-wall regions display strong losses, while the central core flow remains largely unaffected. In contrast, Figure 4.71 reveals a noticeably cleaner (loss free) flow field, with lower overall losses and more confined high-loss regions near the inlet expansion and separation zones. The core flow maintains low dissipation throughout the diffuser length, indicating a more stable attached flow. Consequently, the optimized T-rHEX diffuser demonstrates superior flow efficiency compared to the existing ORCHID diffuser.

4.3.5. Coolant velocity

The coolant channel modeling approach has changed compared to the ORCHID diffuser as a recuperator. The coarsening of the mesh implies that the results may have decreased accuracy. While secondary flows may not be correctly captured, the general bulk flow can be considered to be acceptable as the effect of wall treatment models becomes consistent along the channel.

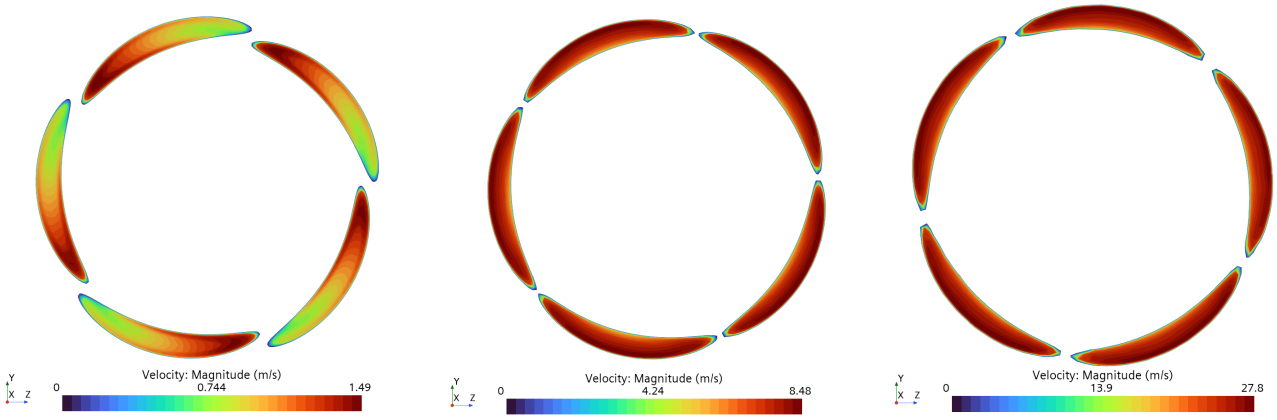

(a) Radial plane view at 5% coolant length. **(b)** Radial plane view at 50% coolant length. **(c)** Radial plane view at 95% coolant length.

Figure 4.73: Comparison between coolant channel velocity contours at different axial locations of the optimized T-rHEX.

Figure 4.73 illustrates how the channel velocity increases along the coolant channel. This increase in bulk velocity also leads to an increase in radial differences in velocity within the channel due to centrifugal effects. Due to the additional channel length contributing to higher frictional losses, the comparison between bulk flow velocities results in lower values for the optimized T-rHEX coolant than the ORCHID with recuperator.

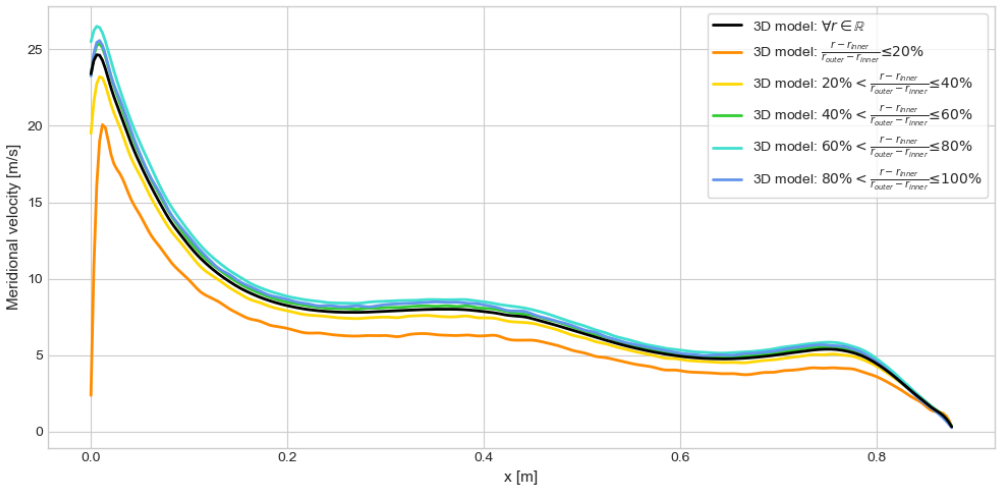

Figure 4.74: 3D meridional velocity variations per radial segment for the optimized T-rHEX coolants.

Figure 4.74 shows how the velocity increases along the coolant. The velocity trend is expected due to the variation in diffuser exterior wall radius along the recuperator, which dictates the cross sectional area of the coolant. The fluid close to the inner surface is the slowest due to centrifugal effects, shifting momentum towards the outer surface of the coolant channel. On the other hand, flow close to the outer walls undergoes high losses due to friction.

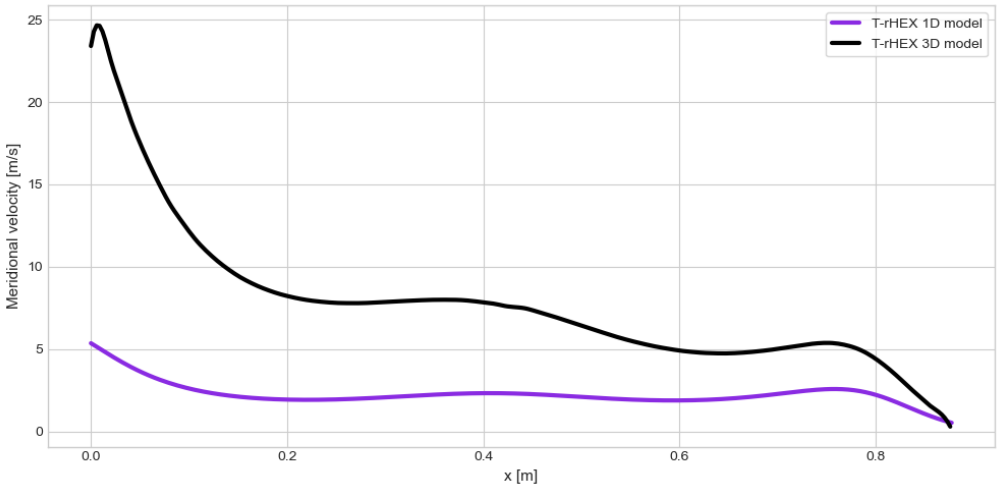

Figure 4.75: Meridional velocity comparison between 1D and 3D coolant models along the optimized T-rHEX.

When comparing the low fidelity (1D) model results to the high fidelity (3D) model results, Figure 4.75 shows that once again the coolant velocity is significantly under predicted by the low fidelity (1D) model. Once again, mass conservation imbalance is present in the high fidelity model results, which artificially increases the fluid velocity. The effect of the inlet and outlet boundaries has a clear impact on the results (as seen in Figure 4.74), generating a non-physical radial variation in velocity. This confirms that future work on coolant modeling must use adequate boundary conditions, by means of implementing orthogonal boundaries to the flow direction.

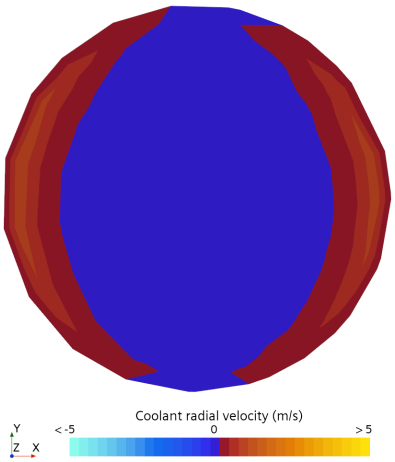

(a) Coolant channel radial velocity (u_r) contours due to centrifugal forces.
Orientation: Centrifugal forces act downwards. The blue contours indicates flow towards outer wall while the yellow/red indicates recirculated flow away from the outer wall.

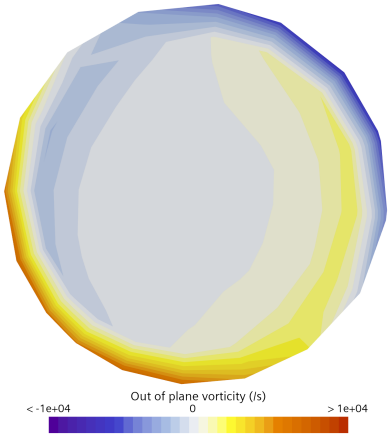

(b) Coolant channel vorticity contours due to centrifugal forces.
Orientation: Centrifugal forces act downwards. Out of plane vorticity is positive, while into the plane vorticity is negative.

Figure 4.76: Secondary flows within the coolant channel due to the effects of centrifugal forces.

Although the secondary flows within the coolant channel of the ORCHID diffuser with recuperation setup were considered significant, the coolant channel of the T-rHEX setup is not refined enough to capture such secondary flows. Computing the Dean number using the low fidelity (1D) model yields to values above the turbulence limit (De>400). This implies that the effect of centrifugal forces is relevant in the generation of secondary flows. However, when attempting to compute such effects, it is clear that these secondary flows are numerically dampened (compare Figure 4.76 to Figure 4.32). This could potentially decrease local heat transfer with respect to the true values, reducing the total thermal power of the heat exchanger. Heat transfer results are presented in subsection 4.3.8.

4.3.6. Coolant temperature

The temperature in the coolant dictates heat transfer capabilities. Previously, Figure 4.59 illustrated how temperature varies both in the meridional and the radial direction.

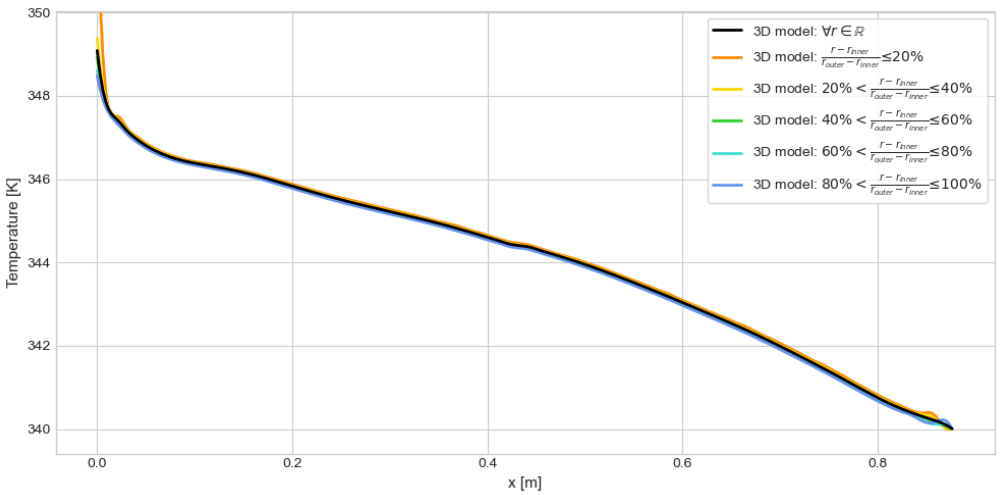

Figure 4.77: 3D temperature variations per radial segment for the optimized T-rHEX coolants.

As seen in Figure 4.77, radial temperature gradients are small, mainly dominated by both heat transfer heating from the inner walls and also due to the increase of static temperature at the low velocity sections close to the inner wall. Furthermore, the effect of heat transfer between coolant channels can be estimated. The difference between coolant channel temperature is found to be around $0.1\,\mathrm{K}$. Furthermore, the structural temperature

at the gap between coolant channels is found to be always greater than coolant temperatures. This confirms that no heat transfer is induced between coolant channels, thus neglecting the effect of heat transfer between coolant channels is considered acceptable for the low fidelity model.

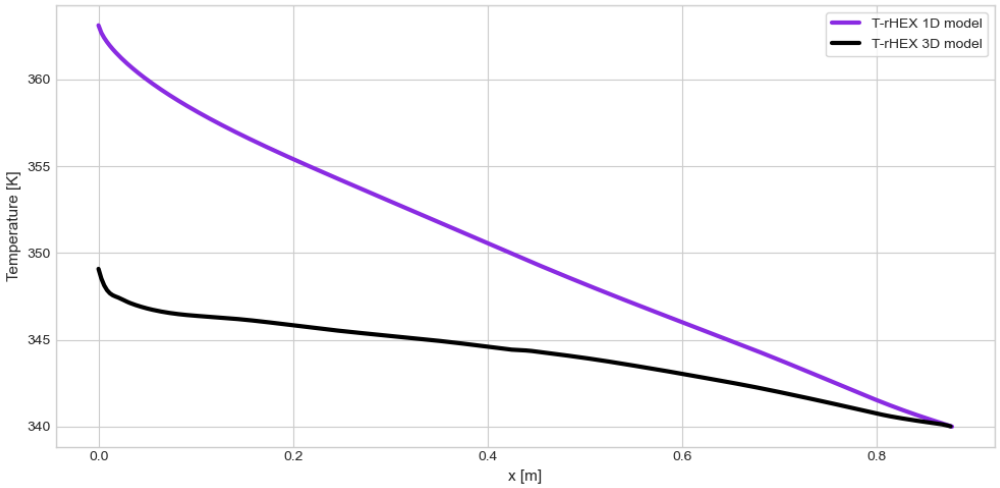

Figure 4.78: Temperature comparison between 1D and 3D coolant models along the optimized T-rHEX.

Comparing temperature profiles between the low fidelity (1D) model and the high fidelity (3D) model shows a clear difference. As seen in Figure 4.78, the meridional temperature gradient for the low fidelity (1D) model is higher than for the high fidelity (3D) model. While Figure 4.83 shows that the net thermal energy transfer into the coolant channel is similar, the cause for the lower temperature changes has to do with two main aspects. The first consideration is the introduction of the thermal resistance of the solid structure. The solid structure has an idealized thermal resistance considering pure aluminium properties, on top of numerical dissipation due to poorly refined structural mesh. This causes a net reduction in thermal power reaching the coolant channels. The effect is approximately uniform across the recuperator, which causes the temperature profiles of the coolant channel to decrease uniformly. Secondly, mass imbalance plays a role in the reduction of temperature gradients. Artificial increments in mass flow rate lead to increased heat capacitance of the channel, which reduce temperature changes given a fixed amount of thermal energy transferred. Both effects are believed to be the primary cause of the difference in temperature gradients between the low fidelity (1D) and high fidelity (3D) model results.

4.3.7. Coolant pressure

From Figure 4.63, it can be seen that pressure undergoes a significant pressure decrease along the meridional direction of the channels. This is expected since the inlet velocity and channel twist are similar to the coolant channel of the ORCHID diffuser as a recuperator.

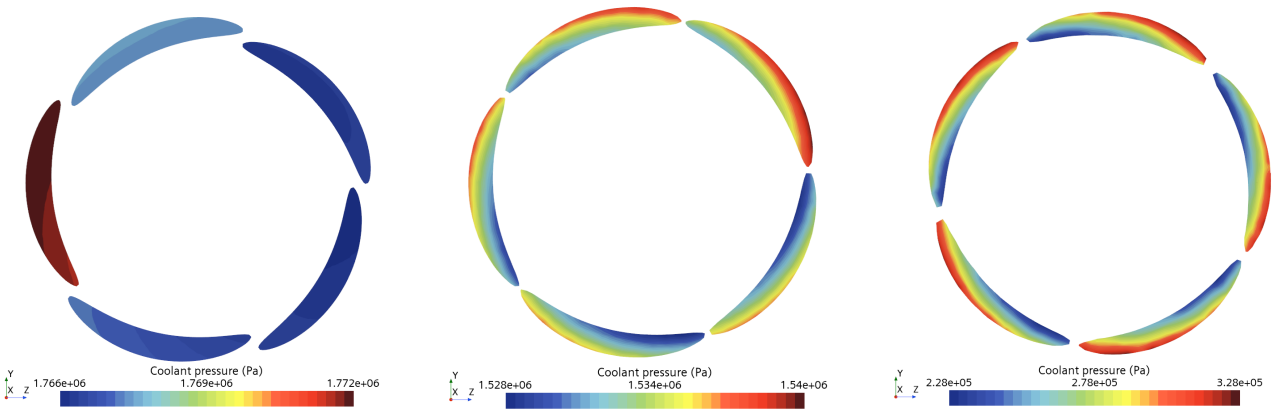

(a) Radial plane view at 5% coolant length. **(b)** Radial plane view at 50% coolant length. **(c)** Radial plane view at 95% coolant length.

Figure 4.79: Comparison between coolant channel pressure contours at different axial locations of the optimized T-rHEX.

The radial plane cuts in Figure 4.79 also show how the centrifugal effects of the coolant are also reflected in the T-rHEX. Once again, both bulk velocity increment along the channel combined with curvature diameter decrement lead to higher radial pressure gradients. However, comparing the radial pressure gradients from Figure 4.37 to Figure 4.79, it can be seen that the radial pressure difference has decreased. While the curvature diameters at such locations remains approximately similar, the main difference is the reduction in coolant bulk velocity.

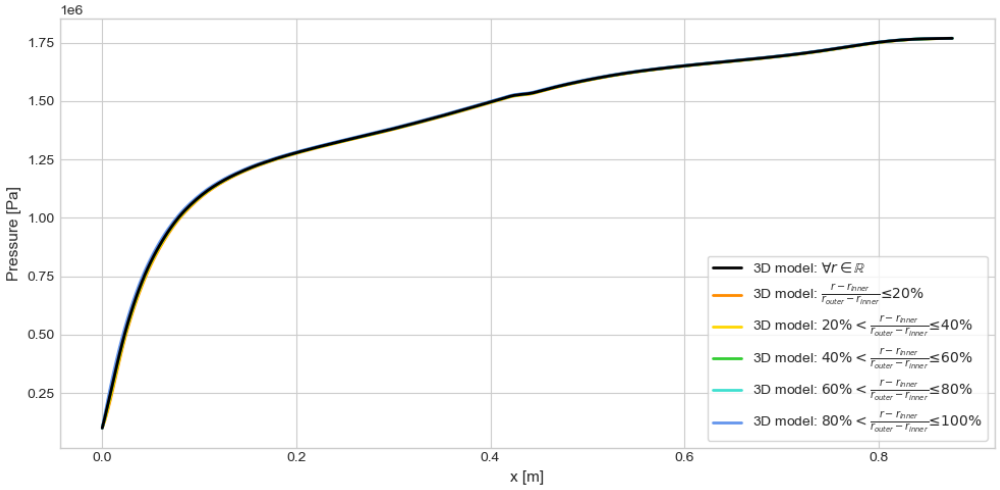

Figure 4.80: 3D pressure variations per radial segment for the optimized T-rHEX coolants.

Figure 4.80 shows how meridional pressure gradients dominate in coolant channel flows. As the bulk flow is reduced, the centrifugal effects of radial pressure gradients are reduced. While static pressure is expected to follow the inverse of velocity, Figure 4.80 shows that this is not directly the case. Instead, coolant pressure is dominated by frictional losses, causing significant total pressure reduction which reflects on static pressure reduction.

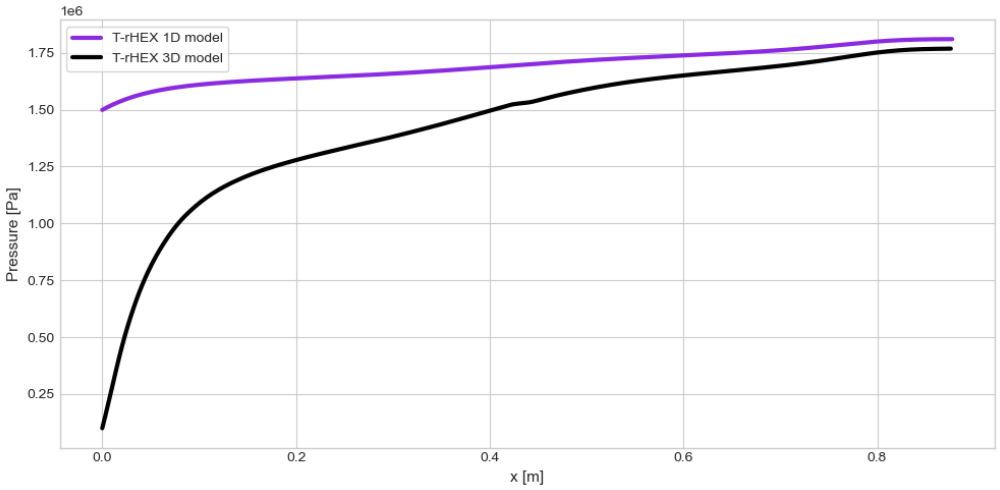

Figure 4.81: Pressure comparison between 1D and 3D coolant models along the optimized T-rHEX.

When comparing the pressure distribution between the low fidelity (1D) model and high fidelity (3D) model results, a similar trend to the coolant channels results of the ORCHID diffuser as recuperator are seen (see Figure 4.39). As Figure 4.81 shows, the static pressure drop is much higher than the static pressure drop of the low fidelity (1D) model. While the low fidelity (1D) model predicts a 17.2% pressure decrement, the 3D results conclude on a 94.3% pressure loss. To further understand what is the main drive of such high pressure drop, the total pressure distribution is considered.

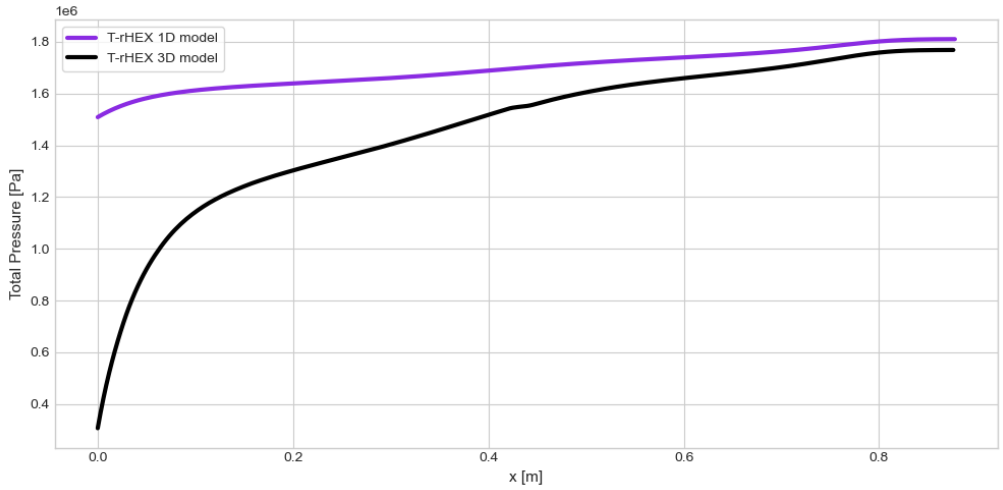

Figure 4.82: Total pressure comparison between 1D and 3D coolant models along the optimized T-rHEX.

Both friction and heating lead to a reduction in total pressure. As seen in Figure 4.82, total pressure shows similar trends in distribution compared to static pressure. This means that, although velocity plays an important role, the pressure field within the diffuser is strongly dominated by friction losses reflected as total pressure losses.

4.3.8. Heat transfer

Given the understanding of each individual component of the recuperator flow, an overall heat transfer assessment can be performed.

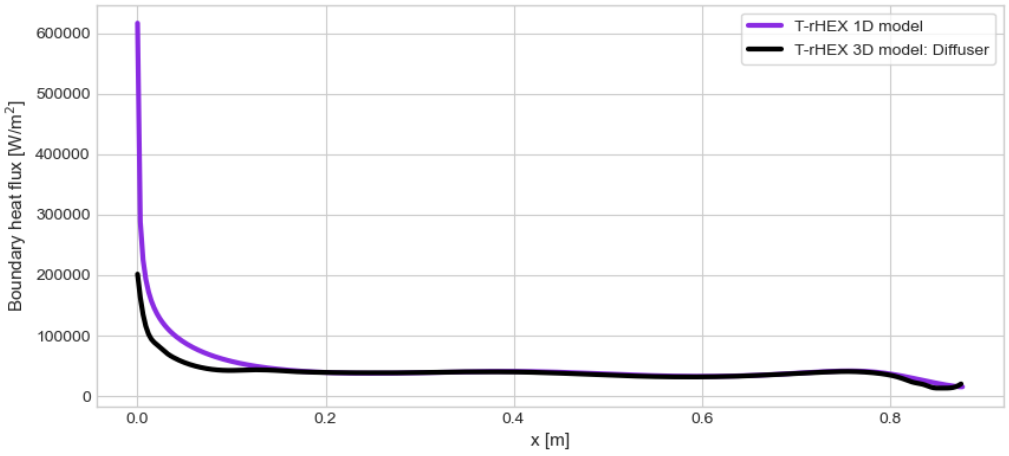

Figure 4.83: Comparison of the heat flux across the diffuser wall between low fidelity (1D) and high fidelity (3D) models along the optimized T-rHEX.

Figure 4.83 shows the heat flux distribution across the recuperator. Excluding the diffuser inlet region, the heat flux trend across the recuperator similar for both models. The effects of flow expansion are well captured which overall presents a satisfactory results by the low fidelity (1D) model. On the other hand, the low fidelity (1D) model continues to overestimate diffuser inlet heat transfer. This is explained by considering the convective heat transfer of the diffuser in Figure 4.85. Moreover, the low fidelity model deviates from the high fidelity model results, due to separation effects at the outlet.

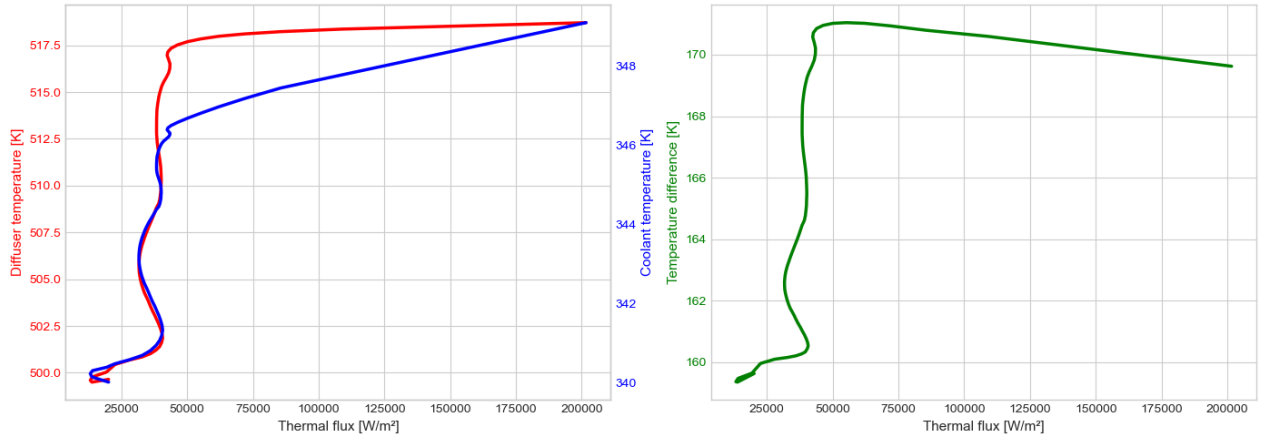

Figure 4.84: Thermal plots along the recuperator for the given optimized T-rHEX.

Figure 4.84 illustrates how temperature gradients drive heat transfer. Due to the countercurrent arrangement of the recuperator, the temperature profiles of the coolant channels and the diffuser are alike, with the diffuser flow having a higher temperature drop than the coolant channel temperature increment. This indicates that the thermal capacitance of the coolant is greater than the diffuser, which contradicts low fidelity model results (see Figure 3.34), and therefore explains the change in temperature difference profile. While the diffuser temperature profile is similar, the coolant temperature profile differs. The same conclusions can therefore be given as in subsection 4.3.6. Given that the high fidelity model under predicts coolant temperature rise, the induced heat transfer between streams can be considered to be slightly overestimated.

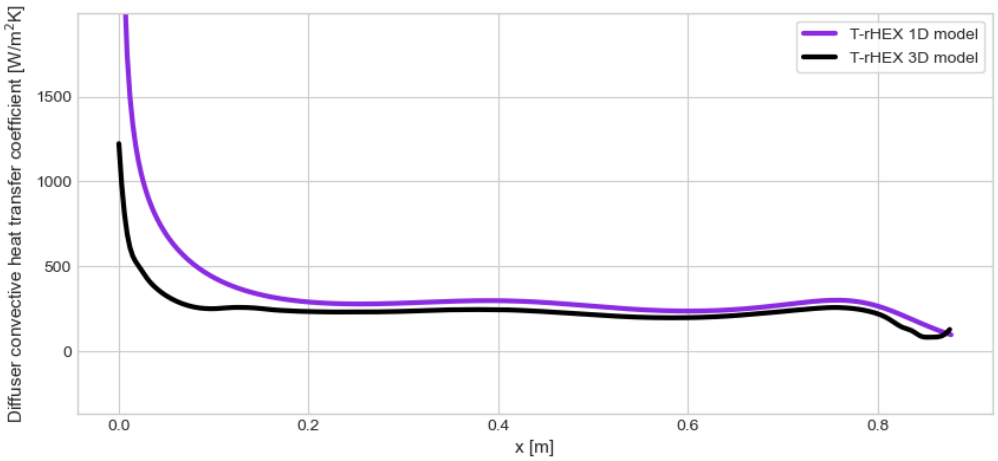

Figure 4.85: Comparison of the convective heat transfer coefficients between 1D and 3D diffuser models along the optimized T-rHEX.

Similar to heat flux distribution, Figure 4.85 shows that the 1D and 3D convective heat transfer models are similar. The low fidelity (1D) model significantly overpredict the convective heat transfer coefficient at the diffuser inlet. While thermal boundary layer development effects are important, the effect predicted by the low fidelity (1D) model is once again overestimated. Moreover, the low fidelity (1D) model accounts well for flow changes due to changes in cross-sectional area. However, a small systematic over prediction of convective heat transfer coefficient is found. As separation no longer plays a mayor role, it can be confirmed that the low fidelity (1D) convective model slightly overestimates convective heat transfer. This aligns with the expectations from the model validation performed in section 3.2.

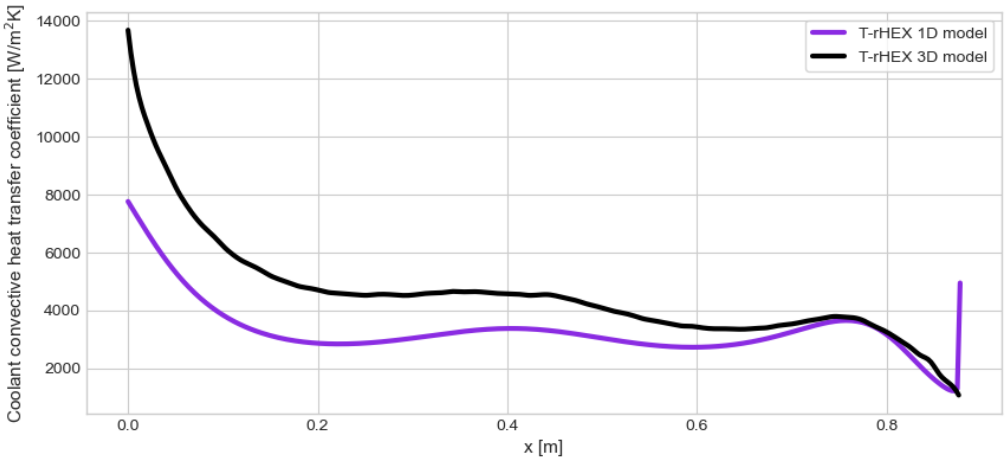

Figure 4.86: Comparison of the convective heat transfer coefficients between 1D and 3D coolant models along the optimized T-rHEX.

Figure 4.86 shows how both low fidelity (1D) and high fidelity (3D) models predict changes in convective heat transfer due to coolant velocity changes. Excluding the reoccurrence of the inlet low fidelity (1D) model effects, both models follow similar results. As the coolant flow progresses along the channel, the low fidelity model starts to deviate from the high fidelity model results, by under predicting convective heat transfer coefficient. This is due to the over prediction of coolant channel velocity by the high fidelity model (see Figure 4.75).

In conclusion, the `T-rHEX.py` heat transfer solver is able to account adequately for heat transfer effects, specially with results related to diffuser flow. While flow separation has been shown to create discrepancies between low fidelity (1D) model predictions and 3D flows, surprisingly, its impact remains limited even in cases of highly separated flow (see existing ORCHID diffuser results in Figure 4.41). Additionally, helicoidal channel flows affect convection in two opposing ways. On one hand, stronger centripetal effects push the flow toward the outer walls of the coolant, which limits the temperature at the inner surface where heat transfer occurs. On the other hand, these same stronger centripetal effects induce Dean vortices (Figure 4.32), which enhance recirculation along the coolant channel walls and locally increasing the convective heat transfer rate. A critical improvement to the convective heat transfer model is to correct for the systematic bias in overprediction of heat transfer at the inlet of both the diffuser and coolant channels.

4.3.9. Friction

Once again, the Fanning friction factor is used to compare friction effects between the low fidelity (1D) model and the high fidelity (3D) model.

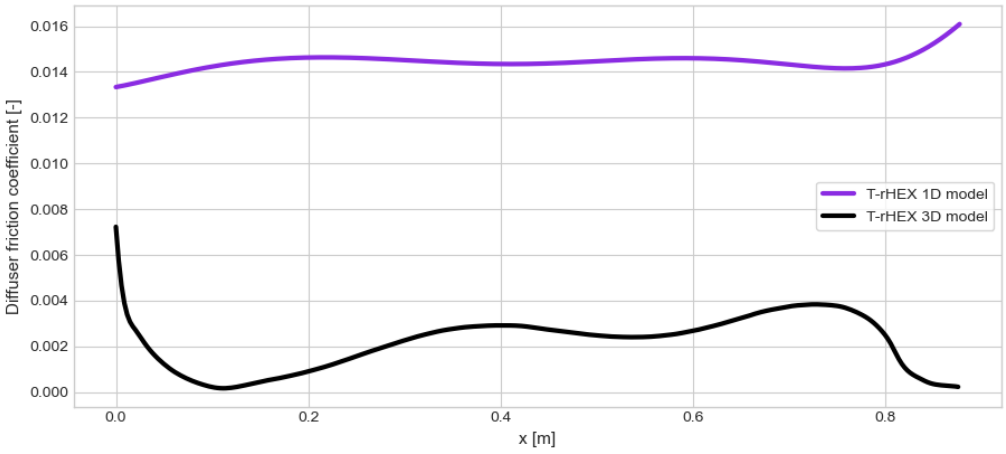

Figure 4.87: Comparison of the Fanning friction coefficient between 1D and 3D diffuser models along the optimized T-rHEX.

Similarly to the existing ORCHID diffuser results, the low fidelity (1D) friction model overestimates the friction coefficient compared to the high fidelity model friction coefficient. Additionally, while the 1D friction coefficient

is limited in variation, the 3D averaged friction coefficient variates severely across the channel. Naturally, wall shear is dependent on the velocity gradients close to the wall. Looking at Figure 4.51, the region of low friction coefficient coincides with regions of lowest velocity close to the wall, due to boundary layer thickening or separation. The resulting flow then undergoes much smaller friction effect, while other loss mechanisms such as mixing become more relevant. These mechanisms are not accounted for in low fidelity (1D) models. To obtain a conclusion of the overall losses, loss coefficient (k_{loss}) can be computed.

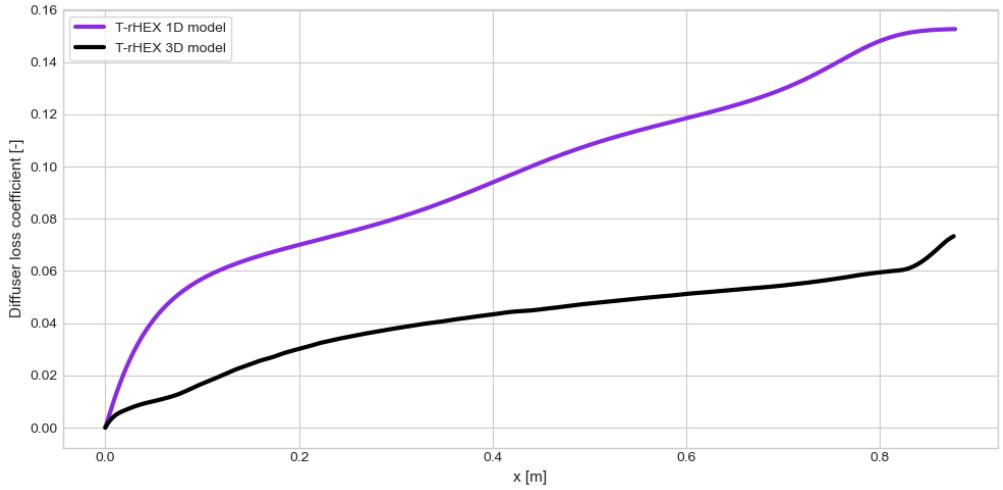

Figure 4.88: Comparison of the loss coefficient between 1D and 3D diffuser models along the optimized T-rHEX.

Figure 4.88 confirms that considering both mixing and frictional effects, the losses estimated by the low fidelity (1D) model are superior over the high fidelity (3D) model. This coincides with the results comparison of total pressure drop in subsection 4.3.4. As heat transfer prediction is greater for the low fidelity model (thus the total pressure increases should be greater), the only remaining conclusion for the reduced pressure drop is that the Osnaghi 1D model implementation within `T-rHEX.py` overestimates friction.

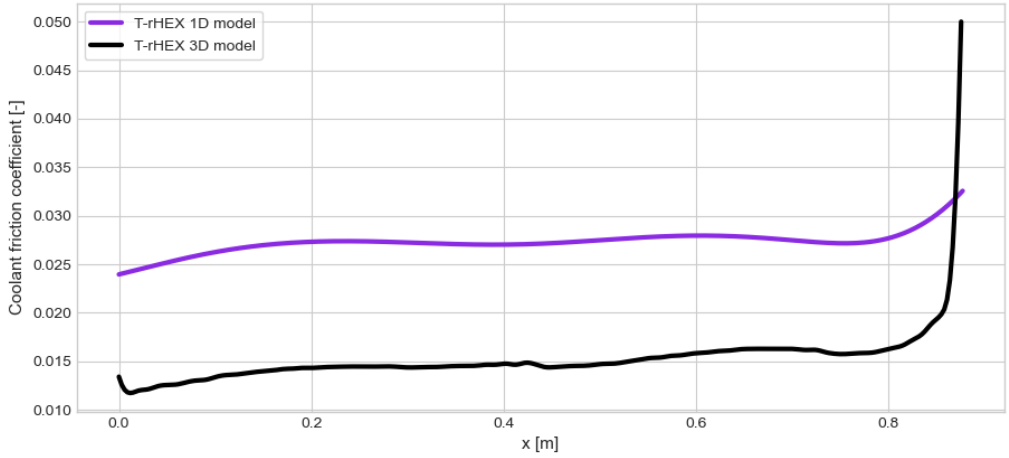

Figure 4.89: Comparison of the Fanning friction coefficient between 1D and 3D coolant models along the optimized T-rHEX.

In terms of coolant friction, Figure 4.89 shows similar trends to the coolant friction results of the ORCHID diffuser as a recuperator. The inlet and outlet friction model peaks are believed to be caused by the flow at the boundary conditions. Along the remainder of the coolant channel the low fidelity model overestimates of friction coefficient, primarily due to the reduced secondary flow strength caused by the artificial increase in curvature radius and by mesh coarsening, as well as the increase in bulk velocity which raises the Reynolds number and alters the near wall velocity gradient. Because the high fidelity coolant channel model relies on a wall treatment approach to estimate wall shear on coarse meshes, its friction predictions are less reliable

than those obtained for the diffuser flow. To account for all losses, the loss coefficient is once again computed for the coolant channel flow.

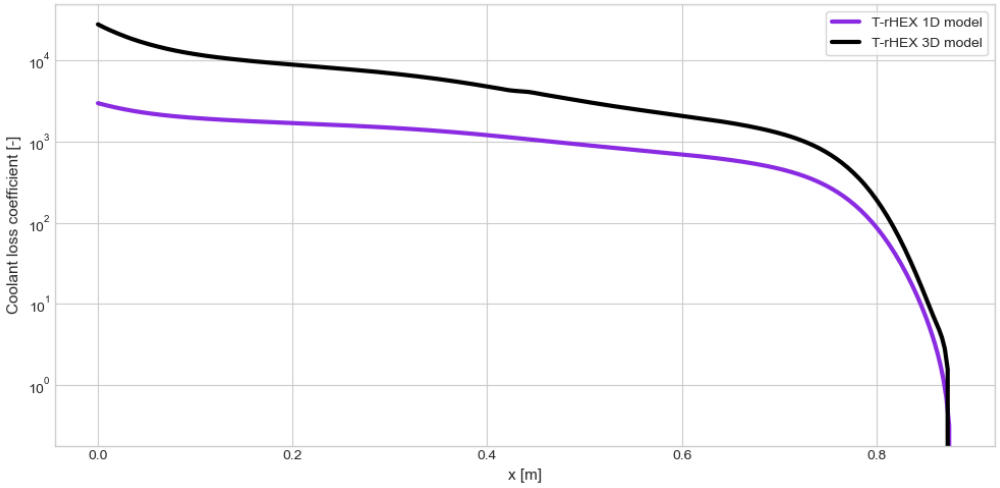

Figure 4.90: Comparison of the loss coefficient between 1D and 3D coolant models along the optimized T-rHEX.

Figure 4.90 shows that coolant channel losses predicted by the high fidelity model are approximately an order of magnitude larger than those obtained with the low fidelity solver. Since heat transfer levels are comparable, the dominant contribution arises from friction and mixing losses driven by the increase in coolant bulk velocity. Because this artificial velocity increase compromises the coolant predictions a definitive quantitative conclusion cannot be drawn. Nonetheless the similarity in the coolant friction coefficient profiles indicates that the pipe flow friction model used in the low fidelity model captures the Reynolds number dependent friction coefficient behavior reasonably.

Research Sub-Question RSQ3

How accurately does the low fidelity (1D) model predict the heat transfer performance of the T-rHEX recuperator compared to the high fidelity (3D) model?

To conclude the higher fidelity modeling of the optimized T-rHEX diffuser, an overview table is given. Table 4.3 displays a comparison between adiabatic and regenerative cases, for both low fidelity (1D) and high fidelity (3D) models.

Table 4.3: Results comparison between low fidelity (1D) and high fidelity (3D) models for the optimized T-rHEX.

	Low fidelity (1D) model: adiabatic	Low fidelity (1D) model: recuperation	High fidelity (3D) model: adiabatic	High fidelity (3D) model: recuperation
Diffuser pressure coefficient [-]	0.879	0.896	0.871	0.907
Thermal power [W]	0	7017	0	6222
Required pump power [W]	0	65.8	0	338.9
Effectiveness [%]	0	22.2	0	19.7
Cycle efficiency[1] [%]	12.09	13.14	12.09	12.64
Total volume [m^3]	0.00245	0.00336	0.00245	0.00351

In terms of diffuser performance, both low fidelity (1D) and high fidelity (3D) models predict pressure recovery similarly, with the high fidelity (3D) model predicting a higher benefit from diffuser cooling. Although a

[1] These efficiency values does accounts for reduced back pressure effects. Without effects, values are 12.11%, 13.16%, 12.11% and 12.66% respectively.

separation bubble is present at the bottom surface of the diffuser outlet, the high fidelity (3D) model still predicts satisfactory exit pressures compared to the low fidelity (1D) model results. Once again, this proves that cooling increases not only ORC efficiency, but also diffuser performance.

In terms of recuperator performance, the low fidelity (1D) model results slightly overpredict recuperated thermal power. subsection 4.3.8 shows how low fidelity (1D) model heat flux distribution along the recuperator aligns well with high fidelity (3D) model results. The inclusion of a solid structure acting as a thermal resistance, however its effect can be considered negligible as the heat flux along the recuperator between the low fidelity model(no conductive resistance) and high fidelity models is approximately the same. Considering convection individually, the diffuser stream shows limited convection capabilities, including a significant overestimation at the inlet by the low fidelity model. The coolant channel shows higher capabilities of heat transfer by convection. Results presented in Figure 4.86 show the high fidelity model undergoes an artificial increase in velocity. Combining both effects allows to conclude that the achievable thermal power is likely slightly lower than values reported in Table 4.3. However, considering that friction effects are also overestimated, the efficiency improvement to the ORC is expected to remain of similar magnitude.

In conclusion, the T-rHEX concept provides a net benefit to the ORC WHR system. Recuperation reduces the thermal duty of the evaporator, as well as cooling of the diffuser increases back pressure while locally improving boundary layer stability against adverse pressure gradients effect on separation. Regarding the validity of the low fidelity model, interchannel heat transfer between adjacent coolant passages is negligible compared to heat transfer from the diffuser to the coolant channel. In addition, the thermal resistance contribution by solid conduction is found to be much smaller than convection thermal resistance by the streams. In particular, diffuser side convection remains the limiting mechanism in heat transfer of the recuperator. Lastly, centrifugal effects have been shown to influence both friction and heat transfer. Given the coolant channel limitations of the high fidelity model in this study, dedicated future work on coolant channel flow is recommended to validate both low and high fidelity model results presented in this study.

5
Conclusions and future work recommendations

5.1. Conclusions

This study evaluates the fluid dynamic and thermal performance characteristics of the Turbo-recuperator Heat Exchanger (T-rHEX) when it is integrated into a high-temperature Organic Rankine Cycle waste heat recovery system. The T-rHEX concept implements the turbine diffuser as an active heat exchanging component by passing a coolant channel around the wetted area of the diffuser. To investigate the fluid dynamics and thermal performance of the T-rHEX, a low fidelity quasi-1D model is developed to establish an analysis tool for the T-rHEX. This model is then compared against a high fidelity conjugate heat transfer model created to capture detailed flow structures and heat transfer effects that are not present in the low fidelity model.

The T-rHEX diffuser is discretized by diving the domain into cells that allow varying semi-opening angles along the diffuser. Additionally, the coolant channel is wrapped around the diffuser. This helicoidal design significantly increases heat transfer compared to pure countercurrent layout. Despite the penalty of two dimensional temperature gradients due to cross-flow effects, the interaction between the diffuser and coolant streams greatly enhances convection locally, resulting in a **53.7**% increase in heat exchanger effectiveness. In contrary, the increased length of the coolant channel results in higher frictional pressure losses, which in turn raises the required pump power for the ORC cycle. Overall, the helicoidal coolant channel design still provides a net efficiency gain of **0.13** percentage points for the ORC system, showcasing the small but relevant increase in cycle efficiency.

The first consideration in developing the T-rHEX is to repurpose the original ORCHID turbine diffuser as a recuperator. However, the unconventional nature of the heat exchanger limits the convection abilities of both the diffuser and coolant streams. Thermal boundary layer development within the diffuser causes the highest heat flux to occur near the inlet, while the remaining diffuser maintains an approximately constant heat flux across its wetted area. The low-fidelity (1D) model predicts a heat-exchanger effectiveness of **8.36**%, which is relatively low compared to commercial heat exchangers. However, the inclusion of the recuperated thermal power allows for an increases in ORC efficiency by **0.42** percentage points, with only a reduced volumetric increase due to the inclusion of the coolant channels. As a result, the thermal duty of the primary evaporator and condenser is proportionally downsized, reducing the overall weight of each component and therefore increasing the power density of the waste heat recovery system.

Geometrical optimization of the T-rHEX shows that improvements are possible. The optimized T-rHEX increases heat transfer effectiveness from **8.36**% to **22.2**%, more than doubling recuperated thermal power. This leads to an ORC efficiency increase of **1.05** percentage points (**8.7**% relative efficiency increase with respect to the baseline without recuperation), which significantly reduces the thermal duty of the evaporator and condenser. On the other hand, the increase in length of the diffuser leads to an increase in length of the coolant channel. For this reason, pressure losses due to friction increase, leading to higher pump power requirements that limit the potential further increase in cycle efficiency. Furthermore, the elongated T-rHEX increases volumetric requirements, which is expected to increase the recuperation component weight of the WHR system. However, the beneficial downsize of the primary heat exchanger components (evaporator and condenser) is expected to offset or even surpass the additional increment in recuperator weight. Finally, the comparison between the original turbine diffuser as a recuperator, the baseline T-rHEX presented in literature, and the optimized T-rHEX shows how the optimized T-rHEX outperforms both previous models in heat transfer performance, cycle efficiency, and heat exchanger compactness. In contrast, the optimized T-rHEX diffuser has reduced pressure recovery, which leads to a reduction in diffuser back pressure and therefore

condenser saturation pressure. This effect increases heat rejection, which in effect leads to a lower ORC efficiency. Nevertheless, the predicted effect on cycle efficiency reduction is minor compared to the efficiency increment due to recuperation, leaving the optimized T-rHEX as the preferred choice for recuperator design.

To verify low fidelity (1D) model results, both the original ORCHID turbine diffuser and optimized T-rHEX geometries are analyzed using the high fidelity (3D) model. The high fidelity model of the existing ORCHID diffuser with recuperation reveals that flow separation forms downstream of the diffuser inlet and persists along the bottom wall. Cooling of the diffuser contributes to the stabilization of the boundary layer by means of viscosity gradients and baroclinic torque. Both effects mitigate destabilizing effects of adverse pressure gradients within boundary layer flow. Additionally, non-axisymmetric buoyancy effects play a role, increasing thermal mixing in the top surface while decreasing thermal mixing in the bottom surface. The combination of both effects leads to a change of the separation bubble within the diffuser compared to their adiabatic case. With regard to the comparison of quasi-1D results to 3D results, the low fidelity model shows good approximations with respect to diffuser fluid dynamic trends. Naturally, the presence of the separation bubble leads to discrepancies, however regions where flow remains attached show acceptable correlation between low and high fidelity models. Thermodynamic properties that have strong radial variations such as temperature show slightly more deviation from quasi-1D model results. In terms of the coolant channel, the high fidelity model predicts a significant velocity increase compared to the low fidelity model. The pressure losses due to friction are therefore significantly under predicted by the low fidelity model. Moreover, high fidelity model errors are found due to the coolant coarse mesh resolution and due to poor orientation of the inlet and outlet coolant boundary conditions. The transition in wall treatment models due to increasing y+ values leads to inaccuracies of convective heat transfer and friction estimates, which then propagate through the coolant domain. Overall, despite the presence of a separation bubble within the diffuser, its influence on heat transfer performance is limited because the upward displacement of the core flow increases local convection on the upper wall. The high fidelity model therefore predicts an ORC efficiency of **12.06**%, compared to the low fidelity model ORC efficiency of **12.53**%. This is due not only to a decrease in recuperated thermal power but instead due to the increase in required pump power to overcome pressure losses.

As the volume of the optimized T-rHEX is larger, the discretization requires a higher number of cells. Due to computational cost, a decision to sacrifice coolant channel resolution is taken. This allows to maintain the resolution of the diffuser flow and solid region while applying a consistent wall treatment for the coolant region. The optimized T-rHEX displays significantly improved fluid dynamic behavior with delayed separation, leading to similar flow expansion results between low and high fidelity models. Diffuser pressure coefficients match results of the low fidelity model as well as show how cooling increases affect pressure recovery. In terms of heat transfer, the low fidelity model results closely match the values predicted by the high fidelity model, except for the diffuser inlet thermal boundary layer development effects, which are over predicted by the low fidelity model. Diffuser fluid dynamic properties between low and high fidelity models shows close resemblance, allowing the conclusion that the `N1D-Flow` module performs well when calculating fluid dynamic properties for quasi-1D flows. On the other hand, the coolant channel properties deviate due to mesh coarsening and mass conservation imbalance. This effect compromises the magnitude of the coolant channel results. Nevertheless, the general qualitative trends between the low fidelity and high fidelity model results remain consistent, making them valuable for evaluating the thermal performance of the T-rHEX. Overall, the high fidelity model results in an ORC efficiency of **12.64**%, which is lower than the low fidelity model value of **13.14**%. Primarily, the low fidelity mode overestimates heat transfer at the inlet of the diffuser. Moreover, the estimated coolant channel pressure losses are much higher for the high fidelity model than the low fidelity model, once again leading to higher required pump power, and thus a lower thermal efficiency

The combined numerical results demonstrate that the optimized T-rHEX improves cycle efficiency compared to the original organic Rankine cycle without recuperation. The addition of a compact recuperator such as the T-rHEX not only reduces thermal duty of the primary heat exchanger components of the cycle but also may increases diffuser pressure recovery. Cooling increases total pressure, allowing for higher pressure rise when expanding flows. Furthermore, cooling is found to delay flow separation by reducing the effect of the adverse pressure gradient on boundary layer stability. While this study is limited to the implementation of the recuperator component for the representative high-temperature ORC system, the T-rHEX concept can be used for other industrial applications for the purpose of waste heat recovery or improving diffuser performance.

5.2. Recommendations for future work

Throughout this study, several modeling limitations have been identified. These limitations highlight opportunities for further research aimed at improving the T-rHEX concept. From a modeling perspective the following future work recommendations are given to enhance both the low fidelity and high fidelity frameworks:

1. **Coupled turbine-diffuser modeling:** Currently, the implementation of the numerical scheme within the flow solver (`N1D-Flow`) starts from prescribed inlet conditions. This is appropriate for the coolant channel as inlet conditions are imposed by the condenser. However, variations in diffuser back pressure lead alter the condenser operation point. For a more realistic analysis, both turbine inlet conditions and diffuser exit conditions should be fixed. The diffuser flow should then be solved starting from exit conditions upstream, thus the work done of the turbine should be modeled as a function of achieved diffuser inlet conditions. By coupling the turbine and diffuser, the effect of the T-rHEX can be analyzed not only on diffuser and turbine performance but also on the cycle itself.
2. **Implementation of a valid quasi-1D separation criterion:** The current quasi-1D solver used in `T-rHEX.py` cannot predict boundary layer separation. Introducing a separation criterion consistent with diffuser flow physics would enable the model to predict flow conditions where quasi-1D assumptions break down and provide a more reliable basis for geometry optimization.
3. **Improvement of the high fidelity modeling:** To improve coolant channel predictions in the high fidelity model, an improved mesh and boundary conditions are required. Given the complexity of the conjugate heat transfer problem, a split iterative approach between the diffuser flow simulation and coolant channel flow simulation connected using mapped thermal interfaces could be employed, allowing to increase mesh resolution per simulation. This improvement could allow for an improved comparison to the low fidelity (1D) model to further tune it for improved accuracy. Additionally, the currently used uniform diffuser inlet conditions introduces numerical instabilities near the walls which could potentially affect separation downstream. A more realistic inlet velocity profile derived from turbine exit measurements or validated sources (such as [9]) would reduce these errors and allow for a more accurate simulation of the diffuser wall bounded effects.
4. **Turbulence modeling under thermal gradients:** Heat transfer has been shown to play a central role in diffuser flow separation. Further investigation on the interaction of baroclinic instabilities with the boundary layer under adverse pressure gradients can be beneficial to understand the turbulence mechanism effects due to heat transfer on diffuser flows. The use of a different turbulence model such as Reynolds Stress Models (RSM), or by using a higher-fidelity solver, for instance through Large Eddy Simulation (LES), can be used to understand the turbulence mechanisms of baroclinic instabilities on diffuser flows. Insights from such studies could support the development of a quasi-1D boundary layer stability indicator for future optimization work.

References

[1] I. H. Bell et al. “Pure and Pseudo-pure Fluid Thermophysical Property Evaluation and the Open-Source Thermophysical Property Library CoolProp”. In: *Industrial & Engineering Chemistry Research* 53.6 (2014), pp. 2498–2508. DOI: 10.1021/ie4033999.

[2] P. Colonna. “T-rHEX: A Study on a Novel Concept of Integrated Turbo Recuperator for Airborne Waste Heat Recovery”. MA thesis. TU Delft, 2024.

[3] E.M. Greitzer, C.S. Tan, and M.B. Graf. *Internal Flows Concepts and Applications*. First edition. [Accessed: 24-03-2025]. Cambridge University Press, 2004. ISBN: 978-0-511-19553-2.

[4] A. Guardone et al. “Nonideal Compressible Fluid Dynamics of Dense Vapors and Supercritical Fluids”. In: *Annual Review of Fluid Mechanics* 56 (2024). DOI: https://doi.org/10.1146/annurev-fluid-120720-033342.

[5] J. E. Hesselgreaves, R. Law, and D. A. Reay. *Compact Heat Exchangers*. Butterworth-Heinemann, 2016. ISBN: 978-0-08-100305-3.

[6] W. J. Kelnhofer. “Wall Temperature and Prandtl Number Effects on Turbulent Boundary Layers”. In: *Journal of Engineering for Power* 91.4 (1969), pp. 281–290. DOI: 10.1115/69-GT-55.

[7] K Kowalski and D. Downarowicz. “Heat transfer in helical coil heat exchanger: An experimental parametric study”. In: *Chemical and Process Engineering* 40.1 (2019), pp. 101–114. DOI: 10.24425/cpe.2019.126104.

[8] D. Krempus. “Organic Rankine Cycle Waste Heat Recovery Systems for Aircraft Engines”. PhD thesis. TU Delft, 2025.

[9] L. Matabuena. “Radial Turbine - Diffuser Interaction”. MA thesis. TU Delft, 2023.

[10] VDI Gesellschaft mbH, ed. *Heat Atlas*. 2nd ed. Heidelberg, Germany: Springer, 2018. ISBN: 978-3-540-77876-9.

[11] D. Orrego et al. “Experimental and CFD study of a single-phase cone-shaped helically coiled heat exchanger: an empirical correlation”. In: *ECOS 2012: The 25th International Conference on Efficiency, Cost, Optimization and Simulation of Energy Conversion Systems and Processes*. 2012.

[12] C. Osnaghi. *Teoria delle turbomacchine*. [Accessed: 02-04-2025]. Esculapio, 2002. ISBN: 978-88-9385-218-0.

[13] S.B. Pope. *Turbulent FLows*. First edition. [Accessed: 05-05-2025]. Cambridge University Press, 2000. ISBN: 978-0-521-59125-6.

[14] D. Serrano et al. “Experimental determination of the convection heat transfer coefficient in an eccentric annular duct”. In: *Experimental Thermal and Fluid Science* 136 (2022), p. 110664. ISSN: 0894-1777. DOI: https://doi.org/10.1016/j.expthermflusci.2022.110664.

[15] Siemens Digital Industries Software. *STAR-CCM+ User Guide*. Version 2310. 2025. URL: https://support.sw.siemens.com.

[16] F. Tosto. “Modelling and Characterization of Non-Ideal Compressible Flows in Unconventional Turbines”. MA thesis. TU Delft, 2023.

[17] H. Zhao et al. “Friction factor and Nusselt number correlations for forced convection in helical tubes”. In: *International Journal of Heat and Mass Transfer* 155 (2020), p. 119759. DOI: 10.1016/j.ijheatmasstransfer.2020.119759.

A

Derivation of Boundary Layer Stability Criterion

Let us consider once again the RANS momentum equation (Equation 2.27).

$$< u_j > \frac{\partial\left(< u_i >\right)}{\partial x_j} + \frac{\partial\left(< u_i' u_j' >\right)}{\partial x_j} + \frac{1}{\rho}\frac{\partial < p >}{\partial x_i} - \frac{1}{\rho}\left(\mu\frac{\partial^2 < u_i >}{\partial x_j^2} + \frac{\partial\mu}{\partial x_j}\frac{\partial < u_i >}{\partial x_j}\right) = 0 \tag{A.1}$$

Since the stability criterion is applicable at the wall, the velocities at the wall must be zero ($< u_j >$=0), thus the first term cancels out ($< u_j > \frac{\partial(< u_i >)}{\partial x_j} = 0$). For the Reynolds Stress tensor term, if the boundary layer is laminar, the term becomes zero. However for a turbulent channel flow, this is not the case.

For evaluating the stability condition, the axial component is used ($i = x$) since it is the most relevant component to account for adverse pressure gradients and velocity profiles in diffusers with limited semi-opening angles.

$$\frac{\partial\left(< u_x' u_j' >\right)}{\partial x_j} + \frac{1}{\rho}\frac{\partial < p >}{\partial x} - \frac{1}{\rho}\left(\mu\frac{\partial^2 < u_x >}{\partial x_j^2} + \frac{\partial\mu}{\partial x_j}\frac{\partial < u_x >}{\partial x_j}\right) = 0 \tag{A.2}$$

With the following expanded terms:

$$\frac{\partial\left(< u_x' u_j' >\right)}{\partial x_j} = \frac{\partial\left(< u_x' u_x' >\right)}{\partial x} + \frac{\partial\left(< u_x' u_y' >\right)}{\partial y} + \frac{\partial\left(< u_x' u_z' >\right)}{\partial z} \tag{A.3}$$

$$\frac{\partial^2 < u_x >}{\partial x_j^2} = \frac{\partial^2 < u_x >}{\partial x^2} + \frac{\partial^2 < u_x >}{\partial y^2} + \frac{\partial^2 < u_x >}{\partial z^2} \tag{A.4}$$

$$\frac{\partial\mu}{\partial x_j}\frac{\partial < u_x >}{\partial x_j} = \frac{\partial\mu}{\partial x}\frac{\partial < u_x >}{\partial x} + \frac{\partial\mu}{\partial y}\frac{\partial < u_x >}{\partial y} + \frac{\partial\mu}{\partial z}\frac{\partial < u_x >}{\partial z} \tag{A.5}$$

Now, assuming scale similarity principle, the axial viscous term $\frac{\partial^2 < u_x >}{\partial x^2}$ is much smaller than the perpendicular terms $\frac{\partial^2 < u_x >}{\partial y^2}$ & $\frac{\partial^2 < u_x >}{\partial z^2}$. This is based on comparison of shear stresses and their characteristic length scales. Since the diffuser length being much larger than the boundary layer height, it can be said that the contribution of shear stress axially is much smaller than its perpendicular components (pg. 171, ch. 4.2 *"The boundary layer equations"*[3]).

Now to remove the dependency on Cartesian frame of reference, all terms with non-axial components are transformed to cylindrical coordinates where $y = r\sin\theta$ and $z = r\cos\theta$. For the Laplacian term, the following is obtained:

$$\frac{\partial^2 < u_x >}{\partial x_j^2} = \frac{\partial^2 < u_x >}{\partial x^2} + \frac{\partial^2 < u_x >}{\partial r^2} + \frac{1}{r}\frac{\partial < u_x >}{\partial r} + \frac{1}{r^2}\frac{\partial^2 < u_x >}{\partial\theta^2} \tag{A.6}$$

From the scale similarity principle, $\frac{\partial^2 < u_x >}{\partial x^2}$ was negligible. Additionally, by assuming radial symmetry condition, which implies conditions only vary along the radial direction, then derivatives of the tangential direction are null ($\frac{\partial}{\partial\theta} = 0$). Because of this assumption, $\frac{\partial^2 < u_x >}{\partial\theta^2}$ is also null.

For the first derivative terms:

$$\frac{\partial}{\partial x} = \frac{\partial}{\partial x} \tag{A.7}$$

$$\frac{\partial}{\partial y} = \frac{\partial}{\partial r}\frac{\partial r}{\partial y} + \frac{\partial}{\partial \theta}\frac{\partial \theta}{\partial y} = \frac{y}{r}\frac{\partial}{\partial r} \tag{A.8}$$

$$\frac{\partial}{\partial z} = \frac{\partial}{\partial r}\frac{\partial r}{\partial z} + \frac{\partial}{\partial \theta}\frac{\partial \theta}{\partial z} = \frac{z}{r}\frac{\partial}{\partial r} \tag{A.9}$$

Substituting terms into Equation A.2 and exploiting the trigonometric identity that $\frac{y^2}{r^2} + \frac{z^2}{r^2} = 1$, the cylindrical frame of reference momentum equation at the wall is obtained.

$$\rho\frac{\partial\left(< u_x' u_x' >\right)}{\partial x} + \rho\left(\frac{y}{r} + \frac{z}{r}\right)\frac{\partial\left(< u_x' u_r' >\right)}{\partial r} + \frac{\partial < p >}{\partial x} = RHS \tag{A.10}$$

$$LHS = \mu\left(\frac{\partial^2 < u_x >}{\partial r^2} + \frac{1}{r}\frac{\partial < u_x >}{\partial r}\right) + \frac{\partial \mu}{\partial x}\frac{\partial < u_x >}{\partial x} + \frac{\partial \mu}{\partial r}\frac{\partial < u_x >}{\partial r} \tag{A.11}$$

Considering the right hand side, the fluctuations at the wall must be null due to the no slip condition. Thus considering the diffuser semi-opening angle to be relatively small (both ORCHID and baseline T-rHEX implement semi-opening angles below 10 degrees[2]), the derivative of the fluctuations along the axial can be assumed negligible ($\frac{\partial\left(< u_x' u_x' >\right)}{\partial x} \approx 0$), since it approximates the derivatives of the fluctuations along the wall. For the perpendicular component, the component must be evaluated by numerical or experimental data. Pope[13] described using Spalart's Direct Numerical Simulation (DNS) data how each component behaves near the wall with respect to $y+$.

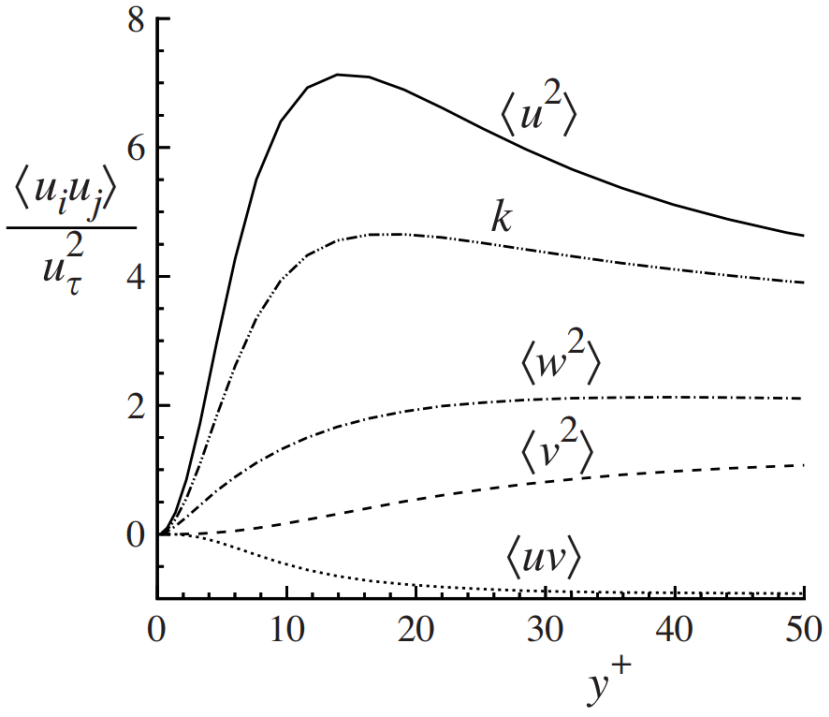

Figure A.1: Profiles of Reynolds stresses and kinetic energy normalized by the friction velocity in a turbulent boundary layer at Re_θ = 1410) in the viscous near-wall region (Figure 7.33 of Turbulent Flows by Pope[13]).

From the description of Figure 7.33 of the Turbulent Flows book[13], it can be seen that the stream wise fluctuations ($< u_x' u_x' >$) are dominant along the boundary layer. Their growth is significant as you get away from the wall. This has to do because in a turbulent boundary layer, turbulence production is mostly in the streamwise component ($< u_x' u_x' >$)[13]. This component then redistributes to other components ($< u_y' u_y' >$ and ($< u_z' u_z' >$)), which follow in growth shortly after. On the other hand, the cross stream fluctuations ($< u_x' u_y' >$ for example), show development further from the wall. These components gain kinetic energy

by shear of streamwise components. Because of this, the cross stream components have a mayor delay in growth compared to streamwise components. This delay is shortened as the Reynolds number increases[13].

Going back to Equation A.10, since only the gradient of the cross stream component shows up, it can be assumed that at the wall, this component is small. For the purpose of this study, since Figure A.1 shows $\frac{\partial(<u'_x u'_r>)}{\partial r} \approx 0$ until y_+ values of 5 (all of the viscous sublayer), the contribution of the term at the wall can be considered negligible.

After all of these considerations, expanding remaining terms of Equation A.10 results in Equation 2.28, where the velocity profile is dependent on the adverse pressure gradient, both axial and radial velocity gradients, and dynamic viscosity gradients.

$$\frac{1}{\mu}\frac{\partial\langle p\rangle}{\partial x} - \frac{1}{\mu}\frac{\partial\mu}{\partial x}\frac{\partial\langle u_x\rangle}{\partial x} - \frac{1}{\mu}\frac{\partial\mu}{\partial r}\frac{\partial\langle u_x\rangle}{\partial r} - \frac{1}{r}\frac{\partial\langle u_x\rangle}{\partial r} = \frac{\partial^2\langle u_x\rangle}{\partial r^2} < 0 \tag{A.12}$$

B

Low fidelity Friction Model Descriptions

Within this section of the appendix, models implemented both for N1D_Flow and TrHEX are described to a basic standard with the goal to provide further understanding to the reader. For specific details, please refer to original source.

B.1. Osnaghi's diffuser friction model

Osnaghi uses the power dissipation analogy across the boundary layer of a diffuser to define the enthalpy loss by the fluid, by defining the loss coefficient as the following:

$$\zeta_1 = \frac{\Delta h_f}{\frac{1}{2}u_1^2} = \bar{c}_f \Phi_1 \tag{B.1}$$

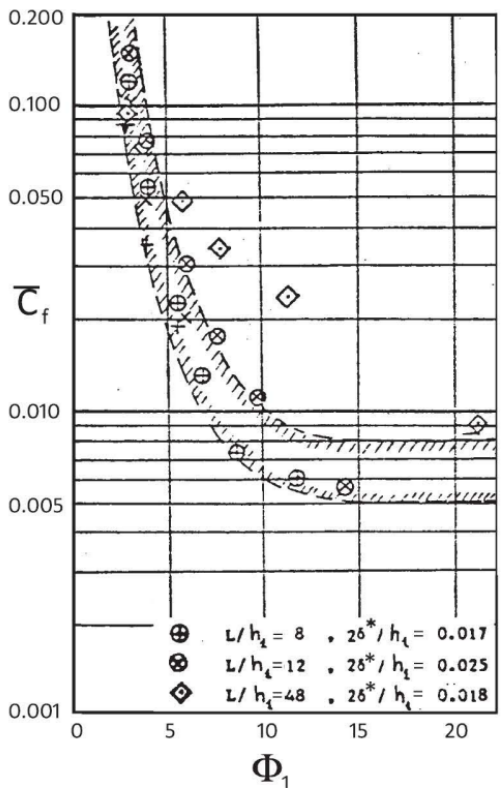

Figure B.1: Friction coefficient for rectangular diffusers as a function of the form factor.

In Equation B.1, the friction coefficient ($\bar{c}_f$) is defined as a local property of the fluid based on the shear stress divided by the dynamic pressure component, leading to dissipation of kinetic energy of the flow. Additionally, the dimensionless form factor (Φ_1) accounts for geometric changes along the diffuser.

$$\bar{c}_f = \frac{\tau}{\frac{1}{2}\rho u^2} \tag{B.2}$$

$$\Phi_1 = \int_1^2 \left(\frac{\rho_1 S_1}{\rho S}\right)^2 \frac{c}{S} dl \tag{B.3}$$

While the friction coefficient is a function of the shear stress of the flow and inlet dynamic pressure, the dimensionless factor can be used as a direct scaling parameter to understand how much kinetic energy loss is present due to wall shear.
Now consider the dimensional form factor, Osnaghi derived that for a incompressible conical diffuser, considering the effect of adverse pressure gradients on boundary layers, the form factor can be written as follows:

$$\Phi_1 = \frac{1}{2\tan\theta}\left[1 - \left(\frac{r_{\text{inlet}}}{r_{\text{outlet}}}\right)^4\right] \tag{B.4}$$

Generally friction coefficient values for diffusers are much greater than for constant cross-section ducts, due to the development of the boundary layer in presence of a positive pressure gradients[12].

The form factor is an index of recompression gradient. Small values of Φ_1 imply faster recompression (higher pressure recovery). Thus it is logical to assume that the friction coefficient is a function of the form factor.

Osnaghi performed experiments with different length to inlet radius ratios on rectangular diffusers, to understand the behavior of friction coefficient with form factor.

As you can see in Figure B.1, as the form factor increases, the friction coefficient of the diffuser reduces. An increase in form factor implies that the diffuser has a decreased semi-opening angle as well as an increase in length, approaching similar flow conditions as a pipe flow. This flow condition does not encounter adverse pressure gradients and separation losses are significantly reduced. When the form factor is smaller, the semi-opening angle of the diffuser is larger as well as the length of the diffuser is reduced. This leads to higher pressure recovery and thus stronger adverse pressure gradients. This leads to stronger separation losses. Osnaghi compiled both separation effects with wall friction into the same parameter, as $\bar{c}_f$ is labeled dissipation coefficient. For the purpose of this study, this friction model will account both for friction losses as well as separation losses.

B.2. Pipe friction model

Pipe friction models have been extensively studied to model friction in a 1-dimensional flow. Many authors have come to different conclusions on what the true semi-empirical formula should contain to best model friction in 1D flows. However, almost all authors conclude that the most critical parameters affecting friction are the turbulence state of the flow, which is measured by the pipe Reynolds number (Re_D), the surface roughness ratio (roughness in length over channel diameter), and geometrical factors accounting for channel path effects on the flow. This study has only focused on simple straight channels, and helicoidal channels.

To model the simple straight channels, an adapted version of the Blasius equation have been used as describeb, which later during validation is slightly modified to fit better with experimental results.

To model the simple straight channels, an adapted version of both the Mishra and Gupta, as well as White models were implemented considering the curvature ratio of the channel (δ) based on validatino data comparison[17].

$$\text{For } Re_D < 10^5: \quad C_f = 0.317\, Re_D^{-1/4} + 0.0075\sqrt{\delta} \tag{B.5}$$

$$\text{For } Re_D \geq 10^5: \quad C_f = \left(1.8\log_{10}\left(\tfrac{Re_D}{6.9}\right)\right)^{-2} + 0.014\sqrt{\delta} \tag{B.6}$$

By adding the curvature ratio term, the secondary flow effects can be considered, which allows to introduce effects due to centripetal forces on the helicoidal channel flow are taken into account in a simplified manner. Both straight and helicoidal models only consider skin friction, thus separation must be considered in an alternative model. In addition, both of these models are simple. As given in chapter 4, the low fidelity friction models over predict high fidelity results. The author suggest to split the friction model into a a straight pipe model and a helicoidal pipe model. This allows to integrate the full effect of secondary flows by means of the Dean number ($De = Re\sqrt{\delta_{\text{curvature}}}$).